Downloaded from orbit.dtu.dk on: Dec 19, 2017

Technical University of Denmark

Quasi-3d aerodynamic code for analyzing dynamic flap response

Ramos García, Néstor; Sørensen, Jens Nørkær; Shen, Wen Zhong

Publication date:
2011

Document Version
Publisher's PDF, also known as Version of record

Link back to DTU Orbit

Citation (APA):
Ramos García, N., Sørensen, J. N., & Shen, W. Z. (2011). Quasi-3d aerodynamic code for analyzing dynamic flap response. Kgs. Lyngby, Denmark: Technical University of Denmark (DTU).

DTU Library
Technical Information Center of Denmark

General rights
Copyright and moral rights for the publications made accessible in the public portal are retained by the authors and/or other copyright owners and it is a condition of accessing publications that users recognise and abide by the legal requirements associated with these rights.

- Users may download and print one copy of any publication from the public portal for the purpose of private study or research.
- You may not further distribute the material or use it for any profit-making activity or commercial gain
- You may freely distribute the URL identifying the publication in the public portal

If you believe that this document breaches copyright please contact us providing details, and we will remove access to the work immediately and investigate your claim.

Unsteady Viscous-Inviscid Interaction Technique for Wind Turbine Airfoils

PhD Thesis

$$(EIv'')'' = q - \rho A \ddot{v}$$

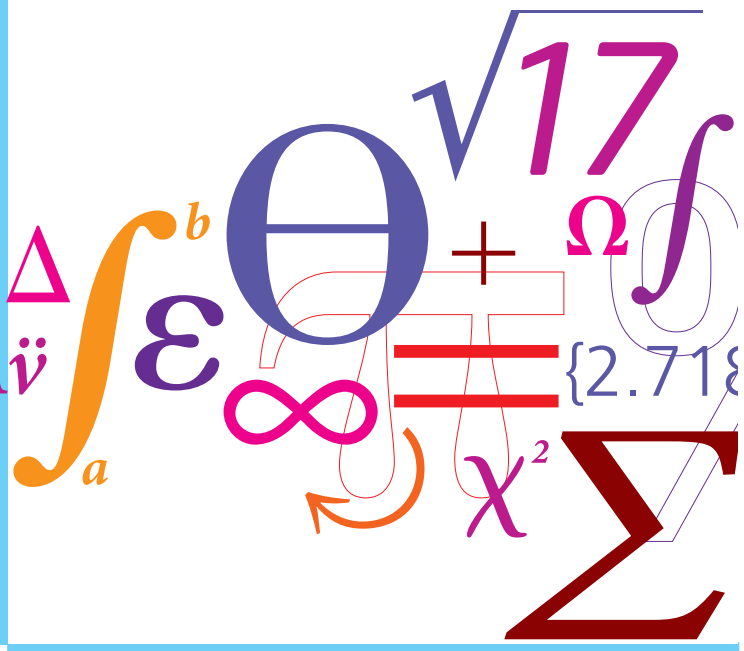

Néstor Ramos García
DCAMM Special Report no. S127
April 2011

DTU Mechanical Engineering
Department of Mechanical Engineering

MEK-PHD 2011-04

Unsteady Viscous-Inviscid Interaction Technique for Wind Turbine Airfoils

Néstor Ramos García

Dissertation submitted to the Technical University of Denmark in partial fulfillment of the requirements for the degree of Doctor of Philosophy in Mechanical Engineering

Fluid Mechanics
Department of Mechanical Engineering
Technical University of Denmark
April, 2011

Fluid Mechanics
Department of Mechanical Engineering
Nils Koppels Allé, Building 403
Technical University of Denmark
DK-2800 Lyngby, Denmark

Copyright © Néstor Ramos García, 2011

Printed in Denmark, Lyngby

MEK-PHD 2011-04 / ISBN 978-87-90416-53-9

DCAMM Special Report no. S127

This thesis has been typeset using LaTeX2e.

Preface

This dissertation is submitted in partial fulfillment of the requirements for the PhD degree from the Technical University of Denmark. The dissertation is based on research work conducted during the period from April 2009 to April 2011 at the Department of Mechanical Engineering, Fluid Mechanics Section.

It is a pleasure to thank my supervisors Professor Jens Nørkær Sørensen and Associate Professor Wen Zhong Shen for their guidance and support during the course of this work. I would also like to thank all my colleagues in the Fluid Mechanics section at DTU for creating a wonderful working atmosphere in which I could develop my research skills.

I would also like to express my sincere thanks to my parents Miguel and Maria Rosa for their constant support and encouragement. Finally, I would like to thank Freya for her love, support and understanding which enabled me to fully focus on my research.

This study has been funded by Højteknologifonden.

Technical University of Denmark

København, April 2011

Néstor Ramos García

Abstract

A computational model for predicting the aerodynamic behavior of wind turbine airfoil profiles subjected to steady and unsteady motions has been developed. The model is based on a viscous-inviscid interaction technique using strong coupling between the viscous and inviscid parts. The inviscid part is modeled using a panel method whereas the viscous part is modeled by using the integral form of the the laminar and turbulent boundary layer equations and with extensions for 3-D rotational effects. Laminar to turbulent transition can be forced with a boundary layer trip or computed with a modified e^9 transition model. Validation of the steady two dimensional version of the code has been carried out against experiments for different airfoil geometries and Reynolds numbers. The unsteady version of the code has been benchmarked against experiments for different airfoil geometries at various reduced frequencies and oscillation amplitudes, and generally a good agreement is obtained. The capability of the code to simulate a trailing edge flap under steady or unsteady flow conditions has been proven. A parametric study on rotational effects induced by Coriolis and centrifugal forces in the boundary layer equations shows that the effect of rotation is to decrease the growth of the boundary layer, delay the onset of separation, and hence increase the lift coefficient and decrease the drag slightly.

Nomenclature

α	Airfoil angle of attack
α_m	Airfoil mean angle of attack during its harmonic pitch motion
β	Trailing edge flap deflection
β_m	Mean flap deflection during the harmonic flap oscillation
β_w	Angle in between the external and limiting streamlines
χ	iWings angle of attack
χ_m	iWings mean angle of attack during its harmonic pitch motion
ΔH	Jump in total pressure inside the separation bubble
δ	Boundary layer thickness
$\Delta\chi$	iWings amplitude during its harmonic pitch motion
δ_1^*	Streamwise displacement thickness
δ_2^*	Spanwise displacement thickness
δ_N	Nominal boundary layer thickness
γ	Vortex strength
Γ_B	Total airfoil circulation
γ_H	Specific heat
γ_{lower}	Lower wake constant vorticity strength
Γ_{SiW}	iWings circulation
γ_{upper}	Upper wake constant vorticity strength
Γ_{wiW}	iWings wake vortex strength
Γ_W	Wake vortex strength
κ^*	Curvature of the displacement surface
λ	Thwaites parametric function
λ	Wind turbine tip speed ratio

$\mathbf{u_W}$	Velocity induced by the wake
$\mathbf{U}$	Velocity on a random point P
$\mathbf{u}$	Velocity induced by the body
μ	Doublet strength
μ	Fluid viscosity
ν	Kinematic viscosity
Ω	Blade angular velocity
ω	Relaxation factor
Φ	Flow potential
ρ	Fluid density
σ	Source strength
σ^R	Rotating onset flow related source strength
σ^W	Single wake influence related airfoil source strength
σ_{w_T}	Transpiration velocity related source strength
τ_θ	Shear stress in the streamwise direction
τ_r	Shear stress in the spanwise direction
τ_w	Wall shear stress
θ, r, z	Cylindrical coordinates
θ^*	Kinetic energy thickness
θ_1	Streamwise momentum thickness
θ_2, θ_{22}, δ_{2xr}	Momentum thickness parameters due to crossflow
$\underline{\underline{A}}$	Influence matrix of the potential flow, alternative notation to A_{ij}
$\underline{\underline{B}}$	Influence matrix of the potential flow, alternative notation to B_{ij}
$\underline{n}$	Normal vector
$\underline{t}$	Tangential vector
$\underline{v}$	Flow velocity vector
φ	Phase shift between the airfoil and the flap motions
A	Amplitude of the airfoil harmonic pitch motion
a, a'	Tangential and axial interference factors

A_{ij}	Influence matrix of the potential flow
B_{ij}	Influence matrix of the potential flow
c	Chord length
$C_L^{Dynamic}$	Lift coefficient during dynamic airfoil motion
C_L^{Static}	Lift coefficient under static conditions
$C_{\tau EQ}$	Equilibrium shear stress coefficient
C_τ	Shear stress coefficient
C_{Df}	Friction drag force coefficient
C_{Di}	Dissipation coefficient
C_{Dp}	Pressure drag force coefficient
C_D	Drag force coefficient
C_f	Friction coefficient
$C_{L_{MAX}}$	Maximum lift force coefficient
C_L	Lift force coefficient
C_M	Pitch moment coefficient
$C_{N_{MAX}}$	Maximum normal force coefficient
C_N	Normal force coefficient
C_p	Surface pressure coefficient
C_T	Tangential force coefficient
CEN_r	Centrifugal force term in the integral r momentum equation
$CONV$	Relative convective terms in both the integral r and θ momentum equation
COR_θ	Coriolis force term in the integral θ momentum equation
COR_r	Coriolis force term in the integral r momentum equation
D	Drag force
dS	Differential of surface
dt	Differential of time
dV	Differential of fluid volume
ex	Airfoil extremity point
f_A	Airfoil harmonic motion frequency
f_{iW}	iWings harmonic motion frequency

G_{MATRIX}	Viscid-Inviscid system global matrix
H	Shape factor
H^*	Kinetic energy shape parameter
H_{inner}	Total pressure inside the separation bubble
H_{outer}	Total pressure outside the separation bubble
k_A	Airfoil harmonic motion reduced frequency
k_F	Flap harmonic motion reduced frequency
k_H	Double wake correction constant
k_{iW}	iWings harmonic motion reduced frequency
k_{PI}	PI controller constant
L	Arc length from the leading edge to the trailing edge
L	Lift force
ls	Local aspect ratio
M	Pitch moment
m	Mass flow
Ma	Mach number
N	Normal force
N	Number of panel elements
n	Amplification factor
n_C	Critical amplification factor
OVR	Overshoot of the maximum lift coefficient
p	Pressure
p_∞	Pressure at ∞
P_e	Real flow pressure at the edge of the boundary layer
p_{inner}	Static pressure inside the separation bubble
P_{IW}	Wall pressure of the equivalent inviscid flow
p_{outer}	Static pressure outside the separation bubble
p_r	Airfoil surface projector
P_W	Wall pressure of the real flow
Q_W	Wind speed

R	Radius of a wind turbine rotor
r	Distance in between two points
r	Local spanwise position on a wind turbine blade
r_{WT}	Wind tunnel panels reduction factor; atanh function
Re	Reynolds number
$Re_{\theta_1}^{CR}$	Critical Reynolds number based in θ_1
Re_{θ_1}	Reynolds number based in θ_1
RHS	Right hand side vector
RO	Rotational number
S	Surface
s	Streamwise position
s'	Coordinate from the stagnation chordwise towards the trailing edge
S_∞	Fluid volume boundaries
S_a	Length of the airfoil contour
S_B	Solid body surface
s_{real}	Arc length from the stagnation point to the trailing edge
s_w	Sign function
T	Tangential force
t	Time
$TH1, TH2$	Double wake directions initial directions
TI	Turbulence intensity
$tstep$	Number of time steps during an unsteady computation
u	Tangential velocity induced by a singularity in global coordinates
u, v, w	Boundary layer velocities
$U_{\infty x}$	Component of U_∞ measured along the chord
$U_{\infty y}$	Component of U_∞ measured normal to the chord
U_∞	Free stream velocity
u_τ	Wall friction velocity, $\sqrt{\tau_W/\rho}$
u_e	Boundary layer edge parallel velocity

u_{LE}	Tangential velocity induced in global coordinates by a leading edge vortex
$u_{p\,LE}$	Tangential velocity induced in panel coordinates by a leading edge vortex
$u_{p\,TE}$	Tangential velocity induced in panel coordinates by a trailing edge vortex
u_p	Tangential velocity induced in panel coordinates
U_{rel}	Blade relative velocity
u_R	Rotating onset flow induced tangential velocity component
U_s	Equivalent normalized wall slip velocity
u_{TE}	Tangential velocity induced in global coordinates by a trailing edge vortex
u_{w_T}	Transpiration velocity induced tangential velocity component
u_W	Wake induced tangential velocity component
u_x	Translating onset flow induced tangential velocity component
V	Fluid volume
v	Normal velocity induced by a singularity in global coordinates
v_{LE}	Normal velocity induced in global coordinates by a leading edge vortex
$v_{p\,LE}$	Normal velocity induced in panel coordinates by a leading edge vortex
$v_{p\,TE}$	Normal velocity induced in panel coordinates by a trailing edge vortex
v_p	Normal velocity induced in panel coordinates
v_R	Rotating onset flow induced normal velocity component
v_{TE}	Normal velocity induced in global coordinates by a trailing edge vortex
v_{w_T}	Transpiration velocity induced normal velocity component
v_W	Wake induced normal velocity component
v_x	Translating onset flow induced normal velocity component
W_F	Wake factor
W_H	Wake height
W_L	Wake length
w_T	Transpiration velocity / injection function

wTR	Weighted average for laminar to turbulent transition parameters
x_{TR}	Chordwise transition location

List of Tables

List of Figures

Contents

Chapter 1

Introduction

1.1 Introduction

Computer resources are becoming more powerful with the years, but it is still beyond our limits to perform an optimum design of blades using Navier-Stokes solvers, because of the computing intensive iterative design work in between geometry and aerodynamic forces. Historically, it is possible to predict the overall forces on a rotor blade by adding up the aerodynamic forces of each section of the blade using strip theory, such as it is used in the the blade-element theory to compute thrust and power. Nowadays aerodynamic force coefficients used as inputs to the blade-element models (BEM) are obtained from two dimensional airfoil data based on experiments. Occasionally three dimensional corrections are used, usually based in curve fitting.

An alternative method to computing heavy Navier-Stokes solutions, is to use viscous-inviscid interaction. In this method a viscous approach is used to compute the boundary layer, while the outer part the flow is modeled as purely inviscid. Initially an independent solution was obtained for both regions and combining it allowed to solve the overall problem. During the last century a lot of effort was put into the development of this technique. During the present work a viscous-inviscid interactive code has been developed where the inviscid part is solved using a potential panel method and the viscous effects are take into account solving the integral form of the Quasi3D boundary layer r and θ momentum equations using the kinetic energy shape parameter equation in its two dimensional form. It is possible to approximate this higher-order effect by considering the integral boundary layer, obtaining a higher order of accuracy than for a potential method solution. As a higher order treatment the variation of pressure across the boundary layer is introduced as a post processing correction. This may be of importance where the boundary layer is not thin and the streamlines are highly curved, just before separation appears is the most critical location.

At relatively high Reynolds number, standard conditions on the wind turbine operational range, turbulent flow will be present in large regions around the blade surface due to the viscous nature of the air. A turbulence modeling was implemented in order to deal with the effects of turbulence in the boundary layer. An integral boundary layer set of quasi three dimensional closure equa-

tions in their turbulent form are implemented. An extra set of equations in its two dimensional form is used as closure to the kinetic energy integral equation permitting variances in shape factor caused by the flow pressure gradients. [1] [2] [3]

The final step in the process is to couple the two separate parts, viscous and inviscid, to interact within each other in order to determine the final solution to the fluid problem. Four different approaches to this aspect are present in previous literature: "direct", "semi-inverse"', "quasi-simultaneous" and "strong interaction". The viscous-inviscid technique via strong interaction has been implemented in the present study due to his higher stability, portability and capability to solve separated boundary layers. The strong interaction permits the integral boundary layer equations to be solved at and after separation takes place, even with large separated regions.

The reduction in computational time of the methods employed in the present work together with the high accuracy obtained should not bade the effort being done for solving the full Navier-Stokes equations with improved turbulence models. Both methods should continue developing filling each others holes, and for the time being, the viscous-inviscid models seem to have the capacity to become the next generation of rotor blade design tools.

In the following subsections an overview of different topics of great interest for the work presented herein is done. The airfoil design during the last decades is reviewed with a special emphasis in the wind turbines airfoil characteristics. The use of adaptative trailing edge flaps is introduced as a solution capable of optimize the airfoil shape in order to reduced the airfoil aerodynamic forces. The wind tunnel walls influence is analyzed, which can have a important impact during the validation of our predictions against wind tunnel measurements. Finalizing with a introduction to rotational effects influence in airfoil aerodynamic performance, of enormous importance due to the rotating nature of the wind turbine blade sections.

1.1.1 Airfoil design

Since the 50s, the problem of airfoil design has been of great interest for the engineering community. Aerodynamicists have put an enormous amount of effort optimizing the airfoil shape in order to improve the aerodynamic performance of aircraft, wind turbines, F1 cars, sailing boats, etc. Since the early days, airfoil design for airplanes focus in obtaining an airfoil shape with a good behavior in attached flow conditions at low angles of attack. More recently wind turbines design is becoming of higher interest for the wind turbine blade manufacturers. Knowing that many turbines operate under stalled conditions, airfoil shape has not only to behave good at low angles of attack, it has also to retain good aerodynamic properties after separation appears, increasing the difficulty during the design process. A small reduction in the drag coefficient can be the difference between a winner or a second place in a F1 race, or may result in an important fuel saving for a long flights aircraft.

A wind turbine blade section should have the following standard characteristics: high maximum lift coefficient and lift to drag ratio but low drag and pitch

moment coefficient. Thickness constrains come in play due to structural reasons, the inboard sections close to the root will have a thick profile, while sections closer to the blade tip will be thiner. Design of blades with sweep, taper and winglets, already studied concepts in the aeronautics field, are nowadays being revisited by wind turbine designers, where the rotational nature of the wind turbine and its dimensions could channel the analysis to different solutions.

Methods for designing airfoils can be sorted in two categories. The first category is optimization methods, where an optimization algorithm is used for obtaining the airfoil geometry that maximizes lift and the glide ratio or minimizes drag. The methods embraced into this category are also known direct methods. The second category of methods, inverse methods, is the ones where a potential flow method is inverted, like Theodorsen conformal mapping method, in this kind of methods the input is the pressure distribution and the output is the airfoil shape. Originally solved only by potential methods or the so called "conformal mapping", airfoil aerodynamics can be solved with the addition of viscous effects, whether with viscous-inviscid solvers or through Navier-Stokes equations.

Geometric airfoil characteristics affects strongly the blade performance, i.e thickness, camber, leading edge shape, roughness insensitivity. A thick wing increases drag and reduces the angle of stall, although it has good structural properties. Modifying the camber of the airfoil one can win lift at lower angles of attack but. For example an acrobatic airplane needs a symmetric airfoil to make it easier to maneuver during the rotations and upside down flights. The shape of the leading edge is of great importance for the stall performance of the airfoil. While a sharp leading edge will generate an abrupt lift drop after stall is reached, a blunt leading edge will give a smoother reduction in lift. During the lifetime of a wind turbine blade there is a slow process that turns the clean surface in a rough or dirty surface, hence roughness insensitivity gives the airfoil constant aerodynamic properties during its complete lifetime.

1.1.2 Use of adaptative trailing edge flaps

New developments in the early 90s have been used to investigate the use of active parts on wings, capable of optimize the airfoil shape in order to reduce aerodynamic forces, reduce noise level, vibration, etc. From the aviation industry flaps are known to change the effective angle of attack of the wing. Downward flap positions will displace the lift curve to the left, increasing the lift for the same angle of attack, similar effect as the positive increment in camber.

As the birds, that can adapt their wings in order to optimize their aerodynamic shape, the airfoil aerodynamics can be improved with an adaptative trailing edge system, or trailing edge flap. This system, as was proven in tests performed in a wind tunnel, can manage turbulence, reduce aerodynamic loads and have a positive overall effect on the whole wind turbine. The use of adaptative flap in rotors can be found in the helicopter research where the flap is used for noise reduction and vibrations.

The present work will help to analyze the local aerodynamic behavior of a moving trailing edge flap, and can be used by blade designers for assisting in

the definition of an optimum design with respect to geometry of the flap and the position of the sensors.

1.1.3 Wind tunnel walls

Most common wind tunnel test sections are enclosed by Plexiglas walls in order to have a good visibility. There are wind tunnels with open test section but the turbulence level is difficult to control, usually it is too high and measurements are trigged by the high turbulence intensity. The effects of tunnel walls on the airfoil aerodynamics can be divided in:

- Blocking of the airfoil in the tunnel increases the local velocity around the airfoil surface.
- The walls influence the curvature of the streamlines, and so the airfoil pressure distribution.
- Influence on the strength and geometry of the wake.

An implementation of the wind tunnel walls has been added to the viscous-inviscid interactive solver in order to perform future comparisons against measurements from the DTU red wind tunnel. The narrow test section of the wind tunnel is expected to play an important role on the aerodynamic behavior of the airfoil. The tunnel walls are simulated by a constant strength distribution of source panels.

1.1.4 Rotational effects

Blade-element momentum theory (BEM) is often used as a design tool for wind turbines. As an input to the BEM model, lift and drag forces at different angles of attack are given, commonly obtained from two dimensional measurements. It is known that two dimensional measurements underpredict lift forces in stalled conditions.

Centrifugal and Coriolis forces that appear in the rotational boundary layer are the cause of the increment in the aerodynamic forces if compared with two dimensional non rotational case, reaching higher lift coefficients. The centrifugal force will produce a spanwise outward velocity component which will give rise to Coriolis forces that will act as a favorable pressure gradient in the chordwise direction, an additional chordwise pressure drop. The centrifugal force also acts reducing the thickness of the boundary layer by the outward movement of the fluid, more commonly known as centrifugal pumping effect.

It is known that rotational effects are stronger in regions close to the rotational axis and close to stall conditions even though a detailed study of the phenomena has not yet been done. One of the objectives of the present study is to obtain a deeper understanding of the influence of rotation in the boundary layer. Rotational effects are strongly related with the existence of a radial flow in the boundary layer of rotating blades, which following [4] arises from :

1. Yawed flow seen by the blade cross sections.

2. Chordwise pressure distribution.

3. Spanwise pressure distribution.

4. Centrifugal force acting on the spanwise direction.

5. Coriolis force acting on both the spanwise and streamwise directions.

In the present work an interactive viscous-inviscid model has been developed with capability of solving the quasi3D unsteady incompressible boundary layer equations. To reduce the 3D boundary layer equations to the quasi3D ones, an assumption that simplifies the radial derivatives has been implemented. Hence the three dimensional boundary layer equations have been reduced to two dimensional boundary layer equations in its integral form with extra rotational terms that take into account the spanwise velocity profile. The errors introduced by this assumptions are known to be small due to the small order of magnitude of the radial components of the boundary layer.

With the present method we thrust having capability for studying the influence of rotation on lift and drag performance of a two dimensional airfoil section part of a rotating blade induced by different effects derived from rotation. Yawed flow falls outside the capabilities of our code. Radial derivatives are simplified assuming a high local aspect ratio of the blade cross section.

1.2 Historical survey

1.2.1 Viscous-Inviscid methods

Preston [5] in the 1940s was the first who studied the influence of the displacement effect of a laminar boundary layer on an airfoil. The viscosity affects the pressure distribution near the trailing edge so that the lift is reduced if compared with potential flow computations. Conformal mapping techniques were used in order to solve the inviscid part of the problem. The viscous effects of the boundary layer were taken into account using a transpiration model fitted with boundary layer thicknesses.

Spence [6] in the 50s extended Preston´s work, adding the effect of turbulent boundary layers. Spence calculated the reduction on lift coefficient due to viscous boundary layer effects for a Joukowski airfoil. Compared with inviscid computations, the viscous effects reduce the lift coefficient with 15% at a Reynolds number of 5.10^6 while at a Reynolds number of 5.10^7 where the flow is more potential the reduccion in lift is only 5%.

In 1958, Lighthill [7] studied the influence of boundary layer and wakes in the flow outside them, depicting four theoretical treatments of the displacement thickness. One of them, the equivalent sources technique is used to obtain a viscous-inviscid strong interaction in the present work. The equivalent sources create an extra flow in the region between the surface and the streamlines of the irrotational flow.

Neither Preston nor Spence were able to calculate the effect of viscosity on the whole airfoil surface, this was impossible due to the absence of electronic

computers. It was not until 1965, when Powell [8] solved the whole system as an iterative process, calculating on an iterative manner the inviscid pressure distribution over the displacement surface using a small perturbation method, while for the turbulent boundary layer he used an integral method.

The displacement effect of the wake was not calculated until some years later, when Firmin [9], used the entrainment method of Green [10]. Firmin was the first one who took into account the wake curvature, modeling it by a vortex sheet leaving the trailing edge of the airfoil. The wake curvature effect help reducing the lift coefficient in the computations approximately a 3% if compared with the viscous predictions where this effect was neglected.

Le Balleur presented in 1981 [11] his viscous-inviscid method in which using a transonic potential solver was combined iteratively with an integral formulation of the boundary layer equations. Using this technique it became possible to solve laminar and turbulent boundary layers around airfoil sections at high angles of attack. Using an iterative relaxation technique in combination with a semi inverse method the solver was able to compute small regions of trailing edge separated flow, without reaching stalled flows.

In 1986 Drela [2] published the basic closure equations that later were used in the Xfoil software, [12]. In first place Drela used the Euler equations in the non-viscous part of the viscous-inviscid strong coupling, using a transpiration velocity to account for the influence of the boundary layer. Later in the Xfoil code the Euler equations were substituted by a linear vorticity panel method, reducing the fully 2 dimensional mesh to a surface mesh, faster and still accurate. In this case source distributions are in charge of adding the viscous effects into the inviscid part, obtaining in this way an strong viscous-inviscid interaction. A two equations model was used with the standard momentum and kinetic energy shape parameter equations.

In the early nineties unsteady effects were taken into account by Cebeci in [13] and [14]. An interactive boundary layer method was used for computing harmonically oscillating airfoils and ramp increments in angle of attack. Concluding that the effects of variation of lift coefficient in function of pitch reduced frequency are important at angles of incidence that involve boundary layer separation.

Maskew and Dvorak in April 1974 [15] developed a new approach to the viscous-inviscid solver, producing highly accurate surface pressure data for stalled airfoils. They introduced the concept of double wake model using the boundary layer equations to predict the onset of separation location. In their model two wakes with constant vorticity are leaving the airfoil, one from its leading edge and the other one from the separation point. In this way an isolated region is created in between both wakes, simulating the separated flow around the suction surface of the airfoil.

Riziotis and Voutsinas in 2008 [16] implemented an unsteady viscous-inviscid solver that used a double wake model in order to predict highly accurate lift, drag forces and pitch moment coefficients at dynamic stall conditions. They compared dynamic force predictions at high angles of attack for two wake models, single and double wake, obtaining qualitatively much better results for the last one.

1.2.2 Rotational Boundary Layer

Wind turbines design method are commonly based on two dimensional aerodynamic data. However, this data normally needs to be corrected for three dimensional effects due to rotational effects in the boundary layer arising due to the rotational nature of the flow, [17]. Different authors have demonstrated the importance of rotational effects on wind turbine aerodynamics, in accordance, the design methods should take into account three-dimensional effects in order to mimic more realistic aerodynamic forces, [18].

In April 1983 the HAWT Aerodynamics Specialist Meeting was held at Wichita State University. During the meeting the causes of the lack of accuracy for the presented codes to predict wind turbine performance were analyzed: higher power production of the inboard sections of the blade and higher power production of the rotor at higher angles of attack due a secondary outward flow caused by centrifugal pumping. These effects induce a delay in the stalling of the lift coefficient, thereby causing the lift to maintain its increment rate at high values of angle of attack at the same time that the drag remains low. [19]

In 1990, SERI´s experiment on a full scale wind turbine [20] showed the importance of the three dimensional effects arising from a rotating blade boundary layer, suggesting important changes in blade performance prediction if the three dimensional rotation effects were taken into account.

In the 50s Sears and Fogarty [21] considered the problem of an infinite long cylinder rotating around an axis perpendicular to the cylinders axis. His conclusions are used in the derivation of the Quasi3D developed in the present work. They found out that the three dimensional boundary layer edge velocities can be written in function of the two dimensional potential solution. This work was extended by Rott and Smith [22], Graham [23], Sears [24], Moore [25] and [26]. Concluding that the rotational effect on the boundary layer will become more important in the area closer to the rotational axis. All the interest in the early stages was directed towards ship propellers and turbomachinery.

Horlock and Wordsworth in 1965 [27] developed laminar boundary layer equations for turbomachinery showing the different flow patterns at diverse radial positions. Lakshminarayana et al in 1972 [28] introduced for the first time a method for analyzing the turbulent boundary layer with rotational effects. The method based on a momentum integral technique using the entrainment equation as a closure for the shape parameter. Coriolis and Centrifugal forces were taken into account via the spanwise and streamwise momentum equations. In their study an excellent agreement against measurements for boundary layer parameters was obtained at attached flow condition. At separated flow conditions the agreement was poor. It was concluded that the three dimensional rotational effects play an important role in the boundary layer flow characteristics.

In 1966, Franklin and Vertol [4] realized a study of radial flow effects on rotor blades, concluding that the radial flow arising from yawed or oblique local velocity, spanwise and chordwise pressure gradients and centrifugal and Coriolis forces alters substantially the stall characteristics of airfoils, reducing the lift boards in the near hub regions. The classical BEM theory understimates rotor power and drag components due to the airfoil skin friction drag.

McCroskey and Yaggi in 1968 [29] studied the influence of rotating boundary layers on separation, finding out that separation is retarded due to the rotation. In 1972 McCroskey, Nash and Hicks [30] extended the previous work by including turbulent boundary layers, concluding that the three dimensional effects are less important in the case of turbulent flow. Noting that the laminar flow, with lower momentum is more affected by rotation than turbulent flow with high momentum. The centrifugal pumping energizes the low momentum flow helping it to be more resistant to separation. Takemasu in 1972 [31] found that the airfoil shape and the radial position of this one will have an important influence in the crossflow characteristics.

In 1985, Savino and Nyland [32] carried out flow visualization experiments on the NASA/DOE Mod-0 Machine, finding a strong crossflow downstream of the separation line, followed by a delay of the stall, and the location of the separation line was found 0.1-0.2 chord downstream when comparing it with two dimensional flow conditions.

Sørensen in 1996 [33] developed a viscous-inviscid computational model for turbulent separated flows around rotating wings. The flow is treated in three layers: a three-dimensional boundary layer, an external inviscid flow field and an inviscid wake. He ran the first full computation of a wind turbine rotating blade, concluding that the effect of rotation is to delay the onset of separation, increase the lift coefficient and slightly decrease the drag coefficient.

In 1994 Snel [34] developed an integral boundary layer method for computing aerodynamic forces on rotating airfoils. He used the integral r and θ momentum equations, taking into account the variations of the shape factor via the entrainment equation, obtaining impressive lift coefficient agreements against NREL measurements performed at 30% of the blade span.

1.3 Purpose of the project

In the project a fast and efficient quasi-3D aerodynamic code has been developed to analyze the local aerodynamic behavior of an airfoil section of a wind turbine with a moving trailing edge flap and associated sensor response. The code uses the well known concept of unsteady viscous-inviscid interaction via transpiration velocity. The inviscid calculations are carried out by an unsteady potential flow panel method; meanwhile the viscous flow is calculated using the unsteady quasi 3-D integral boundary layer equations. Simulations are carried out for flow around an airfoil with a moving trailing edge on a static or rotating blade. These calculations will provide some guidelines for designing and evaluating the Adaptative Trailing Edge Flap (ATEF) system on a wind turbine.

Chapter 2

Potential Methods

In the present chapter the foundations of potential flow for external flow aerodynamics are presented. Green´s theorem is analyzed and linked to the panel method for incompressible irrotational flows. Sources, vortex and linear vorticity distributed elements are introduced as the elementary solutions to the potential flow problem. Further is presented the basics of the inviscid part of the strong viscous-inviscid solver. Finally, the double wake model, capable of predicting accurately airfoil aerodynamic performance in deep stall conditions, will be presented.

2.1 Potential flow foundations and general solution based on Greens identity

Inviscid flows are described on the bases of the continuity equation and the inviscid momentum equations. Regarding the problem of an arbitrary solid body immersed in a fluid and considering the flow incompressible and irrotational, defining a velocity potential and combining it with the continuity equation gives rise to the following second-order linear partial differential equation, for the velocity potential Φ

$$\nabla^2 \Phi = 0 \tag{2.1}$$

Considering the immersed body in the fluid, and assuming the solid surfaces are not penetrable the following boundary condition is applied stating that the velocity normal to its boundary surface is expressed as,

$$\nabla \Phi \cdot \underline{n} = 0 \tag{2.2}$$

A second boundary condition states that the disturbance created by the solid body should become zero as the position of study $\underline{r}$ tends to infinity,

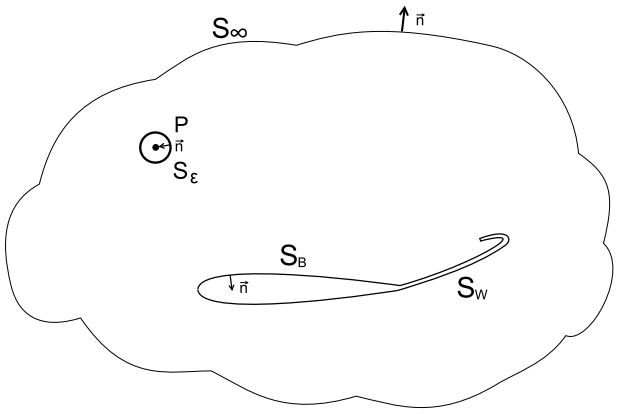

Figure 2.1: Flow field sketch

$$\nabla\Phi \rightarrow \underline{U_\infty} \; for \; \underline{r} \rightarrow \infty \tag{2.3}$$

where $\underline{U_\infty}$ is the freestream velocity.

There is a unique solution to Laplace's equation satisfying the boundary conditions. As vorticity can not be created or destroyed, the vorticity generated at the body surface must be convected downstream, hence infinitesimally thin wake surfaces have to be introduced to carry the vorticity downstream of the trailing edge and the separation location. A description of the problem can be found in Figure 2.1.

Potential flow solution based on Greens identity. The divergence theorem is applied to a flow velocity vector, $\underline{v}$, which states that the fluid flux through the boundary of the control surface is equal to the rate of expansion of the fluid inside the control volume, [35]. In this way the flow of a vector field through a surface is related to the vector field in the volume inside the surface. Being the solid body surface, S_B, immersed in a fluid within a volume, V, and boundaries, S_∞. The divergence theorem yields,

$$\int_{C.S} \underline{v} \cdot \underline{n} dS = \int_{C.V} \nabla \cdot \underline{v} \, dV \tag{2.4}$$

Replacing the velocity vector , $\underline{v}$, in the equation above by $\Phi_1 \nabla\Phi_2 - \Phi_2 \nabla\Phi_1$, where Φ_1 and Φ_2 are two scalar functions of position, Equation 2.4 yields,

$$\int_{C.S} \Phi_1 \nabla\Phi_2 - \Phi_2 \nabla\Phi_1 \cdot \underline{n} dS = \int_{C.V} \Phi_1 \nabla^2\Phi_2 - \Phi_2 \nabla^2\Phi_1 dV \tag{2.5}$$

Setting $\Phi_1 = 1/r$ and $\Phi_2 = \Phi$, the velocity potential of the flow where r is the distance from a point P, locating the point P outside of the volume V, Equation 2.5 produces,

$$\int_S \left(\frac{1}{r} \nabla \Phi - \Phi \nabla \frac{1}{r} \right) \cdot \underline{n} dS = 0 \tag{2.6}$$

where Equation 2.1 is used.

It is wanted to compute the flow field at the point P, located on the surroundings of the body surface inside the flow volume, V. The point P has to be excluded from the integration region in order to avoid a singularity, for that purpose it has to be created a sphere of radius ϵ around it. Outside the sphere the potential satisfies Laplace equation, $\nabla^2 \Phi_1 = \nabla^2 (1/r) = 0$ in the same way as $\nabla^2 \Phi_2 = 0$. The Equation 2.5 becomes,

$$\int_{S+S_\epsilon} \left(\frac{1}{r} \nabla \Phi - \Phi \nabla \frac{1}{r} \right) \cdot \underline{n} \, dS = 0 \tag{2.7}$$

Supposing that the vector $\underline{n}$ is pointing inwards the sphere that surrounds the point P, it is possible to write, $\underline{n} = -\underline{e}_r$, $n \cdot \nabla \Phi = -\partial \Phi / \partial r$ and $\nabla (1/r) = -\left(1/r^2\right) \underline{e}_r$, applying changes, the Equation 2.7 above yields,

$$-\int_{S_\epsilon} \left(\frac{1}{r} \frac{\partial \Phi}{\partial r} + \frac{\Phi}{r^2} \right) dS + \int_S \left(\frac{1}{r} \nabla \Phi - \Phi \nabla \frac{1}{r} \right) \cdot \underline{n} \, dS = 0 \tag{2.8}$$

The radius of the sphere surrounding P it is chosen to be very small, $r = \epsilon \to 0$, its surface can be integrated as follows, $\int dS = 4\pi\epsilon^2$. Assuming Φ_2 and its derivatives are well behaved functions, meaning that the potential has not variations inside the sphere. As ϵ tends to zero, the first terms in the sphere integral vanishes, and the second one can be integrated, Equation 2.8 yields,

$$-4\pi\Phi(P) + \int_S \left(\frac{1}{r} \nabla \Phi - \Phi \nabla \frac{1}{r} \right) \cdot \underline{n} \, dS = 0 \tag{2.9}$$

Clearing the velocity potential from Equation 2.9,

$$\Phi(P) = \frac{1}{4\pi} \int_S \left(\frac{1}{r} \nabla \Phi - \Phi \nabla \frac{1}{r} \right) \cdot \underline{n} \, dS \tag{2.10}$$

So it is possible to obtain the velocity potential at any point in the flow field, Φ_P, if the velocity potential and its normal derivative, Φ and $\partial \Phi / \partial n$, are known at the body surface. In order to relate the potential equation with the singularity elements a form of the first one that includes the influence of the inner potential is formulated, [35]

$$\Phi(P) = \frac{1}{4\pi} \int_S \left(\frac{1}{r} \nabla (\Phi - \Phi_I) - (\Phi - \Phi_I) \nabla \frac{1}{r} \right) \cdot \underline{n} \, dS + \Phi_\infty(P) = 0 \tag{2.11}$$

where Φ_I is the internal potential inside the body boundary.

From here it is possible to define the following singularity elements and relate them to the velocity potential, with $\underline{n}$ pointing inside the body surface,

$$-\mu = \Phi - \Phi_I \tag{2.12}$$

$$-\sigma = \frac{\partial \Phi}{\partial n} - \frac{\partial \Phi_I}{\partial n} \tag{2.13}$$

The doublet in Equation 2.12 is defined as the difference in between the external and internal potentials. In Equation 2.13 the source element is defined as the difference in between the normal derivative of the external and internal potentials. Substituting the definitions above in the velocity potential, Equation 2.14, produces

$$\Phi(P) = \frac{1}{4\pi} \int_S \left(\sigma \left(\frac{1}{r} \right) - \mu \frac{\partial}{\partial n} \left(\frac{1}{r} \right) \right) dS + \Phi_\infty(P) \tag{2.14}$$

It can be concluded that the solution to Laplace's equation, $\nabla^2 \Phi = 0$, can be reached by the distribution of elementary solutions on the body surface boundaries. In this way the boundary conditions are satisfied everywhere on the fluid volume but at the point where $r = 0$ a singular solution has to be forced. Two different kinds of problems arise, if the potential on the boundaries is specified it is known as a Dirichlet problem, while if the non penetration condition is specified as a zero normal flow on the body boundaries it is called a Neumann problem.

2.2 Steady potential flow basics

The solution to the steady potential flow problem is obtained by modeling the flow around a body with a distribution of singularities located on its surface.

If the flow around a body with surface S_B is considered, the velocity on any point P could be expressed as the sum of two velocities: one defined as the free stream velocity, $\mathbf{U}_\infty$, and the induced velocity $\mathbf{u}$.

$$\mathbf{U} = \mathbf{U}_\infty + \mathbf{u} \tag{2.15}$$

$$\mathbf{u} = -\nabla \phi \tag{2.16}$$

As the boundary condition, considering the body surface S_B impermeable, the normal velocity component to the surface has to be zero,

$$\mathbf{U} \cdot \underline{n} = \frac{\partial \phi}{\partial n} = 0 \tag{2.17}$$

Where $\underline{n}$ is the normal component to the body surface, S_B.

As presented in the previous section, the body induced velocity $\mathbf{u}$ will tend to 0 as the distance between the point P and the body B increases to infinity. From the above boundary equations, a Neumann problem is defined.

Green´s third identity has to be applied in order to obtain the flow field solution as a superposition of the different flow singularity elements solutions in a two dimensional case. The singularity elements are distributed on the body surface, depending on the nature of these singularity elements the velocity potential at a control point P is given as follows,

The velocity potential created by a constant strength source distribution σ_j at a point P is

$$\phi_\sigma(P) = \frac{\sigma_j}{2\pi} \int ln\,(r_{Pj})\,dS \tag{2.18}$$

where r_{Pj} the distance between the control point P and each source differential j

The velocity potential created by a constant strength vortex distribution γ_j at a point P is,

$$\phi_\gamma(P) = -\frac{\gamma_j}{2\pi} \int \arctan\,(\theta_{Pj})\,dS \tag{2.19}$$

where θ_{Pj} is the angle between the control point P and each vortex differential j.

The total velocity potential at a point P will be obtained adding the solutions of the different singular elementary solutions as follows,

$$\phi(P) = \frac{\sigma_j}{2\pi} \int ln\,(r_{Pj})\,dS - \frac{\gamma_j}{2\pi} \int \arctan\,(\theta_{Pj})\,dS \tag{2.20}$$

Satisfying equation 2.17, the non-slip boundary condition, can be written as follows,

$$\frac{\partial \phi}{\partial n} = \frac{\partial}{\partial n}\phi_\sigma(P) + \frac{\partial}{\partial n}\phi_\gamma(P) = \mathbf{U}_\infty \cdot \underline{n} = 0 \tag{2.21}$$

$1/r_{Pj}$ is a Greens function, or the Kernel of an integral. Which combined with the first term of the equation forms an inhomogeneous Fredholm integral equation.

2.3 Unsteady potential flow basics

In the present section the attention is centered in the case where the airfoil is moving inside the flow field. The airfoil circulation, $\Gamma_B(t)$, is now dependent of time. Each time step the circulation will change in order to fulfill Kelvin´s theorem, stating that the total circulation on the flow field has to be zero meaning that a vortex with strength $(\partial\Gamma_B/\partial t)dt$ has to be shed out of the airfoil. That vortex will leave the airfoil surface at its trailing edge and will become part of the wake, [36].

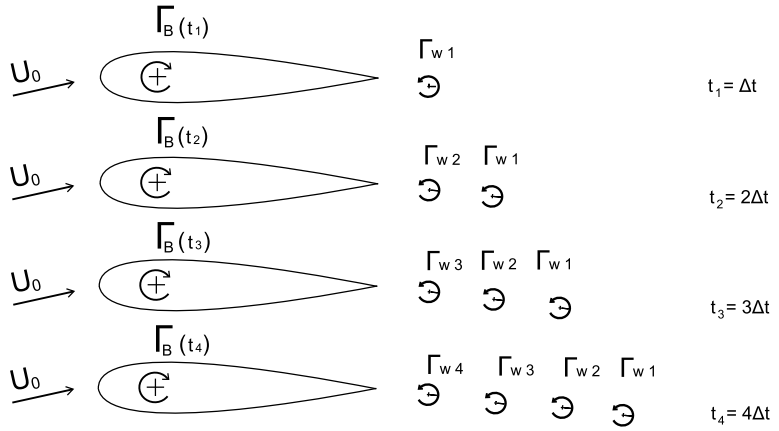

Figure 2.2: Downstream convection of point vortices at different time steps

In the next figure it is explained the mechanism followed to create the trailing edge wake which convects downstream the airfoil, Figure 2.2. Four time steps are sketched with different wake shapes,

In the unsteady case, the velocity on a random point P situated in the flow field surrounding the airfoil has to be expressed as the sum of three velocities, the free stream velocity, $\mathbf{U}_\infty$, the influence of the body itself disturbing the free stream flow, $\mathbf{u}$, and the influence of the wake, $\mathbf{u_W}$, the last one will have an important effect on the airfoil pressure distribution, with a special importance in the airfoil trailing edge area.

$$\mathbf{U} = \mathbf{U}_\infty + \mathbf{u} + \mathbf{u_W} \tag{2.22}$$

The wake shape will change in function of the unsteady movement of the airfoil. If the reduced frequency at which the airfoil moves is high, the strength of the wake will increase due to a larger change of circulation between time. From here it is possible to state that the wake influence on the airfoil will grow as the movement frequency increases. This effect has to be taken into account when the viscous effects are added into the potential flow model. If the frequency is too high, the pressure difference on the airfoil surface, in between the collocation points, especially in between the ones situated in the trailing edge area will be too large and will be the cause of lack or slow convergence.

The wake length will be chosen in function of the model setup. For example, when the airfoil is situated inside a wind tunnel the wake will be cut as soon as the vortex blobs reaches the end of the wind tunnel. In the case of open space computations, the wake has been cut off after one vortex blob is shed, in this way a simplified wake model is introduced.

The direction of the wake first vortex blob will be the same as the airfoil trailing edge panel with the highest absolute velocity, the upper or lower trailing edge panel. The position of the vortex blob will be computed as following the velocity of that side of the trailing edge.

If the airfoil is modeled with a constant panel source plus a uniform vorticity distribution and the trailing edge wake is simulated with point vortex converging downstream, the velocity potential at a point P can be written as,

$$\phi(P) = \frac{\sigma_j}{2\pi} \int ln\left(r_{Pj}\right) dS - \frac{\gamma_j}{2\pi} \int \arctan\left(\theta_{Pj}\right) dS - \frac{\Gamma_j}{2\pi} \theta_{Pj} \tag{2.23}$$

In the present work has not been taken into account the influence of the velocity at which the airfoil panels move, which will act as an extra induced velocity term into the panel method formulation, introduced in a similar way as the freestream component of the velocity. This term will grow in magnitude as the airfoil movement frequency increases, and it will be of great importance when implementing a controllable trailing edge due to its high frequency response. It is encouraged here that future versions of the code should include that extra term.

2.4 Singularity elements, influence matrices and problem discretization

In the present report two different ways of modeling an airfoil are presented. In the single wake model, the singularity elements are chosen to model the airfoil were constant-strength source distribution, parabolic vorticity distribution and point vortices. The point sources have been distributed all over the contour off the airfoil as well as the parabolic strength distribution. A parabolic vorticity distribution is added around the airfoil surface in order to model the airfoil circulation and satisfy the Kutta condition. The point vortices singularities are used for modeling the single wake, leaving the trailing edge of the airfoil and moving downstream. In the double wake model, two wakes, one from the trailing edge and the other one leaving the airfoil at the separation point, are modeled with a constant vorticity distribution.

2.4.1 Singularity elements and induced velocities

Constant source distribution If a constant source with strength σ distributed along a panel is considered and positioned as shown in Figure 2.3.

The velocities induced at a point P are obtained as the integral of the influences of each one of the point sources generating the constant source distribution along the panel,

$$u_p = \frac{\sigma}{2\pi} \int_{x_1}^{x_2} \frac{x - x_0}{\left(x - x_0\right)^2 + y^2} \, dx_0 \tag{2.24}$$

$$v_p = \frac{\sigma}{2\pi} \int_{x_1}^{x_2} \frac{y}{\left(x - x_0\right)^2 + y^2} \, dx_0 \tag{2.25}$$

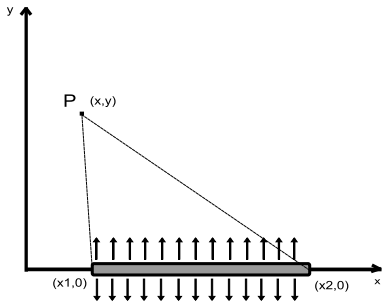

Figure 2.3: Panel influence at a point P

The velocity components in differential form can be obtained differentiating the potential function. So it is possible to write the velocity equations as follows for a more practical use, viscid

$$u_p = \frac{\sigma}{4\pi} ln \frac{(x-x_1)^2 + y^2}{(x-x_2)^2 + y^2} \tag{2.26}$$

$$v_p = \frac{\sigma}{2\pi} \left[tan^{-1} \frac{y}{x-x_2} - tan^{-1} \frac{y}{x-x_1} \right] \tag{2.27}$$

An exception of the above equations is when the point P is located on the center of the panel, in that case the induced velocities are,

$$u_p = 0 \tag{2.28}$$

$$v_p = \pm \frac{\sigma}{2} \tag{2.29}$$

The velocities calculated above, induced by a panel distributed singularity are in panel coordinate system, in that case it is needed to transform them into the global coordinates system. Defining α as the angle in between the panel and the global coordinates system x axis,

$$u = u_p \, cos\alpha - v_p \, sin\alpha \tag{2.30}$$

$$v = u_p \, sin\alpha + v_p \, cos\alpha \tag{2.31}$$

Point vortex If a point vortex with circulation Γ located at x_0, y_0 is considered, the velocity induced on a particle situated in x, y, in this case the induced velocity are computed in the global coordinate system so no transformation has to be done as in the case of panel distributed singularities. The induced velocities can be formulated as follows,

$$u = \frac{+\Gamma}{2\pi} \frac{y - y_0}{(x-x_0)^2 + (y-y_0)^2} \tag{2.32}$$

$$v = \frac{-\Gamma}{2\pi} \frac{x - x_0}{(x-x_0)^2 + (y-y_0)^2} \tag{2.33}$$

Where u is the tangential velocity induced by a point vortex with strength Γ in global coordinates and v is the normal one.

In the single wake model approach, the airfoil vorticity distribution is assumed to follow a parabolic shape, being zero at the upper and lower trailing edge panels.

Linear vorticity distribution For the double wake model, described further in Section 2.5, a linear strength vorticity distribution is used to model the airfoil surface. A vorticity distribution is placed along the panels with strength $\gamma = \gamma_i + \gamma_{i+1}(x - LE_i)$.

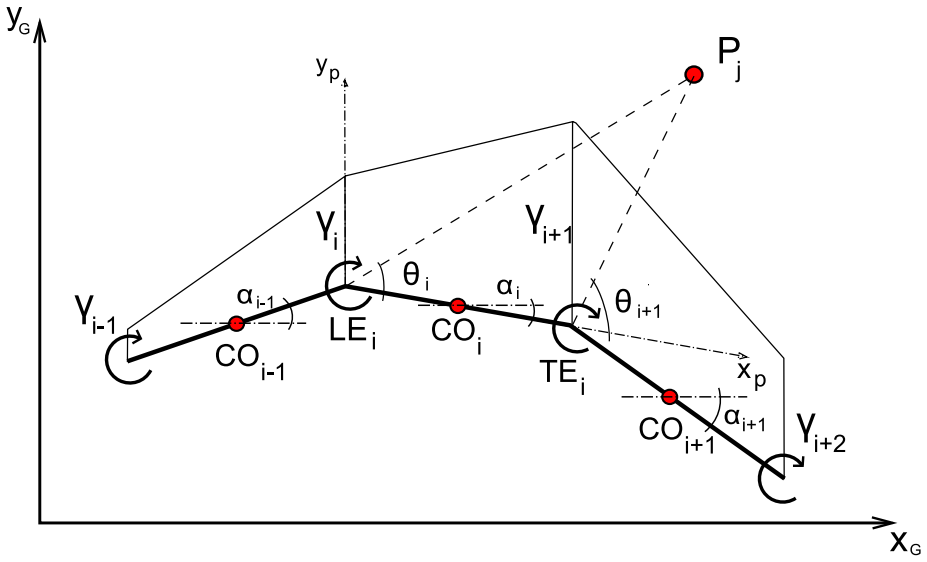

Figure 2.4: Linear Vortex Influence from element i to control point P_j

$$x_2 = (TE_{i,1} - LE_{i,1})\ cos\,(\alpha_i) + (TE_{i,2} - LE_{i,2})\ sin\,(\alpha_i) \tag{2.34}$$
$$y_2 = 0 \tag{2.35}$$
$$x = (P_{x_G} - LE_{i,1})\ cos\,(\alpha_i) + (P_{y_G} - TE_{i,2})\ sin\,(\alpha_i) \tag{2.36}$$
$$y = -(P_{x_G} - LE_{i,1})\ sin\,(\alpha_i) + (P_{y_G} - LE_{i,2})\ cos\,(\alpha_i) \tag{2.37}$$
$$R_1 = \sqrt{x^2 + y^2} \tag{2.38}$$
$$R_2 = \sqrt{(x - x_2)^2 + y^2} \tag{2.39}$$
$$\theta_1 = atan\left(\frac{y}{x}\right) \tag{2.40}$$
$$\theta_2 = atan\left(\frac{y}{x - x_2}\right) \tag{2.41}$$

From Figure 2.4 it is possible to defined all the dimensions used in the following induced velocity equations,

Where x and y are the positions of P in the panel local coordinate system with origin at LE_i. x_2 and y_2 are the local coordinates of TE_i.

For convenience the influence of each panel is divided in two parts, the leading edge vortex and the trailing edge one, see Figure 2.4. Considering the panel i, with collocation point CO_i, a vortex with strength γ_i is placed on its leading edge, while the one placed at its trailing edge has a strength γ_{i+1}. Hence the vorticity will vary linearly in the panel from the positions LE_i to TE_i in between the values γ_i and γ_{i+1}.

The velocity components in the panel coordinates can be obtained as follows,

$$u_{p\,LE} = -\frac{y\,log\left(\frac{R_2}{R_1}\right) + x\ (\theta_2 - \theta_1) - x_2\ (\theta_2 - \theta_1)}{2\,\pi\,x_2} \tag{2.42}$$

$$u_{p\,TE} = \frac{y\,log\left(\frac{R_2}{R_1}\right) + x\ (\theta_2 - \theta_1)}{2\,\pi\,x_2} \tag{2.43}$$

$$v_{p\,LE} = -\frac{x_2 - y\ (\theta_2 - \theta_1) - x\,log\left(\frac{R_1}{R_2}\right) + x_2\,log\left(\frac{R_1}{R_2}\right)}{2\,\pi\,x_2} \tag{2.44}$$

$$v_{p\,TE} = \frac{x_2 - y\ (\theta_2 - \theta_1) - x\,log\left(\frac{R_1}{R_2}\right)}{2\,\pi\,x_2} \tag{2.45}$$

With suffix LE are denoted the velocities induced by the leading edge vortex while with suffix TE are the velocities induced by the trailing edge one.

The influence of the linearly distributed vorticity on its middle point is as follows,

$$u_{p\,LE} = -\frac{1}{2}\frac{x - x_2}{x_2} \tag{2.46}$$

$$u_{p\,TE} = \frac{1}{2}\frac{x}{x_2} \tag{2.47}$$

$$v_{p\,LE} = -\frac{1}{2\pi} \tag{2.48}$$

$$v_{p\,TE} = \frac{1}{2\pi} \tag{2.49}$$

Transforming the induced velocities to global coordinates yields,

$$u_{LE} = u_{p\,LE}\,cos\,(-\alpha_i) + v_{p\,LE}\,sin\,(-\alpha_i) \tag{2.50}$$

$$u_{TE} = u_{p\,TE}\,cos\,(-\alpha_i) + v_{p\,TE}\,sin\,(-\alpha_i) \tag{2.51}$$

$$v_{LE} = -u_{p\,LE}\,sin\,(-\alpha_i) + v_{p\,LE}\,cos\,(-\alpha_i) \tag{2.52}$$

$$v_{TE} = -u_{p\,TE}\,sin\,(-\alpha_i) + v_{p\,TE}\,cos\,(-\alpha_i) \tag{2.53}$$

Adding the influence of the leading edge and the trailing edge we obtain the total velocities induced by the linear vorticity distributed panel in a point,

$$u = u_{LE} + u_{TE} \tag{2.54}$$
$$v = v_{LE} + v_{TE} \tag{2.55}$$

2.4.2 Influence matrices

The Influence matrices contain information of the induced velocities and a panel singularity (or other kind of singularity) creates in all the collocation positions (or other points in the flow domain) and itself.

The influence matrix A_{ij} is defined as the matrix that contains the induced velocity components normal to the surface, created by the contribution of a unit strength source j at the location i. While the influence matrix B_{ij} contains the velocity components parallel to the airfoil surface induced by a constant unit strength source j at the location i.

$$A_{ij} = (u, v)_{ij} \cdot \underline{n_i} \tag{2.56}$$
$$B_{ij} = (u, v)_{ij} \cdot \underline{t_i} \tag{2.57}$$

Where the induced velocities u, v are in global coordinates system, Equations 2.32 and 2.33. Developing the equations above can be written as follows,

$$A_{ij} = v\, cos\,(\alpha_i) - u\, sin\,(\alpha_i) \tag{2.58}$$
$$B_{ij} = u\, cos\,(\alpha_i) + v\, sin\,(\alpha_i) \tag{2.59}$$

Where α_i is the panel angle in the global coordinate system.

The induced coefficient matrix for the influence of a panel source with uniform strength distribution on its middle point is,

$$A_{ij} = \frac{1}{2} \tag{2.60}$$
$$B_{ij} = 0 \tag{2.61}$$

According to theory, a two-dimensional point vortex creates the same unit induced velocity in a point as a source but rotates 90 degrees [35]. Therefore, we can link the normal and tangential induced velocities by a vortex with the ones induced by a source in the following way, see Figure 2.5

$$u_\Gamma = +v_\sigma \tag{2.62}$$
$$v_\Gamma = -u_\sigma \tag{2.63}$$

The relation in between the induced matrices, A_{ij} and B_{ij} of a source and a vortex is the following,

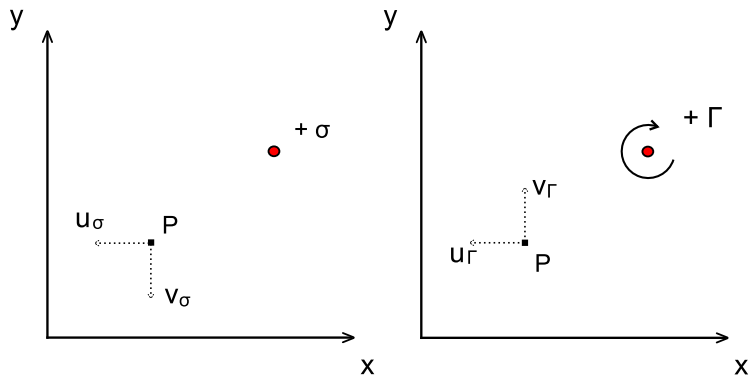

Figure 2.5: Singularities induced velocities, (a) Point source induced velocities (b) Point vortex induced velocities

$$B_{ij\,\Gamma} = +A_{ij} \tag{2.64}$$
$$A_{ij\,\Gamma} = -B_{ij} \tag{2.65}$$

Where $A_{ij\,VORTEX}$ and $B_{ij\,VORTEX}$ are vortex induced normal and tangential influence coefficient matrices, while A_{ij} and B_{ij} are source induced ones.

To compute the induced coefficients matrix of a linear vortex distribution one has to proceed in the following way. Each coefficient of the matrix has the influence of a leading edge (LE) and a trailing edge vortex (TE). Each vortex, γ_i, except for the ones located on the first and the last edges of the panels 1 and N, will act as a LE vortex belonging to the panel i and as a TE vortex of the panel $i-1$.

$$A_{ij} = -u_{LE}\, sin(\alpha_i) + v_{LE}\, cos(\alpha_i) - u_{TE}\, sin(\alpha_{i-1}) + v_{TE}\, cos(\alpha_{i-1}) \tag{2.66}$$
$$B_{ij} = u_{LE}\, cos(\alpha_i) + v_{LE}\, sin(\alpha_i) + u_{TE}\, cos(\alpha_{i-1}) + v_{TE}\, sin(\alpha_{i-1}) \tag{2.67}$$

The vortex located at the first edge of the first panel will only act inducing velocities as a LE vortex, the induced coefficients matrix can be written as follows,

$$A_{i1} = -u_{LE}\, sin(\alpha_i) + v_{LE}\, cos(\alpha_i) \tag{2.68}$$
$$B_{i1} = u_{LE}\, cos(\alpha_i) + v_{LE}\, sin(\alpha_i) \tag{2.69}$$

The vortex located on the last edge of the last panel, N, will only induce velocities as a TE vortex, the induced coefficients matrix for this vortex location can be formulated as shown below,

$$A_{iN} = -u_{TE}\, sin(\alpha_i) + v_{TE}\, cos(\alpha_i) \tag{2.70}$$
$$B_{iN} = u_{TE}\, cos(\alpha_i) + v_{TE}\, sin(\alpha_i) \tag{2.71}$$

2.4.3 Single wake model, problem discretization

The airfoil contour S is discretized with N panel elements. At each panel center a control point, i, is located. On each element the surface source density is taken to be of constant strength, while the vorticity is modeled with a parabolic distribution around the surface of the airfoil being zero in both, the upper and lower trailing edge panels. The sources strength is defined as σ_i, it starts with subindex $i = 1$ on the trailing's edge lower panel moving towards the leading edge and finalizing in the upper trailing edge panel with subindex $i = N$, as depicts the following figure 2.6.

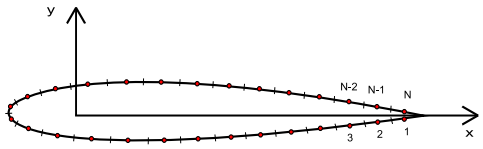

Figure 2.6: Airfoil discretization

In order to model the flow around the airfoil, a superposition of different fundamental solutions is generated. The translating offset flow created by a distribution of constant panel sources around the airfoil, the rotating offset flow induced by a parabolic distribution of vorticity together with a source distribution. In order to satisfy the Neumann condition of no penetration, the viscous shear layer is taken into account with the introduction of a injection function, more usually known as transpiration velocity, taking into account the influence of the viscous boundary layer into the inviscid potential flow. To finalize the single wake, the influence of the point vortex is added to the potential model.

The orientation of the airfoil panels will be denoted using the components of the tangent vectors, $\underline{t}_x$ and $\underline{t}_y$. From now the matrix and vector notation introduced in the dissertation of Sørensen [33] will be used for simplicity in explaining the method. In this notation the operation $\sum_{i=1}^{N}\sum_{j=1}^{N} A_{ij}\sigma_j$ is substituted by $\underline{\underline{A}}\,\underline{\sigma}$.

The translating onset flow For convenience the translating onset flow U_∞ will be divided into a chordwise member, $U_{\infty x} = U_\infty cos\alpha$, and a contribution

perpendicular to the chord, $U_{\infty y} = U_\infty sin\alpha$. In order to obtain the local tangential and normal velocities on the panels coordinate system, the velocity $U_{\infty x}$ has to be projected on the surface element multiplying by the tangent vectors. In this way are obtained the local tangential velocity component, $U_{\infty x}\underline{t}$ and the local normal velocity component, $-U_{\infty x}\underline{n}$. In regarding the normal component of the freestream velocity $U_{\infty y}$, its local tangential and normal components in the local panel reference system will be respectively $U_{\infty y}\underline{t}$ and $U_{\infty y}\underline{n}$.

In order to satisfy the Neumann condition a point source distribution, σ, is introduced so that the following normal and tangential velocities in all the panels are,

$$\underline{u}_x = \underline{\underline{B}}\,\sigma + U_{\infty x}\underline{t} + U_{\infty y}\underline{n} \tag{2.72}$$

$$\underline{v}_x = 0 \tag{2.73}$$

The velocities induced by the source distribution outside the airfoil contour can be obtained in the following way, being all the quantities with $*$ related with the off body locations,

$$\underline{u}^*_x = \underline{\underline{B}}^*\,\sigma + U_{\infty x}\underline{t} + U_{\infty y}\underline{n} \tag{2.74}$$

$$\underline{v}^*_x = \underline{\underline{A}}^*\,\sigma - U_{\infty x}\underline{n} + U_{\infty y}\underline{t} \tag{2.75}$$

Where the $*$ will be used from now on to refer to location points outside the airfoil contour.

In order to ensure a unique solution, an auxiliary condition has to be applied to our problem, this condition, known as the Kutta condition, is related with the flow characteristics at the airfoil trailing edge. It is known, when the flow is attached, that the effects of viscosity are confined to thin shear layers on the airfoil surface and the downstream wake, formed by the merging of the upper and lower boundary layers when leaving the airfoil on its trailing edge. The Kutta condition will force a singularity in the potential flow field, located at the sharp trailing edge and allowing the streamlines to leave the airfoil at this point, generating in a way a more physical solution. The Kutta condition will force the velocities to remain finite at the trailing edge.

The Kutta condition in its steady or unsteady form [36] will be set in adding a rotating onset flow into the equations above, see section 4.5.

The rotating onset flow The rotating onset flow is added to the system using a vortex distribution, γ_j, around the airfoil surface, in which the vorticity is parabolically distributed along the airfoil contour, with zero strength at the 1st and N'th panels.

For an airfoil with vortex strength Γ, vortex distribution is defined as follows, where ΔS_k is the length of the panel element k,

$$\gamma_j = \Gamma \frac{(j-1)(N-j)}{\sum_{k=1}^{N}(k-1)(N-k)\Delta S_k} \tag{2.76}$$

As seen in the equation above, the local vorticity distribution is dependent of the total circulation around the body. The total circulation is obtained as the addition of all the vorticity distributed along the airfoil contour multiplied by their panel length,

$$\Gamma = \sum_{j=1}^{N} \gamma_j \Delta S_j \tag{2.77}$$

Using the relation in between the source / vortex influence matrices shown in 2.64 and 2.65, the velocities induced by a rotating onset flow, that is, the parabolic vorticity distribution, in the tangential and normal directions in function of the induced coefficient matrix can be written as follows

$$u_R = \underline{\underline{A}}\,\underline{\gamma} \tag{2.78}$$

$$v_R = -\underline{\underline{B}}\,\underline{\gamma} \tag{2.79}$$

Further, in order to counteract the effect of the normal velocities created by the vortex distribution at the airfoil surface, and satisfying in this way the Neumann boundary condition, a new source, $\underline{\sigma}^R$, is introduced,

$$\underline{\underline{A}}\,\underline{\sigma}^R = \underline{\underline{B}}\,\underline{\gamma} \tag{2.80}$$

$$\underline{\sigma}^R = \underline{\underline{A}}^{-1}\underline{\underline{B}}\,\underline{\gamma} \tag{2.81}$$

In a similar way, the tangential and normal velocities induced by the vorticity distribution together with the extra source introduced above, σ^R,

$$u_R = \underline{\underline{B}}\underline{\sigma}^R + \underline{\underline{A}}\underline{\gamma} \tag{2.82}$$

$$v_R = 0 \tag{2.83}$$

Evaluating the velocities outside the airfoil surface yields,

$$u_R^* = \underline{\underline{B}}^*\underline{\sigma}^R + \underline{\underline{A}}^*\underline{\gamma} \tag{2.84}$$

$$v_R^* = \underline{\underline{A}}^*\underline{\sigma}^R - \underline{\underline{B}}^*\underline{\gamma} \tag{2.85}$$

Where $\underline{\underline{A}}^*$ and $\underline{\underline{B}}^*$ contain the influence coefficients from the panel to the point considered.

The influence of the boundary layer In order to simulate the influence of the viscous boundary layer, a transpiration velocity is introduced, adding the effects of the viscous flow into the inviscid potential flow solution.

$$w_T = \frac{\partial}{\partial s}\left(u_e \delta^*\right) \tag{2.86}$$

The displacement thickness δ^* is obtained from the boundary layer calculations, that in the present case follows a strong viscous-inviscid boundary layer coupling. The strong coupling is obtained via a source distribution that will create a transpiration velocity in the airfoil surface replacing the non penetration Neumann conditions coupling the viscous and inviscid parts of the system.

$$w_T = \underline{\underline{A}}\, \underline{\sigma}_{w_T} \tag{2.87}$$

$$\sigma_{w_T} = \underline{\underline{A}}^{-1}\, \underline{w}_T \tag{2.88}$$

Normal and tangential velocities induced by the latest source distribution,

$$u_{w_T} = \underline{\underline{B}}\, \underline{\underline{A}}^{-1}\, \underline{w}_T \tag{2.89}$$

$$v_{w_T} = w_T \tag{2.90}$$

Evaluating the velocities in a point outside the airfoil surface yields,

$$v^*_{w_T} = \underline{\underline{A}}^*\, \underline{\underline{A}}^{-1}\, \underline{w}_T \tag{2.91}$$

$$u^*_{w_T} = \underline{\underline{B}}^*\, \underline{\underline{A}}^{-1}\, \underline{w}_T \tag{2.92}$$

The single wake influence An inviscid wake is considered for the unsteady case, in which every time step a vortex is shed from the airfoil trailing edge with a strength, Γ_W. The vortex strength is equal to the change of circulation on the airfoil contour. The vortices shed by the airfoil convect downstream with the freestream,

$$\Gamma_W = \Gamma_{t-1} - \Gamma_t \tag{2.93}$$

Where S_a is the length of the airfoil contour, Γ_{t-1} is the airfoil circulation at time $(t-1)$ and Γ_t is the airfoil circulation at time t.

Surface body velocities induced by the vortex blobs that form the wake can be written as follows,

$$u_W = \underline{\underline{B}}_W\, \underline{\Gamma}_W \tag{2.94}$$

$$v_W = -\underline{\underline{A}}_W\, \underline{\Gamma}_W \tag{2.95}$$

Where $\underline{A}_W$ is the wake normal induction matrix and $\underline{B}_W$ is the wake tangential induction matrix. It is a NxN_w matrix, where N is the number of panels distributed around the airfoil and N_w is the number of point vortices that forms the wake.

In order to satisfy the Neumann condition on the airfoil surface, a source distribution σ_W has to be created on the airfoil contour. The strength of the source distribution, σ_W, added to the system in order counteract the normal velocity induced by the wake vortices on the airfoil surface is,

$$\sigma_W = -\underline{\underline{A}}^{-1}\, v_W \tag{2.96}$$

The airfoil surface distribution of velocities induced by the wake vortices and the extra source distribution added to the airfoil is,

$$u_W = \underline{\underline{B}}_W\, \underline{\Gamma}_W + \underline{\underline{B}}\, \underline{\sigma}_W \tag{2.97}$$
$$v_W = 0 \tag{2.98}$$

The velocities induced by the wake, vortex blobs and source distribution around the airfoil, in an off body location are,

$$u^*_W = \underline{\underline{B}}^*_W\, \underline{\Gamma}_W + \underline{\underline{B}}^*\, \underline{\sigma}_W \tag{2.99}$$
$$v^*_W = -\underline{\underline{A}}^*_W\, \underline{\Gamma}_W + \underline{\underline{A}}^*\, \underline{\sigma}_W \tag{2.100}$$

THE FULL POTENTIAL FLOW SYSTEM To obtain the full potential flow solution all the different fundamental inviscid solutions have to be added.

At the airfoil surface the distribution of tangential and normal velocities it is obtained from the following formulas,

$$\begin{aligned}\underline{u}_I = {} & \underline{\underline{B}}\, \sigma + U_{\infty x}\underline{t} + U_{\infty y}\underline{n} + \underline{\underline{A}}\, \underline{\gamma} \\ & + \underline{\underline{B}}\underline{\sigma}^R + \underline{\underline{B}}\, \underline{\underline{A}}^{-1}\, \underline{w}_T + \underline{\underline{B}}_W\, \underline{\Gamma}_W + \underline{\underline{B}}\, \underline{\sigma}_W\end{aligned} \tag{2.101}$$
$$\underline{v}_I = \underline{w}_T \tag{2.102}$$

When the velocities are evaluated in the off body locations, the distribution of tangential and normal velocities is,

$$\begin{aligned}\underline{u}^*_I = {} & \underline{\underline{B}}^*\, \sigma + U_{\infty x}\underline{t} + U_{\infty y}\underline{n} + \underline{\underline{A}}^*\, \underline{\gamma} \\ & + \underline{\underline{B}}^*\underline{\sigma}^R + \underline{\underline{B}}^*\, \underline{\underline{A}}^{-1}\, \underline{w}_T + \underline{\underline{B}}^*_W\, \underline{\Gamma}_W + \underline{\underline{B}}^*\, \underline{\sigma}_W\end{aligned} \tag{2.103}$$
$$\begin{aligned}\underline{v}^*_I = {} & \underline{\underline{A}}^*\, \sigma - U_{\infty x}\underline{n} - U_{\infty y}\underline{t} - \underline{\underline{B}}^*\underline{\gamma} \\ & + \underline{\underline{A}}^*\underline{\sigma}^R + \underline{\underline{A}}^*\, \underline{\underline{A}}^{-1}\, \underline{w}_T - \underline{\underline{A}}^*_W\, \underline{\Gamma}_W + \underline{\underline{A}}^*\, \underline{\sigma}_W\end{aligned} \tag{2.104}$$

2.5 Double wake model, theory and problem formulation

Due to the lack in performance of the single wake model at high angles of attack, for the stall range of the airfoil, a new model has been implemented. Knowing that the low performance is due to the lack of accuracy of solving the integral boundary layer equations for flow around surfaces with a considerable amount of separation, in the new model the boundary layer is neglected and the flow is considered purely potential. This model will be known from now on as the double wake model, due to the dual treatment of the separated region in two shear layers leaving the airfoil and converging downstream.

Separation is one of the phenomena with the strongest influence on the aerodynamic design of wind turbine blades. Lift and drag forces are strongly affected when the flow undergoes separation, causing an exponential increment of drag at the same time as the lift curve stalls. The bubble type of separation has been studied widely, the difficulties of modeling this kind of phenomena stems from predicting the pressure in the separated region at the right level as well as predicting the exact position where the attached boundary layer undergoes separation. The double wake model will allow us to compute with a high degree of accuracy the pressure distribution all over the airfoil, including the separated region.

2.5.1 Theory

The double wake model will generate a vortex sheet that leaves the airfoil from the separation point at the same time that the trailing edge is releasing vorticity through another vortex sheet. The uniform vortex distribution around the two wakes will influence the tangential velocities at the airfoil surface creating a region of reverse flow for simulating the separation effect of the flow around an airfoil at high angles of attack.

The region of fluid surrounding the airfoil and the separated wake is irrotational, and, assuming that the Mach number is low, compressibility is negligible. The area in between the two wakes does not have significant vorticity and has a constant total pressure, and thus it is taken to be a potential flow region. The flow will be then irrotational everywhere except in the two confined sheets of vorticity that forms the separated wake, this sheets are dotted with uniform vorticity.

The initial shape of the wake is obtained iteratively starting from an initial condition. As initial condition the wake sheets are represented by two straight lines in between the separation points and a common point downstream, see Figure 2.7.

In Figure 2.7 TH1 and TH2 are the wake directions when the vorticity sheet leaves the airfoil at the separation and trailing edge positions respectively. The wake length is related with the airfoil thickness through figure, Figure 2.8, $WL = W_F \cdot W_H$, where W_H is the wake height and W_F is the wake factor. Once a first computation has been realized using the initial condition, a particle leaving

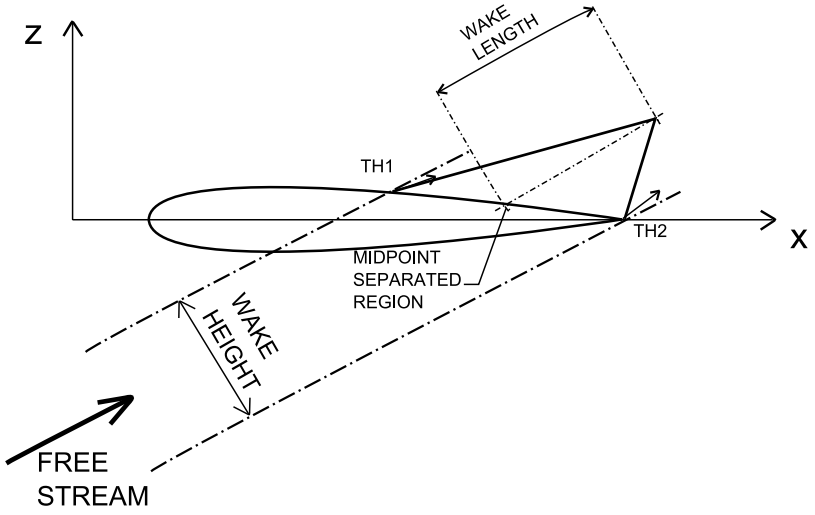

Figure 2.7: Double wake initial shape

the separation point and another one leaving the trailing edge are followed, finding the wake shape for both, the upper and the lower separation points.

The relation in between the airfoil chord to thickness ratio and the wake factor is fruit of a study with different airfoil shapes, see Figure 2.8. During the study different wake length were implemented, the ones that give better predictions were chosen for the different types of airfoil geometries. A linear relation was obtained in between the thickness to chord ratio and the wake factor.

The potential model implemented consists of a linear distribution of vorticity placed around all the individual panels that represent the airfoil and the free vortex sheets are represented by a number of panels with uniform vorticity. In this way, there are N+1 vorticity values, where N is the total number of panels. The following conditions are required in order to close the system of equations:

- The boundary condition applied at each panel collocation point is that the normal velocity is equal to zero.
- At the upper surface separation point, the right edge of the panel has the same vorticity as at the lower trailing edge, $\gamma_{SEP} = -\gamma_1$
- The vorticity value just downstream of the separation point on the upper surface is set equal to zero, left edge of the panel SEP+1. This edge will only have vorticity when forming part of the panel SEP (right edge).
- The vorticity value on the upper trailing edge is set equal to zero. $\gamma_{N+1} = 0$
- The free vorticity sheets are located on streamlines, hence there are no static pressure drop across them. The upper wake has the same uniform

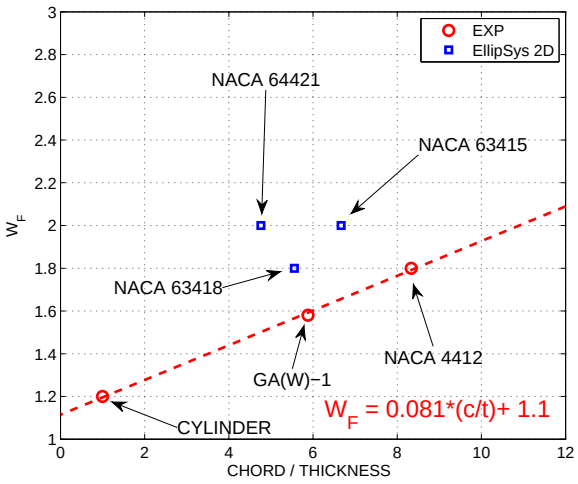

Figure 2.8: Wake Factor, WF, as function of thickness/chord ratio

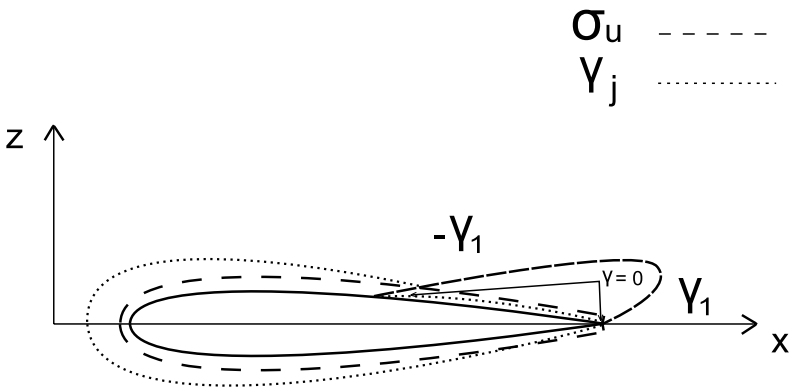

Figure 2.9: Double wake vorticity distribution

vorticity as the lower one but with different sign, and it is equal to the vorticity of the lower trailing edge, $\gamma_{upper} = -\gamma_1$ and $\gamma_{lower} = \gamma_1$

In order to close the system a source strength is distributed uniformly around the airfoil surface.

The airfoil area situated between the two wakes it is isolated from the rest of the flow, a jump of total pressure has to be added to the airfoil panel stations situated on the separated area,

$$C_p = 1 - \left(\frac{u_e}{U_\infty}\right)^2 + k_H \frac{\Delta H}{p_\infty} \tag{2.105}$$

Where ΔH is the increase in total pressure inside the separation bubble, being equal to zero all over the airfoil except in the separation wake region. The

constant k_H is equal to 2, while $p_\infty = 1/2\rho U_\infty^2$. The assumption of zero static pressure drop across the free shear layer is use to find the total pressure in the wake, writing the average velocity in the following way,

$$V_m = \frac{1}{2}\left(V_{out} + V_{in}\right) \tag{2.106}$$

Since the $\gamma_{upper} = V_{out} - V_{in}$ and $\gamma_{lower} = V_{in} - V_{out}$,

$$V_{outer} = V_m + \frac{\gamma_{upper}}{2} \; and \; V_{in} = V_m - \frac{\gamma_{upper}}{2} \tag{2.107}$$

The change in total pressure of the wake area will be,

$$\begin{aligned}\Delta H = H_{inner} - H_{outer} = p_{inner} + \frac{1}{2}\rho\left(V_m - \frac{\gamma_{upper}}{2}\right)^2 \\ - p_{outer} - \frac{1}{2}\rho\left(V_m + \frac{\gamma_{upper}}{2}\right)^2 = -\rho V_m \gamma_{upper} = \rho V_m \gamma_{lower}\end{aligned} \tag{2.108}$$

In regards of the SEP location, it can be obtained in two different manners. The first approach is, using a downstream matching integral boundary layer solution until separation is found based on the friction coefficient parameter, separation is located when $C_f \leq 0$. The second approach is forcing the flow to separate at a specific point, usually obtained from experimental or computational pressure distributions.

The implementation of the first approach has been done, but the separation location obtained in this way does not move as fast downstream in function of angle of attack as it does in experiments, over predicting the airfoil forces. The second approach has been implemented with a great success. The downside of the method is that the separation location has to be known in advance. A future study will be aimed in order to find a relation between the onset of separation and the airfoil geometry, Reynolds number, angle of attack of the aforementioned airfoil.

2.6 Summary

In this chapter the foundations of potential flow theory have been reviewed. Based on the potential flow theory the formulation of a panel method has been presented herein. The basic theory behind steady as well as unsteady potential flow modeling was presented.

The different singularity elements used in the present approach have been defined in this chapter. Focusing in the velocity induced in a point P by: constant source distribution, point vortex and linear vorticity distribution. The generation of influence matrices has been explained.

Discretization of the single and the double wake models has been depicted. In the single wake model, the final solution will be obtained by superposition of the different singularity solutions:

- The translating onset flow. Constant panel source distribution, σ_j
- The rotating onset flow. Parabolic vortex distribution, Γ
- The influence of the viscous boundary layer. Transpiration velocity source distribution, σ_{wT}
- The influence of the vortex wake. Wake point vortices, Γ_W

Whereas in the double wake model, in which viscous effects are not taken into account, the full potential flow system is composed of:

- The translating onset flow. Constant source distribution around the airfoil contour, σ_u
- The rotating onset flow. Linear panel vortex distribution, γ_j
- The influence of the double wake. Constant wake vortex distribution, γ_{lower} and γ_{upper}

In the double wake model a correction of the pressure in the separated region has been introduced in order to take into account the increase in total pressure inside the separation bubble.

Chapter 3

Boundary Layer

3.1 Boundary layer theory

Prandtl in 1904 presented for first time the concept and theory of boundary layers, approximately one year after the first flight of a powered aircraft by the Wright brothers [37]. His studies became the foundation in which aerodynamic research was based, helping the rapid development of this branch of science.

The effect of viscosity is directly linked to the Reynolds number quantity. While at high Reynolds number the influence of viscosity is confined to thin layers around the solid wall, at low Reynolds numbers this layers grow in thickness increasing the viscous effects upon the body. This area around the body where the viscous effects are confined is most commonly known as a boundary layer. It can be defined as the fluid region around a solid body inside which the fluid is subjected to frictional forces that retard the fluid motion, [38].

Bases of Prandtl's boundary layer theory, [39]:

- At the surface of the body the fluid is at rest relatively to the body, no slip condition between the fluid and the surface. The relative fluid velocity increases from zero at the surface of the body to a value close to the main stream at the edge of the boundary layer.
- Near the body there are large velocity gradients and therefore rates of strain. Shear stresses due to viscosity are directly related to these rates of strain.
- The Reynolds number becomes a essential parameter for defining the flow nature as a rate between inertia and viscous forces, $Re = \rho UL/\mu$. The region near the body where the viscous stresses are important is thin and becomes thinner with increase in Reynolds number.
- The small thickness of the boundary layer at high Reynolds numbers permits some simplifications of the full Navier-Stokes equations, which lead to a set of parabolic equations more easily to be solved, the boundary layer equations, see Section 3.1.2. The boundary layer equations are used to model the flow in the vicinity of the body surface while inviscid theory can be applied in the outer region, in which the viscous terms are neglected.

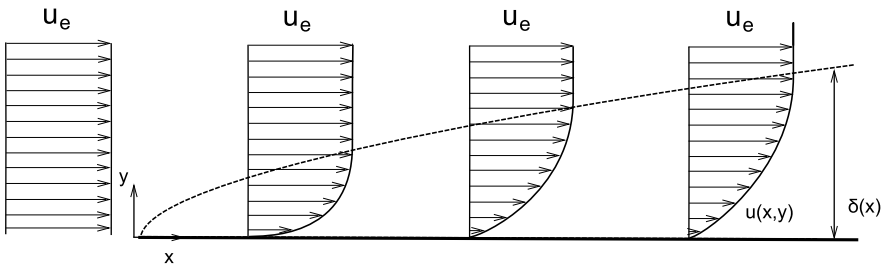

Figure 3.1: Sketch of the boundary layer on a flat plate

In Figure 3.1 is sketched the velocity profile of the boundary layer on a flat plate with flow at zero angle of attack. The velocity distribution entering the leading edge is uniform, the thickness of the boundary layer increases as the flow moves downstream from the leading edge. Further, the boundary layer thickness will decrease as the Reynolds number increases, the viscous forces become smaller in relation with the inertial ones.

The boundary layers are regions where vorticity is concentrated around bodies. Vorticity is generated at the surfaces of the bodies due to the presence of viscous stresses and it is convected downstream the surface forming the boundary layer and the wake behind it, formed when the boundary layer leaves the rear of a body, in the wake the influence of viscosity is still large, playing an important role in the downstream convection of the wake.

Defining circulation around a closed circuit as the integrated vorticity that threads it, is possible to define the viscosity as the the source of circulation and vorticity in a fluid. Hence the vorticity is only create in regions where viscous effects are important, therefore it is generated in the boundary layer and wake of the body itself. In a flat plate, due to the zero pressure gradient, vorticity is only be created in the leading edge converging downstream.

A thin boundary layer will not exist once the flow has undergone separation, for example on the rear side of bluff bodies or on the suction surface of airfoils at high enough angles of attack. In most of the cases, the boundary layer increases its thickness in the downstream direction until it can not be contain anymore and the flow becomes reversed. The reversal flow forces the fluid particles outside the boundary layer which is identified as boundary layer separation, [39]. The separation phenomena is associated with the formation of vortices on the separated region that converge downstream and produce large energy losses in the wake of the body.

Separation is delayed with the increasing of the Reynolds number, thinner boundary layers are more resistant against separation. In the case of airfoils, their shape is crucial, generally thin airfoils will separate later than thick airfoils, although a deeper stall will appear on the first ones. The nose shape of the airfoil is important in order to determine the type of separation, rounded airfoil noses will be more given to trailing edge separation while sharp noses will usually undergo leading edge separation due to the large pressure gradients created on the airfoils nose suction side.

3.1.1 Laminar flow, transition and turbulent flow

In order to explain the changes in nature that experiences the flow around a solid body, an airfoil section is considered, and a high Reynolds number flow is assumed. This flow will create a thin boundary layer around the airfoil contour that variates in thickness in function of its streamwise position.

Supposing that from the stagnation point downstream the flow in the boundary layer is composed by smooth and stable streamlines parallel to the airfoil surface, the flow in this case is referred as laminar. At a position downstream the stagnation point, depending of the Reynolds number, the flow in the boundary layer becomes unstable and changes from laminar to turbulent state. This change can be triggered by the pressure gradient, the roughness of the surface or the influence of external disturbances like noise or turbulence intensity. The turbulent boundary layer has irregular fluctuations in velocity magnitude and direction added to the mean flow, that still remains parallel to the surface.

Velocity fluctuations due to turbulence can be of orders of magnitude smaller than the mean velocity. The mixing effect in the boundary layer driven by the velocity fluctuations increases the rates of diffusion of momentum, vorticity and heat transfer. Since the rates of momentum transport due to the relatively large eddy movements, created by the velocity fluctuations, are larger than those due to the molecular movements, governed by the viscosity, the eddy shears stresses are generally much larger than the viscous shear stresses except in the viscous inner and overlap layers. The viscous sub-layer is a thin layer adjacent to the surface of the order of a hundred of the thickness of the turbulent boundary layer, in which the turbulent fluctuations tends to be decremented due to the proximity of the body surface, [38]. In the viscous sub-layer the dominant shear stresses are the viscous ones. The overlap layer is the transition in between the viscous inner and outer layer. In the outer layer the eddy shear stresses are dominant.

The larger rate of strain close to the surface in the turbulent boundary layer make the wall shear stresses, $\tau_w = \mu \partial u / \partial y$, to be larger than for a laminar boundary layer at the same Reynolds number, creating a higher friction drag.

The process by which the flows changes laminar state to turbulent is most commonly known as transition. Laminar to turbulent transition occurs by fast growing laminar instabilities in the longitudinal and transversal directions, driven by the strong instability of the boundary layer under adverse pressure gradients. The chordwise position at which transition occur variates in function of the Reynolds number. At low Reynolds number the transition mechanism could use a large portion on the chord, while at higher Reynolds numbers transition occurs much earlier.

3.1.2 Boundary layer equations for steady 2D flow

Assuming thin layer theory the boundary layer equations can be derived from the full Navier-Stokes equations via an order of magnitude analysis as follows. Using as starting point the dimensionless x momentum equation,

$$\rho' u' \frac{\partial u'}{\partial x'} + \rho' v' \frac{\partial u'}{\partial y'} = -\frac{1}{\gamma_H Ma^2} \frac{\partial p'}{\partial x'} + \frac{1}{Re} \frac{\partial}{\partial y'} \left[\mu' \left(\frac{\partial v'}{\partial x'} + \frac{\partial u'}{\partial y'} \right) \right] \tag{3.1}$$

Where γ_H is the specific heat, Ma is the Mach number and Re is the Reynolds number.

As a first assumption of boundary layer theory the boundary layer thickness, δ, is supposed to be very small in comparison with the body scale, c,

$$\delta << c \tag{3.2}$$

An order of magnitude analysis of the non dimensional continuity equation is done in order to find the magnitude of the velocity v',

$$\frac{\partial (\rho' u')}{\partial x'} + \frac{\partial (\rho' v')}{\partial y'} = 0 \tag{3.3}$$

Assuming a freestream velocity equal to the unity, the velocity u' varies from 0 at the body surface to 1 at the boundary layer edge, so u' can be assumed to have an order of magnitude equal to 1, $O(1)$. The density ρ' and x' have the same order of magnitude. y' has a smaller order of magnitude since it varies from 0 to δ. Following this reasoning, from Equation 3.3, the velocity v' must have an order of magnitude $O(\delta)$, the same as the y'.

Extending the forehead adimensional analysis to the x momentum equation the orders of magnitude of the different terms can be written as follow,

$$O(1) + O(1) = -\frac{1}{\gamma_H Ma^2} O(1) + \frac{1}{Re} \left[O(1) + O\left(\frac{1}{\delta^2} \right) \right] \tag{3.4}$$

The second assumption of boundary layer theory states that the Reynolds number is large enough that its inverse has the same order of magnitude as the displacement thickness squared,

$$\frac{1}{Re} = O(\delta^2) \tag{3.5}$$

From Equation 3.4 and 3.4 it follows that the term $(1/Re)\partial/\partial y'(\mu(\partial v'/\partial x'))$ has an order of magnitude $O(\delta^2)$. Therefore much smaller that all the other terms from the x momentum equation and possible to neglect it. In this way the boundary layer approximation of the x momentum equation is obtained, in dimensional variables as follows,

$$\rho u \frac{\partial u}{\partial x} + \rho v \frac{\partial u}{\partial y} = -\frac{\partial p}{\partial x} + \frac{\partial}{\partial y} \left(\mu \frac{\partial u}{\partial y} \right) \tag{3.6}$$

Realizing a similar order of magnitude analysis to the y momentum equations, in adimensional variables can be written,

$$\rho' u' \frac{\partial v'}{\partial x'} + \rho' v' \frac{\partial v'}{\partial y'} = -\frac{1}{\gamma_H Ma^2} \frac{\partial p'}{\partial y'} + \frac{1}{Re} \frac{\partial}{\partial x'} \left[\mu' \left(\frac{\partial v'}{\partial x'} + \frac{\partial u'}{\partial y'} \right) \right] \tag{3.7}$$

In terms of orders of magnitude the Equation 3.7 above can be written,

$$O(\delta) + O(\delta) = -\frac{1}{\gamma_H Ma^2} \frac{\partial p'}{\partial y'} + O(\delta^2) \left[O(\delta) + O\left(\frac{1}{\delta}\right) \right] \tag{3.8}$$

Assuming that $\gamma_H Ma^2$ has $O(1)$, being γ_H the specific heat. The term $\partial p/\partial y$ has to be of order of magnitude $O(\delta)$ or smaller. Since the Reynolds number is very high, the boundary layer thickness, δ, is very small so for boundary layer flow can be stated that,

$$\frac{\partial p}{\partial y} = 0 \tag{3.9}$$

Stating that the pressure is constant through the boundary layer in a direction perpendicular to the body surface. Or what is the same, the pressure at the boundary layer edge is the same as the one at the body surface.

In the case of steady incompressible flow and Cartesian coordinates, the system of equations that governs a boundary layer flow is formulated as follows, [40]

$$u \frac{\partial u}{\partial x} + v \frac{\partial u}{\partial y} = -\frac{1}{\rho} \frac{dp}{dx} + \mu \frac{\partial^2 u}{\partial y^2} \tag{3.10}$$

$$\frac{\partial u}{\partial x} + \frac{\partial v}{\partial y} = 0 \tag{3.11}$$

$$\frac{\partial p}{\partial y} = 0 \tag{3.12}$$

Even though the boundary layer equations are non linear, as the Navier Stokes equations, they have a parabolic nature which makes them simpler and easier to be solved due to its upstream dependence. The boundary conditions applied to the boundary layer equations are,

$$y = 0 : u = 0; v = 0 \tag{3.13}$$

$$y = \infty : u = u_e \tag{3.14}$$

3.2 Two dimensional integral boundary layer

A study of a viscous fluid flow at high Reynolds number past a flat plate is used herein in order to present the integral form of the boundary layer parameters. As presented in the following figure, Figure 3.2, the fluid interacts with the plate surface causing a frictional drag force. The velocity profile changes and in order to satisfy the mass conservation the streamlines will be bended outwards. The outwards deflection that the external streamline is subjected too is defined as displacement thickness, δ^*.

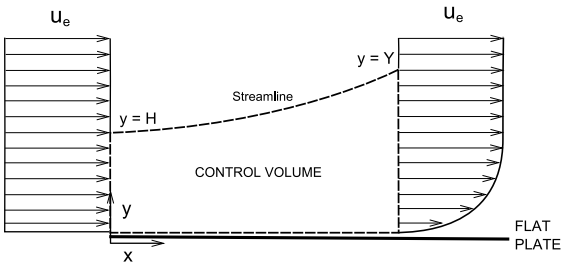

Figure 3.2: Control volume for the momentum analysis of flow past a flat plate

The control volume is chosen so the velocity distributions are known at its inlet and outlet. The upper side of the control volume is defined by a streamline and the lower by the flat plate surface. In this manner there is no mass nor momentum crossing the control volume upper nor lower boundaries.

The displacement thickness integral parameter can be obtained assuming steady flow and applying conservation of mass to the control volume in Figure 3.2,

$$\int\int \rho V \cdot dA = 0 = \int_0^Y \rho u dy - \int_0^H \rho u_e dy \tag{3.15}$$

If incompressible flow is assumed, the Equation 3.15 above yields,

$$u_e H = \int_0^Y u dy = \int_0^Y (u_e + u - u_e)\, dy = u_e Y + \int_0^Y \{u - u_e\}\, dy \tag{3.16}$$

From figure 3.2 can be seen that $Y = H + \delta^*$, rewriting the Equation 3.16 produces,

$$u_e (Y - H) = u_e \delta_1^* = \int_0^Y (u_e - u)\, dy \tag{3.17}$$

Following the displacement thickness quantity is defined as,

$$\delta_1^* = \int_0^\delta \left(1 - \frac{u}{u_e}\right) dy \tag{3.18}$$

Physically the displacement thickness can be interpreted as the decrement of the mass flow due to the presence of the boundary layer. Knowing that for a fully inviscid fluid flow, the mass flow, m_i, in between the body surface and a point outside the boundary layer, y_0, is defined as,

$$m_i = \int_0^{y_0} \rho_e u_e dy \tag{3.19}$$

In the case of a real flow, with a viscous boundary layer that varies its velocity from the body surface to the edge of the boundary layer. The mass flow, m_r, is formulated as,

$$m_r = \int_0^{y_0} \rho u dy \tag{3.20}$$

Subtracting the real mass flow from the mass flow of a pure inviscid flow, $m_i - m_r$, the decrement in mass flow due to the presence of the boundary layer is obtained and it relates with the boundary layer thickness quantity, δ_1^*, as follows,

$$m_i - m_r = \int_0^{y_0} (\rho_e u_e - \rho u)\, dy = \frac{1}{\rho_e u_e} \delta_1^* \tag{3.21}$$

The displacement thickness can also be seen as the deflection of the external streamline caused by the partial obstruction of the boundary layer to the freestream flow. Note that due to the integration of y variations, δ_1^* as all the other integral boundary layer quantities are only function of x. What makes possible to treat them numerically without a two dimensional fluid mesh, a surface fitted $1D$ mesh is used.

The momentum thickness θ_1 is defined as the loss of momentum of the real viscous flow due to the presence of the boundary layer. Its is obtained applying conservation of x momentum to the control volume in Figure 3.2,

$$\sum F_x = -D = \int\int u\,(\rho V \cdot dA) = \int_0^Y (\rho u dy) - \int_0^H u_e\,(\rho u_e dy) \tag{3.22}$$

$$D = \rho u_e^2 H - \int_0^Y \left(\rho u^2 dy\right) \tag{3.23}$$

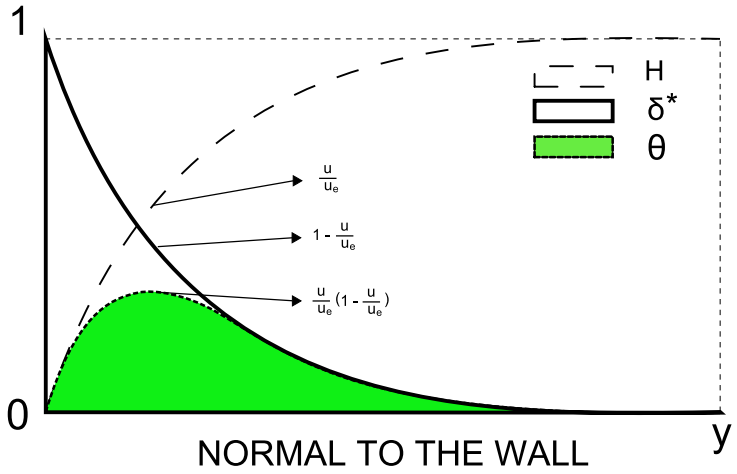

Figure 3.3: Displacement and Momentum thickness relation

If incompressible flow is assumed, and using the following relation for the shape factor, $H = \delta^*/\theta$,

$$H = \int_0^Y \frac{u}{u_e} dy \tag{3.24}$$

The drag can be written in the following form,

$$D = \rho \int_0^Y u\,(u_e - u)\,dy \tag{3.25}$$

Knowing the relation in between drag and momentum thickness for a flat plate, one can write as follows,

$$\theta_1 = \frac{D}{\rho u_e^2} = \int_0^\delta \frac{u}{u_e}\left(1 - \frac{u}{u_e}\right) dy \tag{3.26}$$

The following figure is added in order to clarify the relation in between the quantities $\frac{u}{u_e}$, $\left(1 - \frac{u}{u_e}\right)$ and $\frac{u}{u_e}\left(1 - \frac{u}{u_e}\right)$. Directly related via integration with the boundary parameters of interest.

Other parameters of interest in the two dimensional integral boundary layer approach are:

$$H = \frac{\delta_1^*}{\theta_1} \tag{3.27}$$

$$C_f = \frac{\tau_w}{\frac{1}{2}\rho u_e^2} \tag{3.28}$$

$$C_{Di} = \frac{1}{\rho_e u_e^3} \int_0^\delta \tau \frac{\partial u}{\partial y} dy \tag{3.29}$$

$$C_\tau = \frac{\tau_{max}}{\rho_e u_e^2} \tag{3.30}$$

$$H^* = \frac{\theta^*}{\theta_1} \tag{3.31}$$

$$Re_{\theta_1} = \frac{\rho_e u_e \theta_1}{\mu_e} \tag{3.32}$$

$$u_\tau = \sqrt{\frac{\tau_{wall}}{\rho}} \tag{3.33}$$

$$\theta^* = \int_0^\delta \frac{u}{U}\left(1 - \frac{u^2}{u_e^2}\right) dy \tag{3.34}$$

$$\tag{3.35}$$

3.3 Laminar boundary layer, Thwaites method.

The present method has been implemented as an alternative to Mark Drelas two equations laminar method, in order to solve attached laminar flow conditions around the airfoil. Thwaites abandoned the family of profiles idea and fitted the whole set of analytical and experimental results using a set of average one-parameter functions. Thwaites methods solves the momentum integral equation in terms of a parameter λ, therefore it is more stable and faster for computing attached laminar boundary layers.

The Kármán integral momentum equation can be written as follows,

$$\frac{d\theta_1}{dx} + \frac{\theta_1}{u_e}\frac{du_e}{dx}(2 + H) = \frac{C_f}{2} \tag{3.36}$$

Following Holstein and Bohlen in 1940, the momentum integral equation can be multiplied by $u_e\theta/\nu$, obtaining an equation with a right-hand side composed by dimensionless boundary-layer functions. The equation can be correlated by a single parameter λ.

$$\frac{d\theta_1}{dx}\frac{u_e\theta_1}{\nu} + \frac{\theta_1^2}{\nu}\frac{du_e}{dx}(2 + H) = \frac{\tau_w\theta_1}{\mu u_e} \tag{3.37}$$

The dimensionless boundary layer functions that appears in Equation 3.37 can be written as,

$$S(\lambda) \approx \frac{\tau_w \theta_1}{\mu u_e} \tag{3.38}$$

$$H(\lambda) \approx \frac{\delta^*}{\theta_1} \tag{3.39}$$

Knowing that $\theta_1 d\theta_1 = d(\theta_1^2/2)$, the Equation 3.37 above yields,

$$u_e \frac{d}{dx}\left(\frac{\lambda_1}{\partial u_e/\partial x}\right) = 2\left[S(\lambda) - \lambda\left(2 + H(\lambda)\right)\right] = F(\lambda) \tag{3.40}$$

Where the parameter λ is given as,

$$\lambda = \frac{\theta_1^2}{\nu}\frac{\partial u_e}{\partial x} \tag{3.41}$$

Following the idea of abandoning the family profiles to evaluate the parametric function λ, Thwaites studied the entire collection of analytic and experimental results trying to fit them by a set of one parameter functions. He found an outstanding correlation for the function F and proposed the following linear fit, where a = -6 and b = 0.45,

$$F(\lambda) = b + a\lambda \tag{3.42}$$

In order to find the solution to Equation 3.40 it is necessary to use the definition of F formulated in Equation 3.42

$$\begin{aligned} u_e \frac{d}{dx}\left(\frac{\lambda}{\partial u_e/\partial x}\right) &= b + a\lambda \\ \frac{u_e}{\nu}\frac{d}{dx}\left(\theta_1^2\right) &= a\frac{\partial u_e/\partial x\, \theta_1^2}{\nu} + b \end{aligned} \tag{3.43}$$

Setting $\theta_1^2 = Y$ we can write the following first order ordinary differential equation

$$Y' - a\frac{\partial u_e/\partial x}{u_e} Y = \frac{\nu}{u_e} \tag{3.44}$$

The equation above can be solved analytically in the following way

$$\begin{aligned} Y &= e^{\int a\partial u_e/\partial x/u_e dx}\left[C + \int_0^x \frac{\nu}{u_e} b \;\; e^{-\int a\partial u_e/\partial x/u_e dx} dx\right] \\ &= u_e^a\left[C + \int_0^x \frac{\nu}{u_e} b u_e^{-a} dx\right] = b\nu u_e \int_0^x u_e^{-a-1} dx \end{aligned} \tag{3.45}$$

Where constant C is set to zero in order to avoid the infinite momentum thickness for $u_e = 0$.

$$\boxed{\theta_1^2 = b\nu u_e \int_0^x u_e^{-a-1} dx} \tag{3.46}$$

In the present work the correlations used for $H(\lambda)$ and $C_f(\lambda)$ are,

$$H(\lambda) \approx a_H \lambda^2 - b_H \lambda - c_H \tag{3.47}$$

$$C_f(\lambda) \approx 2\left(a_S \lambda^2 + b_S \lambda + c_S\right)\left(\frac{\mu}{\rho \theta_1 u_e}\right) \tag{3.48}$$

The constants in Equation 3.47 are set the following values,

$$a_H = 15 \tag{3.49}$$

$$b_H = -6 \tag{3.50}$$

$$c_H = 2.5 \tag{3.51}$$

$$a_S = -2.17 \tag{3.52}$$

$$b_S = 1.73 \tag{3.53}$$

$$c_S = 0.23 \tag{3.54}$$

$$\tag{3.55}$$

The accuracy of Thwaites method is about ±5 percent for favorable or mild adverse gradients but may be as much as ±15 percent near the separation point,[38].

3.4 Quasi 3D turbulent boundary layer

In this section, an overview of the Quasi 3D boundary layer approach is done. The differential form of the Quasi 3D boundary layer equations is presented, as a basis for the integral form introduced later herein. To conclude, corrections in order to adapt the equations, based on flat plate theory, to an airfoil geometry will be presented.

The streamlines in the boundary layer edge of a flat plate follow circular arcs, there is no radial velocity at the edge of the boundary layer. But in the present case, involving a blade, the presence of pressure gradients change the forehead affirmation. Rotation and curvature effects changes the flow structure around the airfoil creating radial velocities along the span of the wind turbine blade, the Coriolis and centrifugal forces modify the pressure distribution and the skin friction stress on the blade surface. In order to include these effects into the integral boundary layer analysis an effort has been done to transform the full three dimensional boundary layer equations into the Quasi 3D ones.

3.4.1 Blade geometry and coordinate system

The system is composed by a 3D wind turbine blade, Figure 3.4, although in order to simplify the analysis, in a first step, the real blade is simplified into a flat plate, Figure 3.5. The system is presented in cylindrical coordinates (θ, r, z) with velocities (u, v, w) in the respective directions. The coordinate system is rotating with the blade, which turns at constant angular velocity Ω around the z axis. The wind is entering the system from the negative z direction, θ is the azimuthal angle, r is the distance to the center of rotation and z is the axis of rotation. u is the streamwise velocity while v, w are respectively the radial and the velocity component in the direction of rotation.

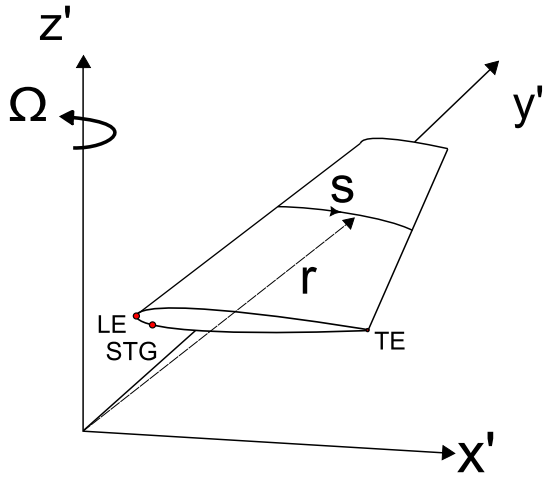

Figure 3.4: 3D Blade System,

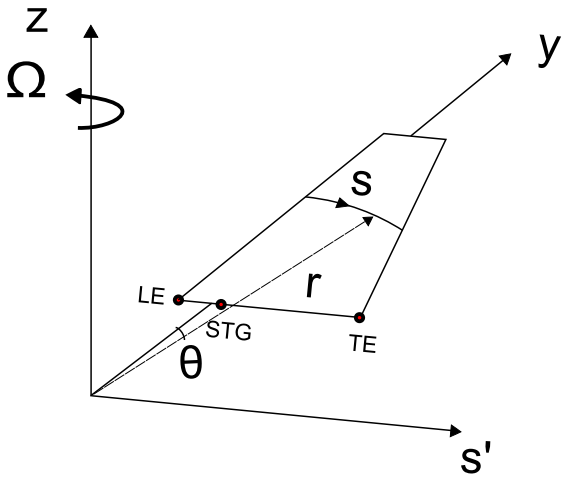

Figure 3.5: Flat Plate System,

Far away from the flat plate surface the influence of the boundary layer is negligible and the streamlines of the potential flow around a flat plate are circular arcs with constant radius, following s, Figure 3.5. In order to simplify the problem a relation in between the s and s' is introduced. Where s is the arc followed by the undisturbed free streamlines of the inviscid flow, while s' is the coordinate of s_{real} on the surface of the blade from the stagnation point to the trailing edge. First of all the relation in between s_{real} and s' is formulated, where s_{real} starts at the stagnation point and ends at the trailing edge following the surface,

$$s' = s_{real}\frac{c}{L} \tag{3.56}$$

Where L is the arc length from the leading edge to the trailing edge and c is the airfoil chord. From the flat plate reference can be assumed that $s' = rsin\,(\theta)$. Following this reasoning it can be stated for small θ that $r\theta = s \approx s'$.

In order to gain simplicity useful in the posterior parametric study, the following definitions are introduced.

The ratio between the chord length and the radial position, or local aspect ratio, ls,

$$ls = \frac{c}{r} \tag{3.57}$$

The ratio between the rotational speed and the relative velocity, RO,

$$RO = \frac{\Omega r}{U_{rel}} \tag{3.58}$$

where Ω is the blade angular velocity.

The relative velocity, U_{rel}, is defined typically following [41],

$$U_{rel} = \sqrt{\left((1+a')\,\Omega r\right)^2 + \left((1-a)\,Q_W\right)^2} \tag{3.59}$$

where Q_W is the wind speed and a' and a are the tangential and axial interference factors. In the present study both factors are set to be zero for simplicity.

The four dimensional variables of interest c, r, Ω, Q_W have been reduced to two adimensional parameters ls, RO, providing the base of a parametric study, Section 5.7.

3.4.2 The boundary layer equations in differential Form

The steady incompressible continuity and r, θ momentum equations in cylindrical coordinates can be written as follows, [42]

Continuity,

$$\frac{1}{r}\frac{\partial u}{\partial \theta} + \frac{1}{r}\frac{\partial}{\partial r}(rv) + \frac{\partial w}{\partial z} = 0 \tag{3.60}$$

$\theta-$Momentum

$$\frac{u}{r}\frac{\partial u}{\partial \theta} + w\frac{\partial u}{\partial z} + v\frac{\partial u}{\partial r} - \frac{v}{r}(2\Omega r - u) = -\frac{1}{\rho r}\frac{\partial p}{\partial \theta} + \frac{1}{\rho}\frac{\partial \tau_\theta}{\partial z} \tag{3.61}$$

$r-$Momentum

$$\frac{1}{r}\frac{\partial}{\partial \theta}(uv) + \frac{\partial v^2}{\partial r} + \frac{\partial}{\partial z}(vw) + \frac{v^2}{r} - \frac{u}{r}(u - 2\Omega r) = -\frac{1}{\rho}\frac{\partial p}{\partial r} + \Omega^2 r + \frac{1}{\rho}\frac{\partial \tau_r}{\partial z} \tag{3.62}$$

τ_θ and τ_r are shear stresses in the θ and r direction respectively and can be either laminar or turbulent stresses. In order to facilitate the derivation of the integral form of the equations, the θ momentum equation is shown in a convective form whereas the r momentum equation is represented in its conservative formulation. It is assumed that the pressure distribution at the edge of the boundary layer and at the wall is the same, following boundary layer theory, Section 3.1.2. Pressure gradients perpendicular to the wall are negligible, due to the small thickness of the boundary layers at high Reynolds numbers compared the surface curvature.

The centrifugal term, $\Omega^2 r$ appears only on the r-momentum equation and has a effective favorable spanwise pressure gradient. However Coriolis related terms appears in both momentum equations. In the r-momentum equation, $2\Omega u$, appears as an effective not favorable spanwise pressure gradients. While in the θ-momentum, the Coriolis term $2\Omega v$, appears as a favorable streamwise pressure gradient.

The pressure gradients are formulated in function of the velocity, following Bernoulli´s equation in a rotating frame of reference,

$$p + \frac{1}{2}\rho V^2 - \frac{1}{2}\rho(\Omega r)^2 = constant \tag{3.63}$$

Applying Bernoulli´s equation at the edge of the boundary layer, both θ and r pressure gradients terms from the boundary layer momentum equations yield,

$$-\frac{1}{\rho}\frac{1}{r}\frac{\partial p}{\partial \theta} = u_e\frac{1}{r}\frac{\partial u_e}{\partial \theta} + v_e\frac{1}{r}\frac{\partial v_e}{\partial \theta} + w_e\frac{1}{r}\frac{\partial w_e}{\partial \theta} \tag{3.64}$$

$$-\frac{1}{\rho}\frac{\partial p}{\partial r} = u_e\frac{\partial u_e}{\partial r} + v_e\frac{\partial v_e}{\partial r} + w_e\frac{\partial w_e}{\partial r} - \Omega^2 r \tag{3.65}$$

3.4.3 The Quasi3D boundary layer equations in differential form

The 3D differential boundary layer equations have to be reduced to the Quasi 3D version. For beginning with this approach is considered the flow around a rotating cylinder of arbitrary cross section, following [21]. The cylinder rotates steadily about the z axis. It was shown by Fogarty and Sears that the three inviscid velocity components can be found, assuming potential flow at the edge of the boundary layer, in function of a two dimensional potential solution which is the same at all spanwise positions. The outward velocity component V it is then dependent of the potential of the two dimensional solution and independent of y'.

$$U' = \Omega y' \frac{\partial \phi_1 (x', z')}{\partial x'} + V_W \frac{\partial \phi_2 (x', z')}{\partial x'} \tag{3.66}$$

$$V' = \Omega \left[\phi_1 (x,' z') - 2x' \right] \tag{3.67}$$

$$W' = \Omega y' \frac{\partial \phi_1 (x', z')}{\partial z'} + V_W \frac{\partial \phi_2 (x', z')}{\partial z'} \tag{3.68}$$

Where U', V', W' are the inviscid velocity components in x', y', z' and ϕ_1 and ϕ_2 are the two dimensional potentials. Following this reasoning, the edge velocity, u_e, can be found using a two dimensional solution of the flow if potential flow is assumed at the edge of the boundary layer.

$$u_e (s, r) = U_{rel} u'_e \tag{3.69}$$

Thereby the velocity u'_e is obtained from the viscous-inviscid flow solution and it changes iteratively with the solution of the 2D boundary layer equations. The term $\frac{\partial u_e}{\partial s}$ is also found from the viscous-inviscid flow solution. On the other hand, assuming that u'_e is independent of r, the quantity $\frac{\partial u_e}{\partial r}$ can be written as,

$$\frac{\partial u_e}{\partial r} = \frac{\partial U_{rel}}{\partial r} u'_e = \frac{2 \left(\Omega^2 r \right)}{2\sqrt{(\Omega r)^2 + Q_w^2}} = \frac{\Omega^2 r}{U_{rel}} u'_e \tag{3.70}$$

Using adimensional parameters for simplicity,

$$\frac{\partial u_e}{\partial r} = u_e RO^2 \frac{ls}{c} \tag{3.71}$$

The following terms containing v_e and w_e velocity gradients on the radial and theta direction can be neglected following a previous order of magnitude analysis [43],

$$v_e \frac{\partial v_e}{r \partial \theta}, w_e \frac{\partial w_e}{r \partial \theta}, v_e \frac{\partial v_e}{\partial r}, w_e \frac{\partial w_e}{\partial r} \tag{3.72}$$

3.4.4 Quasi 3D boundary layer equations in integral form

It is needed to introduce a new set of parameters of interest in the three dimensional approach of the integral boundary layer equations capable of taking into account rotational effects. Already known parameters such $\delta_1^*, \theta_1, H and C_f$ will still be in use, among others that will parametrize the characteristics of the outward component of the flow,

$$\delta_2^* = -\int_0^\delta \frac{v}{u_e} \tag{3.73}$$

$$\theta_{22} = -\int_0^\delta \frac{v^2}{u_e^2} \tag{3.74}$$

$$\theta_2 = -\int_0^\delta \frac{uv}{u_e^2} dz = \delta_{2xr} + \delta_2^* \tag{3.75}$$

$$\delta_{2xr} = \int_0^\delta \left(1 - \frac{u}{u_e}\right) \frac{v}{u_e} \tag{3.76}$$

$$tan\left(\beta_w\right) = \frac{\tau_{w,r}}{\tau_{w,\theta}} \tag{3.77}$$

Where β_w is the angle in between the external and limiting streamlines. Parameters with subindex 1, introduced in the former section, are related with the streamwise profile while the ones with subindex 2, introduced above, are related with the spanwise one.

In the case of a rotating blade, due to the spanwise pressure gradient, yawed conditions and changes in thickness the streamlines do not follow the arcs at the edge of the boundary layer. Hence the spanwise velocity profiles do not tend to zero as approaching δ and the streamwise profiles have inviscid variations after the boundary layer edge is reached.

As an important assumption done in the present work, the streamwise and spanwise velocity profiles characteristics of a rotating flat plate were used to derive the three dimensional closure equations of the integral boundary layer quantities, see Figure 3.6,

The differential boundary layer equations in three dimensional form will be integrate including all terms. In second place, the Quasi3D approximations presented earlier in this chapter will be applied in order to obtain the Quasi3D boundary layer equations in its integral form.

θ integral momentum equation. For obtaining the integral formulation of the θ-momentum equation, the continuity equation has to be multiplied by the term $u - u_e$ and added to the θ momentum, Equation 3.61

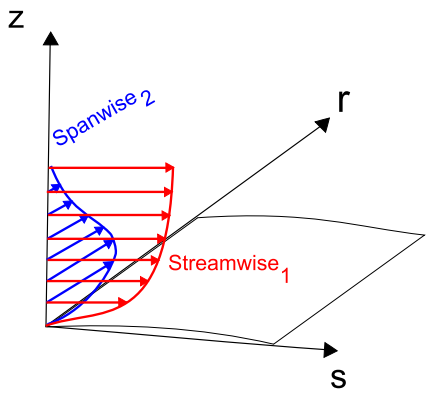

Figure 3.6: Velocity profiles,

$$
\begin{aligned}
&(u-u_e)\left(\frac{1}{r}\frac{\partial u}{\partial \theta}+\frac{\partial v}{\partial r}+\frac{v}{r}+\frac{\partial w}{\partial z}\right)+\frac{u}{r}\frac{\partial}{\partial \theta}(u-u_e)+\frac{u}{r}\frac{\partial u_e}{\partial \theta}+\\
&w\frac{\partial}{\partial z}(u-u_e)+v\frac{\partial}{\partial r}(u-u_e)+v\frac{\partial u_e}{\partial r}-\frac{v}{r}(2\Omega r-u)\\
&=\frac{u_e}{r}\frac{\partial u_e}{\partial \theta}+\frac{1}{\rho}\frac{\partial \tau_\theta}{\partial z}+v_e\frac{v_e}{r\partial \theta}+w_e\frac{\partial w_e}{r\partial \theta}
\end{aligned}
\tag{3.78}
$$

The equation above can be reduced to

$$
\begin{aligned}
&\frac{1}{r}\frac{\partial}{\partial \theta}(u(u-u_e))+\frac{\partial}{\partial z}(w(u-u_e))+\frac{\partial}{\partial r}(v(u-u_e))+\frac{v}{r}(u-u_e)\\
&+v\frac{\partial u_e}{\partial r}-\frac{v}{r}(2\Omega r-u)=\frac{1}{r}\frac{\partial u_e}{\partial \theta}(u_e-u)+\frac{1}{\rho}\frac{\partial \tau_\theta}{\partial z}+v_e\frac{v_e}{r\partial \theta}+w_e\frac{\partial w_e}{r\partial \theta}
\end{aligned}
\tag{3.79}
$$

Integrating from the airfoil surface, $z=0$, to the boundary layer edge $z=\delta$ and multiplying by the term $\frac{1}{u_e}$, Equation 3.79 yields to,

$$
\begin{aligned}
&\frac{1}{u_e^2}\frac{1}{r}\frac{\partial}{\partial \theta}\left(u_e^2\theta_1\right)+\frac{1}{u_e^2}\int_0^\delta\frac{\partial}{\partial z}(w(u-u_e))\,dz-\frac{1}{u_e^2}\frac{\partial}{\partial r}\left(u_e^2\delta_{2xr}\right)\\
&-\frac{1}{u_e}\frac{\partial u_e}{\partial r}\delta_2^*-\frac{2(\delta_{2xr}+\delta_2^*)-\delta_2^*}{r}\frac{2\Omega}{u_e}\delta_2^*-\frac{1}{u_e}\frac{1}{r}\frac{\partial u_e}{\partial \theta}\delta_1^*\\
&=-\frac{\tau_{w,\theta}}{\rho u_e^2}+\frac{v_e}{u_e^2}\frac{\partial v_e}{r\partial \theta}\delta+\frac{w_e}{u_e^2}\frac{\partial w_e}{r\partial \theta}\delta
\end{aligned}
\tag{3.80}
$$

Therefore,

$$\frac{1}{r}\frac{\partial\theta_1}{\partial\theta}+\frac{\partial\theta_1}{u_e}\frac{1}{r}\frac{\partial u_e}{\partial\theta}(2+H)=\frac{C_f}{2}+\frac{2\Omega}{u_e}\delta_2^*-\frac{\partial}{\partial r}(\theta_2-\delta_2^*)$$
$$-\frac{1}{u_e}\frac{\partial u_e}{\partial r}(2\theta_2-\delta_2^*)-\frac{2\theta_2-\delta_2^*}{r}+\frac{v_e}{u_e^2}\frac{\partial v_e}{r\partial\theta}\delta+\frac{w_e}{u_e^2}\frac{\partial w_e}{\partial s}\delta \tag{3.81}$$

In order to simplify for the parametric study, the non-dimensional variables and assumptions presented before are used: $s=r\theta$ having $\frac{\partial s}{\partial\theta}=r$, RO, and ls, the above equations yields to

$$\frac{\partial\theta_1}{\partial s}+\frac{\partial\theta_1}{u_e}\frac{\partial u_e}{\partial s}(2+H)=\frac{C_f}{2}+\frac{2ROls}{u_e c}\delta_2^*-\frac{\partial}{\partial r}(\theta_2-\delta_2^*)$$
$$-\frac{1}{u_e}\frac{\partial u_e}{\partial r}(2\theta_2-\delta_2^*)-\frac{ls}{c}(2\theta_2-\delta_2^*)+\frac{v_e}{u_e^2}\frac{\partial v_e}{\partial s}\delta+\frac{w_e}{u_e^2}\frac{\partial w_e}{\partial s}\delta \tag{3.82}$$

r integral momentum equation. The integral formulation of the r momentum equation is obtained by integrating its differential form, Equation 3.62, and multiplying the result by $1/u_e^2$

$$-\frac{1}{u_e^2}\frac{\partial}{r\partial\theta}\left(u_e^2(\delta_{2xr}+\delta_2^*)\right)-\frac{v_e}{u_e}\frac{\partial\delta}{r\partial\theta}-\frac{1}{u_e^2}\frac{\partial}{\partial r}\left(u_e^2\theta_{22}\right)-\frac{v_e^2}{u_e^2}\frac{\partial\delta}{\partial r}$$
$$+\frac{1}{u_e^2}\int_0^\delta\frac{\partial}{\partial z}(vw))\,dz-\frac{\theta_{22}}{r}+\frac{\theta_1+\delta_1^*-\delta}{r}-\frac{2\Omega}{u_e}(\delta_1^*-\delta)-\frac{\delta}{u_e}\frac{\partial u_e}{\partial r}$$
$$=-\frac{\tau_{w,r}}{\rho u_e^2}+\frac{v_e}{u_e^2}\frac{\partial v_e}{\partial r}\delta+\frac{w_e}{u_e^2}\frac{\partial w_e}{\partial r}\delta \tag{3.83}$$

Which can be written as,

$$\frac{\theta_2}{r\partial_\theta}+\frac{2\theta_2}{u_e}\frac{\partial u_e}{r\partial\theta}=tan\beta_w\frac{C_f}{2}+\frac{1}{r}\left(\theta_1+\delta_1^*-\delta-\theta_{22}+\frac{2\Omega r}{u_e}(\delta-\delta_1^*)\right)$$
$$-\frac{1}{u_e}\frac{\partial u_e}{\partial r}(2\theta_{22}+\delta)-\frac{v_e}{u_e}\frac{\partial\delta}{r\partial\theta}-\frac{v_e^2}{u_e^2}\frac{\partial\delta}{\partial r}+\frac{v_e w_e}{u_e^2}$$
$$-\frac{\partial\theta_{22}}{\partial r}+\frac{v_e}{u_e^2}\frac{\partial v_e}{\partial r}\delta+\frac{w_e}{u_e^2}\frac{\partial w_e}{\partial r}\delta \tag{3.84}$$

Using the adimensional variables introduced earlier in this chapter, ls and RO, together with the assumption that $\frac{\partial s}{\partial\theta}=r$,the Equation 3.84 can be formulated as,

$$\frac{\partial \theta_2}{\partial s} + \frac{2\theta_2}{u_e}\frac{\partial u_e}{\partial s} = tan\beta_w \frac{C_f}{2} + \frac{ls}{c}\left(\theta_1 + \delta_1^* - \delta - \theta_{22} + \frac{2RO}{u_e}\left(\delta - \delta_1^*\right)\right)$$
$$- \frac{1}{u_e}\frac{\partial u_e}{\partial r}\left(2\theta_{22} + \delta\right) - \frac{v_e}{u_e}\frac{\partial \delta}{r\partial \theta} - \frac{v_e^2}{u_e^2}\frac{\partial \delta}{\partial r} + \frac{v_e w_e}{u_e^2}$$
$$- \frac{\partial \theta_{22}}{\partial r} + \frac{v_e}{u_e^2}\frac{\partial v_e}{\partial r}\delta + \frac{w_e}{u_e^2}\frac{\partial w_e}{\partial r}\delta \tag{3.85}$$

In this manner a suitable set of equations that form the viscous core of our viscous-inviscid system is obtained. The system is formed by two momentum equations that combined with the kinetic energy parameter equation and a set of closure equations makes it amenable to solution via a strong viscous-inviscid coupling. Assumptions are done in order to neglect low order of magnitude terms that appears in Equations 3.82 and 3.85.

Again, following [43], the four terms that were neglected during the differential analysis are neglected herein,

$$\frac{v_e}{u_e^2}\frac{\partial v_e}{\partial s}\delta, \frac{w_e}{u_e^2}\frac{\partial w_e}{\partial s}\delta, \frac{v_e}{u_e^2}\frac{\partial v_e}{\partial r}\delta, \frac{w_e}{u_e^2}\frac{\partial w_e}{\partial r}\delta \tag{3.86}$$

There are still some r derivatives of the boundary layer parameters that can not be computed using the Quasi3D integral boundary layer approach,

$$\frac{\partial}{\partial r}\left(\theta_2 - \delta_2^*\right), \frac{v_e^2}{u_e^2}\frac{\partial \delta}{\partial r}, \frac{\partial \theta_{22}}{\partial r} \tag{3.87}$$

Following [44] we can assume that they are negligible. In order to be sure that these terms do not play an important role in the Quasi3D approach of the boundary layer equations an study of order of magnitude was realized previously to the present work.

In order to compute the derivative terms with a differential boundary layer code [45], the following approximation has been done. The approximation is shown only for the δ_2^* parameter, but the same procedure is carried out for the parameters θ_2, δ and θ_{22}. From Blasius solution for a flat plate it is known that,

$$\frac{\delta}{x} \approx \frac{c}{\sqrt{Re_x}} \tag{3.88}$$

were,

$$Re_x = \frac{\Omega r x}{\nu} \tag{3.89}$$

following that,

$$\delta \approx cr^{-1/2} \tag{3.90}$$

$$\delta_2^* \approx cr^{-1/2} \tag{3.91}$$

So its derivative respect to the radial direction can be written as follows,

$$\frac{\partial \delta_2^*}{\partial r} = c\,(-1/2)\,r^{-3/2} = -\frac{c}{2r}r^{-1/2} = -\frac{\delta_2^*}{2r} \tag{3.92}$$

The following terms were computed using the existing finite differences code, where the denominators are chosen because they are characteristic terms in the r and θ momentum equations,

$$\frac{(\theta_2 - \delta_2^*)\,/2r}{\partial\theta_1/\partial s} \tag{3.93}$$

$$\frac{v_e^2/u_e^2\ \delta/2r}{\partial\theta_2/\partial s} \tag{3.94}$$

$$\frac{\theta_{22}/2r}{\partial\theta_2/\partial s} \tag{3.95}$$

The order of magnitude analysis showed that the ratios above are of the order of $O(10^{-3})$, being the related terms in in Equation 3.87 negligible.

3.4.5 Airfoil geometry adaption

In order to adapt the flat plate equations to the real geometry of an airfoil, some modifications have to be performed to the integral boundary layer equations presented above for taking into account the differences in between both geometries:

- From the stagnation point, STG, to the extremity point, ex, the flow will be reverse. Meaning that the normal and tangential velocities are negative, so a sign function negative between the points and positive otherwise, s_w, has to be multiplying u and w, forcing the Coriolis force to be negative in this region and positive elsewhere in the airfoil surface,

- For a plate with zero pitch angle the rotation and the velocity are orthogonal, so the Coriolis terms don not need to be modified. When an airfoil is considered, due to its surface curvature, the terms that take into account Coriolis forces have to be multiplied by a projector, p_r. The factor is obtained from the cosine of the angle between the direction of the flow and the plane normal to the axis of rotation, $p_r = |cos\varphi|$.

After the airfoil geometry adaption, the quasi 3D integral boundary layer equations for an airfoil geometry can be written as follows,

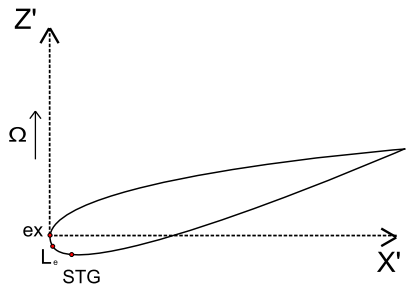

Figure 3.7: Flat plate to airfoil adaption, sign function

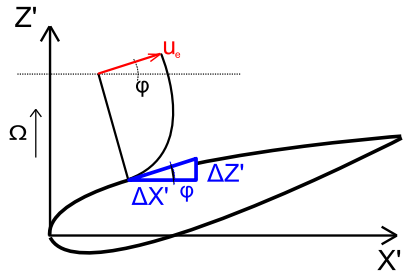

Figure 3.8: Flat plate to airfoil adaption, projector of Coriolis terms

$$\frac{\partial \theta_1}{\partial s} = -\frac{\partial \theta_1}{u_e}\frac{\partial u_e}{\partial s}(2+H) + \frac{C_f}{2} + s_w p_r \frac{2ROls}{u_e c}\delta_2^* - \dots$$
$$\frac{1}{u_e}\frac{\partial u_e}{\partial r}(2\theta_2 - \delta_2^*) - \frac{ls}{c}(2\theta_2 - \delta_2^*) \tag{3.96}$$
$$\frac{\partial \theta_2}{\partial s} = -\frac{2\theta_2}{u_e}\frac{\partial u_e}{\partial s} + tan\beta_w \frac{C_f}{2} + \frac{ls}{c}\left(\theta_1 + \delta_1^* - \delta - \theta_{22} + s_w p_r \frac{2RO}{u_e}(\delta - \delta_1^*)\right) - \dots$$
$$\frac{1}{u_e}\frac{\partial u_e}{\partial r}(2\theta_{22} + \delta) - \frac{v_e}{u_e}\frac{\partial \delta}{\partial s} + s_w \frac{v_e w_e}{u_e^2} \tag{3.97}$$

Further, due to stability problems and following previous work by Dumitrescu [44], the following terms in Equation 3.96 have been neglected,

$$-\frac{1}{u_e}\frac{\partial u_e}{\partial r}(2\theta_2 - \delta_2^*) - \frac{ls}{c}(2\theta_2 - \delta_2^*) = 0 \tag{3.98}$$

Assuming that our spanwise velocity profile has similar shape to the one sketched in Figure 3.6, the spanwise velocity will tend to zero as it approaches the edge of the boundary layer. In this case the following terms are neglected,

$$\frac{v_e}{u_e}\frac{\partial \delta}{\partial s},\ s_w \frac{v_e w_e}{u_e^2} \tag{3.99}$$

The final θ and r momentum equations used in the present approach are,

$$\frac{\partial \theta_1}{\partial s} = -\frac{\partial \theta_1}{u_e}\frac{\partial u_e}{\partial s}(2+H) + \frac{C_f}{2} + s_w p_r \frac{2ROls}{u_e c}\delta_2^* \tag{3.100}$$

$$\frac{\partial \theta_2}{\partial s} = -\frac{2\theta_2}{u_e}\frac{\partial u_e}{\partial s} + tan\beta_w \frac{C_f}{2} + \frac{ls}{c}\left(\theta_1 + \delta_1^* - \delta - \theta_{22} + s_w p_r \frac{2RO}{u_e}(\delta - \delta_1^*)\right) - \ldots$$

$$\frac{1}{u_e}\frac{\partial u_e}{\partial r}(2\theta_{22} + \delta) \tag{3.101}$$

3.4.6 Turbulent Quasi3D closure equations and 2D kinetic energy shape parameter equation

Due to the non availability of three dimensional relations for all stream and spanwise boundary layer variables, a set of equations has been chosen, where the ones use for closure of the kinetic energy shape parameter equation are in two dimensional form and the rest are used in its three dimensional form.

The velocity profiles used in the derivation of the closure relations are of similar shape as the ones sketched in Figure 3.6. The crossflow v velocity profile tends to zero as approaches the boundary layer edge. While the u velocity profile is similar to the one used in the two dimensional closures, where the velocity at the edge of the boundary layer is equal to the freestream velocity.

The streamwise velocity profile assumed for the turbulent mainstream is a power law type velocity profile, [46],

$$\frac{u}{u_e} = \left(\frac{z}{\delta}\right)^{\frac{H-1}{2}} \tag{3.102}$$

The crossflow or spanwise turbulent velocity profile used for derivate the closure relations is, following [47],

$$\frac{v}{u_e} = tan\left(\beta_W\right)\left(1 - \frac{z}{\delta}\right)^2 \tag{3.103}$$

By integrating the velocity profiles the following turbulent boundary layer relations are obtained, [46]

$$\delta_2^* = -\frac{16Htan\beta_w}{(H-1)(H+3)(H+5)}\theta_1 \tag{3.104}$$

$$\theta_2 = -\frac{2tan\beta_w}{(H-1)(H+2)}\theta_1 \tag{3.105}$$

$$\theta_{22} = -\frac{24\left(tan\beta_w\right)^2}{(H-1)(H+2)(H+3)(H+1)}\theta_1 \tag{3.106}$$

$$\theta_1 = \left(\frac{2}{H+1} - \frac{1}{H}\right)\delta \tag{3.107}$$

The skin-friction closure relation for flows with pressure gradients and rotation effects is based on the experimental data for turbulent boundary layer in a rotating channel of Lakshminarayana and Govindan [46]. Due to a better numerical stability the three dimensional component of the C_f equation has only been implemented as a right hand side term,

$$C_f = 0.172 Re_{\theta_1}^{-0.268} 10^{-0.678H} \left(1 + B_1 \sqrt{tan\left(\beta_w\right)\left(s - s_t\right)/c}\right) \tag{3.108}$$

Where B_1 is a constant of value 0.52, Re_{θ_1} is the Reynolds number based on the streamwise velocity at the edge of the boundary layer and the streamwise momentum thickness parameter. s_t is the distance between the leading edge and the laminar to turbulent transition point along the s direction.

In order to take into account the variation of the shape factor parameter, H, the kinetic energy shape parameter equation is chosen in its two dimensional form. It is also a possibility to use the entrainment equation suitable for turbulent boundary layers, but, even thought the last one involves less empiricism in calculating the dissipation integral term, the energy shape integral equation has been implemented due to a better numerical stability, [46]. The following equation is derived by a combination of the standard integral momentum equation and the kinetic energy thickness, following Mark Drela's paper in 1986 [2].

Kinetic energy shape parameter equation The kinetic energy shape parameter equation is produced by multiplying the standard boundary layer integral x-momentum equation, Equation 3.109, by the kinetic energy shape parameter, H^*, and subtracting the result from the kinetic energy thickness equation 3.110.

$$\frac{\partial \theta_1}{\partial x} + (2 + H)\frac{\theta_1}{u_e}\frac{\partial u_e}{\partial x} = \frac{C_f}{2} \tag{3.109}$$

$$\frac{\partial \theta^*}{\partial x} + \left(\frac{\delta^{**}}{\theta^*} + 3\right)\frac{\theta^*}{u_e}\frac{\partial u_e}{\partial x} = 2C_{Di} \tag{3.110}$$

$$\tag{3.111}$$

Where θ^* is the kinetic energy thickness and δ^{**} is the density thickness, defined from integral boundary layer theory as,

$$\theta^* = \int_0^\delta \frac{\rho u}{\rho_e u_e}\left(1 - \frac{u^2}{u_e^2}\right) dy \tag{3.112}$$

$$\delta^{**} = \int_0^\delta \frac{u}{u_e}\left(1 - \frac{\rho}{\rho_e}\right) dy \tag{3.113}$$

The kinetic energy shape parameter equation is written,

$$\theta \frac{dH^*}{ds} + \left[H^*\left(1 - H\right)\right]\frac{\theta_1}{u_e}\frac{du_e}{ds} = 2C_{Di} - H^*\frac{C_f}{2} \tag{3.114}$$

A set of two dimensional relations is introduced in order to obtain a closure to the kinetic energy shape parameter equation, following Drela's model [2].

The shape parameter relation, H, based on the analytical representation of two-dimensional turbulent boundary layer velocities profiles for either attached and separated flow of Swafford, [48].

$$H^* = 1.5050 + \frac{4}{Re_{\theta_1}} + \left(0.165 - \frac{1.6}{Re_{\theta_1}^{0.5}}\right) \frac{(H_0 - H)^{1.6}}{H} \ , \qquad H < H_0 \tag{3.115}$$

$$H^* = 1.5050 + \frac{4}{Re_{\theta_1}} + (H - H_0)^2 \left[\frac{0.004}{H} + \frac{0.007 log Re_{\theta_1}}{(H - H_0 + 4/log Re_{\theta_1})}\right] \ , \qquad H > H_0 \tag{3.116}$$

The dissipation coefficient relation, C_{Di}

$$C_{Di} = \frac{C_f}{2} U_s + C_\tau \left(1 - U_s\right) \tag{3.117}$$

The equivalent normalized wall slip velocity, U_s

$$U_s = \frac{H^*}{2} \left(1 - \frac{4}{3} \frac{H - 1}{H}\right) \tag{3.118}$$

The stress-transport equation. A rate equation for the maximum shear stress coefficient C_τ is used to account for deviations of the outer layer dissipation coefficient C_{Di} from the local equilibrium value. This closure relation simulates a slow response of the Reynolds stresses to changes in the boundary layer, so, in this way C_τ does not only depends on the local boundary layer conditions, [12],

$$\frac{\delta}{C_\tau} \frac{dC_\tau}{ds} = 5.6 \left(C_{\tau EQ}^{1/2} - C_\tau^{1/2}\right) + 2\delta \left\{\frac{4}{3\delta_1^*} \left[\frac{C_f}{2} - \left(\frac{H - 1}{6.7H}\right)^2\right] - \frac{1}{u_e} \frac{du_e}{ds}\right\} \tag{3.119}$$

The nominal boundary layer thickness, δ,

$$\delta = \theta \left(3.15 + \frac{1.72}{H - 1}\right) + \delta_1^* \tag{3.120}$$

The equilibrium shear stress coefficient, $C_{\tau EQ}$,

$$C_{\tau EQ} = H^* \frac{0.015}{1 - U_s} \frac{(H - 1)^2}{H^3} \tag{3.121}$$

The $G - \beta$ locus of equilibrium boundary layers [49] where used by Mark Drela in his derivation of the equations 3.117, 3.118 and 3.121.

3.5 Laminar to turbulent transition model

In order to predict laminar to turbulent transition the n^9 method with Mack's modification to take into account turbulence intensity is used. The method follows the spatial-amplification theory based on the solution of Orr-Sommerfeld equation, [2]. Transition is predicted when the most unstable Tollmien-Schlichting wave in the boundary layer grows more than a factor, n_C, which leads to turbulence. The fast growing of laminar instabilities, in the longitudinal and transversal directions, are driven by the strong instability of the boundary layer velocity profiles in adverse pressure gradient.

The Falkner-Skan velocity profile family is used in this method for solving the Orr-Sommerfeld equation for the spatial amplification rates of a series of shape parameters, unstable frequencies and Reynolds number, [50]. Stability diagrams are used for studying the evolution of the amplitude of a given perturbation with the momentum thickness Reynolds number, Re_{θ_1}. Curves are obtained for different perturbations frequencies, relating the perturbation amplitude rate of the perturbation with the Reynolds number based in momentum thickness and the shape parameter. Via the envelope of this curves, that follows the highest amplification factor of a set of frequencies in function of the momentum thickness Reynolds number, the total amplification of the most unstable frequency n is computed. An example of the Orr-Sommerfeld amplification curves with their respective envelope for two shape factor quantities is presented in Figure 3.9.

Critical Reynolds number, $Re_{\theta_1}^{CR}$, defines the value of Re_{θ_1} under which no perturbation can be amplified. It is obtained as,

$$DGR = \ 0.08 \tag{3.122}$$

$$GRC = \ 2.492\,(\frac{1}{(H-1)})^{0.43} + 0.7\,(tanh(14\frac{1}{H-1} - 9.24) + 1) \tag{3.123}$$

$$GR \ = \ log10(Re_{\theta_1}) \tag{3.124}$$

In the case that $GR < GRC - DGR$, no perturbation can be amplified, so the term $\partial n/\partial Re_{\theta_1} = 0$.

In order to determine the total amplification, n, at a streamwise position, s, starting from the leading edge and moving downstream the envelope slope has to be integrated from the critical Reynolds number, $Re_{\theta_1}^{CR}$, to the Reynolds number of the local streamwise position s, Re_{θ_1}. Transition occurs when $n(s)$ reaches the critical amplification factor n_C.

$$n(s) = \int_{Re_{\theta_1}^{CR}}^{Re_{\theta_1}} \frac{\partial n}{\partial Re_{\theta_1}} \partial Re_{\theta_1} \tag{3.125}$$

Following Drela's code Xfoil, a steep cubic ramp is used in order to smoothly turn on n as Re_{θ_1} grows bigger than its critical value $Re_{\theta_1}^{CR}$.

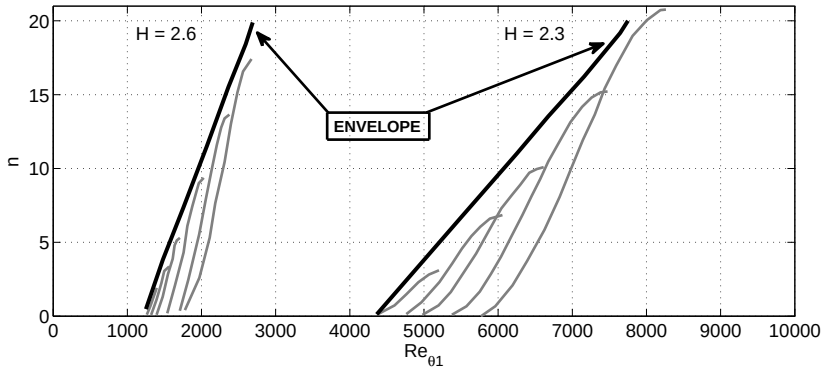

Figure 3.9: Example of Orr-Sommerfeld amplification curves.

$$R_N = \frac{GR - (GRC - DGR)}{2\,DGR} \tag{3.126}$$

$$R_F = 3\,R_N^2 - 2\,R_N^3\ , \qquad R_N < 1 \tag{3.127}$$

$$R_F = 1\ , \qquad R_N \geq 1 \tag{3.128}$$

The amplification envelope slope correlation for Falkner-Skan in the case of attached boundary layers is written as follows,

$$\tag{3.129}$$

$$n = \left(-0.05 + 2.7\left(\frac{1}{H-1}\right) - 5.5\left(\frac{1}{H-1}\right)^2 + 3\left(\frac{1}{H-1}\right)^3\right)$$

$$\left(\frac{0.028(H-1) - 0.0345e^{-\left(3.87\frac{1}{H-1} - 2.52\right)^2}}{\theta_1}\right) R_F \tag{3.130}$$

At chord locations where the shape parameter exceeds the constant $H_1 = 3.8$, highly separated flow conditions, a correction has to be applied to the envelope slope,

$$H_1 = 3.8 \tag{3.131}$$

$$H_2 = 4.2 \tag{3.132}$$

$$H_N = \frac{H - H_1}{H_2 - H_1} \tag{3.133}$$

$$H_F = 3\,H_N^2 - 2\,H_N^3\ , \qquad H_N < 1 \tag{3.134}$$

$$H_F = 1\ , \qquad H_N\ \geq 1 \tag{3.135}$$

$$n1 = n$$

$$n = H_F \frac{\left(0.086\, tanh\left(1.2\left(GR - 0.3 + 0.35\, e^{-0.15(H-5)}\right)\right)\right)}{\theta_1} \tag{3.136}$$

$$- \frac{\frac{0.25}{(H-1)^{1.5}}}{\theta_1} + (1 - H_F)\, n1 \tag{3.137}$$

The laminar to turbulent transition will occur when the amplification factor n grows bigger than its critical value n_C. n_C expressed as a function of the turbulence intensity level can be written as follows, [51],

$$n_C = -8.43 - 2.4\, ln\,(TI) \tag{3.138}$$

At low Reynolds number transition plays an important role. In the case of laminar separated flow a delayed transition will cause the flow not to reattach. In the case of laminar attached flow, a delay transition will be the cause of an underestimation of the boundary layer thickness reaching higher angles of attack without entering flow separation. While early transition prediction will be the cause of an overestimation of the turbulent boundary layer thickness and hence an early boundary layer separation would take place.

An weighted average of the C_f parameter is used to obtain a smooth laminar to turbulent transition. The weighted average of the C_f value is introduced two stations upstream the transition point with a weighted value: $wTR_{STG-2} = 80\%$, $wTR_{STG-1} = 50\%$ and $wTR_{STG} = 20\%$ respectively. Therefore the C_f equations is formulated at each of these three panel stations as $wTR\; C_{f_L} + (1 - wTR)\; C_{f_T} = 0$.

3.6 Unsteady integral boundary layer

Following Riziotis and Voutsinas [16] unsteady viscous terms are introduced into the θ momentum equation and to the kinetic energy shape parameter equation,

$$U1 = \frac{u_e^t \delta_1^{*\,t} - u_e^{t-1} \delta_1^{*\,t-1}}{dt}; \tag{3.139}$$

$$U2 = \frac{(u_e^t)^2 \theta_1^t - (u_e^{t-1})^2 \theta_1^{t-1}}{dt}; \tag{3.140}$$

$$U3 = \frac{\delta_1^{*\,t} - \delta_1^{*\,t-1}}{dt} \tag{3.141}$$

The unsteady formulation of the boundary layer θ momentum and kinetic energy shape parameter equations is:

$$\frac{1}{u_e^2}\,U1 + \frac{\partial \theta_1}{\partial s} = -\frac{\partial \theta_1}{u_e}\frac{\partial u_e}{\partial s}\,(2+H) + \frac{C_f}{2} + \ldots$$
$$s_w p_r \frac{2ROls}{u_e c}\delta_2^* \tag{3.142}$$
$$\frac{1}{u_e^3}\,U2 + \frac{1}{u_e}\,U2 - \frac{H^*}{u_e^2}\,U1 + \theta_1\frac{dH^*}{ds} + \left[H^*\,(1-H)\right]\frac{\theta_1}{u_e}\frac{du_e}{ds}\ldots$$
$$= 2C_{Di} - H^*\frac{C_f}{2} \tag{3.143}$$

3.7 Summary and remarks

In this chapter the idea of describing a rotating blade as a flat plate with an attributed pressure distribution has been presented. In the first term, the Navier-Stokes equations have been reduced to the 3D boundary layer equations applying thin layer theory. In the second term, the 3D differential boundary layer equations formulated in cylindrical coordinates were reduced to the Quasi3D ones. As the final step, after integrating and with further manipulation, the integral form of the Quasi3D boundary layer equations was obtained.

An important assumption has been done in the basis of Sears work, the streamwise edge velocity can be expressed as the product of the relative velocity and the dimensionless chordwise edge velocity. After a dimensional analysis and following earlier literature some of the terms in the integral r and θ momentum equations were neglected in order to make the system amenable to solution using the integral approach. An adaption of the flat plate equations to an airfoil geometry has been done including a sign function and a projection of the Coriolis terms.

The final version of the code uses Thwaites integral method for the laminar part of the boundary layer. The Blasius flat plate solution is used to find the θ_1 and H^* in four stations around the stagnation point ($STG \pm 5$). Transition can be forced or computed with the modified e^9 transition model. The turbulent part of the boundary layer is governed by the unsteady formulation of the Quasi3D θ momentum equation and the steady version of the r momentum equations closing the system with a set of quasi3D closure equations. In order to take into account variations in the shape factor, H, the 2D unsteady version of the kinetic energy shape parameter equation is added to the system together with its set of two dimensional closure relations.

Chapter 4

Viscous-Inviscid Interaction

4.1 Strong coupling method

An alternative approach to the solution of the time-averaged Navier-Stokes equations for turbulent flows is to divide the flow into two domains, a viscous one, governed by the integral form of the boundary layer equations, and an inviscid domain, handled by a panel method. The two sets of equations are coupled by a strong coupling method. The main advantage of using the integral boundary layer formulation is the parabolic nature of the equations that makes them more amenable to be solved assuming incompressible and irrotational flow. The nature of the equations allows an important reduction in CPU time and computer power, the full system can be solved in a nowadays standard computer within a fair amount of time if compared with Navier-Stokes solvers.

The parabolic nature of the boundary layer equations implies that the flow information does not have to travel upstream during the solving procedure, hence a special treatment is necessary when the flow separates, reversal flow. In the present approach the convergence of the method after separation is reached is ensured with the implementation of a strong viscous-inviscid coupling.

The type of coupling used in the present work is known as a strong coupling via "transpiration velocity" or "injection function". One of the advantages of the method is that changes on the airfoil geometry are avoided, hence a better convergence and computational stability can be achieved in comparison with other coupling methods. In a strong coupling the airfoil surface is not longer considered as a solid body surface, the introduction of the transpiration velocity changes the non penetration boundary condition, forcing the normal velocity at the wall to be equal to the injection function, see Figure 4.1. The transpiration velocity is taken into account via the panel method with a distribution along the airfoil surface of equivalent sources. These sources are directly related with variations in the displacement thickness quantity, taking into account the obstruction effect of the boundary layer against the freestream flow and bending outwards the outer streamlines.

The transpiration velocity will take into account the effects of the real flow in the potential flow solver. The first derivation of the transpiration form of the displacement effect was given by Lightill in 1958, [7]. Formulating the

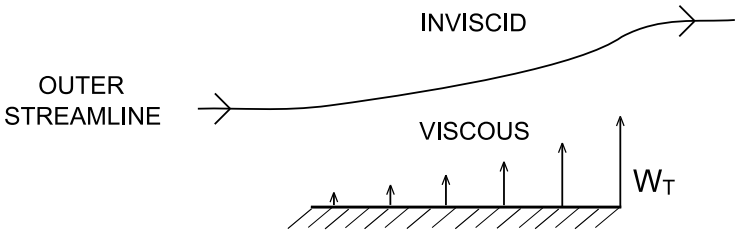

Figure 4.1: Coupling Sketch

continuity equation in terms of the difference between the inviscid and real flow and neglecting the effect of surface curvature,

$$\frac{\partial}{\partial s}\left(\rho_i u_i - \rho u\right) + \frac{\partial}{\partial z}\left(\rho_i w_i - \rho w\right) = 0 \tag{4.1}$$

Integrating the equation above from the wall, $z = 0$, to the edge of the boundary layer δ. At the body surface the inviscid velocity term must be equal to the transpiration velocity and the viscous one is equal to zero, $w_i = w_T$, $w = 0$. At the edge of the boundary layer the two flows must mix together, $\rho_i u_i = \rho u$ and $\rho_i w_i = \rho w$.

$$\rho_i w_T = \int_0^\delta \frac{\partial}{\partial s}\left(\rho_i u_i - \rho u\right) dz = \frac{d}{ds}\int_0^\delta \left(\rho_i u_i - \rho u\right) dz \tag{4.2}$$

Introducing the definition of streamwise displacement thickness, δ_1^*, from 3.18,

$$\delta_1^* = \frac{1}{\rho_i u_i}\int_0^\delta \left(\rho_i u_i - \rho u\right) dz \tag{4.3}$$

Combining the Equation 4.3 above with Equation 4.2, and knowing that the quantities at the edge of the boundary layer are inviscid quantities, the transpiration velocity or injection function is produced,

$$w_T = \frac{1}{\rho_i}\frac{\partial}{\partial s}\left(\rho_i u_i \delta_1^*\right) \tag{4.4}$$

In order to obtain a strong coupling the transpiration velocity has to interact simultaneously with both the panel method and the viscous system of equations. The solution rises from introducing a source distribution capable of creating an outwards flow with a normal velocity equal to the transpiration velocity. This source distribution will change the Neumann condition of no penetration, the the normal velocity at the surface of the airfoil will be no longer zero. According with panel method notation, the strength of the source distribution, σ_{w_T}, is given by,

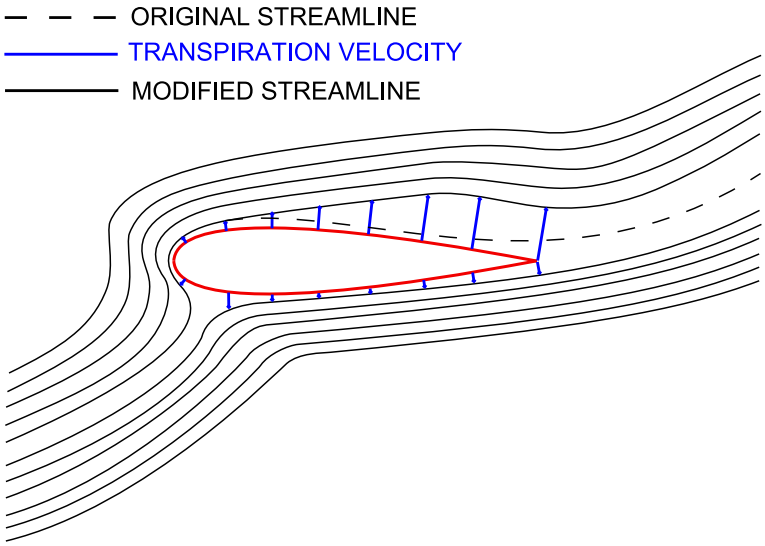

Figure 4.2: Effect of the injection function on the streamlines

$$\underline{w}_T = \underline{\underline{A}}\,\underline{\sigma}_{w_T} \tag{4.5}$$

$$\underline{\sigma}_{w_T} = \underline{\underline{A}}^{-1}\,\underline{w}_T \tag{4.6}$$

where $\underline{\underline{A}}$ is the normal influence coefficients matrix in panel method form.

The injection function sources will induce velocities in all the other panels, obtaining in this way a strong interaction in between the viscous and the inviscid parts of the global matrix.

The injection function can be seen physically as an outflow blowing outwards the airfoil surface due the presence of the boundary layer. It will push away from the wall the streamlines that are close enough to the airfoil surface, mimicking the obstruction of the freestream flow created by the presence of the boundary layer, Figure 4.2. In blue color are represented the transpiration velocities blowing outwards the original streamlines (dashed lines). Only one original streamline is shown to maintain the simplicity of the sketch. It is important to remain that due to its relation with the rate of change of displacement thickness times tangential edge velocity, the injection function usually increases its absolute value from the leading edge to the trailing edge. It is common in computations that after separation takes place the transpiration velocity remains approximately constant, as sketched.

4.2 Numerical methods, other interaction types

An overview of the existing iterative procedures is presented. This coupling techniques have been developed relatively late if compared with the development

of both viscous and inviscid fields separately. Viscous inviscid iterations usually diverges without assistance in the regions where the interaction in between the viscous and the inviscid parts is strong, for example around the trailing edge or near separated flow regions. The stiffness of the boundary layer equations around separation is not inherent to the equations nature, it is a result of the coupling method, [1]. Nowadays there are five different successful or semi-successful interaction techniques, besides the strong one implemented in the present work,

4.2.1 Direct interaction

The displacement effects of the boundary layer are used in an iterative way to correct the inviscid flow solution. The inviscid part is solved to obtain an edge velocity distribution, u_e. The edge velocity is used to solve the viscous equations obtaining a displacement thickness distribution, δ^*. The displacement thickness is used to compute the transpiration velocity. Introducing the new w_T into the inviscid solver a new edge velocity distribution is obtained. The computations follow a downstream order, starting from the stagnation point and moving towards the trailing edge, taking advantage of the parabolic nature of the boundary layer equations. The iterative process continues until convergence is reached for each station. Disadvantages of the method are: convergence only for small displacement thickness and attached flows.

4.2.2 Inverse interaction

In order to handle separation the above method was modified, solving the inviscid and viscous parts inversely. An initial estimate of the velocity gradient is used to determine a value for the source strength, which is used to calculate the velocity gradients induced by the boundary layer equations. The process ends repeating the calculations until convergence is reached, under relaxation is needed with this approach. This method has been used successfully for calculations of internal flows such compressors, however it has not a special advantage for the computation of external flows due to the need of increasing under relaxation as the computational domain is increased.

4.2.3 Semi-inverse interaction

Two estimates of the velocity gradient are obtained from the direct potential method and the inverse viscous method, using them in a correction equation which outputs go again into both the initial methods. The most rigorous formulation of the correction equation was given by Le Balleur, [11], who used a local Fourier analysis of the small perturbation equations and the integral boundary layer equations to study the stability of the method. The coefficients of the linearized correction equation are unknown, because of this Le Balleur used in his method an initial estimate of the source distribution to derive estimates of the inviscid and viscous flows velocity gradients, using them as inputs for the correction formula that gives a new estimate for the source strength, the iterative process continues until convergence is reached. The semi-inverse interaction is a robust formulation for airfoil flows.

4.2.4 Quasi-simultaneous interaction

Developed originally by Veldman [52], in this approach the inviscid flow is described with a simplified linearized equation, solved simultaneously with the viscous flow equations in a local linearized form. The coupling advances station by station. A velocity gradient together with a source strength are obtained. The following iteration of the viscous solution can be obtained using the velocity gradient or the source strength with a direct or inverse mode in that order, as explained on the other iteration types. The new source or velocity gradient is used in the simplified inviscid equation and the iteration process restarts. This scheme is one of the most robust viscous-inviscid schemes with downstream matching scheme.

4.2.5 Fully-simultaneous interaction

A Fully-simultaneous method was introduced based on the assumption that there is no hierarchy between viscous and inviscid solutions. The simultaneous solution of both sets of equations is performed by a Newton kind of iteration process. This method involved the inversion of the full influence matrix, used as a base to the method implemented in the present work, the strong viscous-inviscid interaction. A very good convergence is obtained but with a significant increment in the computational cost due to the full matrix inversion.

4.3 Space discretization of partial derivatives

A first order backward scheme is used for the discretization of differential quantities in the integral boundary layer equations. Even tough other schemes were implemented and tested, like the central difference scheme or the second order backwards scheme, the first order discretization scheme seems to be the more robust.

An example of the discretization of a given variable, δ^*,

$$\left|\frac{\partial \delta^*}{\partial s}\right|_i = \frac{\delta_i^* - \delta_{ii}^*}{S_i} \tag{4.7}$$

Where δ_i^* is the value of the displacement thickness at the control point of the ith panel, δ_{ii}^* is the value of the displacement thickness at the control point of the panel upstream of i, in the case of attached flow. When the boundary layer is separated, the flow becomes reversal, so the value of δ_{ii}^* will be given by the control point downstream of i. It is due to this property that the discretization scheme is not a first order upwind scheme, and it is referred from now on as a backward scheme. S_i is the distance computed in between the control point i and the ii.

4.4 Matrix form

One of the main advantages of the strong viscous-inviscid interactive approach is the treatment of the problem as a full Jacobian matrix system. The Jacobian matrix is used for linearizing the non linear system of equations formed by the

viscous and the inviscid parts. The global Jacobian matrix is formed by sub matrices, each sub matrix represents a panel of the discretized airfoil surface. Sub matrices can be composed of the laminar or turbulent set of equations. If the flow is laminar an extra equation to predict the laminar-turbulent transition is added, including the amplification factor, n, as a new variable of the system. A weighted average of the friction coefficient, C_f, is used in the transition location and two stations upstream of it.

The global Jacobian matrix is composed by: panel method equations, laminar equations, amplification factor equation, turbulent equations, interaction function and Kutta condition, see Figure 4.3.

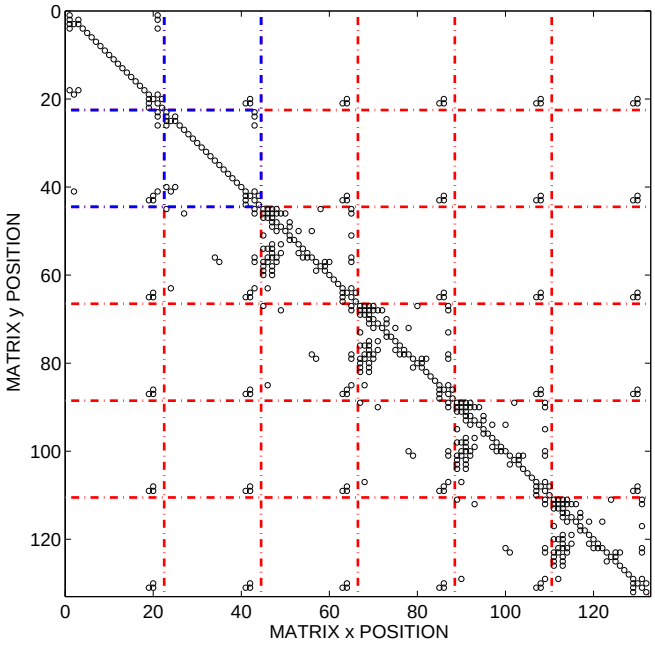

Figure 4.3: Jacobian global matrix for seven panels around the laminar-turbulent transition location. Laminar stations are delimited by blue lines while turbulent ones are delimited by red lines.

In Figure 4.3 are represented with circles the non zero positions of the global Jacobian matrix for seven panels located on the suction side of the airfoil. Sub matrices are limited by red or blue dot-dash lines, the ones delimited by blue dashed lines represent laminar stations while the turbulent locations are delimited by red dashed lines. Sub matrices occupying the main diagonal of the global matrix take into account the influence of the panel in itself and the viscous terms. Jacobian terms of the panel equations will occupy locations in all the sub matrices. Each panel distributed elementary solution induces normal and tangential velocities in all the other panels, in this manner a sparse matrix is formed. Panel method equations are basically two at each panel, the normal

velocity equations or Neumann condition and the tangential velocity equations. The Kutta condition is added to the last row of the matrix.

In Figure 4.3 the first two panels are under laminar conditions and the other four are modeled with the turbulent set of equations. For the surface derivatives in the laminar, turbulent and injection equations the relations are backwards due to the backward scheme implemented. The parabolic nature of the boundary layer equations allows to use backwards discretization without critical stability problems. When the flow is attached the derivative quantities are taken from the upstream neighbor, while if the flow is separated are from the downstream one.

The transition point is found by using amplification theory, a modified n^9 method that takes into account the turbulent intensity effect is implemented, or, if the boundary layer is tripped, the transition point is forced where the user wants it to be located. Thwaites integral momentum equation is used with a set of three closure equations in order to represent the laminar flow, in the following sketch can be appreciated the position of the laminar equations in the main diagonal panel sub matrix, Figure 4.4. Rows with only one space occupied means that even though the equation is not in use, the variable is set to zero being its Jacobian is equal to the unity. For a higher speed up of the code these rows have to be neglected.

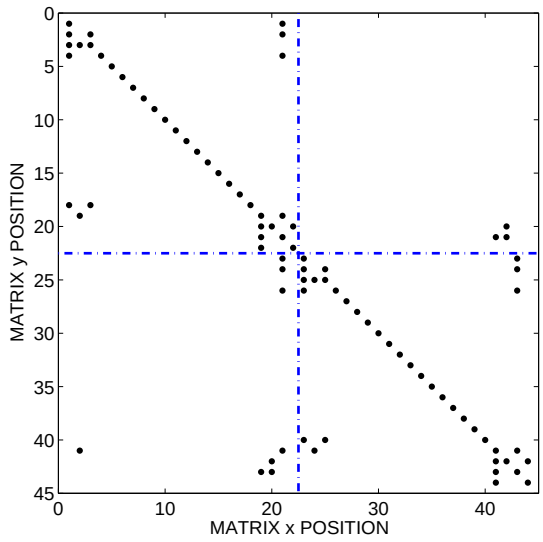

Figure 4.4: Global matrix system modeling the laminar flow for two panels on the suction side of the airfoil

The modified e^9 model appears in the global matrix in the row 18 of the main diagonal sub matrices in the case that the flow is laminar.

The injection function is introduced into the global matrix in the row 19 of the main diagonal sub matrices for both laminar and turbulent panels, it acts as a strong coupling in between the viscous and inviscid part.

The turbulent set of equations will be placed in the positions related with panels under turbulent flow conditions, see Figure 4.5. The turbulent equations are larger in number than the laminar equations, the r and θ momentum equation are used together with the kinetic energy shape parameter equation and a set of closure equations.

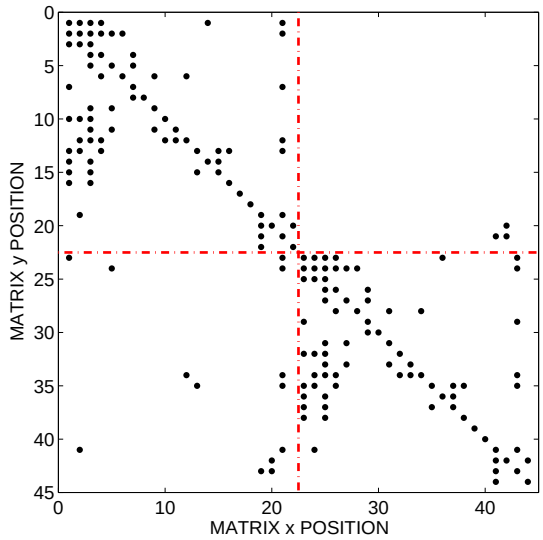

Figure 4.5: Global matrix system for the two panels of the suction of the airfoil under turbulent flow.

In Table 4.1 shows the column position of each system variable on the panel sub matrix for the turbulent case. The row position in which each equation is located in a sub matrix for the turbulent case is presented in Table 4.2.

VARIABLE	COLUMN POS.	VARIABLE	COLUMN POS.
θ_1	1	C_τ	12
δ_1^*	2	θ_2	13
H	3	δ_2^*	14
C_f	4	β_w	15
H^*	5	δ	16
C_{Di}	6	$Empty$	17
Re_{θ_1}	7	n	18
H_0	8	w_T	19
U_s	9	σ	20
δ_N	10	u_e	21
$C_{\tau_{EQ}}$	11	v	22

Table 4.1: Column position of the system variables in each submatrix.

A second implementation was done in which the θ_1 closure equation was not included as a closure for the turbulent boundary layer equations. Consequently

EQUATION	ROW POS.
$\theta - momentum$	1
$Kinetic\,Energy\,Thickness$	2
$Shape\,parameter\,Relation$	3
$C_f\ closure$	4
$H^*\ closure$	5
$C_{Di}\ closure$	6
$Momentum\,Thickness\,Reynolds$	7
$Initial\,Shape\,Factor$	8
$U_s\ closure$	9
$\delta_N\ closure$	10
$C_{\tau_{EQ}}\ closure$	11
$C_\tau\ closure$	12
$r - momentum$	13
$\delta_2^*\ closure$	14
$\theta_2\ closure$	15
$\theta_1\ closure$	16
$Empty$	17
$Amplification\,Factor$	18
$Injection\,Function$	19
$Source\,Distribution$	20
$Parallel\,Edge\,Velocity$	21
$Normal\,Edge\,Velocity$	22

Table 4.2: Row position location of the full system equations in each submatrix.

the nominal boundary layer thickness obtained from equation 10 was used as the value of the boundary layer thickness parameter. Hence the boundary layer thickness, variable number 16 from 4.1 was removed. Validations of the new system of equations was done for a couple of airfoil profiles and as far as the tested airfoil profiles concern there was no change in the final solution. The system in this way can be closed with one equation less. This implementation will be analyzed more in depth to be used as a future implementation for the code.

4.5 Kutta condition

In order to ensure a unique solution to the potential problem, an auxiliary condition commonly know as Kutta condition has to be imposed. This condition is related with the flow characteristics in the airfoil trailing edge surroundings. A body with a sharp trailing edge immersed in a moving fluid has a circulation around itself which forces a stagnation point in the rear side of the airfoil making the flow to leave the surface at this point and hence creating lift.

When an airfoil without camber is situated parallel to the freestream, the circulation around its surface is zero generating no lift. If a particle is followed in both, the upper and the lower surfaces from the stagnation point, at angle of attack zero both particles will meet at the trailing edge and leave the airfoil at

the same time, see Figure 4.6(a) where the position of each particle is plotted every time step. As the angle of attack increases, the particle in the suction surface will travel much faster due to the large pressure gradients existent near the nose of the airfoil. In the steady state both particles will have the same speed once reaching the trailing edge, although the upper one will reach it much faster, see Figure 4.6(b), this will create a circulation around the airfoil contour generating lift. This is know as Kutta condition.

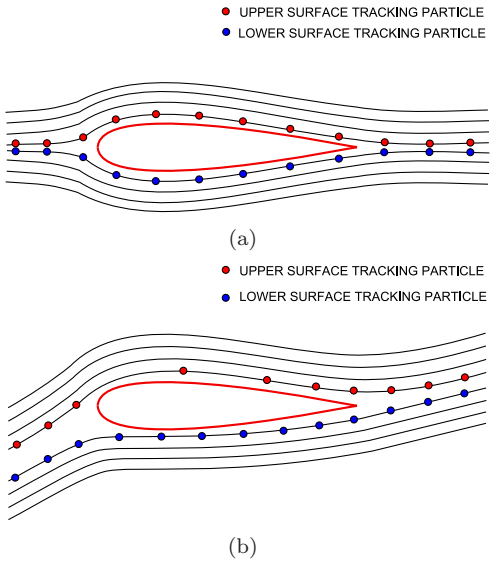

Figure 4.6: Tracking particles around an airfoil surface. (a) $\alpha = 0$, (b) $\alpha > 0$.

4.5.1 Steady Kutta condition

The flow has to leave the airfoil at its trailing edge in order to create lift, in this way the trailing edge becomes a stagnation point. The tangential edge velocities at the upper and lower trailing edge panels are forced to be equal in absolute value, hence the pressure at both positions is equal, in this way a zero loading condition is created on the trailing edge. In practice the Kutta condition is implemented using the velocities induced by the parabolic vorticity distribution, Γ, the point source distribution, σ, the parabolic vorticity related source distribution around the airfoil, σ_R, the source transpiration velocity, σ_{WT}, the single wake vortex influence, Γ_W, the wake related source distribution around the airfoil, σ_W, plus the projection of the freestream velocity into the trailing edge panels $Q_{\infty\, x}$ and $Q_{\infty\, y}$.

$$\sum_{i=1}^{N} B_{1i}\sigma_i + \sum_{i=1}^{N} A_{1i}\gamma_i + \sum_{i=1}^{N} B_{1i}\sigma_{R\,i} + \sum_{i=1}^{N} B_{1i}\sigma_{WT\,i} + \sum_{i=1}^{N} B_{w\,1i}\Gamma_{W\,i}$$
$$+ \sum_{i=1}^{N} B_{Ni}\sigma_{W\,i} + U_{\infty x}\underline{t_1} + U_{\infty y}\underline{n_1} =$$
$$\sum_{i=1}^{N} B_{Ni}\sigma_i + \sum_{i=1}^{N} A_{Ni}\gamma_i + \sum_{i=1}^{N} B_{1j}\sigma_{R\,i} + \sum_{i=1}^{N} B_{Ni}\sigma_{WT\,i} + \sum_{i=1}^{N} B_{w\,Ni}\Gamma_{W\,i}$$
$$+ \sum_{i=1}^{N} B_{Ni}\sigma_{W\,i} + U_{\infty x}\underline{t_N} + U_{\infty y}\underline{n_N} \tag{4.8}$$

4.5.2 Unsteady Kutta condition

In the unsteady case, opposite to what occurs in the steady one, when the flow approaches the trailing edge the differential of pressure in between the upper and lower sides of the airfoil does not tend to zero. This can be explained from the unsteady Bernoulli equation in which appears an unsteady term, that depends of the change in airfoil circulation. A pressure difference in the trailing edge is not admissible on physical backgrounds, so in order to maintain a zero loading of the trailing edge region, a vortex with a strength equal to the change in airfoil circulation has to be shed into the trailing edge wake.

The vorticity of the first wake vortex is equal to the change of circulation in the airfoil contour,

$$\Gamma_W = \Gamma_B^t - \Gamma_B^{t-1} \tag{4.9}$$

The condition of zero loading or equal pressure in between the two trailing edge panels can be written in the following way, following Basu and Hancock implementation [36],

$$u_{e\,1}^2 = u_{e\,N}^2 + 2\frac{\Gamma_B^t - \Gamma_B^{t-1}}{dt} \tag{4.10}$$

Where dt is the time step.

The flow leaves the trailing edge parallel to the upper or the lower trailing edge panels depending which has the highest velocity.

$$\theta_{N+1} = \theta_1 \; if \; u_1 > u_N \tag{4.11}$$
$$= \theta_N \; if \; u_N > u_1 \tag{4.12}$$

Where θ_{N+1} is the angle at which the first trailing edge vortex leaves the airfoil surface while θ_1 and θ_N are the angles of the upper and lower trailing edge panels respectively.

The position of the first vortex is obtained averaging the velocity at which the flow leaves the trailing edge on its upper and lower sides,

$$P_{w1} = \frac{(|u_{e\,1}| + |u_{e\,N}|)}{2} dt \tag{4.13}$$

It is important here to remain that the Kutta condition is placed on the last row of the Jacobian matrix.

4.6 Curvature effects

The high curvature of the airfoil geometry and the appearance of strong adverse pressure gradients, causing the boundary layer thickness to grow rapidly as the flow approaches separation, increases the importance of the streamline curvature. The pressure variation across the boundary layer, neglected in first order theory, can not be neglected in the case of flows around highly curved walls and with rapidly thickening boundary layers.

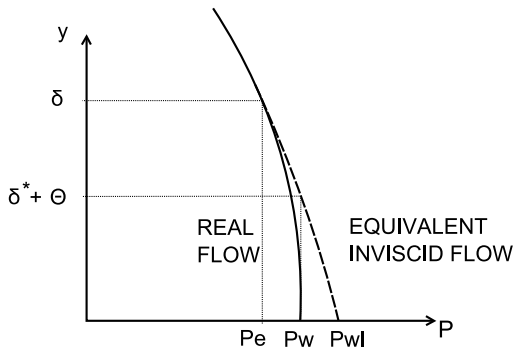

Figure 4.7: Pressure correction due to curvature effect.

For a pre-stalled flow, the curvature effects are significant only in the neighborhood of the separation point, [1]. Curvature effects lower the pressure around the separation location which influences the pressure level of the complete separation plateau. Hence a correction of the separation area pressure distribution is included in the present formulation.

Due to stability problems arising from the roughness of the displacement thickness predicted by the viscous-inviscid interactive code in separated areas, a simplification is introduced. Knowing that the curvature effects are more significantly in the neighborhood of the separation point, the value of κ^* at the SEP position is used for correcting the pressure on the whole separated flow region.

$$P_W = P_{IW} - \kappa^* \rho u_e^2 \left(\delta_1^* + \theta_1\right) \tag{4.14}$$

Where P_W is the wall pressure of the real flow and P_{IW} is the pressure of the equivalent inviscid flow. It was shown by Look in 1985 [1] how evaluating

the equivalent inviscid flow pressure at $y = \delta_1^* + \theta_1$ one gets the wall pressure of the real flow. The value of the curvature of the displacement surface around the separation point, κ^*, is obtained differentiating two times the streamwise displacement thickness, following Sørensen [33],

$$\kappa_{1A} = \frac{\delta^*_{1\,SEP-1} - \delta^*_{1\,SEP}}{S_{SEP-1}} \tag{4.15}$$

$$\kappa_{1B} = \frac{\delta^*_{1\,SEP} - \delta^*_{1\,SEP+1}}{S_{SEP}} \tag{4.16}$$

$$\kappa^* = \frac{\kappa_{1A} - \kappa_{1B}}{\frac{1}{2}\left(S_{SEP-1} + S_{SEP}\right)} \tag{4.17}$$

Hence the correction to the pressure coefficient can be written,

$$\Delta C_p = \frac{P_W - P_{IW}}{\frac{1}{2}\rho U_\infty^2} \tag{4.18}$$

This correction factor will vary from 0 to 0.13 depending on the flow conditions, usually it increases with the angle of attack until stalls and remains almost constant. It is of great importance for an accurate prediction of the drag coefficient.

4.7 Convergence study

4.7.1 Introduction

As a strong coupling has been implemented, the viscous and inviscid equations are computed via a full Jacobian matrix that linearizes them. The following procedure is used for updating the variables each newton iteration,

$$x_n = x_{n-1} + \omega\, \Delta x \tag{4.19}$$

Where x is a system variable and ω is its relaxation factor, it is set to unity for most of the parameters except for the following variables in the turbulent closure relations,

$$\omega_H = 0.6 \tag{4.20}$$

$$\omega_{C_f} = 0.6 \tag{4.21}$$

$$\omega_{C_{Di}} = 0.7 \tag{4.22}$$

In order to obtain a smooth numerical transition in between both sets of equations the following under relaxation factors were used in a six stations radius around the laminar to turbulent transition location,

$$\omega_{\delta_1^*} = 0.7; \tag{4.23}$$

$$\omega_{w_T} = 0.8; \tag{4.24}$$

4.7.2 Interactive boundary layer solver convergence

A convergence study was carried out for the viscous inviscid boundary layer interactive solver running under two dimensional steady flow conditions. A NACA 63415 at Reynolds 3e6 is chosen as the test airfoil. Convergence analysis has been realized at two different flow conditions. The first test is performed at low angle of attack, where the flow is attached to the airfoil. The angle of attack for the second case is higher and the flow is partially separated from the airfoil surface creating a separation bubble. In both cases the solution at a previous angle of attack is used as initial condition.

The maximum value of the right hand side vector is used as a convergence criteria. When maximum residual, $max\,(RHS)$, is lower than 5e-4 convergence is reached. In most of the cases convergence was reached in approximately 10 iterations for attached flow conditions and within 15-20 iterations for partially separated flow. In the cases in which the separation location moves fast upstream the increment of angle of attack in between computations had to be lowered to reach convergence.

The first test was performed at $\alpha = 1°$, using a previous converged solution at $\alpha = 0°$ as initial condition, Figure 4.8,

The case where under relaxation was turned off had a faster convergence, less than 5 newton iterations. The convergence slope when the under relaxation was active is lower, the system needed 9 newton iterations until the convergence criteria was reached.

A second test was performed at $\alpha = 16°$, see Figure 4.9. A previous converged solution at $\alpha = 15°$ was used as initial condition. The flow underwent separation at $0.6878c$ from the leading edge,

At high angles off attack, with highly separated flow, was common the appearance of a lack of convergence in most of the cases and consequently it was necessary to use under relaxation for some of the boundary layer variables to reach a converged solution, see Equations 4.20 and 4.23.

The convergence depends on the airfoil geometry as well as the Reynolds number and the angle of attack. Thick airfoils and profiles with high wall curvature present more convergence difficulties than thin airfoils, low Reynolds number conditions converge slower and with less stability than high Reynolds numbers closer to the potential solution. Convergence for incidence angles higher than 26 degrees has not been obtained with the viscous-inviscid interaction method. For cases far into deep stall conditions, the double wake model without viscous influence is strongly recommended.

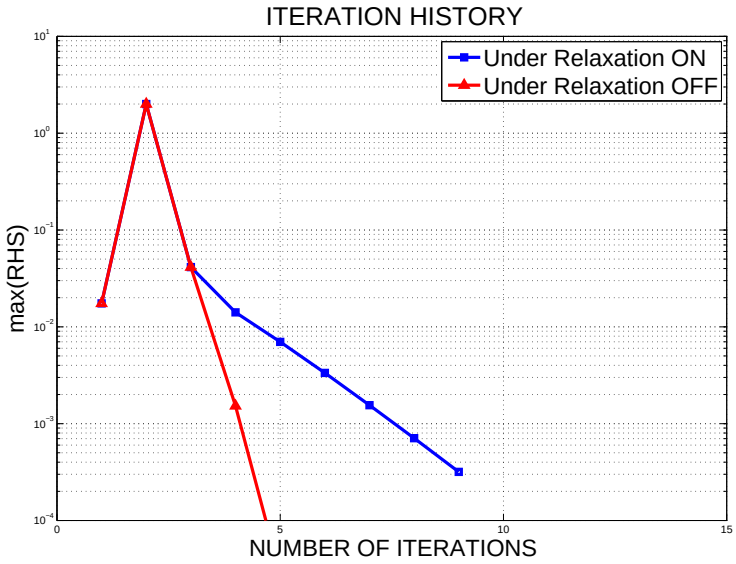

Figure 4.8: Iteration History for an attached flow computation

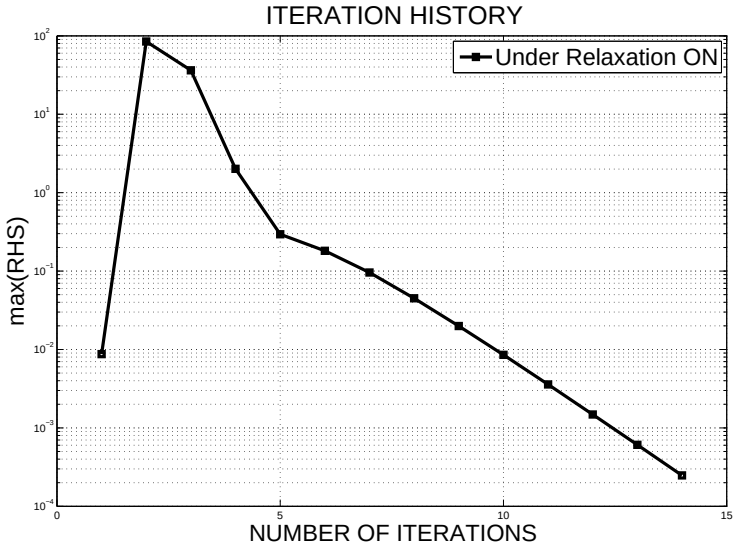

Figure 4.9: Iteration History for a separated flow computation

During the adimensional study of the boundary layer rotational effects in the airfoil aerodynamic performance was found that convergence problems arise when the local aspect ratio c/r and the rotational number approach the unity.

4.8 Initial conditions files

In order to obtain the first initial conditions for the system, the flow around a flat plate at $\alpha = 0$ and Reynolds number $1\,10^6$ was computed using a backward matching boundary layer scheme iteratively with a panel method. Computations started from the stagnation point moving downstream in order to take advantage of the parabolic nature of the integral boundary layer equations. Values for the different boundary layer parameter were saved and used in computing the first airfoil geometry.

A small database with restart files that include initial boundary layer parameters for the different airfoil shapes has been created. Database restart files are used as initial conditions at $\alpha = 0$ when a new simulation is started. In the case that a new airfoil geometry has to be simulated, the initial conditions of an airfoil with similar geometry have to be used to create a new restart file.

4.9 Summary

In this chapter the strong viscous-inviscid coupling selected as the interaction technique for the present approach is described. Other coupling alternatives have been presented and briefly analyzed.

The problem is reduced to a Jacobian matrix system, in this chapter the construction of the Jacobian matrix is depicted.

A deeper insight is taken into the Kutta condition, in its steady and unsteady versions. Its physical meaning as well as numerical implementation has been treated in the present chapter.

The influence of curvatures effects has been analyzed. A pressure correction for the separated region is introduced. The correction takes into account the curvature effects around the separation point that arise due to curvature of airfoil geometry together with the appearance of strong adverse pressure gradients.

A convergence study has been done for two different flow cases. In the first case, a fully attached boundary layer was considered while the other case presented a large separated region. Convergence for attached flows was easier to attain, while under relaxation was needed for the separated case.

Chapter 5

Results and Discussion

In the present chapter validations of the proposed viscous inviscid solver are presented. Benchmarking the VI interactive code with a large set of airfoil types and flow conditions is of great importance in order to probe the range of applicability of the solver.

In Section 5.1 a comparison between viscous and inviscid computations is presented. The improvements obtained in airfoil performance predictions if viscous effects are included in a potential flow solver are discussed.

The steady two-dimensional version of the code is validated against experiments in Section 5.2. A wide range of airfoil types and flow conditions are simulated and presented herein. The airfoil shapes simulated are: NACA 65415, LS(1)-0413, NACA 63-4xx, NACA 4412. The capability of the code to predict changes in the airfoil aerodynamic characteristics when subjected to variations in thickness and Reynolds number is also validated in this section. Further, the VI code running a laminar to turbulent modified e^9 transition model is validated against experiments for the airfoil profiles FFA-W3-211, s089 and NACA 634xx. Simulations with the two-dimensional version of the code are performed with the Quasi3D set of equations with the following values of the rotational parameters $RO = 0.3$ and $ls = 0.001$. These values ensure negligible rotational effects, although convergence at high angles of attack is improved if compared with the two dimensional set of equations.

An analysis of the influence of a trailing edge flap in the airfoil aerodynamics is presented in Section 5.3. Simulations were performed with the steady two dimensional version of the Quasi 3D integral boundary layer code. A comparison against potential flow theory predictions is analyzed herein.

In Section 5.4 the double wake model is validated against experiments. Predicted airfoil surface pressure distribution are compared against experimental ones in stall conditions. The airfoil profiles chosen for validation are: GA(W)-1, NACA 4412 and a cylinder shape. The cylinder cross section is simulated in order to verify the capability of the code to compute highly separated flows over geometries with a high thickness to chord ratio.

Validation of the unsteady version of the code with a single wake model is presented in Section 5.5. In this section, unsteady VI code predictions for different airfoil types with different dynamic flow conditions are compared against

experiments. An harmonic pitch motion of the airfoil was implemented and comparisons at different amplitudes and different reduced frequencies are presented. The airfoils used for validation are NACA 0012, NACA 0015 and NACA 63421.

The unsteady code has been used in its unsteady two dimensional version in order to simulate the aerodynamic behavior of an harmonically pitching airfoil section with a moving trailing edge flap, see Section 5.6. The work carried out by Krzysiak and Narkiewicz [53] has been selected for validation of our results. Influence of the phase shift between airfoil and flap motions is analyzed and presented herein. Comparisons between computations and experiments for different phase shifts are done. The capability of the code to simulate the damping of inflow disturbances using a controlled TEF is presented in this section.

A parametric study of the rotational effects is presented in Section 5.7, where lift and drag predictions for the s809 airfoil geometry are shown as function of the rotation related adimensional parameters RO and ls. An artificial rotor blade with constant chord was designed and simulations were performed at different spanwise positions of the blade. An analysis of the influence of rotation in the boundary layer characteristics is presented in this chapter. Results are shown as an order of magnitude analysis of the terms containing centrifugal and Coriolis forces terms in the r and θ momentum equations.

The following sign convention for the airfoil forces is used in the present chapter, Figure 5.1,

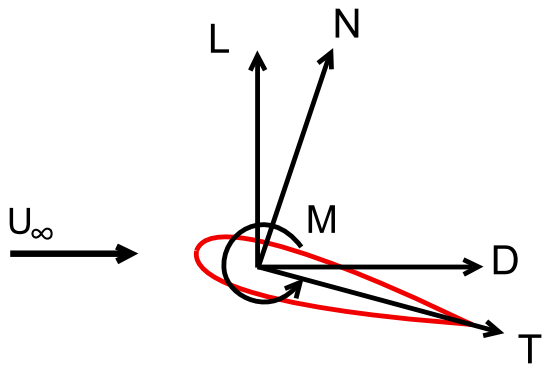

(a)

Figure 5.1: Airfoil Forces

Where,

- U_∞ is the freestream velocity vector.
- L is the lift force, perpendicular to the wind direction.
- D is the drag force, parallel to the wind direction.
- N is the normal force, perpendicular to the airfoil chord line.
- T is the tangential force, in the direction of the airfoil chord line.

- M is the pitch moment, positive in the counterclockwise direction.

Viscid-Inviscid predictions of the airfoil aerodynamic forces have been computed integrating the surface pressure distributions obtained from simulations. The integration was done over the panel discretization. For a higher accuracy of the results the integration could be done over a spline curve that fits the airfoil surface.

5.1 Comparison between viscous and inviscid computations

In this section comparisons between viscous and inviscid computations at Reynolds number of $3\ 10^6$ are presented and discussed. Inviscid computations were carried out using a panel method with a uniform source distribution in combination with a parabolic vorticity distribution around the airfoil contour and a Neumann condition used as boundary condition on the airfoil surface. The viscous simulations were carried out with the steady two dimensional version of the Quasi 3D viscous inviscid integral boundary layer solver that was presented in Chapter 3.

The airfoil chosen for the study of the influence of viscous effects is a NACA 63415. Lift, drag and pitch moment coefficients predictions from viscous and inviscid computations are compared herein for a range of angles of attack in between 0 to 20 degrees. Surface pressure distributions predicted with both approaches are also presented and analyzed. A study of the inviscid computations dependence on the number of panels used for the airfoil discretization is done and results are presented herein for $\alpha = 15°$. Viscous computations are done with a surface mesh of 140 panels, following Drelas discretization for its code Xfoil. Inviscid computations are done with a 1000 panels discretization of the airfoils surface.

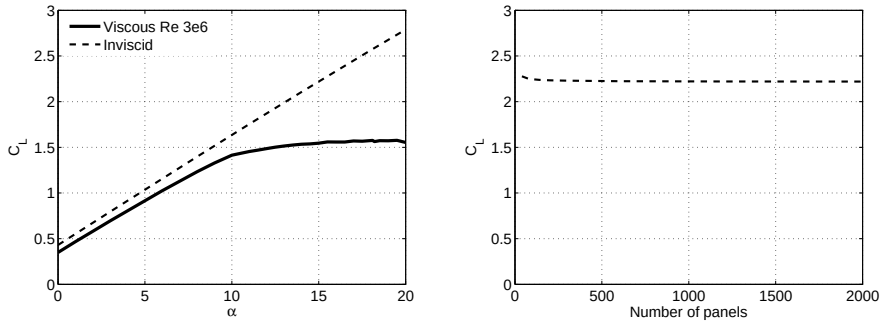

(a) (b)

Figure 5.2: (a) Viscous and inviscid predictions of lift coefficient (b) Inviscid lift dependency on panel number at $\alpha = 15°$

As expected, inviscid computations predict a higher lift coefficient due to the inexistence of a boundary layer that obstructs the freestream flow, and hence reduces the lift. The obstructing effect starts at low angles of attack and it is captured by the viscous-inviscid computations, becoming more important as the boundary layer grows in thickness with increasing α. Differences between the lift predictions increase after the viscous computations enters stalled conditions. As expected the lift dependency on panel number is not important, see Figure 5.3 (b).

VI model predictions of total drag are higher than inviscid computations, which should predict non drag, see Figure 5.3. Inviscid computations predict

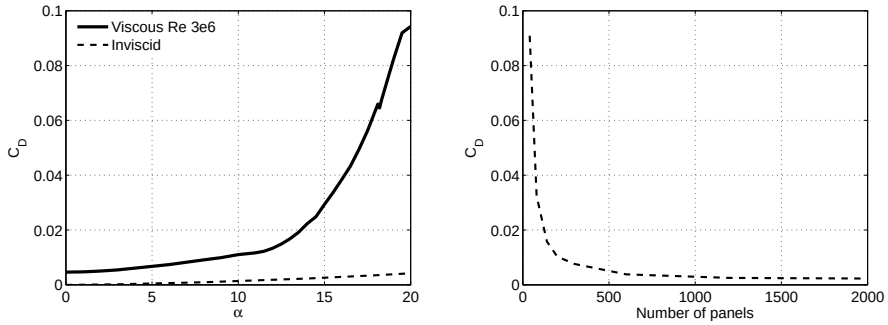

(a) (b)

Figure 5.3: (a) Viscous and inviscid predictions of drag coefficient (b) Inviscid drag dependency on panel number at $\alpha = 15°$

a small amount of drag, this is due to the error introduced by integrating the drag using the panel discretization and due to mesh disturbances around the leading edge of the airfoil. The drag predictions are strongly dependent on the number of panels used for discretization, see Figure 5.3 (b).

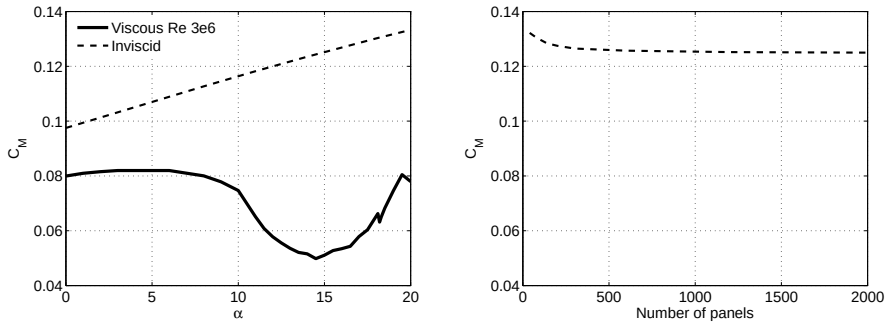

(a) (b)

Figure 5.4: (a) Viscous and inviscid predictions of pitch moment coefficient (b) Inviscid pitch moment dependency on panel number at $\alpha = 15°$

In Figure 5.4, the pitching moment coefficient is plotted as function of α. It is clear that the inviscid computations can not mimic any of the C_M tendencies reflected by the viscous-inviscid solver. Inviscid computations predict an approximately constant increment in C_M from 0 to 19 degrees of angle of attack. Pitch moment dependency on number of panels in not important, see Figure 5.3 (b).

In Figure 5.5 viscous and inviscid model predictions of the surface pressure distribution are presented for different angles of attack. Differences in between viscous and inviscid computations grow as the angle of attack increases, providing similar results until approximately $\alpha = 11°$, and more and more distant results as the angle of attack increases further. The main advantage of the

strong viscous-inviscid approach is its capability to solve the boundary layer at and after separation takes place, overcoming Goldstein's singularity. This allows the VI code to predict the constant pressure distribution characteristic of the separated area in the suction side of the airfoil. Due to the viscous nature of the flow separation mechanism, the inviscid solver can not predict separation by itself. However the introduction of a double wake model could allow the inviscid model to simulate airfoils in deep stall conditions. In this kind of models the separation location has to be known in advance from experiments or viscous computations, see Section 5.4.

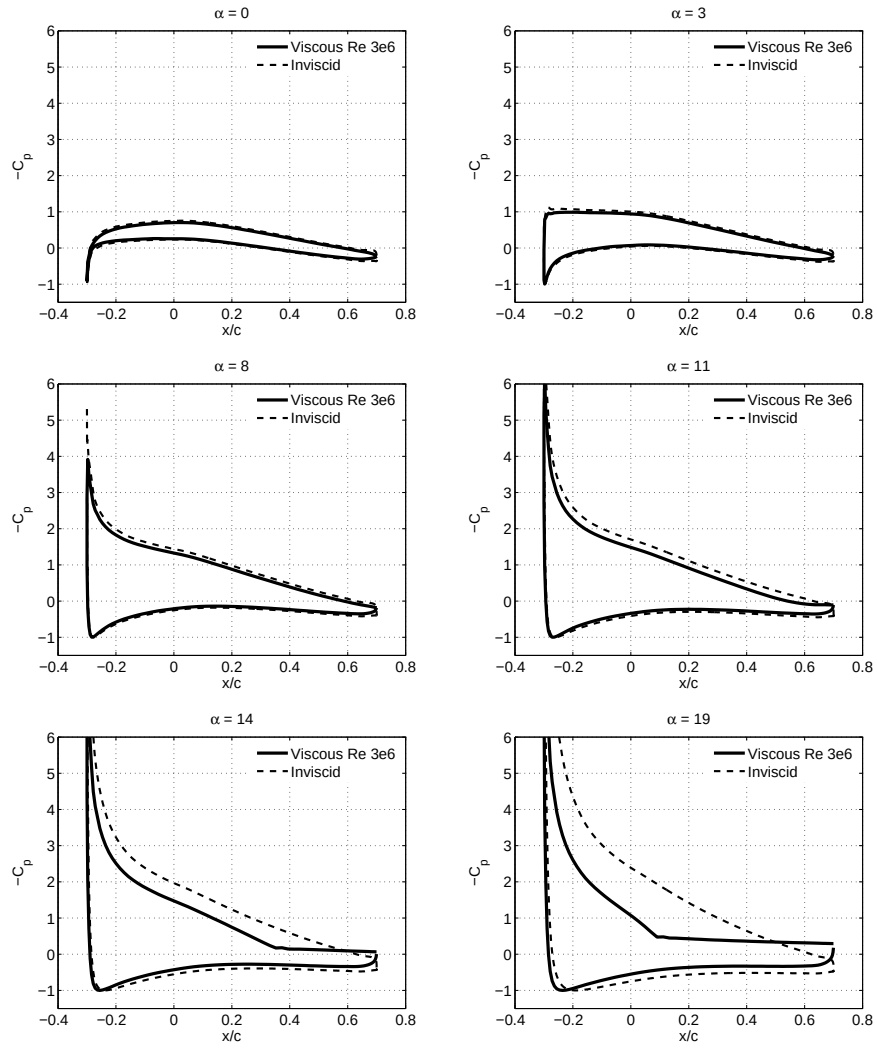

Figure 5.5: Viscous and inviscid surface pressure distributions from 0 to 19 degrees

Summary of viscous vs inviscid comparisons

Viscous-inviscid interactive computations have been compared against potential panel method ones for a NACA 63415 airfoil at a Reynolds number of

$3\ 10^6$. The lack of accuracy of the inviscid method has been proved at high angles of attack, when separation plays an important role. At lower angles of attack, differences due to the neglected influence of the viscous boundary layer, primary in drag and pitch moment predictions, are also important.

5.2 Steady airfoil computations

5.2.1 Validation against Risø W.T Airfoil Catalogue

NACA 65415 Airfoil

In this section is presented a detailed comparison of lift, drag and pitching moment coefficients as function of angle of attack between measurements, EllipSys2D and viscous-inviscid interactive simulations. The NACA 65415 airfoil is chosen as a first study case. This airfoil was designed to attain its minimum pressure at $0.5c$, defined by the 2nd digit, a design lift coefficient at zero angle of attack of 0.4, indicated by the 3rd digit, and a 15% maximum thickness, given by the last two digits.

Measurements were performed at the NASA low-turbulence pressure tunnel [54], and reported in the book Theory of Wing Sections by Abbott and von Doenhoff [55]. The Reynolds number in experiments as well as in computations was 3.10^6. eNRG simulations have been carried out with a boundary layer trip at $0.05c$ from the leading edge. In the following, viscous-inviscid interactive computations are referred to as eNRG in the figures.

In Figure 5.6, lift comparisons are presented for angles of attack from 0 to 20 degrees. At small angles of attack, when the flow is attached to the airfoil surface, the VI interactive solver over predicts slightly the lift, as compared with experimental values. At $\alpha = 9°$ the exponential growth in the boundary layer thickness forces the flow to separate. For angles of attack from 10 to 15 degrees, the separated region expands rapidly upstream the airfoil trailing edge. In this α range the viscous-inviscid lift predictions are in perfect agreement with experiments. EllipSys2D predicts an early stall of the lift curve, while the VI code over predicts slightly the lift values for $\alpha > 16.5°$.

Drag curves are presented in Figure 5.7. Experimental drag data was not available for attack angles higher than 11°. The VI predictions are in better agreement with experiments at low angles of attack where most of the drag arises from friction effects, whereas from 5° to 10° VI computations under predicts drag. Differences in airfoil drag performance influenced by the tripped boundary layer in comparison with a free transitional one will be analyzed at the end of the present section, Subsection 5.2.4. Discrepancies between Ellipsys2D and eNRG drag predictions increase with angle of attack, mainly due to differences in the separated area pressure level.

In terms of pitching moment coefficient, Figure 5.8, the viscous-inviscid code predictions are in better agreement with experimental data at small angles of attack. Note the high level of difficulty for most of the computational fluid dynamics solvers available nowadays to predict accurately C_M values.

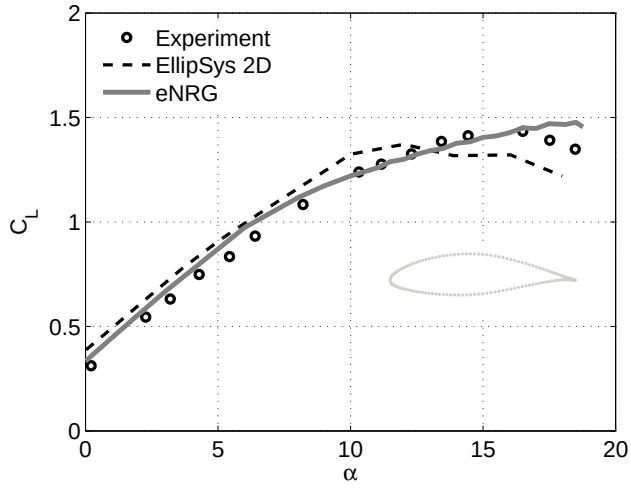

Figure 5.6: Lift coefficient curves, NACA 65415 Airfoil, Reynolds $3\,10^6$.

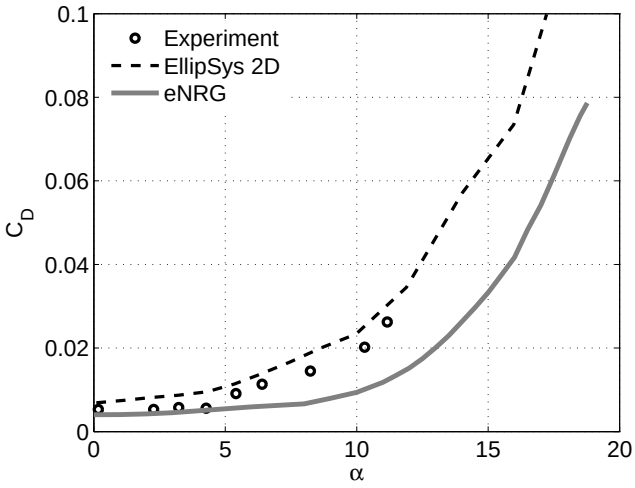

Figure 5.7: Drag coefficient curves, NACA 65415 Airfoil, Reynolds $3\,10^6$.

A good agreement between VI and EllipSys2D predictions of the surface pressure distributions is obtained at low angles of attack, although small discrepancies appears in the suction side of the trailing edge, Figure 5.9(a). With the increasing of the angle of attack, a progressive increase of the pressure peak near the airfoil nose was predicted. A recovery of the pressure from the pressure peak downstream is computed until $\alpha = 9°$, where the turbulent flow undergoes trailing edge separation and hence a region of nearly constant pressure is formed on the trailing edge vicinity. Laminar boundary layers undergo easier separation while turbulent boundary layer offers more resistance against it. The viscous-inviscid computations predict a faster movement upstream of the turbulent separation point if compared with EllipSys2D predictions. At the same

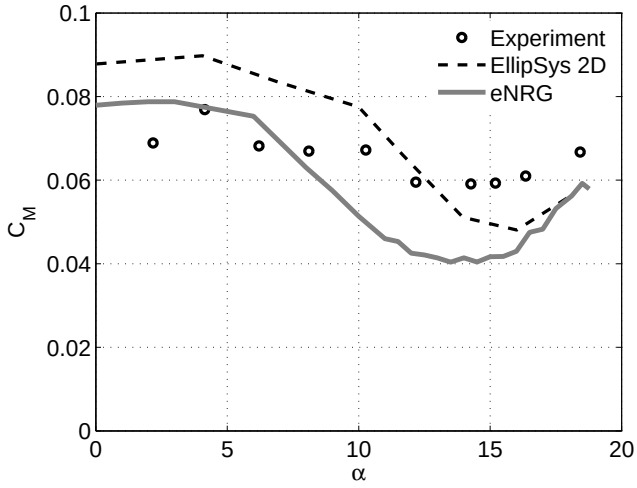

Figure 5.8: Pitching moment coefficient curves, NACA 65415 Airfoil, Reynolds $3\,10^6$.

time, the constant pressure region created by the reversal flow is also predicted at a lower absolute value by VI computations, Figures 5.9(c) and 5.9(d). When the separated region increases in size, the airfoil enters stalled conditions and differences in between both simulations are reduced, Figures 5.9(e) and 5.9(f).

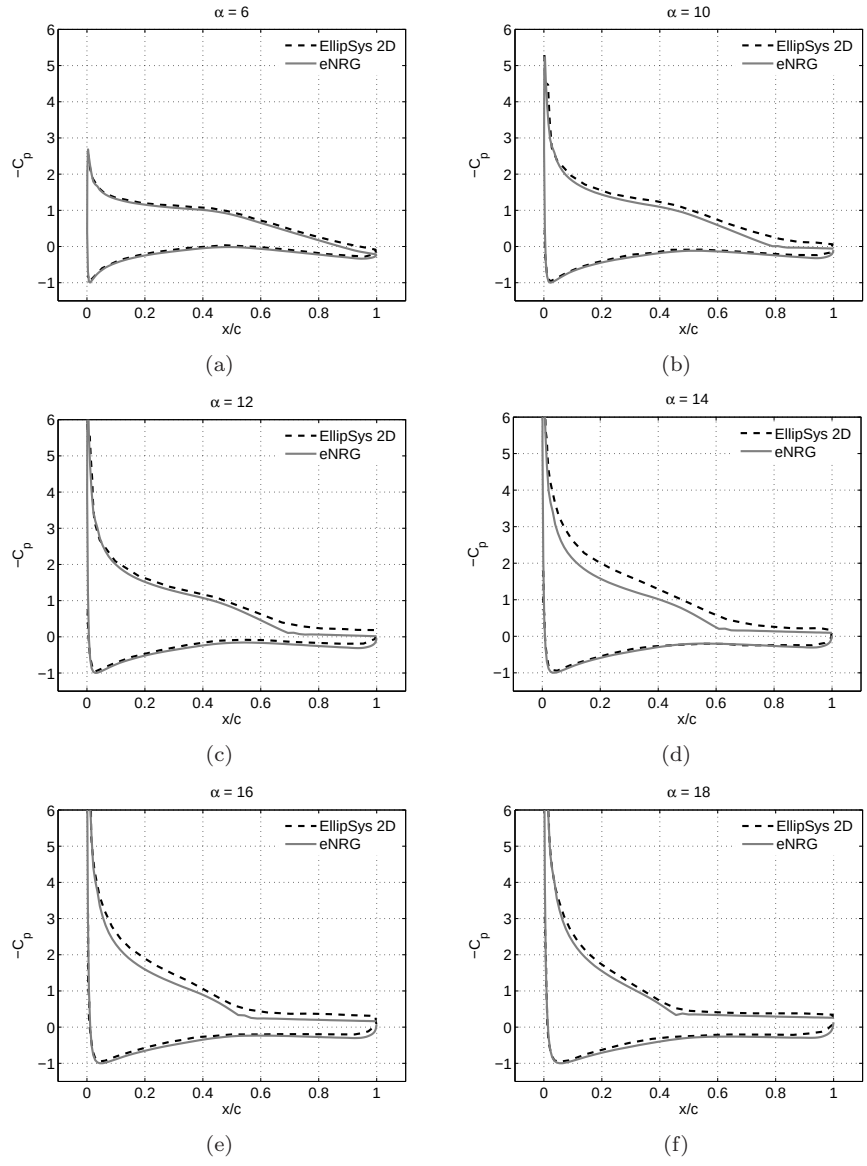

Figure 5.9: Surface pressure coefficients, NACA 65415 Airfoil, Reynolds $3\,10^6$.

LS(1)-0413 Airfoil

The LS(1)-04XX airfoil series were developed at NASA for general aviation applications. Experiments were carried out at the Laminar Wind Tunnel of the Institut fur Aerodynamik und Gasdynamik in Stuttgard University [56]. The Reynolds number in experiments and simulations was $1.5\,10^6$. Simulations with the VI interactive model have been performed with a boundary layer trip at $0.05c$ from the leading edge.

As shown in Figure 5.10, both VI and EllipSys2D computations predict the same lift at low angles of attack, $\alpha < 8°$, although measurements show a slightly

higher lift for $\alpha < 4°$. For $\alpha > 9°$, the flow starts to separate from the rear side of the airfoil, progressing upstream with the further increment in angle of attack. In overall terms, the agreement is good until stall is reached. EllipSys2D predicts a better position of $\alpha_{(C_L=C_{L_{MAX}})}$, while VI computations stalls one degree later than experiments. At $\alpha_{(C_L=C_{L_{MAX}})}$ the flow is separated over almost a 50% of the airfoil chord. Both predictions have the right tendency in the after stall region, although the reduction in lift is not as drastic as in experiments.

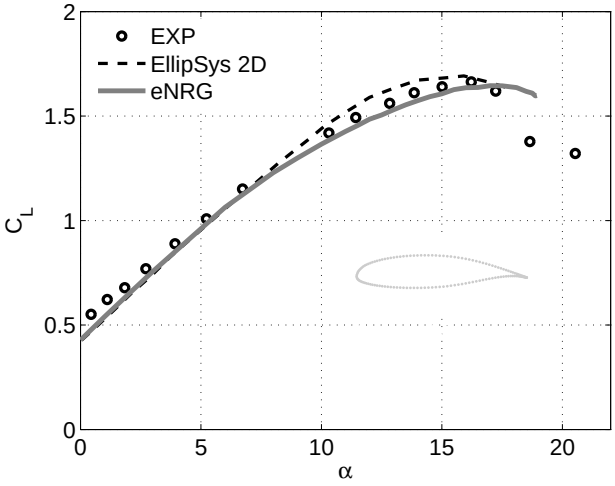

Figure 5.10: Lift coefficient LS0413, Reynolds $1.5\,10^6$.

In terms of drag, Figure 5.11, the viscous-inviscid code predicts a better starting drag but under predicts it as the angle of attack increases. The under prediction of total drag in between 2° to 7° degrees is related with a under prediction in pressure drag due to the boundary layer trip effect. At high angles of attack, where the friction drag is smaller, differences in between both simulations rise mainly due to the VI predictions of a lower absolute pressure in the separated region.

Regarding pitching moment coefficient, Figure 5.12, VI predictions have the same tendency as the experimental data but with a lower absolute value. EllipSys2D C_M predictions does not follow the experiment tendencies as good as VI computations in this case.

Comparing the predicted surface pressure distributions, Figures 5.13, an excellent agreement is obtained at low angles of attack. Even though small discrepancies appear in the trailing edge vicinity, Figure 5.13(a). At higher angles of attack, separation is predicted in the suction side of the airfoil. Separation is related with the value of the boundary layer shape parameter factor. In the case of turbulent flow, previous investigations [57] showed that separation appears when the shape factor, H, reaches the critical value of 2.5. With the appearance of separation, differences in between EllipSys2D and eNRG predictions

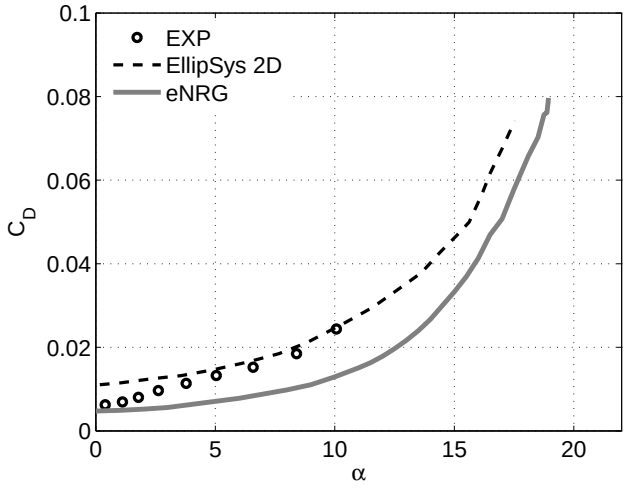

Figure 5.11: Drag coefficient LS0413, Reynolds $1.5\,10^6$.

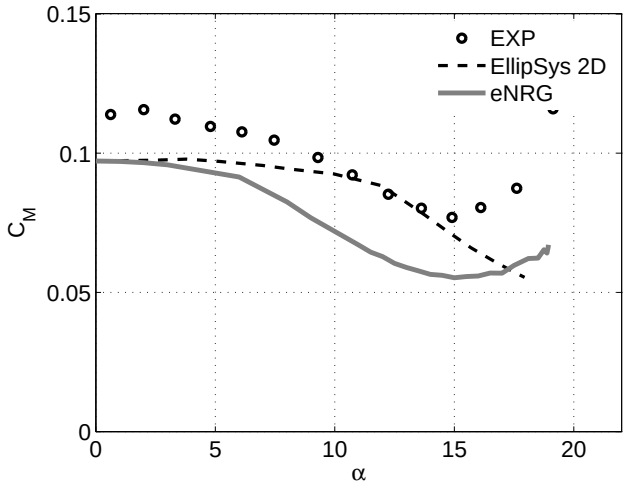

Figure 5.12: Pitching moment coefficient LS0413, Reynolds $1.5\,10^6$.

increases. The VI interactive solver predicted once more a lower absolute pressure of the suction surface of the airfoil, Figures 5.13(b), 5.13(c) and 5.13(d). With the upstream motion of the separation location, differences in between both predictions diminish, Figures 5.13(e) and 5.13(f).

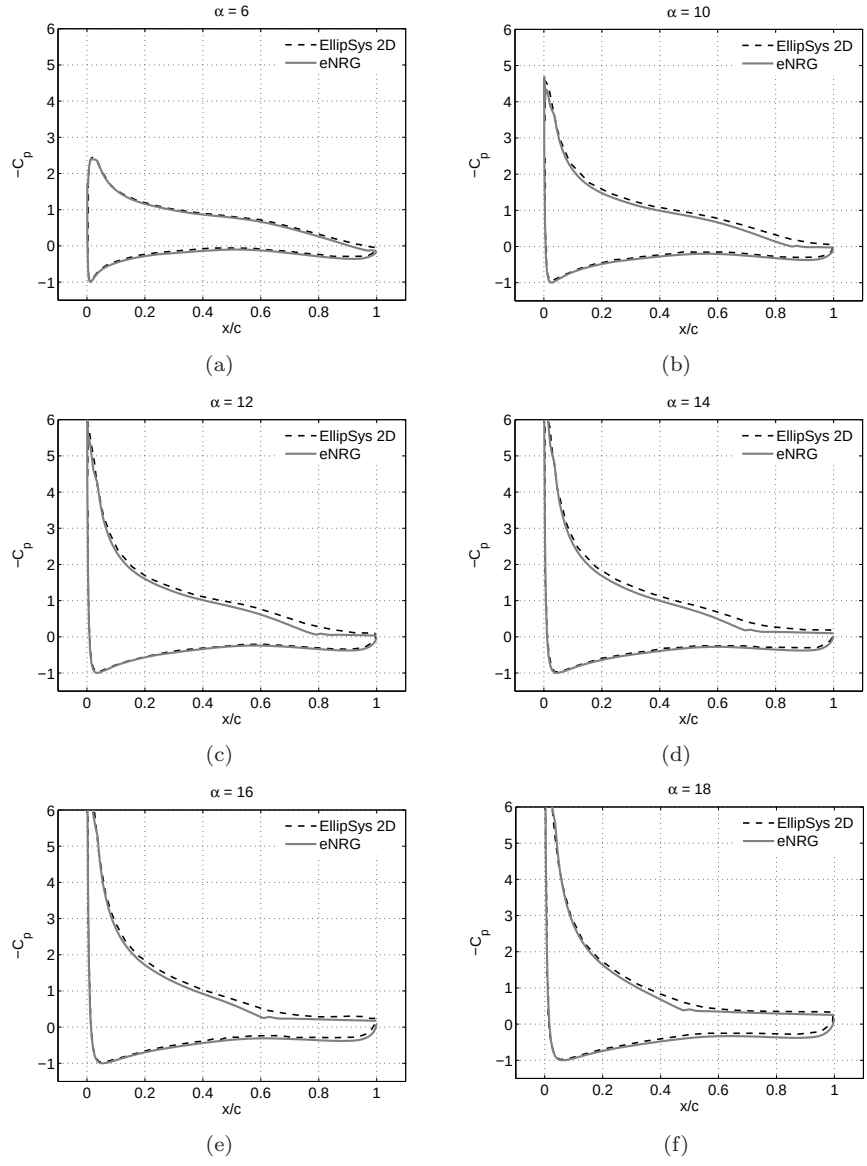

Figure 5.13: Surface pressure coefficient LS0413, Reynolds $1.5\,10^6$.

5.2.2 Thickness variation, NACA 63-4xx

The influence of airfoil thickness variations in the aerodynamic performance of the airfoil family sections NACA 63-4xx and the viscous-inviscid interactive code capability for predicting it is studied in the present subsection. Experimental lift, drag and pitching moment coefficients are compared against Ellipsys2D and VI computations. Three different airfoil thicknesses are simulated 15%, 18% and 21%. Surface pressure distributions at different angles of attack are also analyzed.

Measurements were performed at NASA in a low-turbulence pressure tunnel

and reported by Abbot and von Doenhoff [55]. Navier-Stokes equations were solved with the EllipSys2D code and results reported by Franck Bertagnolio in Risøs airfoil catalogue [58]. Simulations with the VI interactive model have been carried out with a boundary layer trip at $0.03c$ from the airfoils leading edge.

Figure 5.14 compares computed and measured lift distributions for three airfoil with different thickness, ranging from 15% to 21%. From the comparison it is seen that the computed lift distributions follow the experimental data up to stall, after which they start to deviate. The general tendency is that the VI code predicts stall a little bit too early whereas EllipSys maintains attached the flow much longer and therefore predicts a too high $C_{L_{MAX}}$. Furthermore, it is seen that discrepancies between computed and measured values tend to increase with airfoil thickness. As will be seen later, the early stall predicted for the 21% thickness airfoil is related with the transtition location.

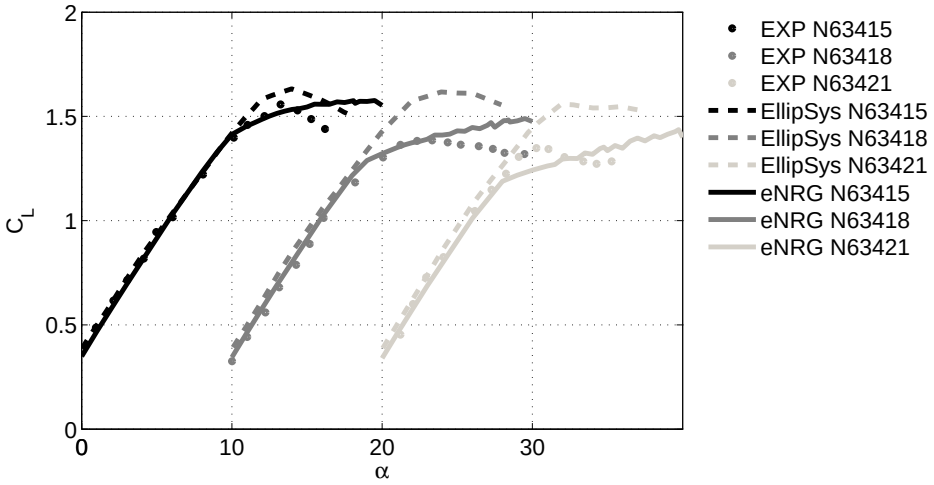

Figure 5.14: Lift coefficient NACA 63-4xx, Reynolds 3.10^6.

In regarding drag coefficient, Figure 5.15, viscous-inviscid computations present good drag predictions at angles of incidence lower than 7 degrees. At $\alpha > 7°$, VI simulations are slightly under predicting the pressure drag and hence the total drag differs from measurements and EllipSys2D computations, in which the drag is higher. At low angles of attack, where the drag is mostly friction drag, the VI interactive solver predicts higher drag coefficients for the thinner airfoil, while in the after stall region, where the pressure drag is dominant, tendencies changes and the thicker profile has slightly more drag. For $\alpha > 18°$ differences in drag due to the airfoil thickness are vanished.

Concerning the pitching moment coefficient, Figure 5.16, a good agreement between experiments and eNRG computations is achieved for angles of attack below 10 degrees. VI as EllipSys2D computations predicted a higher starting pitching moment coefficient for the thinner profile, reducing its value as the airfoil thickness increases. The VI code does not predict a clear effect of the airfoil thickness in C_M for $\alpha > 13°$.

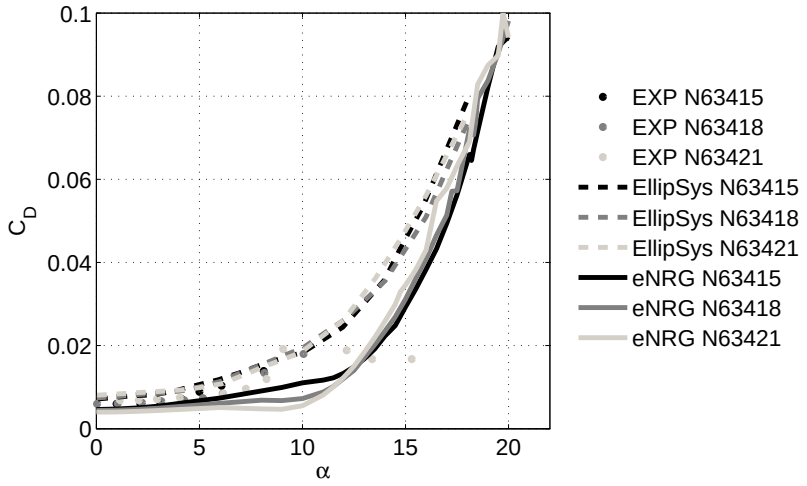

Figure 5.15: Drag coefficient NACA63-4xx, Reynolds 3.10^6.

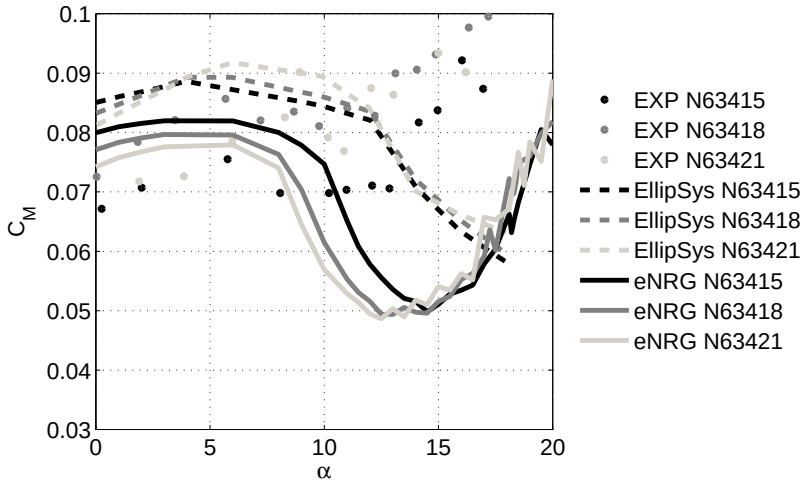

Figure 5.16: Pitching moment coefficient NACA 63-4xx, Reynolds 3.10^6.

Comparisons of the surface pressure distributions between EllipSys2D and VI computations are shown in Figure 5.17. The CFD code as well as the interactive code predict a higher suction pick for the thinner airfoil, reducing its value as the thickness increases. Discrepancies in between VI and EllipSys2D computations grow with the angle of attack. In all the cases, as the airfoil thickness increases, the suction peak smooths out. VI and EllipSys2D simulations present the largest differences in C_p around the separation position. VI simulations predict a too early separation as the airfoil thickness increases, Figure 5.17(b). Although at high angles of attack, $\alpha > 18°$ the separation location is the same for the three airfoil thicknesses, Figure 5.17(c). It is know that the thinner is the airfoil, the later separation appears on its rear side due to

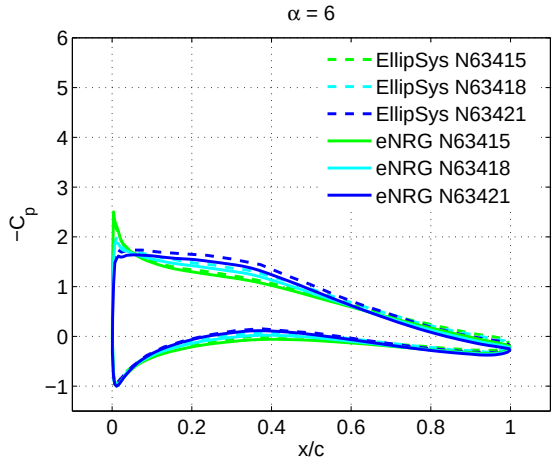

(a)

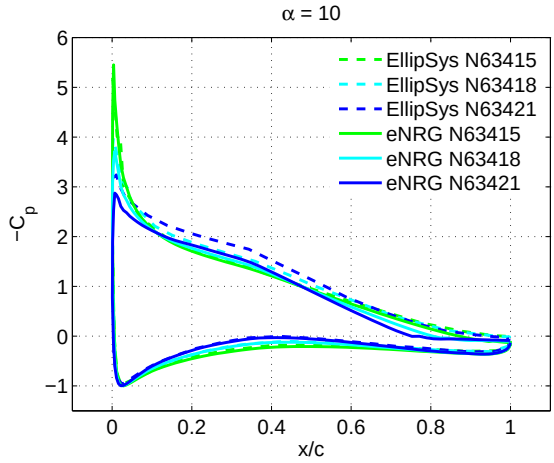

(b)

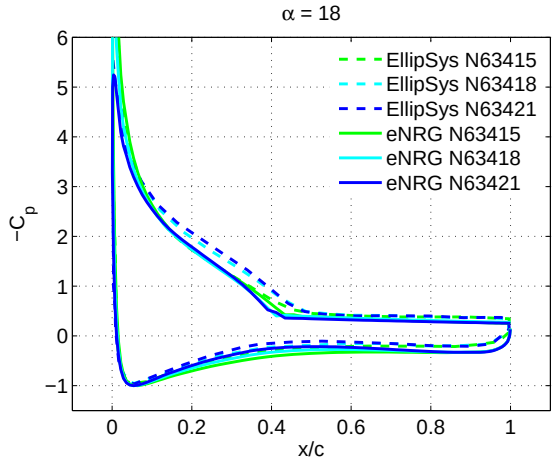

(c)

Figure 5.17: Pressure coefficient NACA 63-4xx series, Reynolds 3.10^6.

the lower obstruction exert against the freestream flow. Ellipsys2D predict no changes in the separation location as function of airfoil thickness at any of the angles of attack studied herein. In the separated flow region, none of the solvers predict changes in pressure as function of the airfoil thickness.

Due to the lack of experimental pressure data it is not possible to assure which of both computations can mimic better the reality.

The addition of curvature effects was key for improving the predictions of aerodynamic forces in thick airfoil simulations, in which the streamline curvature grows in importance due to the growing pressure gradients generated across the boundary layer, [33].

5.2.3 Reynolds number variation, NACA 4412

Validation of VI computations against measurements for a NACA 4412 airfoil subjected to Reynolds number variations is presented herein. Simulations were performed with Reynolds numbers 1.8 10^6, 3.4 10^6, 6.3 10^6 and 8.2 10^6. The Reynolds number indicates the ratio of the mass forces to the viscous forces, the higher is the ratio the more negligible become the viscous forces and the more potential becomes the flow. Experiments were carried at NACA variable-density wind tunnel and reported by Pinkerton [59]. Simulations have been carried out with a tripped boundary layer at $0.03c$ from the leading edge of the airfoil.

Figure 5.18 compares measured and predicted normal force coefficients in function of the angle of attack. For a better clarity of the figure the C_N values at Reynolds number of 3.4 10^6 are moved 10° in the positive α direction, for Reynolds 6.3 10^6 are moved 20° and for Reynolds 6.3 10^6 are moved 30°. As the Reynolds number increases the VI code underpredicts slightly the normal force value in the linear region if compared with measurements. Good prediction of the $C_{N_{MAX}}$ in angle and magnitude is obtained by the VI model at Reynolds 1.8 10^6 and 8.2 10^6. Although $C_{N_{MAX}}$ is slightly under predicted at Reynolds 3.4 10^6 and 6.3 10^6. In all cases $\alpha_{(C_N=C_{N_{MAX}})}$ is predicted accurately. $C_{N_{MAX}}$ is directly dependent on the viscous forces, and hence dependent on the Reynolds number. The viscous-inviscid computations after stall do not predict as steep drop in normal force as measured values.

Regarding the tangential force coefficient, Figure 5.19, a good agreement between experiments and computations is obtained for angles of attack from $\alpha = 0°$ to $\alpha \approx \alpha_{(C_N=C_{N_{MAX}})}$ for the different Reynolds computations. Predictions and experiments present the same tendency to increase C_T in its absolute value with the Reynolds number. The viscous-inviscid computations can not capture as steep decrease in C_T after stall as measured.

In terms of pitching moment coefficient, Figure 5.20, more difficult to predict than the other aerodynamic forces, simulations predict similar trend as experiments. The positive steep slope at high angles of attack is predicted in agreement with the measured data, although its absolute value is under predicted.

Analyzing the pressure distributions, Figures 5.21, at low angles of attack, when the flow remains attached to the surface of the airfoil, pressure distributions are practically unaffected by variations in Reynolds number. For $\alpha < 8°$

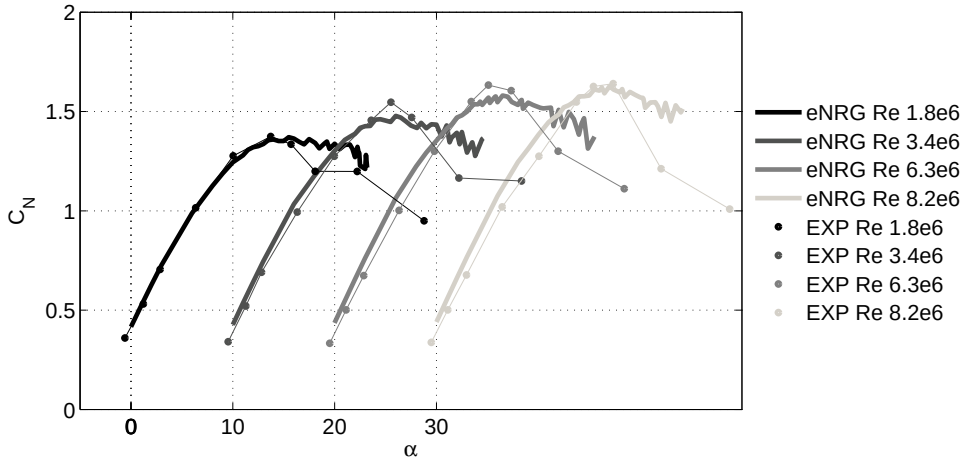

Figure 5.18: Normal force coefficient NACA 4412, Reynolds 1.8 10^6, 3.4 10^6, 6.3 10^6 and 8.2 10^6.

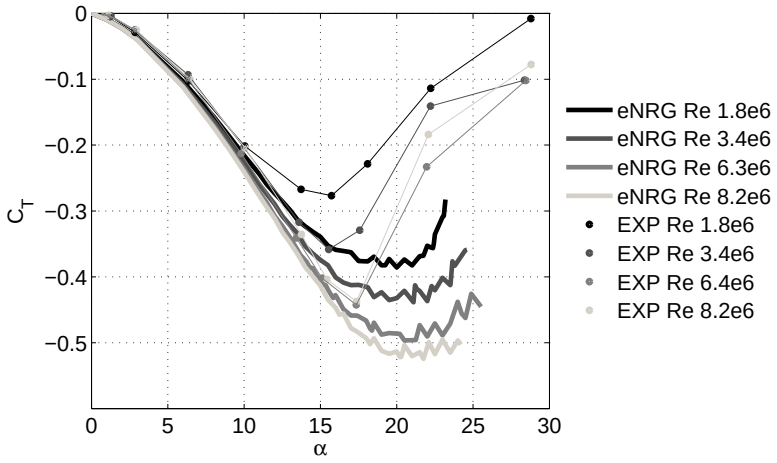

Figure 5.19: Tangential force coefficient NACA 4412, Reynolds 1.8 10^6, 3.4 10^6, 6.3 10^6 and 8.2 10^6.

experiments and computations are in perfect agreement. For $\alpha > 8°$, separation appears on the rear side of the airfoil and differences in pressure distribution between the different Reynolds numbers increases. The separation location is clearly affected by changes in Reynolds number. At low Reynolds numbers the flow separates earlier and moves faster upstream. At high Reynolds numbers the flow separates later allowing the airfoil to reach higher absolutes values of the normal and tangential force coefficients.

The viscous-inviscid model predicts in general more accurately the surface pressure distribution at higher Reynolds numbers, 6.3 10^6 and 8.2 10^6. At post stalled angles of attack, Figures 5.21(c), disagreements expand to the highest

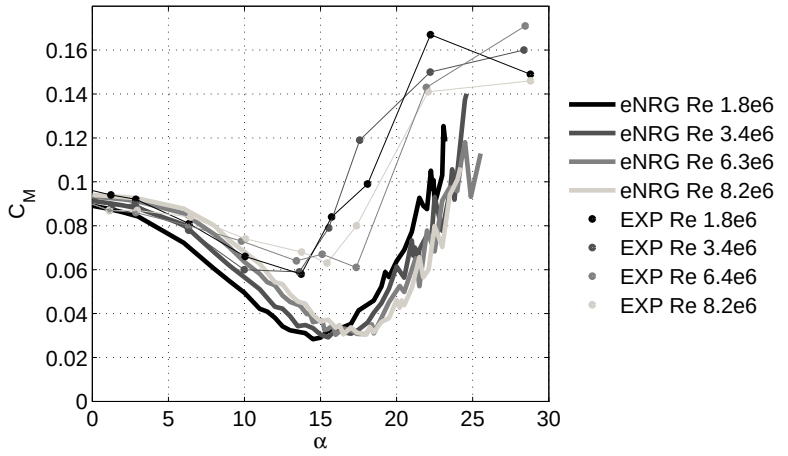

Figure 5.20: Drag coefficient NACA 4412, Reynolds 1.8 10^6, 3.4 10^6, 6.3 10^6 and 8.2 10^6.

Reynolds number computations. In this cases the separation location is predicted further downstream than obtained in experiments. Consequently the separation plateau has a lower absolute pressure, and a lower value of the pressure drag is obtained.

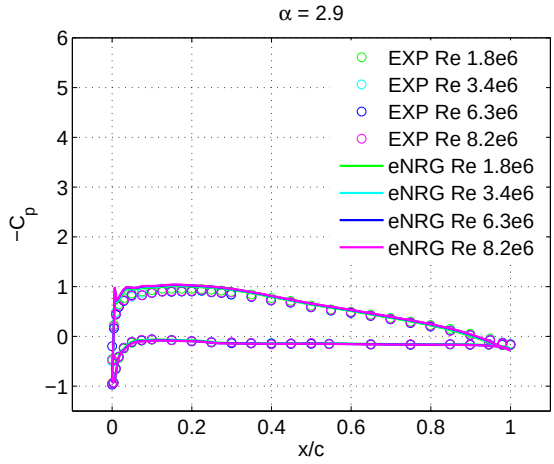

(a)

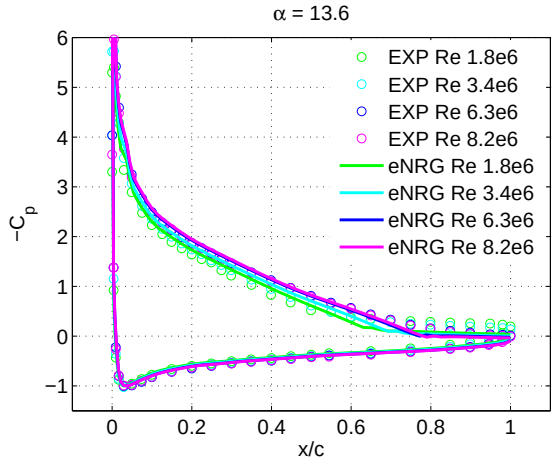

(b)

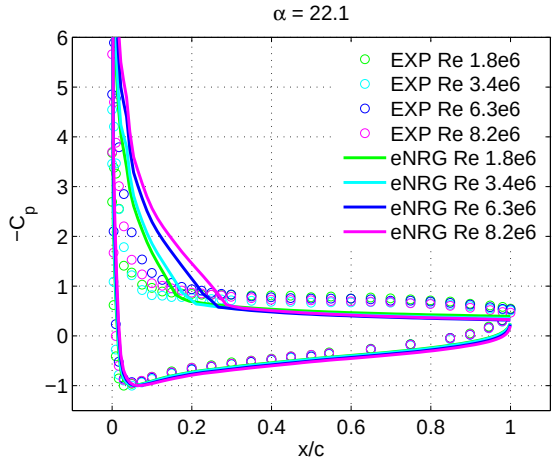

(c)

Figure 5.21: Surface pressure coefficient NACA 4412, Reynolds 1.8 10^6, 3.4 10^6, 6.3 10^6 and 8.2 10^6.

5.2.4 Free transition computations, modified e^9 type transition model

As a first case, the FFA-W3-211 airfoil has been chosen for validation of the VI interactive code running the modified e^9 laminar-turbulent transition model. The airfoil was tested in the low speed wind tunnel L2000 located at KTH Royal Institute of Technology in Stockholm [60], the turbulence intensity during measurements was 0.15%. The Reynolds number of experiments and computations is 1.8 10^6. The critical amplification factor, n_C, related with a turbulence level of 0.15% is computed following Equation 3.138, $n_C = 7.1755$. Comparisons are done between computed and measured lift and drag data. The VI code has been running with and without tripping of the transition point. First, the boundary layer trip was located at $0.025c$ from the leading edge and second at $0.15c$.

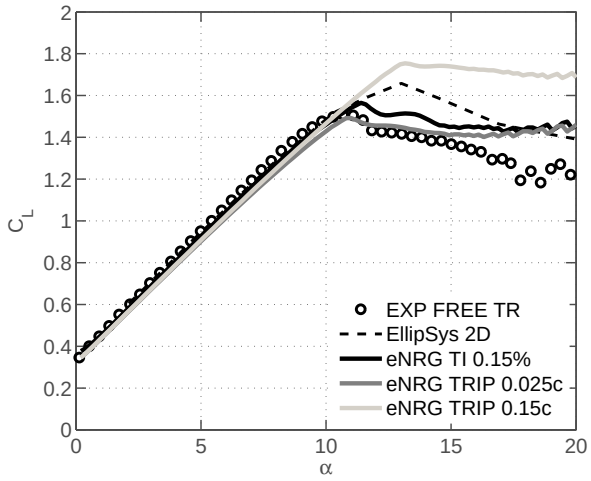

Figure 5.22: Comparisons between computed and measured lift data. The VI code has been running with and without tripping of the transition point. FFA-W3 211 airfoil, Reynolds 1.8 10^6.

In regarding lift force coefficients, presented in Figure 5.22. Stall is reached earlier in the case that transition is forced at $0.025c$ obtaining a better prediction of the $C_{L_{MAX}}$. The modified e^9 transition model computations also follows closely experiments. When the boundary layer is forced to laminar at 0.15% of the chord, the lift curve stalls much later. This is due to the underprediction of the boundary layer thickness as a consequence of the late laminar to turbulent transition, causing a reduction in the shape factor and hence retarding separation.

Concerning drag, Figure 5.23. At low angles of attack all the computations have similar drag predictions. Drag coefficients predicted by the viscous-inviscid model with a boundary layer forced transition at $0.15c$ are lower than the other simulations in the stall region due to the delayed separation. None of the models can predict the large values of drag obtained during experiments in stall conditions.

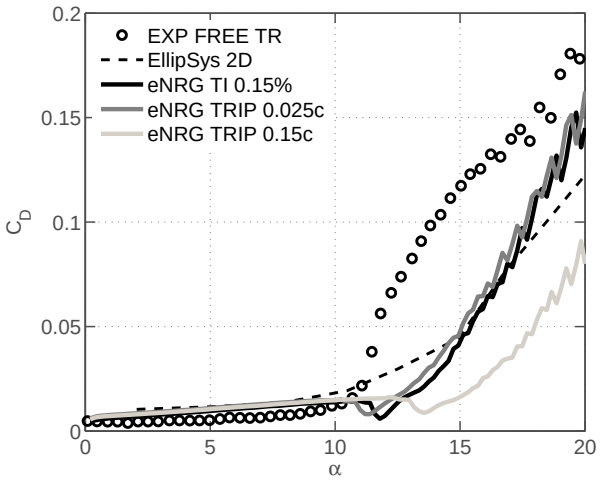

Figure 5.23: Comparisons between computed and measured drag data. The VI code has been running with and without tripping of the transition point. FFA-W3 211 airfoil, Reynolds $1.8\,10^6$.

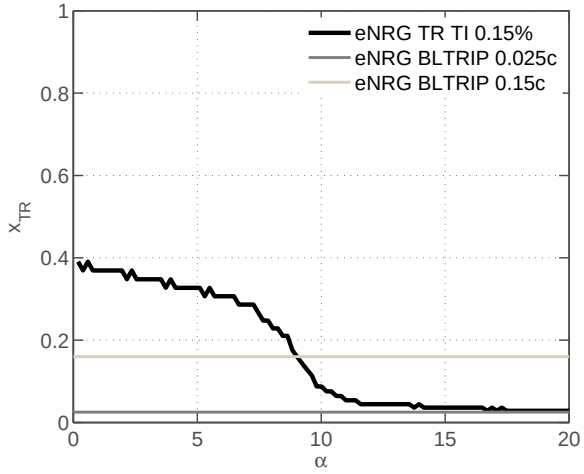

Figure 5.24: Chordwise transition location. The VI code has been running with and without tripping of the transition point. FFA-W3 211 airfoil, Reynolds $1.8\,10^6$.

The predicted laminar to turbulent transition position as a function of the angle of attack is plotted in Figure 5.24. $x_{TR} = 0$ refers to the leading edge and $x_{TR} = 1$ to the trailing edge. Transition moves gradually towards the leading edge between 0° to 11° of angle of attack, reducing considerably its variation at higher angles of attack.

As a second study case the airfoil s809 is selected. Experiments used for

validation were performed in the low-turbulence wind tunnel at Delft University of Technology, The Netherlands. The turbulence intensity in the VI model is set to 0.11%, giving a critical amplification factor of $n_C = 7.9199$. The Reynolds number in experiments and computations is 1.10^6. The airfoil thickness is 21% of the chord length. Note that simulations with the transition model presented convergence problems around $\alpha_{(C_L=C_{L_{MAX}})}$. A reduction of the angle of attack variations between computations had to be applied in order to reach convergence. The fast movement upstream of the transition location makes the convergence more difficult, see Figure 5.27.

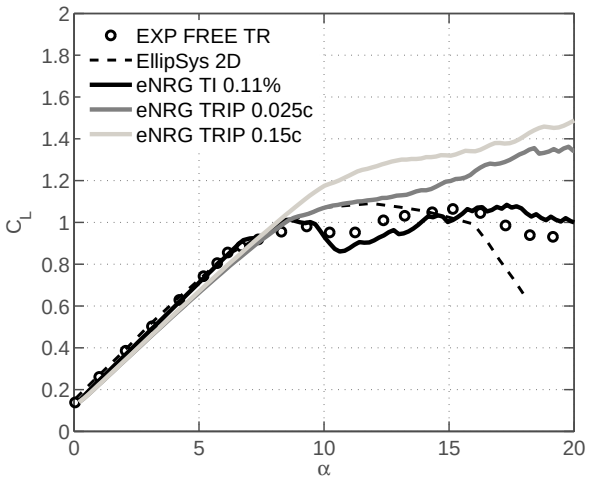

Figure 5.25: Measured Lift coefficients compared against Ellypsis2D and viscous-inviscid computations running with and without tripping of the transition point. Airfoil s809, Reynolds 1.10^6.

In terms of lift, Figure 5.25, VI predictions with free transition are in excellent agreement with experiments, the code is capable of predicting both double stall peaks. Simulations with a forced transition over predict lift in the stalled region and fail in capturing the double stall shape.

Regarding drag comparisons, Figure 5.26, Ellipsys2D predicts larger drag values than the VI solver. As shown before, the further downstream from the leading edge is located the boundary layer trip, the lower is the predicted drag at high angles of attack.

In regards to the onset of transition, Figure 5.27, the s809 airfoil section undergoes a more abrupt transition than the predicted for the FFA-W3 211 airfoil, Figure 5.24. The onset of transition moves from 50% of the chord at incidence angle 6° to 15% from the leading edge at $\alpha = 7°$. At high angles of attack laminar to turbulent transition reaches a steady location at 4% of the chord.

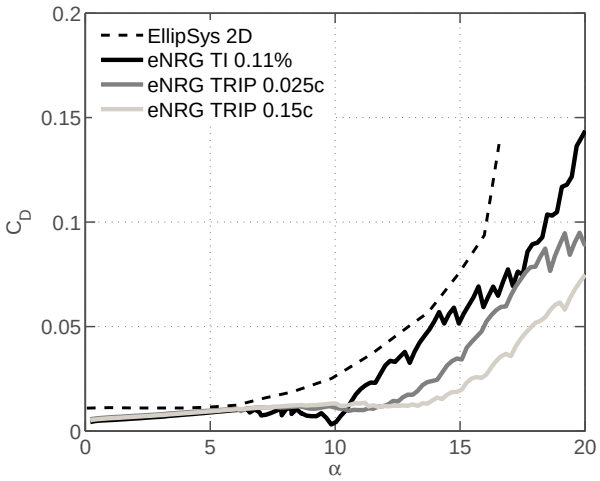

Figure 5.26: Measured Drag coefficients compared against Ellypsis2D and eNRG computations: modified n^9 transition model and boundary layer trips at 15% and 2.5%. Airfoil s809, Reynolds 1.10^6.

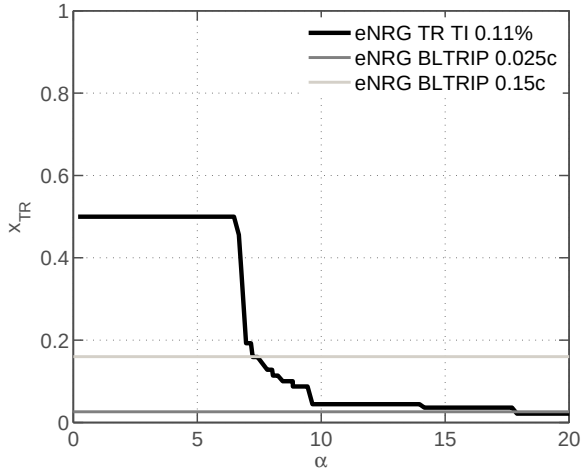

Figure 5.27: Transition predictions of the eNRG code running the modified n^9 transition model and boundary layer trips at 15% and 2.5% as a function of the angle of attack. Airfoil s809, Reynolds 1.10^6.

As a last study case the influence in the aerodynamic behavior of the laminar to turbulent transition location is studied for the airfoil profile family NACA634xx. Following the low turbulence wind tunnel in which measurements were acquired, the turbulence intensity in the modified n^9 transition model is set to 0.1%, obtaining a critical amplification factor of $n_C = 8.1486$. Simulations with a forced laminar to turbulent transition have the boundary layer tripped at $0.03c$. The Reynolds number in both measurements and simulations is 3.10^6

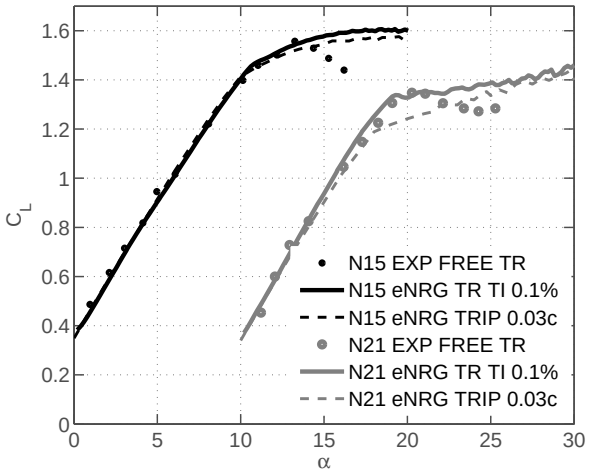

Figure 5.28: Experimental lift compared against VI simulations running with and without tripped boundary layer. Airfoil family NACA 634xx with 15% and 21% of the chord in thickness, Reynolds 3.10^6.

Viscous-inviscid simulations running the transition model are in better agreement with experimental lift data around $C_{L_{MAX}}$, Figure 5.28. In particular for the airfoil with 21% thickness, for which there is a significant improvement of the lift predictions after separation takes place. For thicker airfoils the early forced transition creates a overpredicted boundary layer thickness that promoves an early trailing edge separation, which forces a C_L underpediction around the $C_{L_{MAX}}$ position.

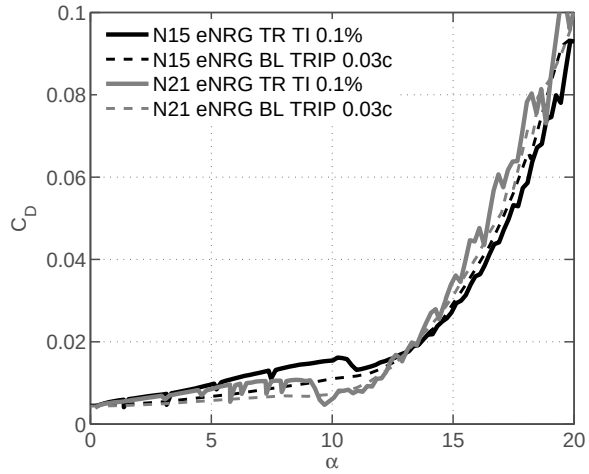

Figure 5.29: Experimental drag compared against VI simulations running with and without tripped boundary layer. Airfoil family NACA 634xx with 15% and 21% of the chord in thickness, Reynolds 3.10^6.

In terms of drag, Figure 5.29, at low angles of attack the VI code with the transition model predicts a larger total drag coefficient, in comparison with tripped boundary layer computations in which the flow is almost fully turbulent. However, the friction drag has a larger value under turbulent flow conditions than under laminar, due to the larger shear stresses created by turbulent velocity fluctuations. Therefore, the higher total drag predicted in the free transition simulations is related with a larger increment in pressure drag if compared with the decrement of friction drag due to the existence of a larger region under laminar flow.

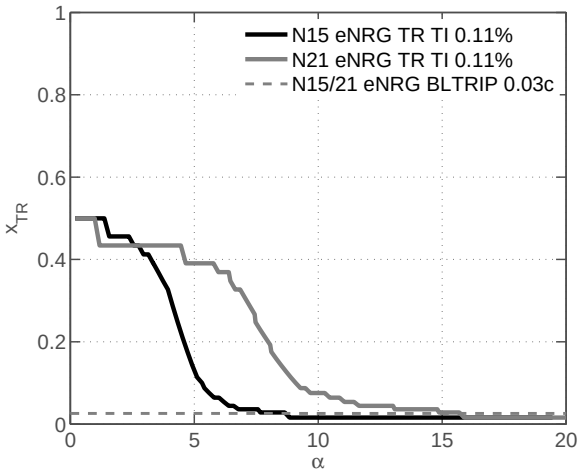

Figure 5.30: VI prediction of the laminar-turbulent transition location. Airfoil family NACA 634xx with 15% and 21% of the chord in thickness, Reynolds 3.10^6.

A faster upstream movement of the transition location is obtained for the thinner airfoil geometry, see Figure 5.30. The largest difference appears at $\alpha = 7°$, the thinner airfoil presents transition at $0.03c$ while the thicker one presents it at $0.33c$. Differences between both transition location are reduced as the angle of attack increases. At high angles of attack both airfoils present the same transition location at $0.015c$.

Summary of steady airfoil computations

A validation of the steady two dimensional version of the VI interactive boundary layer code against experiments and EllipSys2D computations has been presented in this section for the airfoils NACA 65415 and LS(1)-0413. A good accuracy of the lift prediction has been obtained although at high angles of attack there is a tendency to overpredict it. Drag predictions are slightly underpredicted in some of the cases, probably due to the tripped boundary layer implemented in computations. In terms of pitch moment coefficient a fairly good agreement is obtained with a tendency to underpredict it in comparison with experiments.

The influence of airfoil thickness variations in the aerodynamic performance of the NACA 63-4xx has been studied, as well as the capability of the VI interactive code to predict this variations. The VI code appears to be more sensitive to thickness variations than EllipSys2D, although the predicted decrease in lift during stall conditions is too light if compared with experiments. The airfoil thickness has the effect of forcing an earlier and smoother lift stall. In terms of drag, the viscous-inviscid code underpredicted it at low angles of attack if compared with EllipSys computations, although at high angles of attack differences are reduced.

The effects of Reynolds number in the aerodynamic forces have been studied for a NACA 4412. Further, the capability of the code to predict these effects has been benchmarked against experiments. Excellent predictions of $C_{N_{MAX}}$ and $\alpha_{(C_N=C_{N_{MAX}})}$ and their variation with Reynolds number are obtained. In terms of tangential force and pitch moment coefficients the agreement between predictions and experiments is good until stall is reached, after which their values are over predicted, although the right tendency is captured.

Simulations with the viscous-inviscid solver running the modified e^9 transition model have been presented in this section, showing the great importance of the transition location in order to predict aerodynamic lift and drag forces, specially in thick airfoil computations. An early transition location influences an overpredicted boundary layer thickness, forcing an early stall. Whereas a late transition location has the opposite effect, delaying stall and predicting a higher lift.

5.3 Steady airfoil computations with trailing edge flap

This section presents a study of the influence of the trailing edge flap on the aerodynamic behavior of two different airfoils, NACA 63418 and NACA 4412. Lift and drag polars are compared for different flap deflections. More in detail comparison is done analyzing the airfoil surface pressure distribution and which is the TEF effect on it.

As a first study case, the NACA 63418 is doted with a smooth curved trailing edge flap. The length of the flap is 10% of the airfoil chord and there is no gap between the main airfoil and the flap, Figure 5.31. The flap hinge x location is $0.9c$ while the y hinge location is 0. Four flap deflections have been simulated: $\beta = 15°$, $\beta = 10°$, $\beta = 5°$ and $\beta = 0°$. Laminar to turbulent transition is forced at $0.03c$ from the leading edge.

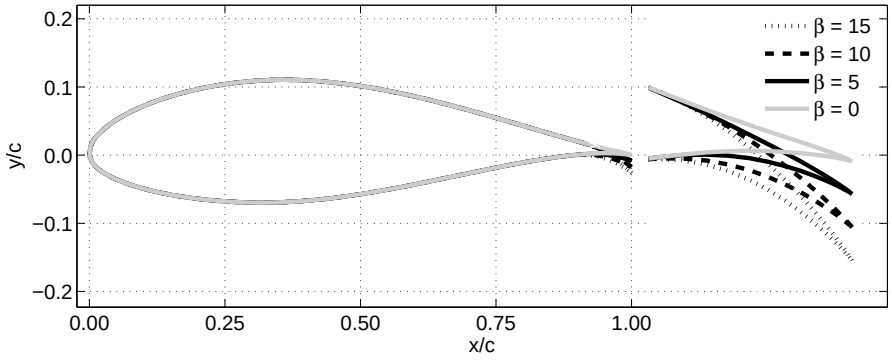

Figure 5.31: NACA 63418 geometry with 10% curved flap. Flap deflections $\beta = 15°$, $\beta = 10°$, $\beta = 5°$ and $\beta = 0°$.

In terms of lift performance, Figure 5.32, the TEF translates the lift curve to the left, obtaining a maximum gain in lift between 10 to 15 degrees of angle of attack for all the flap deflections. The rate at which the lift increments due to the flap is reduced with its downward deflection. Previous studies showed how the rate of increment in lift created by the flap is reduced with the downwards deflection at high angles of attack in stalled conditions, [61]. This tendency is not followed by the present simulations performed with the VI solver. This could be due to the light stall characteristics of the NACA 63418.

The TEF increases slightly the drag coefficient with its downward deflection due to the higher obstruction objected against the freestream flow, see Figure 5.33.

Analyzing the predicted surface pressure distributions, Figures 5.34. The flap alters the entire airfoil loading, not only influencing the trailing edge vicinity. Its overall effect in the surface pressure increases with the deflection angle until the separation position moves closer to the nose of the airfoil. At low angles of attack, Figures 5.34(a) and 5.34(b), the pressure peak is clearly affected by the flap position, increasing in absolute value with the downward flap

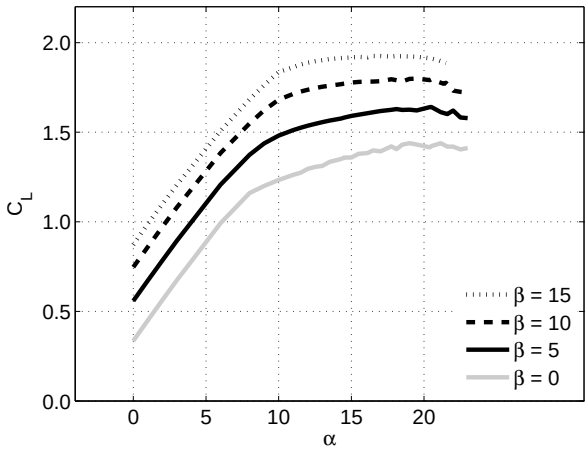

Figure 5.32: Lift force coefficients. NACA 63418, Reynolds $1.5\,10^6$. 10% curved flap with deflections $\beta = 15°$, $\beta = 10°$, $\beta = 5°$ and $\beta = 0°$.

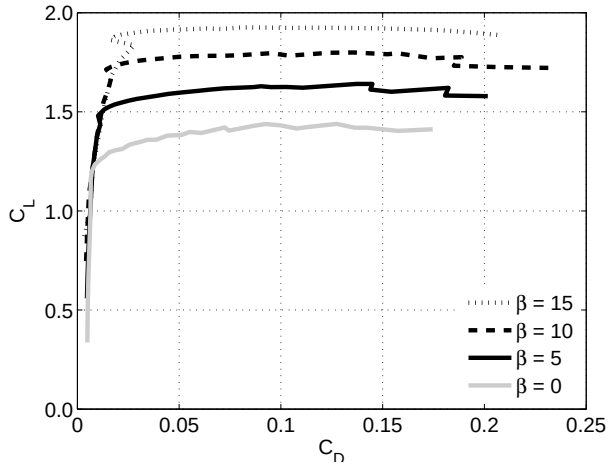

Figure 5.33: Lift versus force coefficients. NACA 63418, Reynolds $1.5\,10^6$. 10% curved flap with deflections $\beta = 15°$, $\beta = 10°$, $\beta = 5°$ and $\beta = 0°$.

deflection. At high angles of attack, when the flow is vastly separated, Figure 5.34(d), the TEF influence on the suction surface is reduced, specially in the separated region, although it does not vanish totally.

Lift predictions of the viscous inviscid interactive solver are compared against inviscid panel method computations in Figure 5.35. The panel method is implemented with a constant source distribution and a parabolic vorticity distribution around the airfoil contour. As the flap deflection increases the differences between the potential and the VI predictions grow in magnitude. Differences arise do to the relatively small Reynolds number of $1.5\,10^6$ used in the VI computations, while the potential panel method solution corresponds to an infinite Reynolds number. Further the panel method in itself is not capable of predict-

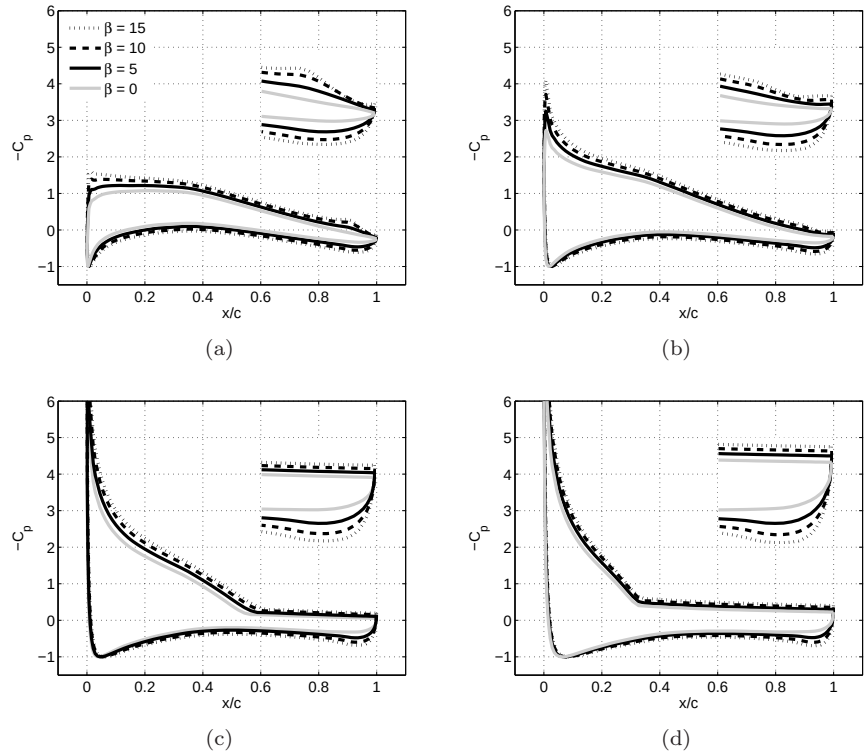

Figure 5.34: Surface Pressure distribution around a NACA 63418. Reynolds $1.5\,10^6$. Incidence angles (a) 3°, (b) 8°, (c) 14.5° and (d) 20.5°. 10% curved trailing edge flap with deflections $\beta = 15°$, $\beta = 10°$, $\beta = 5°$ and $\beta = 0°$.

ing separated flow, making the inviscid lift predictions diverge more an more from the viscous ones after separation takes place.

In order to gain a deeper understanding of the influence of a trailing edge flap in stall conditions, a NACA 4412, with deeper stall characteristics than the previous airfoil is simulated. A 10% of the chord length curved flap has been implemented with a hinge x location $0.9c$ and a hinge y location $0c$. Four flap deflections have been simulated: $\beta = 15°$, $\beta = 10°$, $\beta = 5°$ and $\beta = 0°$, see Figure 5.36. The Reynolds number is set to 1.10^6 while the laminar-turbulent transition is forced at $0.05c$.

Downward deflections of the flap create an increment in the lift force, moving the lift curve to the left as the flap angle increases, Figure 5.37. The influence of the flap influence on lift performance varies as a function of the angle of attack. Dividing the lift curve in three regions for a better understanding of the flap effects:

- The linear lift region, low angles of attack. In this region the rate at which the lift increments decreases with the downwards deflection of the flap. Differences in lift remained approximately constant in function of α until separation appears on the rear side of the upper surface.

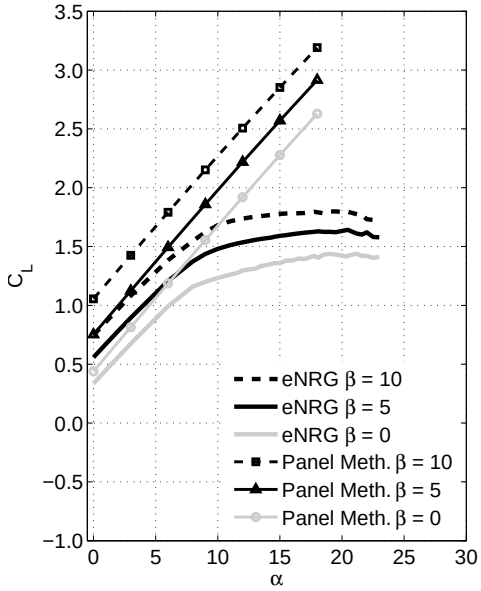

Figure 5.35: Lift curves predicted by VI model at Reynolds $1.5\,10^6$ and the potential panel method. NACA 63418. 10% curved flap with deflections $\beta = 10°$, $\beta = 5°$ and $\beta = 0°$.

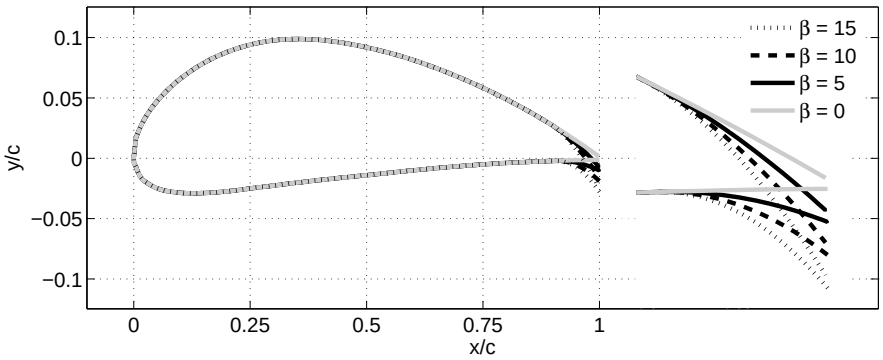

Figure 5.36: NACA 4412 geometry with 10% curved flap. Flap deflections $\beta = 15°$, $\beta = 10°$, $\beta = 5°$ and $\beta = 0°$.

- The second region is located around $C_{L_{max}}$. Here the lift increment due to the flap deflection is maximum. As the flap deflection increases, $\alpha_{(C_L = C_{L_{MAX}})}$ moves to the left, reaching stall at lower angles of attack.
- The third region includes the deep stall area. In this region differences in lift between flap deflections decrease considerably.

In terms of drag, Figure 5.38, the flap increases its value at high angles of attack while no clear effect is seen at low angles of attack.

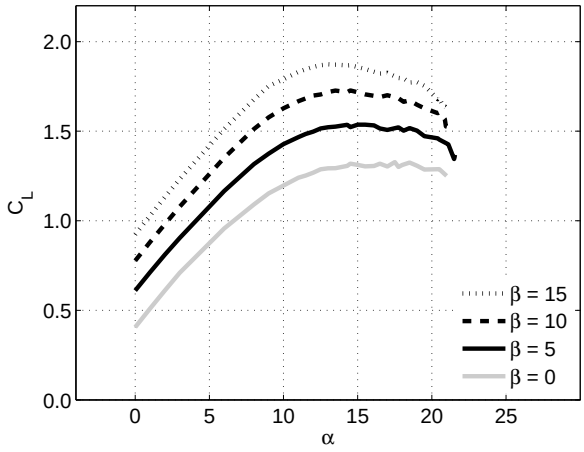

Figure 5.37: Lift force coefficient. NACA 4412, Reynolds 1 10^6 . 10% curved flap with deflections $\beta = 15°$ $\beta = 10°$ $\beta = 5°$ and $\beta = 0°$.

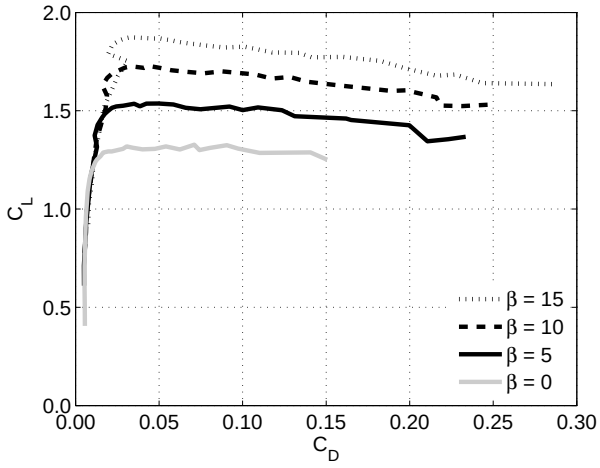

Figure 5.38: Lift versus drag force coefficient. NACA 4412, Reynolds 1 10^6. 10% curved flap with deflections $\beta = 15°$ $\beta = 10°$ $\beta = 5°$ and $\beta = 0°$.

The flap influence is not only localized to the trailing edge region. The TEF affects the pressure distribution all around the airfoil surface. Its influence increases with α until $\alpha_{C_L=C_{L_{MAX}}}$ and decrease after stall is reached. Analyzing the upper and lower surfaces and the trailing edge separately, we may conclude:

- Changes in the loading of the trailing edge. The loading of the pressure side of the trailing edge increases with the downward flap deflection due to the higher bending of the streamlines. A larger obstruction is presented against the freestream inflow. In the suction side of the trailing edge, pressure changes due to the flap deflection are not as large as in the pressure side.

- Changes on the suction side. The suction peak increases in absolute value

with the downward deflection of the flap, see Figures 5.39(a) and 5.39(b). The suction surface load increases between the leading edge and the onset of separation in all the cases with the downwards flap deflection. The flap has a smaller influence inside the separated region, although it affects the separation location, downwards flap deflections retard the onset of separation, see Figures 5.39(b) and 5.39(c). This effect increases with the downward position of the the flap and it vanishes at high angles of attack. In the case presented in Figure 5.39(d), where the airfoil is almost fully separated, the flap has no influence in the location of separation and differences in the loading of the suction side are reduced drastically.

- Changes on the pressure side. Except for the trailing edge area, discussed earlier, the pressure side of the airfoil remains practically invariable to flap deflections.

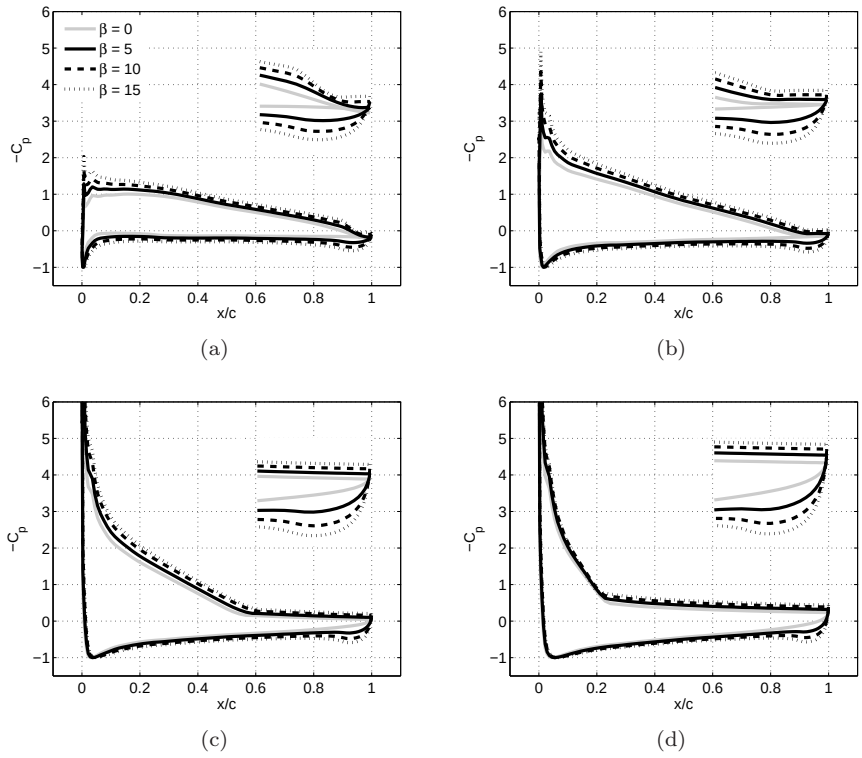

Figure 5.39: VI solver predicted surface pressure distribution for a NACA 4412. Reynolds 1 10^6. Incidence angles (a) 3°, (b) 8°, (c) 14.5° and (d) 20.5∘ respectively. Flap length 10%. Flap deflections $\beta = 15°$ $\beta = 10°$ $\beta = 5°$ and $\beta = 0°$.

Summary of steady airfoil computations with Trailing Edge Flap

The capability of the viscous-inviscid interactive code to predict the trailing edge flap influence in the aerodynamic performance of the NACA 63418 and NACA 4412 airfoils has been presented and analyzed in this section. The VI

interactive code has a good capability to simulate the flap influence on the airfoil section if compared qualitatively with previous works.

In general, downward flap deflections move the lift curve to the left, increasing the lift value for a giving angle of attack. The $C_{L_{MAX}}$ is translated to lower angles of attack with the downward deflection of the flap. Differences in lift between flap deflections are reduced at high angles of attack. The drag force coefficient is not strongly affected by the flap angle at lower angles of attack although a tendency to increase drag with the downward flap deflection is observed at higher angles of attack.

5.4 Double wake model computations

In order to validate the double wake model, the pressure distribution around the airfoil surface has been computed for different airfoils at different angles of attack in stalled conditions. Double wake model predictions are compared against experiments. The separation position at which the upper wake is shed is in all the cases obtained from the experimental pressure distribution.

In Figure 5.40 inviscid double wake model pressure computations are compared against wind tunnel measured data at high Reynolds number, $Re = 6.3\,10^6$. The simulated airfoil is a NACA 4412 at 17.6 and 22.1 degrees of angle of attack. Experimental data used for validation was published in a NACA report by Robert M. Pinkerton, [59].

The airfoil is simulated with a wake factor, $W_F = 1.8$, value obtained from the linear relation between W_F and chord to thickness ratio presented in Chapter 2, Figure 2.8. For an angle of attack of 17.6°, the separation point in simulations is forced at $0.5331c$. The position of separation is obtained from the experimental pressure distributions. Whereas at 22.1 degrees the separation position is forced at $0.1674c$, obtained with similar procedure as in the first case.

At $\alpha = 17.6°$ a good agreement with measurements is achieved for both, the upper and lower surface pressure distributions. The pressure peak is captured with high accuracy and also the rate at which the pressure recovers until separation is reached. In the case of $\alpha = 22.1°$, a fairly good agreement is obtained for the suction surface, despite the fact that the absolute value of the pressure peak is slightly under predicted.

In Figures 5.41(a), 5.41(b) and 5.41(c), wind tunnel measurements of the surface pressure distribution around a GA(W)-1 airfoil are compared against the double wake model predictions. Experiments were carried out at the NASA-Langley Wind Tunnel installation [15]. The Reynolds number in experiments was $6.3\,10^6$ and a boundary layer trip was placed at $0.08c$ from the leading edge. Comparisons are presented herein for the following angles of attack: 19.06°, 20.05° and 21.14°.

The wake factor used to compute the wake length in the double wake model is taken from Figure 2.8, $W_F = 1.58$. Computations at $\alpha = 19.06°$, with a forced separation location at $0.5986c$, exhibit excellent agreement with experiments for both the upper and lower surfaces. In the case that $\alpha = 20.05°$, the separation position is fixed at $0.4889c$ and a perfect agreement with the experiments is

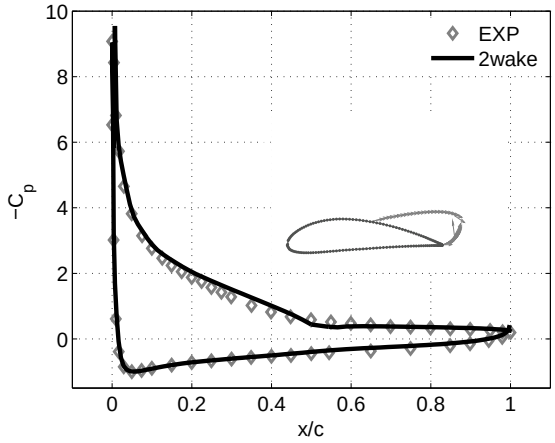

(a)

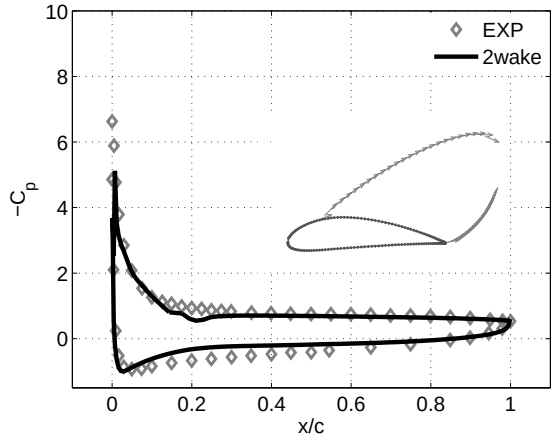

(b)

Figure 5.40: NACA 4412 airfoil at Reynolds $6.3\,10^6$ (a) $\alpha = 17.6°$, (b) $\alpha = 22.1°$

achieved. In deep stall conditions, $\alpha = 21.14°$, the separation position is set at $0.1513c$, good agreement is attained for the suction surface with a slightly under predicted pressure peak. The pressure peak increases with the angle of attack until deep stall is reached, after which it decreases.

In the last study case, Figure 5.42, a Cylinder is chosen. The thickness over chord ratio of a cylinder is equal to unity. Experiments used for validation [62] were performed at a Reynolds number of $6.7\,10^5$.

The separation point was forced at $0.2612c$ for both the upper and the lower surface. The wake factor obtained from Figure 2.8 was $W_F = 1.2$. A good overall agreement was obtained for the pressure distribution. Note that in this case the separation area has the same pressure as the ambient flow.

In Figures 5.43, double wake flow computations around a GA(W)-1 airfoil

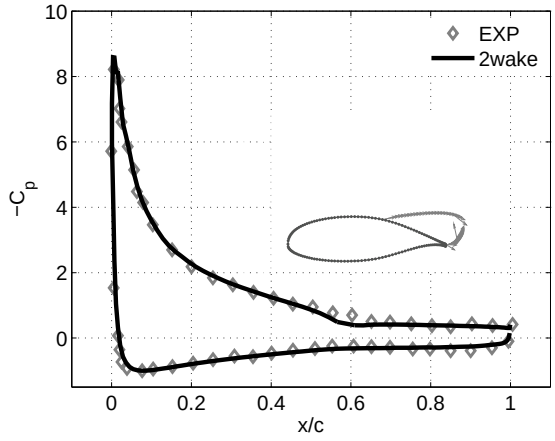

(a)

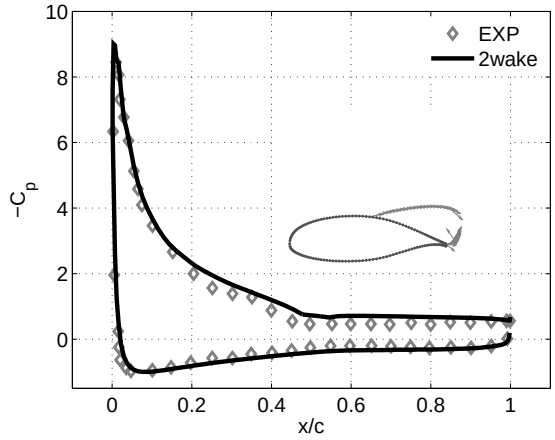

(b)

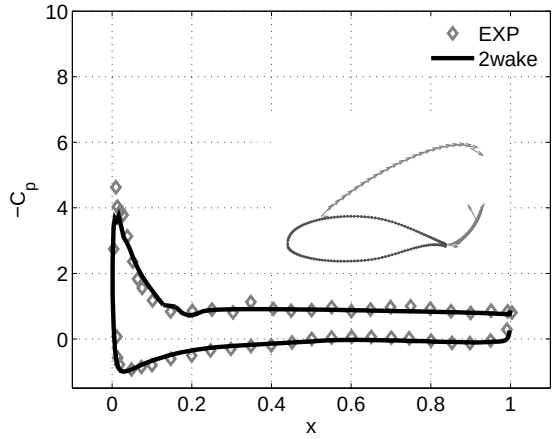

(c)

Figure 5.41: GA(W)-1 airfoil at Reynolds 6.310^6, (a) $\alpha = 19.06°$, (b) $\alpha = 20.05°$ and (c) $\alpha = 21.14°$

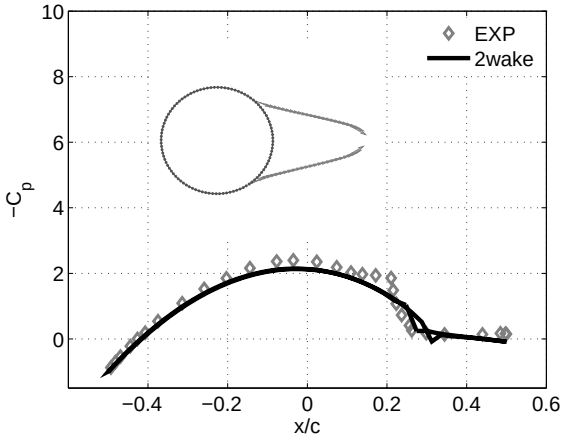

Figure 5.42: Circular cylinder at Reynolds $6.7\,10^5$.

undergoing separation are presented. Velocity vector field, streamlines and potential field are plotted for the airfoil at an angle of attack 21 degrees. Separation is fixed to occur at $0.1513c$, the position in which the double wake is shed. The influence of the linear vorticity and constant source distribution around the airfoil together with the two constant vorticity wake distributions is computed on a Cartesian mesh generated around the airfoil contour.

Studying the figures below, the flow field can be divided in different areas as function of the flow characteristics. Around the leading edge the velocities are low, as seen from the velocity vectors plot, Figure 5.43(b). Some particles will choose to follow the streamlines to the suction side of the airfoil while the others will follow them to the pressure side, see Figure 5.43(a). The ones following streamlines to the suction side of the airfoil will increase gradually its velocity reaching its maximum around the outer side of the separation wake. In the inner side of the separation shear layer the velocities are negative and really close to zero, this tendency it is clear from the potential flow distribution, see Figure 5.43(c). The particles following the streamlines to the pressure side of the airfoil will keep a constant and relatively low velocity until they reach the trailing edge, after which will follow the trailing edge wake increasing gradually their velocity.

In Figure 5.44 are plotted streamlines around a GA(W)-1 airfoil at 19, 20 and 21 degrees of angle of attack. The separation wake changes its shape as function of the angle off attack. When the flow hits the airfoil at 19° the separated wake has a bubble shape. As the angle of attack increases, the separation location moves upstream the airfoil surface and the two wakes that forms it increase the gap between each other on its rear side. At 21 degrees the bubble shape has slowly turned into the characteristic wake geometry behind a fully separated airfoil section.

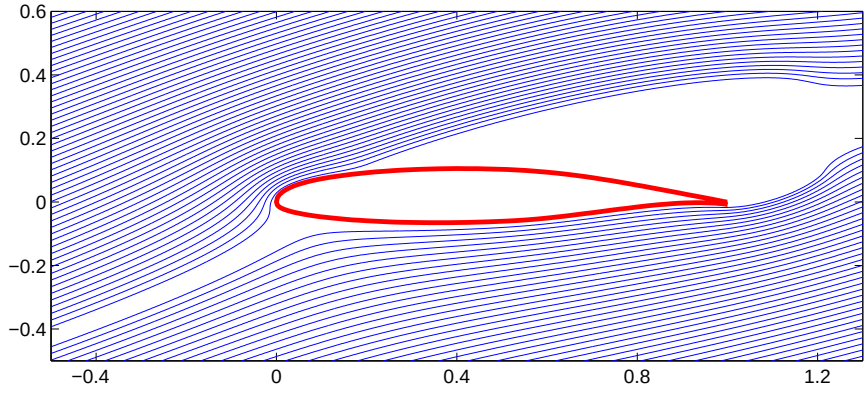

(a)

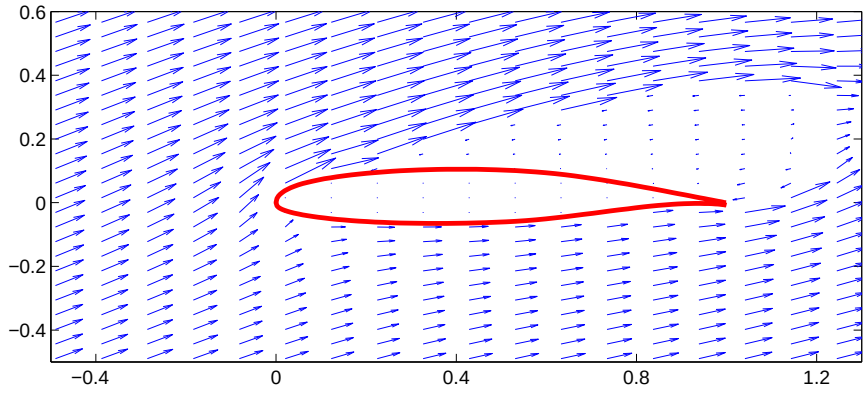

(b)

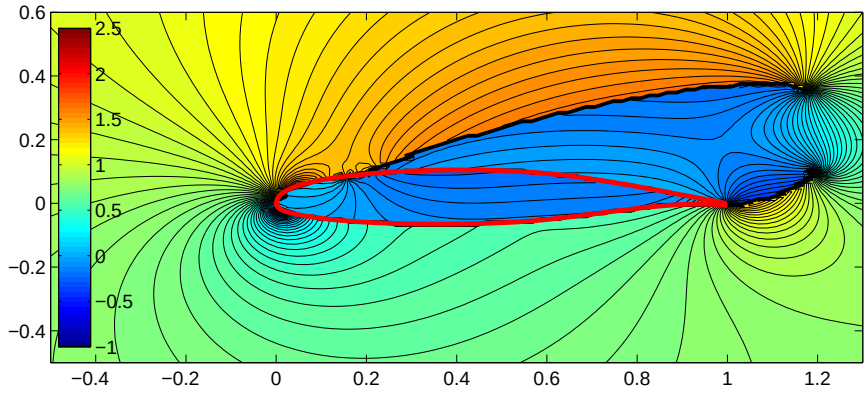

(c)

Figure 5.43: GA(W)-1 $\alpha = 21°$, (a) Streamlines, (b) Velocity flow field ,(c) Potential flow field

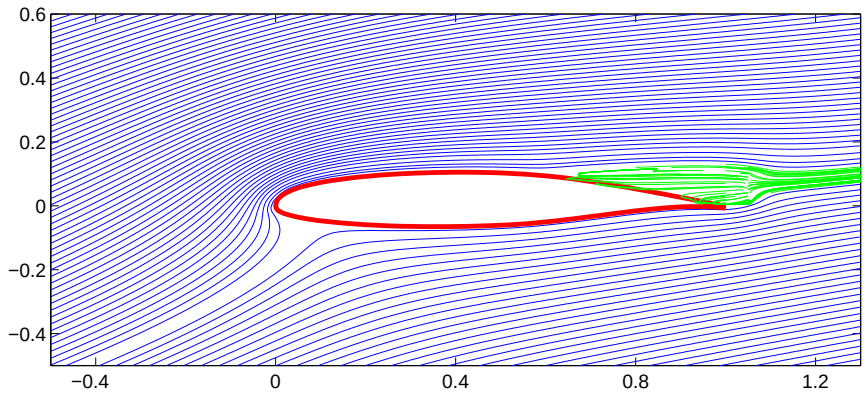

(a)

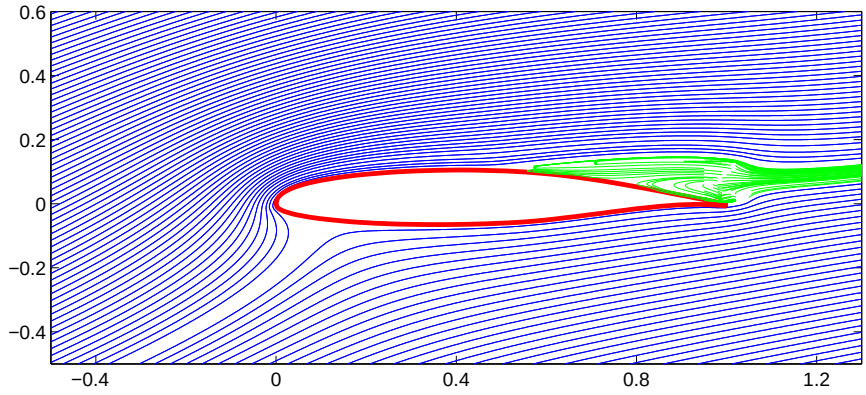

(b)

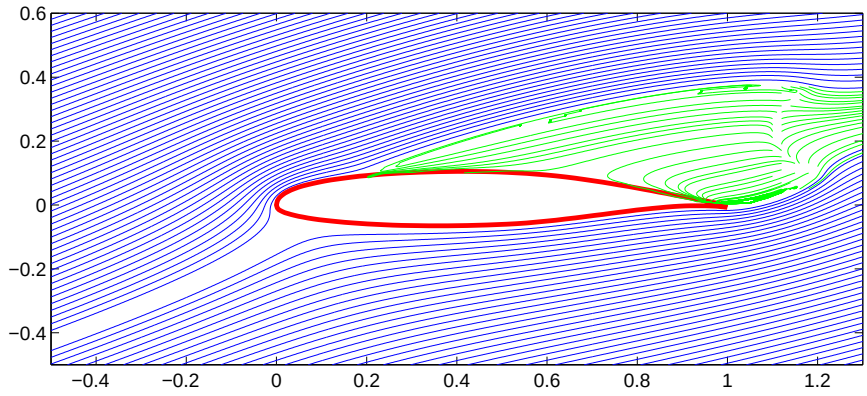

(c)

Figure 5.44: GA(W)-1, Streamlines, (a) $\alpha = 19°$,(b) $\alpha = 20°$,(c) $\alpha = 21°$

Summary of double wake validations

In the present section a validation of the double wake model pressure computations against experimental airfoil pressure data has been presented. An excellent agreement is obtained when the separation location is known in advance.

A linear relation has been found between the chord to thickness ratio and the wake factor, W_F, which relates the wake height to the wake length.

Comparisons have been carried out for different airfoils types, not all presented herein for simplicity. Some comparisons were carried out against CFD computations due to the lack of more experimental pressure distribution data for airfoils at high angles of attack. Concluding that if the separation point is known the agreement is good in all the cases. A linear relation between W_F and chord to thickness ratio was not found in these cases.

Streamlines, velocity vector and potential flow fields have been computed in a Cartesian mesh generated around the airfoil. The influence of the double wake model in the fluid flow that surrounds the airfoil has been analyzed.

Future work has to be done in order to accurately find the separation position in a semi empirical way or using the boundary layer equations.

5.5 Unsteady airfoil computations

Dynamic stall conditions affects actively the aerodynamic performance of the wind turbine rotors. Pitch regulated machines will operate under stall depending on the wind conditions while stall regulated and active stall machines will always operate under dynamic stall conditions. Dynamic stall in a wind turbine blade can be induced by: rotor yaw, blade control dynamics, flow control devices or changes in inflow conditions due to the turbulent nature of the atmospheric boundary layer. Most of these unsteady variations in flow characteristics are seen from the blade as a temporal change of angle of attack. Hence accurate predictions of the blade dynamic loads are of great importance in order to design new wind turbines blades with lower cost and better performance.

To validate the unsteady version of the viscous inviscid interactive model under dynamic performance, including dynamic stall conditions, comparisons of the predicted aerodynamic coefficients C_L, C_D and C_M, are carried out and compared to wind tunnel experiments. Simulations are performed by keeping the airfoil at a fixed position, obtaining the change of the angle of attack according to variations of the freestream flow direction as function of time. Different values of the mean angle of attack around which the airfoil oscillates, α_m, various amplitudes of oscillation, A, as well as reduced frequencies are chosen in order to cover dynamic airfoil performance under a wide span of inflow conditions. Computations are run until a stable solution is reached, usually within no more than a couple of complete loops. In order to force an early turbulent boundary layer, in all the cases the laminar to turbulent transition is forced at $0.05c$ from the leading edge. A modified e^9 method is used when the transition point moves upstream the boundary layer trip position. The simplified single wake model is used in all the computations.

As a first validation test case the NACA 0012 profile is chosen, the profile is subjected to an harmonic pithc oscillation around $\alpha_m = 4°$, with amplitude, $A = 6$, and reduced frequency, $k_A = 0.021$, see Equation 5.1.

$$k_A = \frac{\pi\, f_A\, c}{U_\infty} \tag{5.1}$$

In Figure 5.45, the experimental lift coefficient for static case and oscillating airfoil carried out by Krzysiak and Narkiewicz are compared against predictions of the VI code and static measurements carried out at the Sandia National Laboratories. The static experiments from Sandia Labs were carried out in the Memorial Wind Tunnel at Wichita State University [63]. Krzysiak and Narkiewicz experiments were carried out at the Institute of Aviation wind tunnel in Poland [53]. A counterclockwise loop is formed due to the attached nature of the boundary layer, unsteady terms on the boundary layer equations together with the influence of the unsteady vortex wake induce the hysteresis effects. These effects grow with the frequency of the oscillating movement, at higher k_A differences in lift between upstroke and downstroke motion are larger.

Krzysiak static experiments presented a lower lift in the vicinity of $\alpha = 10°$ if compared with Sandia Labs measurements. The same difference can

be appreciated comparing Krzysiak dynamic lift measurements against the VI code dynamic lift predictions. This effect, could probably be related with their experimental setup. Sandia Labs steady lift data falls inside the dynamic lift curve predicted by the VI code.

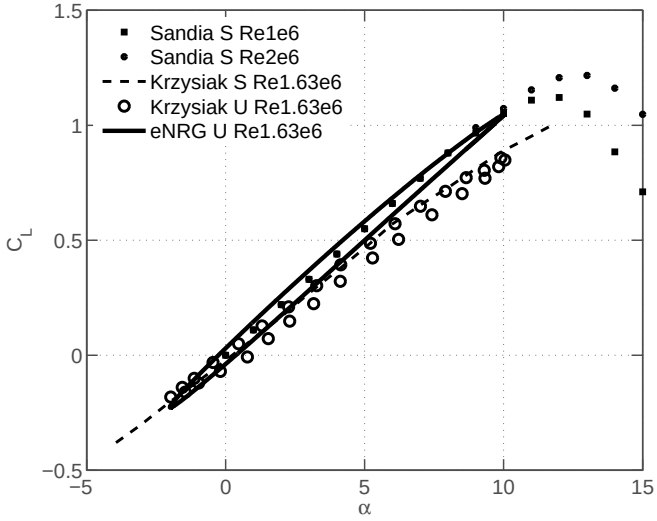

Figure 5.45: Comparison between computed and measured dynamic/static lift data. NACA 0012 airfoil, $\alpha_m = 4°$, $A = 6°$, $k_A = 0.021$.

In regarding drag predictions, Figure 5.46(a), differences in drag between the upward stroke and the downward stroke movement increase with the angle of attack. Drag measurements are not available.

The pitching moment coefficient during the unsteady motion of the airfoil indicates the energy transfer between the airfoil and its surrounding fluid. Integrating the area bound by the pitching moment curve the net energy transferred to the fluid is obtained for each cycle of the airfoil harmonic motion. Experimental pitch moment data is not available for the present case.

As second study case, the NACA 0015 airfoil was chosen. Experiments reported by Galbraith performed at the University of Glasgow are used for validation of the unsteady version of the VI code, [64]. A qualitative comparison of the VI model capability to predict unsteady forces is done against Sørensen and Nygreen vorticity formulated Navier-Stokes solver running a Spallart-Allmaras turbulence model, [65].

The NACA 0015 profile follows in this case an harmonic pitch motion with mean angle of attack, $\alpha_m = 11°$, amplitude of oscillation, $A = 4°$, and reduced frequency, $k_A = 0.1$. Two clearly differentiated hysteresis loops can be observed in both predicted and experimental lift curves, Figure 5.47.

The first loop appears at lower angles of attack and is characteristic of attached boundary layer flows, following a counterclockwise sense. The second loop is formed from 8.5 to 15 degrees of angle of attack and it follows a clockwise direction. The unsteady terms of the boundary layer equations together

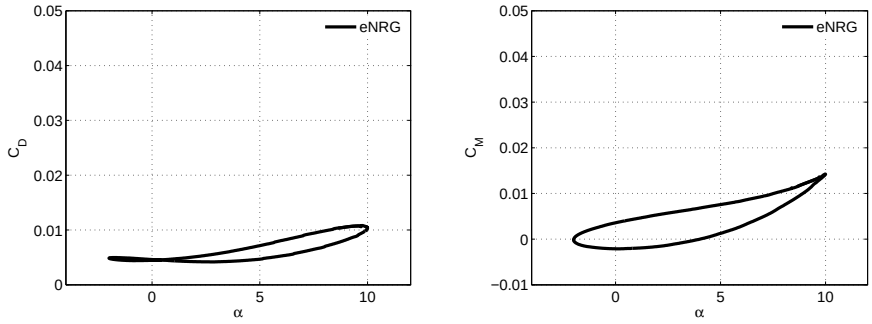

Figure 5.46: Dynamic drag force and pitch moment coefficients. NACA 0012 airfoil, $\alpha_m = 4^\circ$, $A = 6^\circ$, $k_A = 0.021$.

with the vortex wake influence retards the appearance of separation during the upstroke movement of the airfoil if compared with static simulations. During the upward stroke the separation point moves from the trailing edge upstream, while during the downwards stroke the separation position will move in the opposite direction. The downstream movement of the separation point during the downstroke pitching is slower than its upstream movement during upstroke. The difference in the location of separation appears as lift variation between both motions.

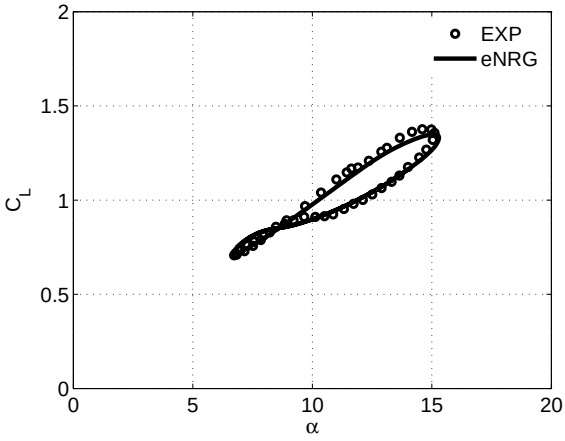

Figure 5.47: Comparison between computed and measured dynamic lift data. NACA 0015 airfoil, $\alpha_m = 11^\circ$, $A = 4^\circ$ and $k_A = 0.1$ at Reynolds $2\,10^6$

Computed C_M values agree qualitatively well in comparison with the measurements, being positive for the whole harmonic motion, Figure 5.48(b). C_D values are underpredicted at angles of attack between 10 to 15 degrees, Figure 5.48(a).

The same airfoil profile, NACA 0015 has also been tested at higher incidence angles. In this case the mean angle of attack is $\alpha_m = 11.37^\circ$, with an oscillation

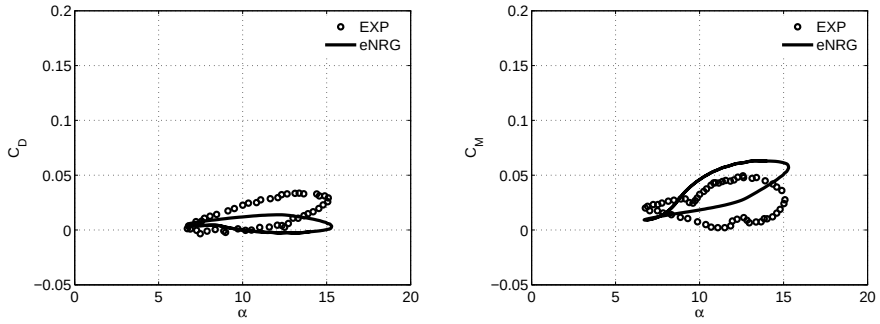

Figure 5.48: Dynamic drag force and pitch moment coefficients. NACA 0015 airfoil, $\alpha_m = 11^\circ$, $A = 4^\circ$ and $k_A = 0.1$ at Reynolds $2\,10^6$

amplitude, $A = 7.55^\circ$ and a reduced frequency: $k_A = 0.102$. Computed values of normal and tangential forces and pitch moment coefficients are compared against measurements from the already introduced experiments performed at the University of Glasgow wind tunnel [64].

From Figure 5.49, predictions of dynamic forces around the airfoil are in good agreement with measurements. The hysteresis loop shape around $\alpha_{(C_N = C_{N_{MAX}})}$ is better predicted by the Navier-Stokes model. Experiments show how the flow fully reattaches to the airfoil surface around $\alpha = 3^\circ$ during the downstroke movement, creating a counter clockwise hysteresis lift loop. VI model predictions capture the counterclockwise loop at low angles of attack while the Navier-Stokes simulations does not.

In terms of C_M, VI and EllipSys2D are in good agreement at angles of attack smaller than 15°, although differ from measurements at $\alpha > 15^\circ$. Positive pitching moment values during the upstroke movement evidence that the airfoil motion is against the aerodynamic moment induced by the surrounding fluid. During downstroke, positive C_M values state that the aerodynamic movement is favorable to the airfoil motion whereas negative C_M state that the aerodynamic movement is against the airfoil motion.

The hysteresis effects have a favorable influence in the surface pressure gradient during upstroke, retarding separation and consequently stall. During the downstroke motion they act destabilizing the boundary layer and therefore making more difficult its reattachment. The different location of the onset of separation predicted during upstroke and downstroke motions for the same angle of attack can be observed from Figures 5.50. The largest difference between the separation location during upstroke and downstroke movements is obtained at $\alpha = 11^\circ$. At this angle of attack, during the nose up movement around a 10% of airfoil chord is under separated flow. However during the nose down motion the separated region expanded over a 50% of the chord, Figures 5.50(c) and 5.50(d).

In order to cover a wider span of airfoil profiles the asymmetric NACA 63421 is chosen as airfoil section commonly used in the wind energy industry. Experiments were carried out in the test section of the S4 wind tunnel located at

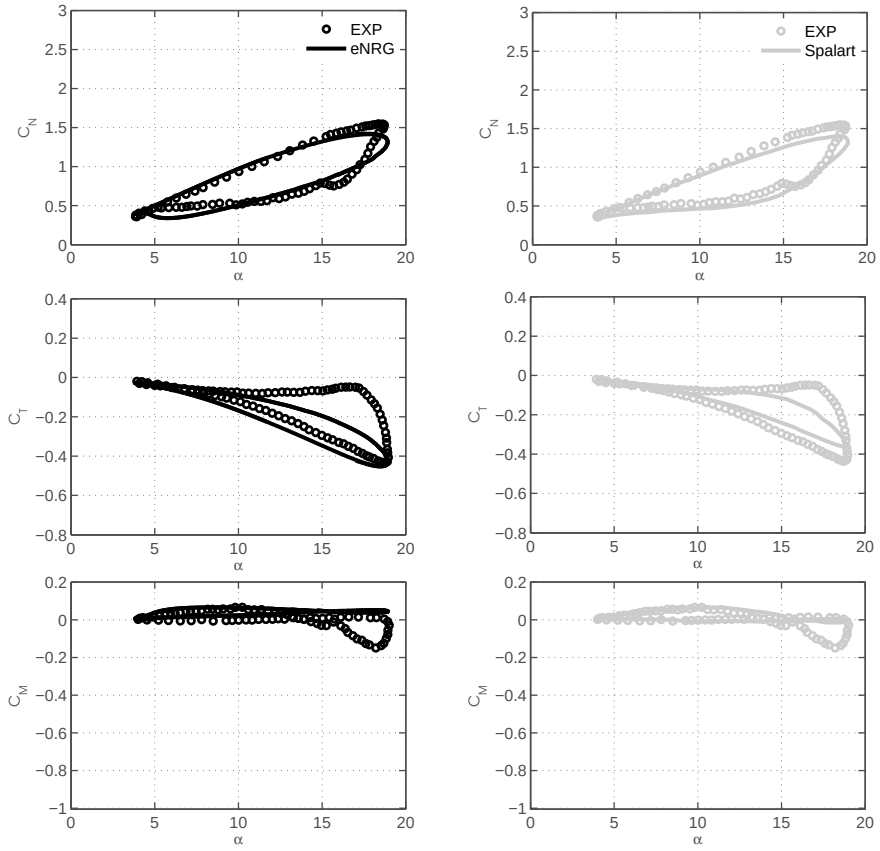

Figure 5.49: Comparison of CFD computations, experiments and viscous-inviscid interactive solver of the normal, tangential forces and pitching moment coefficients for a NACA 0015 airfoil, $\alpha_m = 11.37°$, $A = 7.55°$ and $k_A = 0.102$ at Reynolds $1.5\,10^6$.

the Institut AéroTechnique, Saint Cyr, France and reported by Amandolése [66]. Amanadolése experiments for static lift at Reynolds number 1.10^6 are in good agreement with the ones reported in the book by Abbott and von Doenhoff [55] at a higher Reynolds number, 3.10^6, see Figure 5.51. As Amandolése reported on his paper, the difference could be due to the turbulence level inherent to the wind tunnel. As the turbulence intensity increases the boundary layer becomes more resistant to separation, obtaining higher values of lift at smaller Reynolds number. The experiment realized at Reynolds $3\,10^6$ reported by Abbott was performed in a low turbulence wind tunnel, $TI < 1\%$, while the one reported by Amandolese was performed with $TI = 1.1\%$. Experiments carried out by Amandolese are compared herein against VI computations at Reynolds 3.10^6 with a boundary layer tripped at 5% of the chord from the leading edge.

Figure 5.51 shows the lift coefficient as a function of α for the airfoil pitching with amplitude $A = 8°$ around three different mean angles of attack $8°, 12°, 16°$ with a reduced frequency $k_A = 0.0785$. In the figure, for clarity, the C_L values

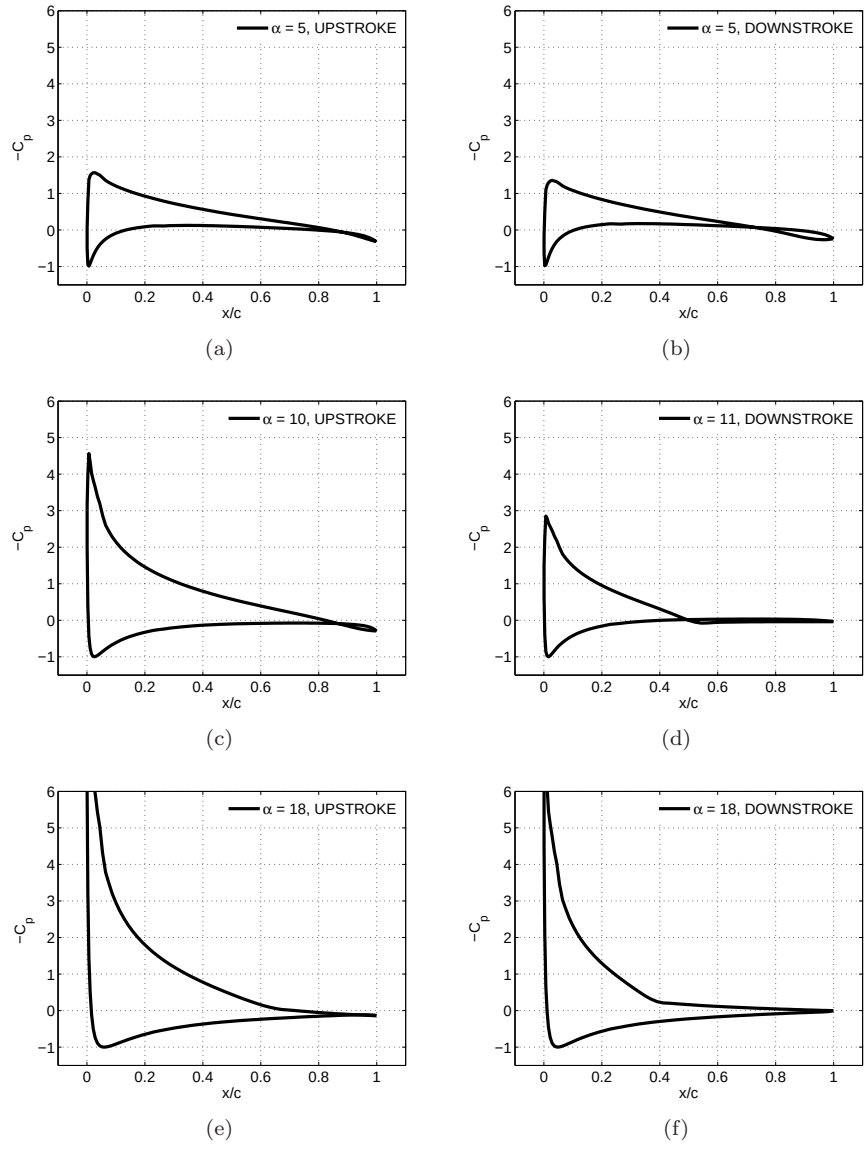

Figure 5.50: VI interactive model predicted upstroke and downstroke surface pressure distribution coefficient during an harmonic pitch motion of a NACA 0015, $\alpha_m = 11.37°$, $A = 7.55°$, $k_A = 0.102$. Reynolds $1.5\,10^6$.

have been moved 15° towards the positive α direction for the $\alpha_m = 12°$ case and 30° for the $\alpha_m = 16°$ case. As the mean angle increases, the counterclockwise hysteresis loop, characteristic of low angles of attack, is reduced, disappearing completely for the case with $\alpha_m = 16°$. In this case the flow is separated during the whole airfoil motion, forming a unique clockwise loop. Although the viscous-inviscid computations have the right tendency in all the cases, predicted lift variations between upstroke and downstroke movements are smaller than measured ones.

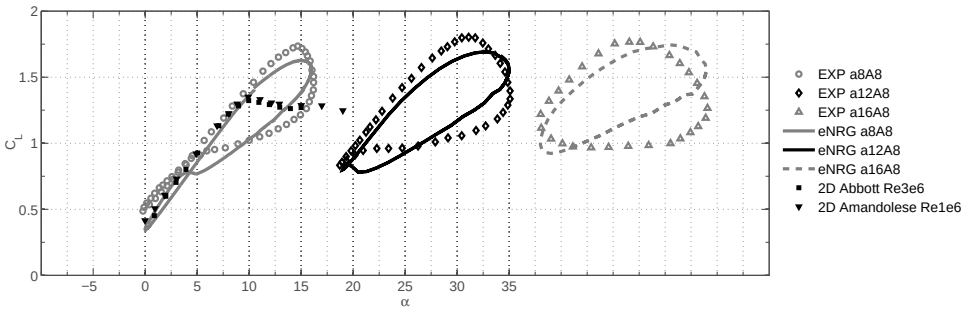

Figure 5.51: Comparison between computed and measured dynamic lift for a NACA 63421 airfoil, $\alpha_m = 8°$, $\alpha_m = 12°$ and $\alpha_m = 16°$. $A = 8°$, $k_A = 0.0785$, Reynolds 3.10^6.

The maximum lift and its angle of attack are chosen for a more quantitative study of the dynamic effects on the lift curve. In all the cases presented in Figure 5.51 an overshoot of the maximum lift coefficient is predicted if compared with the static case. Defining it as follows,

$$OVR = \frac{max\left(C_L^{Dynamic}\right) - max\left(C_L^{Static}\right)}{max\left(C_L^{Static}\right)} \cdot 100 \tag{5.2}$$

For the predicted dynamic lift curve with a mean incidence angle of 8° the overshoot is 18.67%, for $\alpha_m = 12°$ is 25.17% and for $\alpha_m = 16°$ is 28.07%. While the OVR values calculated from Amandoleses experiment were 28.52%, 33.48% and 30.81%. Consequently an underprediction of the dynamic overshoot is obtained with the VI interactive solver. In regarding the position of $C_{L_{MAX}}$, a good agreement between experiments and computations is obtained for $\alpha_m = 8°$. In the other two cases, $\alpha_m = 12°$ and $\alpha_m = 16°$, the viscous-inviscid computations predicted the maximum lift at a higher angle of attack.

In Figure 5.52(a) dynamic drag force coefficients for the different mean angles of attack computations are presented. At low angles of attack drag differences between both motions are not so important. As α increases, drag differences between the upstream and downstream motions increase considerably. No experimental drag data was available for comparison.

C_M predictions are compared against measurements, Figure 5.52(b), in this case the agreement is poor. Among others, difficulties arise in order to predict the lower side of the loop. Experiments show the existence of a unique closed loop while VI computations predicted three different loops.

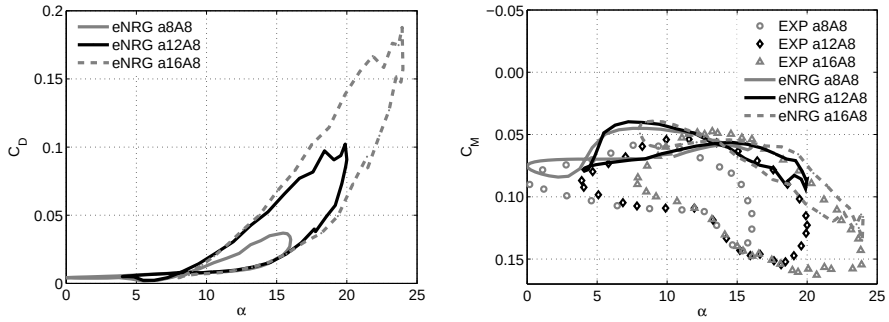

(a) (b)

Figure 5.52: Dynamic drag and pitch moment coefficients for a NACA 63421 airfoil, $\alpha_m = 8°$, $\alpha_m = 12°$ and $\alpha_m = 16°$, $A = 8°$ $k_A = 0.0785$, Reynolds 3.10^6.

Summary of unsteady airfoil computations

The validation of the unsteady version of the viscous-inviscid interactive boundary layer code against experiments has been presented in this section.

Good predictions of the dynamic lift are obtained in most of the cases although drag and pitching moment coefficient predictions does not compare so good with experiments. Computations at different reduced frequencies, amplitudes of oscillation as well as Reynolds number have been presented, verifying the capability of the VI interactive solver to compute different unsteady flow conditions.

In terms of lift, the hysteresis loop formation has been analyzed. Two loops with opposite directions are formed in function of the flow nature around the airfoil. When separated flow is present in the suction surface of the airfoil, the hysteresis loop follows a clockwise direction, obtaining a higher lift during upstroke and lower during downstroke. When the flow is fully attached to the surface, the hysteresis loop has a counterclockwise direction. The shape of the hysteresis loops varies with the amplitude and the reduced frequency of the motion.

5.6 Unsteady airfoil computations with trailing edge flap

5.6.1 Validation against wind tunnel experiments

The unsteady aerodynamic loads on a NACA0012 airfoil with a moving trailing edge flap are computed using the unsteady version of the viscous-inviscid interactive solver and are validated against measurements carried out by Krzysiak and Narkiewicz in the trisonic N-3 wind tunnel located at the Institute of Aviation Warsaw, Poland [53]. The validation is focused on the aerodynamic effect in C_L and C_M of the shift angle between the harmonic motion of the airfoil and flap.

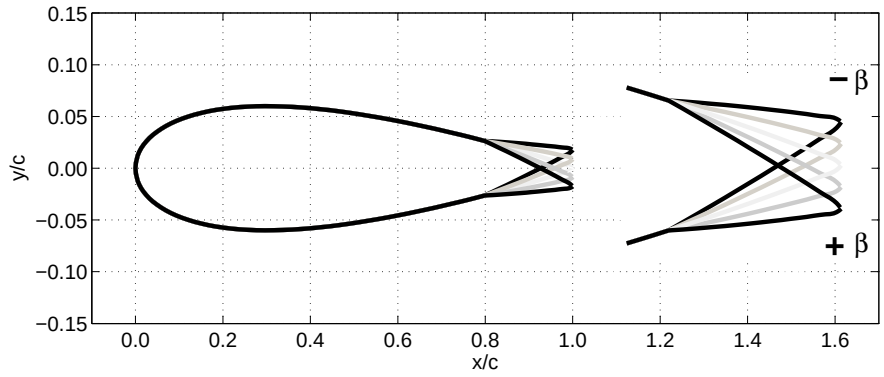

Figure 5.53: NACA 0012 geometry with a 20% of the chord plain trailing edge flap

The Reynolds number is fixed at $1.63\,10^6$ in both experiments and computations. A rigid trailing edge flap is implemented with a length 20% of the airfoil chord, Figure 5.53. In the experimental setup there was a small gap between the flap and the airfoil while in the numerical model the gap has been obvied. The reduced frequency of the airfoil harmonic motion is $k_A = 0.021$, while the flap oscillation doubled this frequency, $k_F = 0.042$.

The viscous-inviscid integral boundary layer solver is used in its unsteady version with the simplified single wake vortex model. The time step used in all the cases presented herein is $dt = 0.2$. Suction side turbulent transition is forced at $0.05c$ from the leading edge.

Comparisons against experiments for the current airfoil performing an harmonic pitch motion without flap are presented and discussed in the former Section 5.5. In all the VI simulations, due to errors in prescribing accurately the motion of the model during experiments, the values of the phase shift and flap amplitude reported by Krzysiak had to be adjusted for the best fitting of the measured airfoil-flap relative motion. These values of the airfoil/flap relative motion are used as input in the VI simulations. It is probable that the lack of accuracy of the computations is partially due to differences in the airfoil/flap motion between experiments and simulations and not to the computations itself.

The equation that governs the airfoil angle of attack can be written as follows,

$$\alpha = \alpha_m + \Delta\alpha \; sin\left(2\, k_A\, t\right)); \tag{5.3}$$

The flap deflection follows,

$$\beta = \beta_m + \Delta\beta \; sin\left(2\, k_F\, t - \varphi\right); \tag{5.4}$$

α_m and β_m are the mean values of the angle of attack and flap deflection around which the airfoil and flap oscillating motions are performed. $\Delta\alpha$ and $\Delta\beta$ are the amplitudes of the airfoil and flap harmonic movement respectively.

φ is the phase shift between the airfoil and the flap. In the case that $\varphi = 2\pi$ there is not delay between airfoil and flap motions.

In all the cases presented herein the flap reduced frequency is twice the airfoil reduced frequency. The airfoil / flap system presents four different relative movements. These relative motions are sketched in the following Figure 5.54,

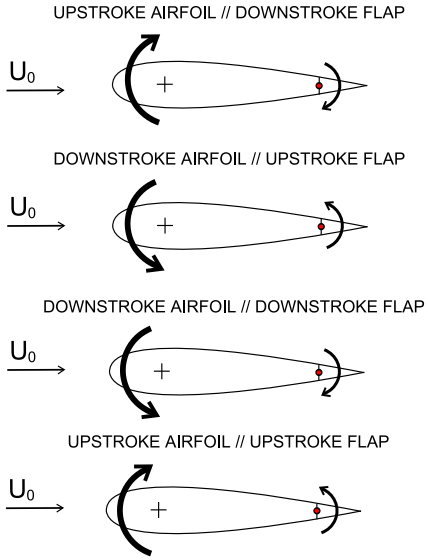

Figure 5.54: Airfoil respect to flap relative motions

As a first study case, the phase shift $\varphi = 148°$ is chosen. The phase shift used in computations is modified to $\varphi = 135°$ in order to fit the measured airfoil / flap relative motion. In Figure 5.55 a comparison between experiment measured and simulations values of the β and α angles is presented. Predictions of the lift force and pitch moment coefficients are also compared against measurements.

In terms of lift, a good agreement is obtained at intermediate angles of attack although around the maximum incidence angle, $\alpha = 10°$, the computed lift is slightly over predicted. In the upper figure it is possible to distinguish a difference between experimental and computational values of the β/α relation at angles of attack after position 1, following the loop direction. In this region, the flap deflection during experiments is more upwards in comparison with the input used in simulations, reducing the profile lift. This can be one of the possible explanations of the lift overprediction. Already discussed in Section 5.5 is the low lift value measured in experiments around 10 degrees, this could be the second cause for the lack of agreement at high angles of attack. The loop intersection region is predicted with a high accuracy in this case.

In terms of pitching moment coefficient, which is always more difficult to predict than the lift, predictions follows similar tendencies as measured values. From Figure 5.55 negative flap deflections are related to higher positive values of the pitch moment and vice versa. In an upstroke pitch movement of the airfoil, the flap undergoes both upstroke and downstroke motions, see Figure 5.54. The flap performs the same motions during the airfoils downstroke. Analyzing

separately each of the relative motions: From position 1 to 2, the airfoil is under upstroke movement and the flap is moving downwards. The flap influence is acting against the airfoil aerodynamic movement, counterclockwise direction, hence decreasing C_M. From position 2 to 3, the airfoil is moving downwards at the same time that the flap moves upwards. The flap effect is opposite to the airfoil motion, clockwise direction, C_M is increased. From position 3 to 4, both the airfoil and flap are in downstroke. The flap effect is favorable to the aerodynamic motion of the airfoil, in the counterclockwise direction, reducing C_M. From position 4 to 1, both the airfoil and flap are in upstroke, the flap influence is favorable to the motion of the airfoil, clockwise direction, increasing C_M. The net amount of energy transfered from and to the fluid can be obtained integrating the C_M curve.

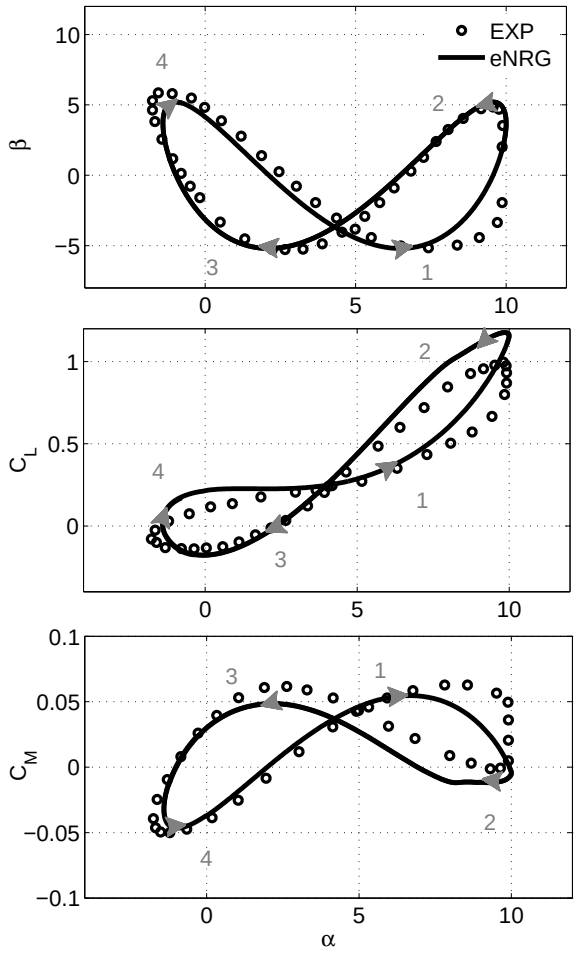

Figure 5.55: Unsteady experiments against viscous-inviscid unsteady solver, $\varphi = 148°$. Experiments (*circles*), VI computations (*solid lines*) .

In the next study case, Figure 5.56, the phase shift reported by Krzysiak is

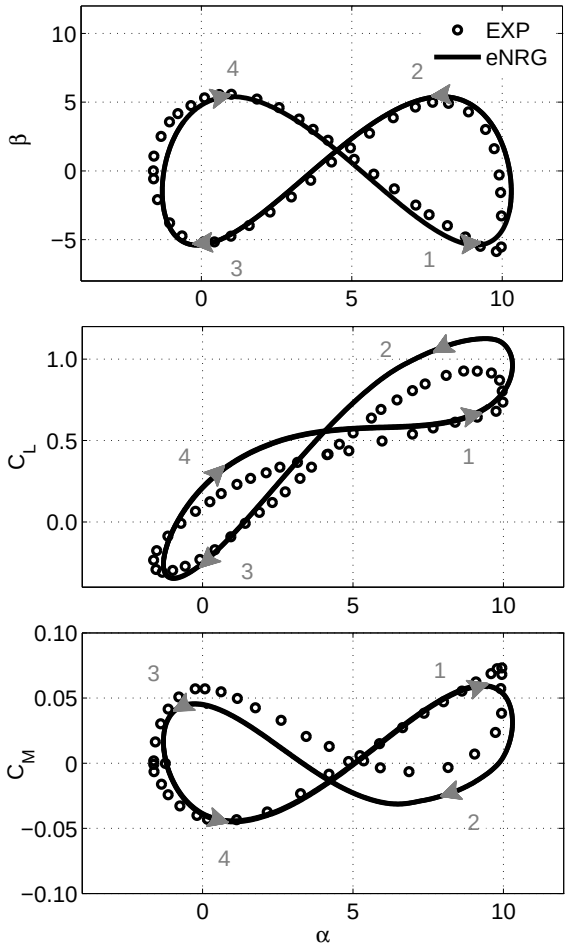

Figure 5.56: Unsteady experiments against viscous-inviscid unsteady solver, $\varphi = 206°$. Experiments (*circles*), VI computations (*solid lines*).

$\varphi = 206°$ while the one used as input for the VI simulations is $\varphi = 196°$. The overall lift predictions are in good agreement with experiments. Although a lift over prediction is obtained during the downstroke motion of the airfoil, between stations 2 and 3. The overprediction of lift at $\alpha_{C_{L_{MAX}}}$ influences the prediction of a higher lift during the airfoils downstroke motion between stations 2 and 3. The unsteady terms of the θ momentum and kinetic energy shape parameter equations act as a boundary layer memory, forcing in this case the lift to remain at a high value.

The predicted pitch moment coefficient is also in good agreement with measured data, although slightly underpredicted during the downward stroke. Again, the most negative deflections of the flap are related with maximum positive values in the pitching moment curve, positions 1 and 3. While the highest positive deflections of the flap are related with the minimum C_M values.

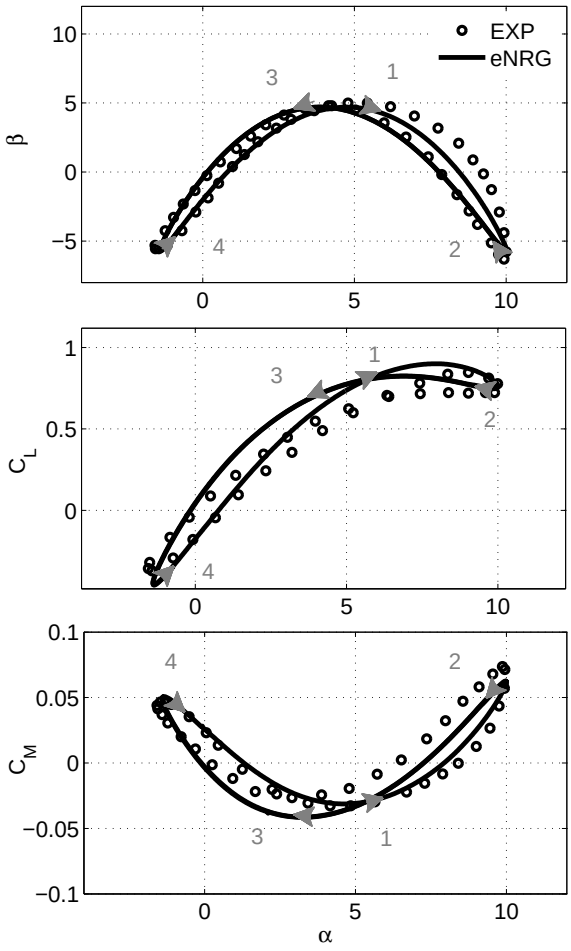

Figure 5.57: Unsteady experiments against viscous-inviscid unsteady solver, $\varphi = 298°$. Experiments (*circles*), VI computations (*solid lines*).

As a third study case the simulations shift angle is set to $\varphi = 280°$ while the experiments reported a $\varphi = 298°$. An excellent agreement is obtained in this case between predicted and experimental lift values. Although the lift is slightly over predicted around $\alpha = 5°$ where the loop intersection takes place. A better agreement than for the first two cases is obtained around the maximum lift. The VI interactive code predicts better slow changes in the α/β relation.

The pitching moment coefficient is predicted with a good accuracy by the VI interactive code. The area enclosed by the pitch moment curve is smaller in this case than in previous cases. This indicates that the net energy transfered to the fluid in a cycle with the shift angle $\varphi = 280°$ is lower than with $\varphi = 135°$ and $\varphi = 196°$.

No measured data of the β and α angles, neither pitch moment coefficient values are available for the next case, Figure 5.58. Although it is of great interest

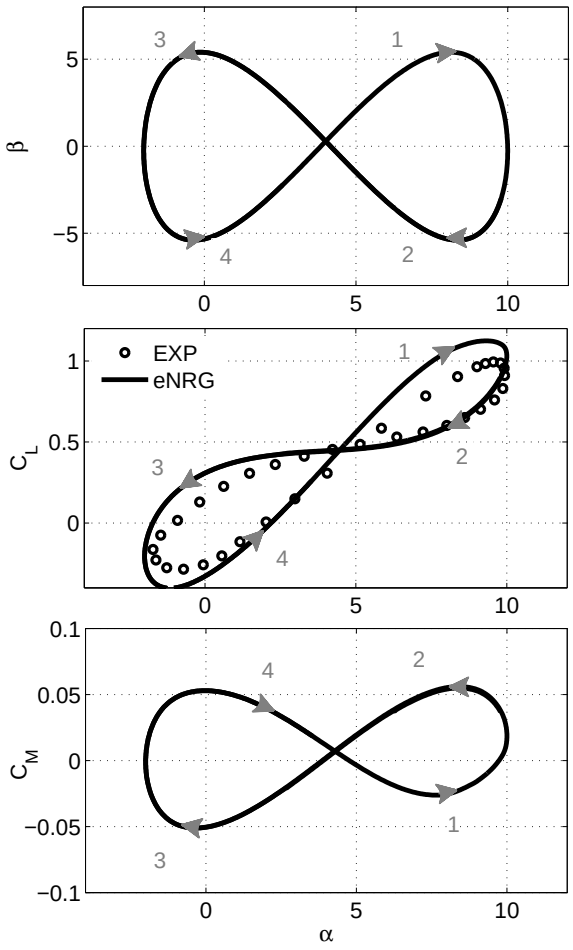

Figure 5.58: Unsteady experiments against viscous-inviscid unsteady solver, $\varphi = 357°$. Experiments (*circles*), VI computations (*solid lines*).

to see how the lift coefficient behaves when there is almost no phase lag between the airfoil and the flap motions, $\varphi = 357°$. As in most of the study cases shown in the present section, $C_{L_{MAX}}$ is in overall overpredicted in its absolute value, although the tendencies are well captured. Predicted lift during downstroke is in this case in good agreement with measurements, although small differences appear around station 3.

In terms of C_M, the area covered by the curve is larger than previous cases, implying that in the case that $k_F = 2k_A$ the net energy exchanged with the fluid is larger when there is no phase delay between airfoil and flap motions. The larger is the difference in the flap position between the upstroke and downstroke movements of the airfoil the larger is the net energy transfered from and to the fluid if a constant angular velocity is assumed.

In the last study case, the capability of the code to simulate dynamic deep

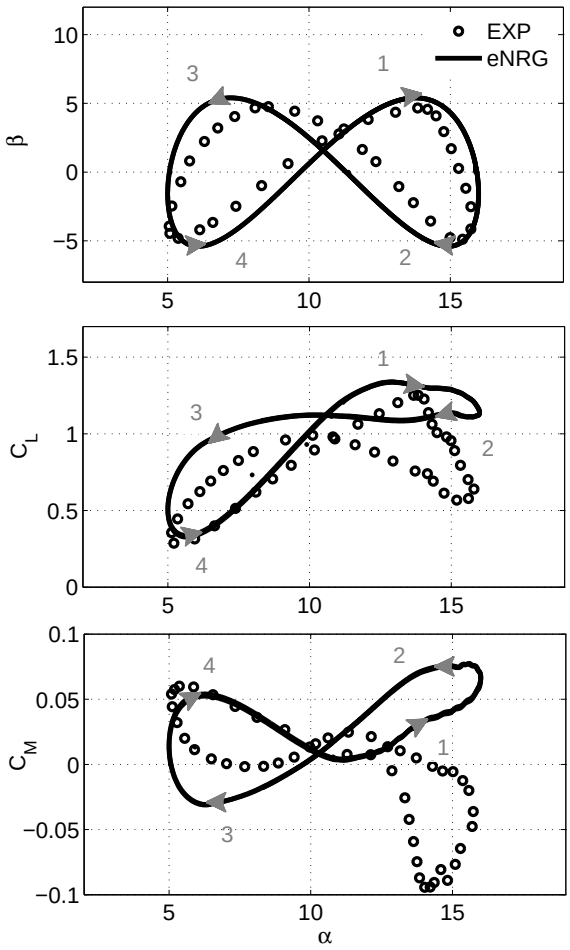

Figure 5.59: Unsteady experiments against viscous-inviscid unsteady solver, $\varphi = 343°$. Experiments (*circles*), VI computations (*solid lines*).

stall conditions influenced by a moving trailing edge flap is exposed, Figure 5.59. Simulations and experiments have the same phase shift, $\varphi = 343°$. Simulations predicted a lighter stall than experiments between stations 1 and 2. Negative flap deflections induced lower pressure gradients in the suction side of the airfoil, keeping the external streamlines closer to the airfoil surface, and therefore retarding slightly separation. The lift force is clearly over predicted during the downwards motion of the profile.

In terms of pitch moment coefficient, an important disagreement between measured and computed values is obtained from 10° to 16°, in both the upstroke and downstroke movements of the airfoil, the predicted pitch moment had opposite sign than the measured one.

5.6.2 Damping inflow disturbances created by the iWings system

In order to validate the computer tools developed in the framework of the ATEF project, a set of experiments will be carried out at DTUs red wind tunnel in the near future. The experiments will involve a pair of oscillating wings situated on the wind tunnel inlet. Such a wings will be referred from now on as iWings. The iWings oscillation creates a disturbance on the flow seen by the main airfoil, which is located a couple of chords downstream. A controlled trailing edge flap is used in order to reduce the lift variations on the main wing induced by iWings flow disturbances. The experiments performed at DTUs red wind tunnel will measure the aerodynamic characteristics of a specific airfoil section under different flow conditions: Reynolds number, angle of attack, pitching reduced frequency, iWings pitching frequency and amplitude. The wind tunnel setup has been simulated with the VI interactive solver in order to probe the capability of the trailing edge flap to reduce flow disturbances and the ability of the VI code to simulate it. Computations will give a valuable knowledge useful for the planning of future experiments.

Wind tunnel walls are modeled using panels with constant source distribution. Each side of the wall is modeled with fifty panels. A coarse distribution is implemented far away from the airfoil, refining the surface tunnel mesh in its vicinity. An inverse hyperbolic tangent function is used in order to generate the wind tunnel panels distribution. The upper and lower tunnel walls have the same panel distribution, obtained as follows,

$$x_T = \frac{\arctan\left(x_{Tc}/r_{WT}\right)}{max\left(\arctan\left(x_{Tc}/r_{WT}\right)\right)} \frac{x_{OUT} - x_{IN}}{2} \tag{5.5}$$

where x_T is the position of the panels edges with the arctan distribution, x_{Tc} are the edges positions if panels with constant length are assumed, r_{WT} is the panel reduction factor of the surface mesh and is set to $r_{WT} = 1.15$, x_{OUT} and x_{in} are respectively the x coordinates of the wind tunnel inlet and outlet.

The iWings are represented by two static point vortex shedding vorticity downstream of them in form of trailing edge vortex wakes. The steady C_L curve of a NACA 0015 at Reynolds 5.10^5 is used for obtaining the correct strength of the shed vortices via Kutta-Joukowski theorem,

$$L = \rho\, U_\infty\, \Gamma \rightarrow \Gamma = \frac{1}{2}\, C_L \tag{5.6}$$

$$\Gamma_{wiW} = \Gamma_{SiW}^{t-1} - \Gamma_{SiW}^{t} \tag{5.7}$$

A screenshoot of the computational setup is presented in Figure 5.60. Where the iWings are located at a position $x = -1.2$ and the main airfoil aerodynamic center is located at $x = 0$. The iWings and airfoil downstream convecting vortices are presented in dark and light filled circles respectively.

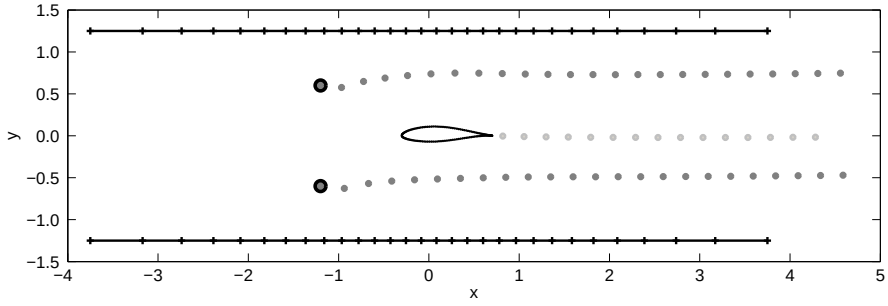

Figure 5.60: Computational Wind Tunnel + iWings setup with downstream convecting vortices. NACA 63418.

The ability of the TEF to minimize iWings induced lift variations on the main wing is presented herein. A PI controller is used in order to maintain the lift at a constant value. Both iWings are set to pitch harmonically with the same motion, creating in this way a disturbance in the main airfoil. The pitching motion of the iWings is governed by the following equation,

$$\chi = \chi_m + \Delta\chi \, sin\left(2 \, k_{iW} \, t\right)) \tag{5.8}$$

Where χ_m is the main iWings angle, $\Delta\chi$ is the amplitude of the motion and k_{iW} is the iWings reduced frequency.

The PI controller computes the necessary flap deflection to maintain a constant lift on the main wing. The following algorithm is used as controller,

$$\beta^t = \beta^{t-1} - k_{PI} \left(C_L^{t-1} - C_L^0\right) \tag{5.9}$$

Where C_L^0 is the reference lift value of the main airfoil, C_L^{t-1} is the value of the lift coefficient on the last time step and k_{PI} is the PI controller constant that relates changes in lift with flap deflections needed to compensate it.

The main airfoil is fixed at 5 degrees of angle of attack, $\alpha_m = 5°$. The iWings are set to pitch harmonically with main angle of attack, $\chi_m = 0°$, amplitude, $\Delta\chi = 8°$ and frequency, $f_{iW} = 1$. The TEF deflection is regulated by the PI controller with constant $k_{PI} = 5$. In the Figure 5.61 lift coefficient variations are shown in function of time step for the iWings pitching. At first the flap deflection is set to zero, turning off the trailing edge PI controller. When $tstep = 3050$ is reached, the PI controller is activated and the flap deflected following Equation 5.9 in order to maintain a constant lift.

Lift variations are reduced drastically due to the effect of the controlled trailing edge flap. Variations in lift are still present, although with a smaller amplitude and higher frequency than the ones created by the inflow perturbations. A better controller, for example a PID, should be used in order to totally reduce lift variations.

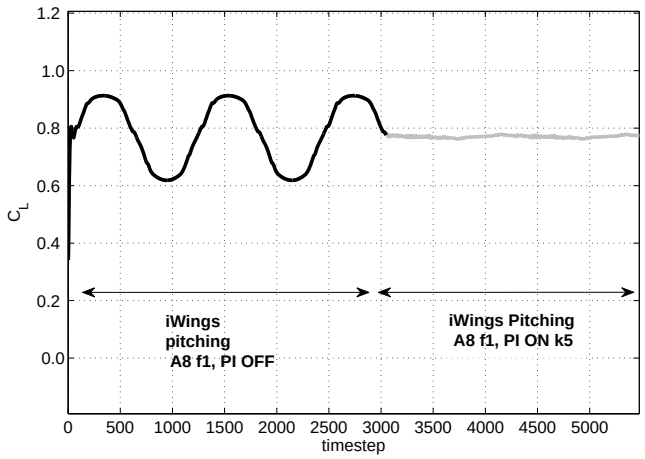

Figure 5.61: iWings with PI controlled TEF. NACA 63418 airfoil, $\alpha = 5°$, iWings $\chi_m = 0°$, $\Delta\chi = 8°$, $f_{iW} = 1$, flap PI $rF = 5$.

Flap deflection in comparison to the iWings angle of incidence is presented in Figure 5.62. Smaller flap deflections are needed to keep constant the C_L value when the iWings are pitching upwards compared with its downwards movement. This difference is related with the appearance of separated flow on the main airfoil suction surface. For a Reynolds number of $1.5\,10^6$ for the main airfoil, separation appears on its rear side at an angle of attack of 9°. At 13° almost a 35% of the airfoil chord is under separated flow. In the present setup, although the airfoil geometric angle is fixed at 5°, the pitching iWings act bending the streamlines seen by the main airfoil, increasing its angle of attack. Forcing in this way the flow to separate on the trailing edge vicinity. The rate of lift increment decreases with the increasing amount of separated flow, hence smaller deflections of the TEF are needed to keep the lift at a constant value. That's why in the case in which the main airfoil is fixed at 0° with the same motion amplitud of the iWings, only small differences appeared between positive and negative values of the PI controlled flap deflections. Such differences are related with the non symmetric airfoil geometry.

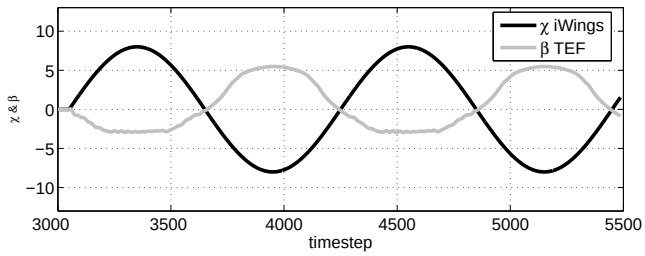

Figure 5.62: iWings pitching with $\chi_m = 0°$, $\Delta\chi = 8°$,$f_{iW} = 1$ and PI controlled flap deflection with constant $rF = 5$

Summary of unsteady computations with TEF

The capability of the unsteady interactive viscous-inviscid boundary layer code to simulate an airfoil at moderate angles of attack with a moving trailing edge flap has been proven. Validations of the VI code predictions have been presented against experiments where the airfoil and flap move harmonically with different phase delays. Disagreements are obtained at angles of attack around $\alpha = 10°$, probably due to the experimental setup. The model accuracy to predict unsteady forces of the airfoil-flap system is in doubt during stall conditions.

The ability of the unsteady VI interactive code for simulating the capability of the TEF to compensate changes in lift produced by inflow variations is proven. Although a better TEF controller should be implemented in order to obtain a total reduction in lift variations. Further analysis of the influence of the iWings amplitude and pitching frequency will be carried out using the VI interactive boundary layer code. In the near future, wind tunnel measurements will be used for the validation of the code.

5.7 Parametric study of the Quasi3D viscous-inviscid method

A parametric study of the influence of a rotational boundary layer in the aerodynamic performance of an airfoil section has been carried out using the Quasi3D viscous-inviscid method and it is presented in this section.

A recapitulation of the adimensional variables used in the present study is done. The variables of interest are: c, r, Ω, Q_w. In non-dimensional form can be reduced to two model variables: The ratio between the chord length and the radial position, $ls = c/r$ and the ratio between the rotational speed and the relative velocity, $RO = \Omega r/U_{rel}$. Where U_{rel} is function of Ω and Q_w. In this way the four variables of interest are reduced to two adimensional parameters ls and RO, basis of our parametric study.

$$U_{rel} = \sqrt{\left((1 + a')\,\Omega r\right)^2 + \left((1 - a)\,Q_W\right)^2} \tag{5.10}$$

The study presented herein is divided in five subsections. In the first and second, lift and drag curves will be analyzed as a function of the rotational parameters ls and RO for the S809 airfoil at Reynolds number 1.10^6. A third section is dedicated to rotor performance under rotational effects, an artificial rotating blade has been simulated and the effects of rotation are depicted in function of radial position and tip speed ratio. A study of the influence of rotation in the boundary layer characteristics is presented in the fourth subsection. Finalizing this section an order of magnitude study of Coriolis and centrifugal forces in the rotating boundary layer is presented.

5.7.1 Influence of rotation on lift performance of a S809 airfoil

To demonstrate the influence of the rotating effects in an airfoil section, a study of the aerodynamic performance of a S809 airfoil subjected to rotation has been done and it is presented herein. Simulations Reynolds number is 1.10^6. The boundary layer laminar to turbulent transition is forced at $0.05c$ from the leading edge.

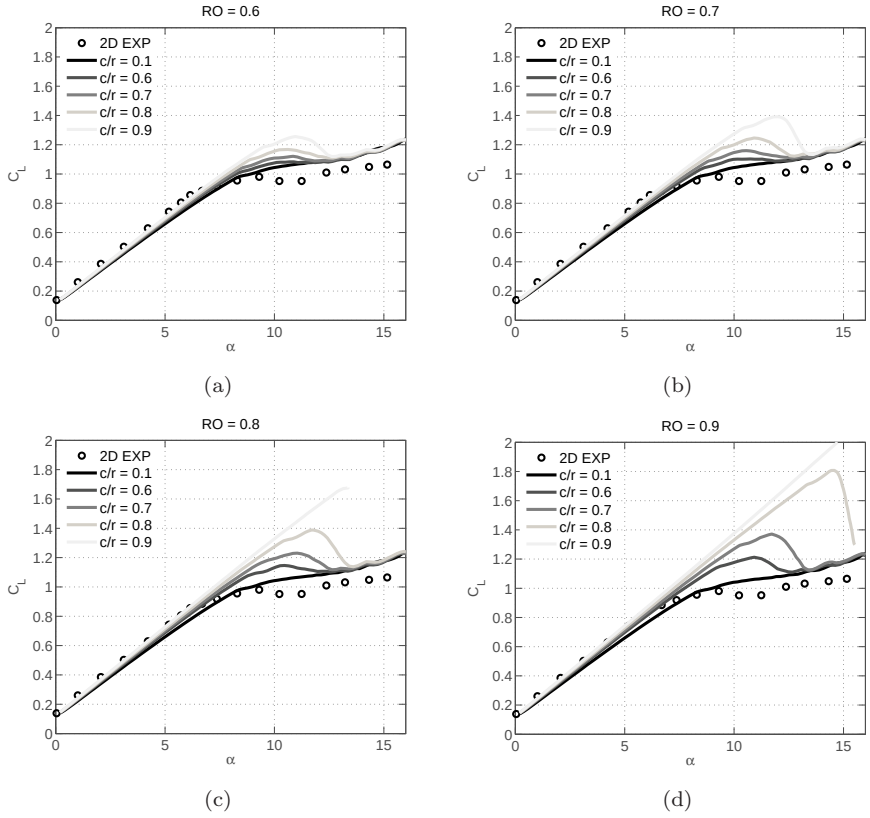

Figure 5.63: Lift curves for RO 0.6, 0.7, 0.8 and 0.9. c/r from 0.1 to 0.9. Reynolds 1.10^6.

In Figures 5.63 lift variations in function of the ratio c/r are shown for four values of the rotational number, RO. Generally as RO increases, maintaining a constant c/r ratio, the lift increases, therefore increasing $C_{L_{MAX}}$. In a similar way, as the ratio c/r increases, maintaining RO constant, $\alpha_{(C_L=C_{L_{MAX}})}$ increases, retarding stall in a similar way. After the maximum lift is reached the airfoil stalls, being the negative lift slope for $\alpha > \alpha_{(C_L=C_{L_{MAX}})}$ steeper for larger c/r ratios. Centrifugal and Coriolis forces create a favorable pressure gradient that thinners the boundary layer and retards separation. At low angles of attack, i.e. attached flow, the rotational forces induce a thinner boundary layer. Since separation is not involved the higher lift obtained is created due to the lower obstruction presented by the thin boundary layer against the freestream

flow. At higher angles of attack a delay in the separation location is predicted due to the favorable pressure gradient generated by rotation, the thinner boundary layer is more difficult to detach from the airfoil surface. A strong radial flow present in the bottom of a separated boundary layer modifies actively the lift characteristics of the airfoil sections. The later separation appears, the faster it moves towards the leading edge after stall is reached, this explains the drastic decrement in lift for $\alpha > \alpha_{(C_L=C_{L_{MAX}})}$. In the cases in which the influence of Coriolis and centrifugal forces is large enough, the flow remains attached to the airfoil surface even at high angles of attack. In these cases lift increases linearly with the angle of incidence avoiding stall, case $RO = 0.9$ & $c/r = 0.9$, Figure 5.63(d). Differences between lift predictions vanish with the reduction of RO, see Figure 5.63(a). For $RO < 0.4$ differences in lift due to rotation effects are inappreciable.

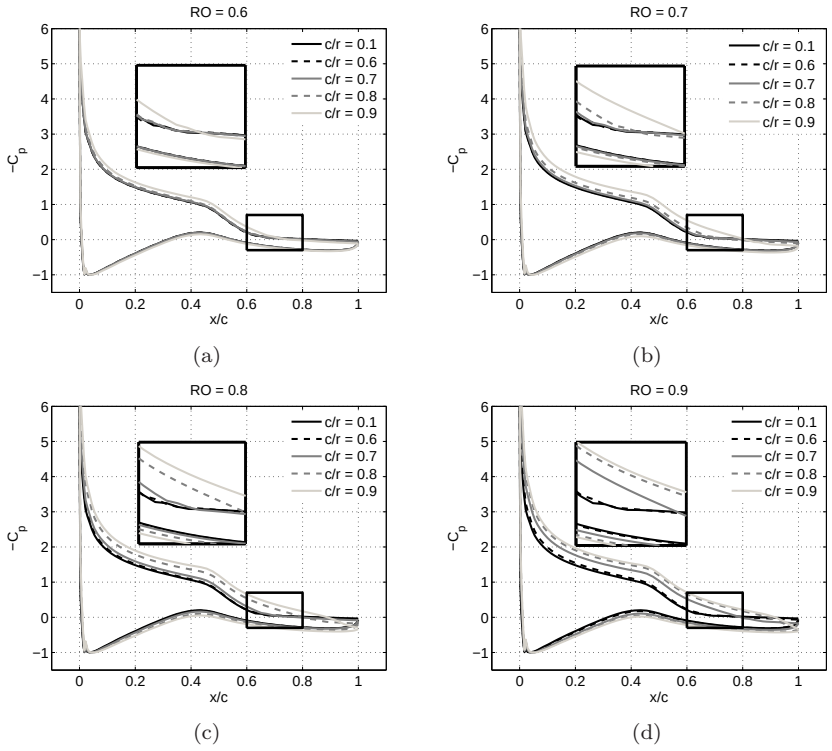

Figure 5.64: Surface pressure distribution for RO 0.6, 0.7, 0.8 and 0.9. c/r from 0.1 to 0.9. Reynolds 1.10^6. Angle of attack, $\alpha = 12°$.

Surface pressure distributions at angle of attack 12° for four different rotational numbers are presented above in Figure 5.64. For the rotational number $RO = 0.6$, Figure 5.64(a), the influence of rotational effects in the pressure distribution is weak although grows with the c/r value. The separation position is slightly delayed and moved towards the trailing edge for the ratio $c/r = 0.9$. Changes in pressure distribution due to rotation are not significant for the lower c/r ratios. As the rotational number increases, $RO = 0.7$, Figure 5.64(b), the separation location moves downstream towards the rear side of the airfoil. A

60% smaller separated area is predicted at $c/r = 0.9$ if compared with the two dimensional flow existent at $c/r = 0.1$. With the further increment in the rotational number, $RO = 0.8$, the separation location moves closer to the trailing edge. See Figure 5.64(c) case $c/r = 0.9$ where a separation bubble is confined to the last 5/10 % of the airfoil chord. For $RO = 0.9$ and $c/r = 0.9$, Figure 5.64(d), the favorable pressure gradients created by Coriolis and centrifugal forces maintain the flow fully attached to the airfoil surface.

Rotation does not only affects the separation location, it affects strongly the whole suction side of the airfoil inducing a favorable pressure gradient and hence decreasing the pressure. The pressure side is not so heavily affected by rotation, although a favorable pressure gradient is also induced which in this case increasing the pressure. In this way a larger pressure difference is created between the upper and the lower surfaces, obtaining a larger loading of the airfoil.

5.7.2 Study of rotation influence on drag performance of a S809 airfoil

The aim of the present section is to analyze the influence of rotation on drag performance of a wind turbine airfoil section. The rotational number, RO, is fixed to 0.9 in all the cases presented herein. Three local aspect ratios are considered, $c/r = 0.4$, where the rotational effects are very small as concluded from the previous lift study, $c/r = 0.7$, where stall is delayed and $c/r = 0.9$, where the rotational effects are large enough to maintain the boundary layer fully attached to the airfoil surface.

The total drag, Figure 5.65(a), is computed with the addition of pressure drag plus friction drag, Figures 5.65(b) and 5.65(c) respectively. At angles of attack smaller than $\alpha_{(C_L=C_{L_{MAX}})}$ a larger total drag is predicted for the higher c/r ratio simulations, in these cases the friction drag is clearly larger due to rotation. The opposite prediction is done for angles of attack higher than $\alpha_{(C_L=C_{L_{MAX}})}$, for which the total drag is smaller. This effect is magnified at $c/r = 0.9$, where the onset of separation is kept on the trailing edge vicinity as a consequence of rotation. Contrary to the other two cases, where at high angles of attack around a 98% of the drag is created by pressure drag, for the ratio $c/r = 0.9$ more than 30% of the total drag arises from friction.

Small kinks appeared on the drag curve before $\alpha_{(C_L=C_{L_{MAX}})}$, cases $c/r = 0.4$ and $c/r = 0.7$. These bumps are related to the sudden decrease in friction drag together with a reduction of the pressure drag. This effect is localized to less than half a degree around $\alpha_{(C_L=C_{L_{MAX}})}$.

The friction drag is the main component of the total drag at low angles of attack for the three spanwise positions, Figure 5.65(c). Differences in C_{Df} between the different c/r ratios remain constant until stall is reached, having a higher C_{Df} the computations with larger c/r. The increment in skin friction is induced by the effects of Coriolis and centrifugal forces in the boundary layer. Once stall is reached, in both cases $c/r = 0.4$ and $c/r = 0.75$ the friction coefficient decreases abruptly reducing the differences. When $c/r = 0.9$, the

friction drag keeps growing with the angle of attack, contributing to maintain the turbulent boundary layer attached to the airfoil surface and hence holding the pressure drag from increase.

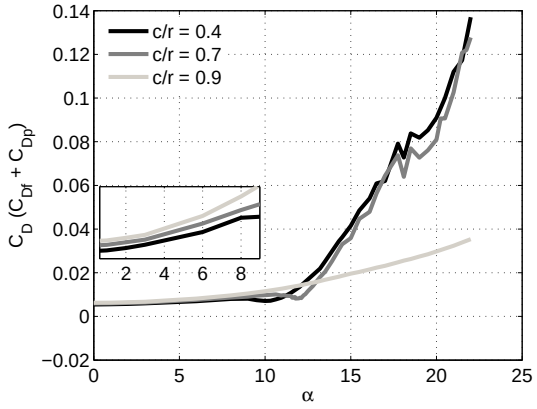

(a)

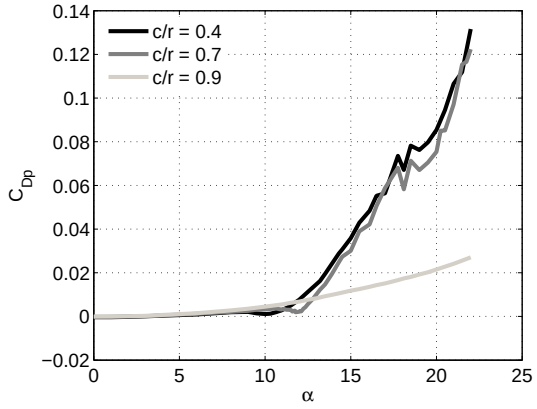

(b)

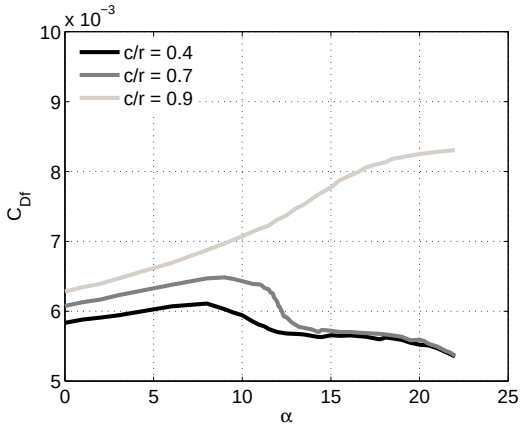

(c)

Figure 5.65: (a) Total drag (b) Pressure drag (c) Friction drag, at c/r cases 0.4, 0.7 and 0.9 with RO = 0.9. Reynolds 1.10^6.

5.7.3 Artificial rotor

An artificial rotor blade has been created in order to analyze the effects of rotation in function of some of the variables used in the design of wind turbine blades: angular velocity, wind speed, blade span, and tip speed ratio. The blade has been generated with a constant chord S809 airfoil geometry along 10 meters span. The Reynolds number in simulations is kept constant at 1.10^6 for the whole blade span using an artificial variation of the viscosity. The angular velocity, Ω, at which the blade rotates is fixed at 70 rpm. Four different cases at different wind speeds, Q_w, and subsequently different tip speed ratios, λ, have been studied. In all the cases the boundary layer transition location is forced at $0.05c$ from the leading edge.

$$\lambda = \frac{\Omega r}{U_{rel}} \tag{5.11}$$

WIND SPEED (m/s))	TIP SPEED RATIO, λ
12.20	6
8.14	9
6.11	12
5.23	14

Table 5.1: Tip speed ratio at different wind speeds.

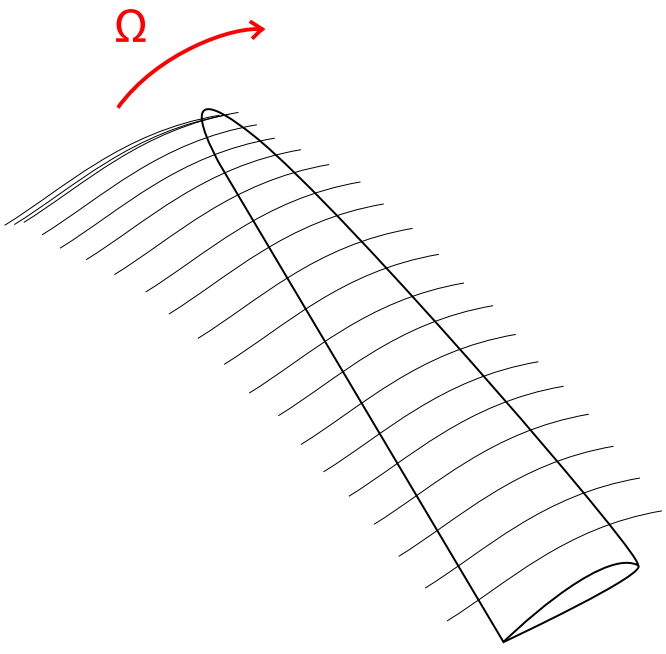

Figure 5.66: Blade streamlines sketch.

The influence of spanwise position and tip speed ratio on lift and separation location has been analyzed. Computations have been carried out at three dif-

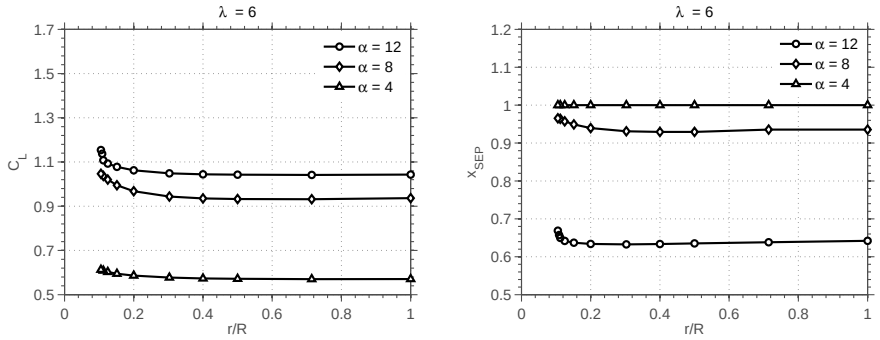

(a) (b)

Figure 5.67: Lift and separation location in function of the local spanwise position at $\lambda = 6$. Angles of attack 4° , 8° and 12°.

ferent incidence angles, $\alpha = 4°$,$\alpha = 8°$ and $\alpha = 12°$. The cases go from fully attach boundary layer over the airfoil surface to large separated flow regions. The turbulent separation location presented in the figures is obtained following Fox [57], he related the onset of separation with the shape factor value in the case of turbulent flows, when H grows bigger than 2.5 separation is reached.

As a first case, the chosen tip speed ratio is $\lambda = 6$, corresponding to a wind speed of $12.20m/s$. At $\alpha = 4°$, the flow remained fully attached to the airfoil surface as shown in Figure 5.67(b), in which the chordwise separation position,x_{SEP}, is plotted in function of the local spanwise location, r/R. A small gain in lift is obtained in this case, the maximum gain of 7.5% is predicted in the closest section to the root, Figure 5.67(a). The gain in lift is achieved in its totality due to the thinner boundary layer created. At angle of attack $\alpha = 8°$, a small separation bubblewith a length 6% of the chord is predicted far away from the root, Figure 5.67(b). As computations move towards the blade root, the bubble is pushed downstream. At the span location $r/R = 0.1$ the buble has been reduced to a 4%, giving a 12% increment in lift, Figure 5.67(a). As the angle of attack increases, the separation location moves upstream. At $\alpha = 12°$ the two dimensional separation, far away from the root, is positioned at $0.64c$ from the leading edge, Figure 5.67(b). In this case the maximum gain in lift is 10.5% with the separation position moved downstream to $0.67c$ at the given span location $r/R = 0.1$.

The wind speed is reduced and simulations are carried out for the new tip speed ratio $\lambda = 9$, Figures 5.68(a) and 5.68(b). Lift and separation position predictions at r/R locations far away from the root remained constant if compared with the previous cases. At $\alpha = 4°$, the boundary layer is fully attached to the airfoil surface, a maximum 10% increment in lift is predicted. At $\alpha = 8°$, the predictions show a maximum lift gain of 17% while the maximum delay in the separation location is 5%. For the highest angle of attack, $\alpha = 12°$, the maximum lift increment is a 33% of the two dimensional lift, almost triple than the previous case with $\lambda = 6$. The onset of separation has been moved dowstream a 33%.

In the third study case, the wind speed is 6.11 m/s with a tip speed ratio

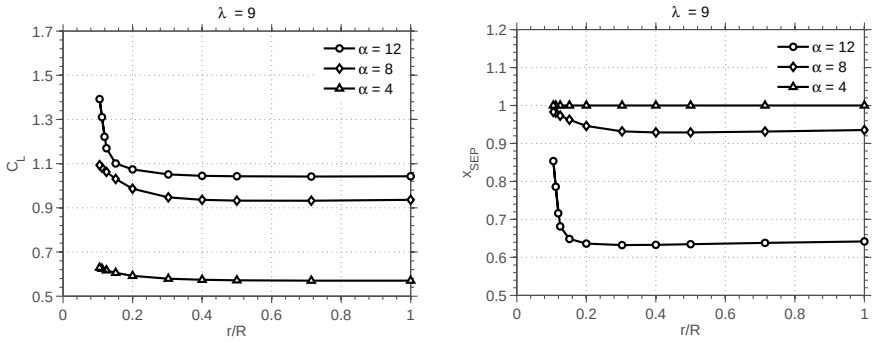

(a) (b)

Figure 5.68: Lift and separation location in function of the local spanwise position at $\lambda = 9$. Angles of attack 4°, 8° and 12°.

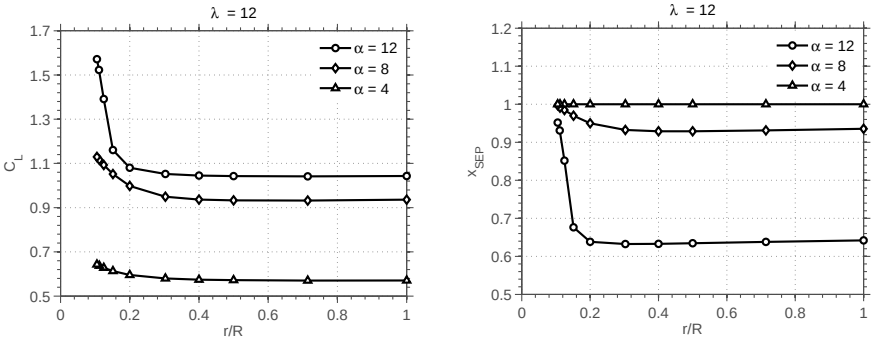

(a) (b)

Figure 5.69: Lift and separation location in function of the local spanwise position at $\lambda = 12$. Angles of attack 4° , 8° and 12°.

of $\lambda = 12$, lift and separation location in function of the local spanwise position are presented in Figures 5.69(a) and 5.69(b). Again lift predictions at locations far away from the root remain constant if compared with the previous λ cases. At $\alpha = 4°$, the maximum gain in lift is 12.7%. At $\alpha = 8°$, predictions show a maximum lift gain of 20.7% with the separation location pushed downstream. At the highest angle of attack, $\alpha = 12°$, a maximum lift increment of 50.5% is predicted, while the separation location is moved towards the trailing edge a 48.23% if compared with two dimensional flow predictions.

As a final case, the wind speed is reduced to $5.23 m/s$ giving a tip speed ratio $\lambda = 14$. For all the different angle of attack simulations, 4°, 8° and 12°, at the given span position $r/R = 0.1$, the favorable pressure gradients created by the rotational forces where enough to maintain the boundary layer fully attached to the blade surface, Figure 5.70(b). Increments obtained in lift force coefficient in the closest region to the root are 14%, 45.3% and 57.6% of the two dimensional predictions for $\alpha = 4°$, $\alpha = 8°$ and $\alpha = 12°$ respectively, Figure 5.70(a).

In order to summarize the effect of rotation in lift performance at different tip speed ratios, lift and separation position are plotted for $\alpha = 12°$. Analyzing the

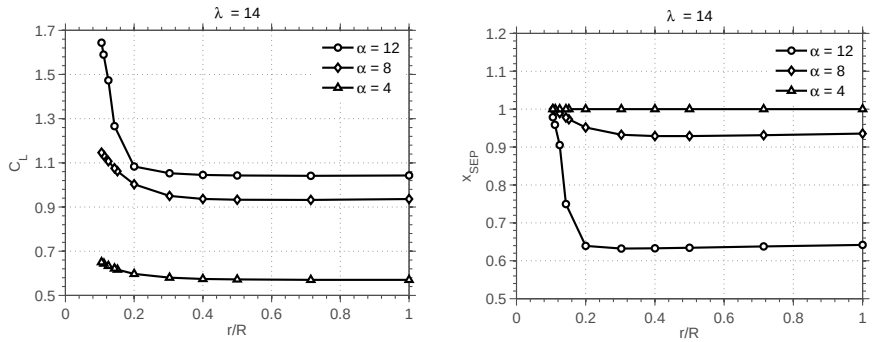

(a) (b)

Figure 5.70: Lift and separation location in function of the local spanwise position at $\lambda = 14$. Angles of attack 4° , 8° and 12°.

lift predictions presented in Figure 5.71(a), the lift gain starts to be significant in all the cases around 30% to 40% of the blade span, increasing as simulations move towards the blade root. The greatest rate of lift increment between tip speed ratios is achieved from $\lambda = 6$ to $\lambda = 9$, while the smallest is obtained between $\lambda = 12$ to $\lambda = 14$. However, the total lift gain grows with the λ value. As the wind speed decreases, maintaining a constant rotational speed, the tip speed ratio increases and the rotational effects in the boundary layer increase with it.

The delay in the separation appears to be significant from 20% of the blade span towards the root, while on the rest of the span it is negligible. The largest delay in separation location appears for the highest tip speed ratio simulation, $\lambda = 14$, at a radial position 10% from the blade root, in this case the separation location is pushed downstream almost a 40% of the airfoil chord.

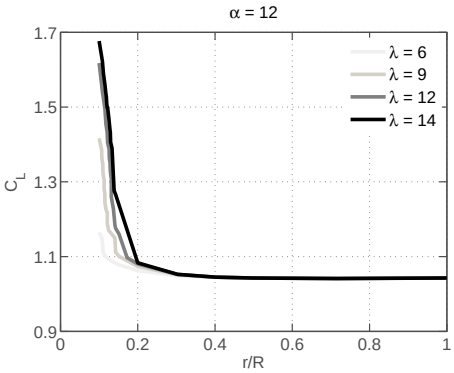

(a)

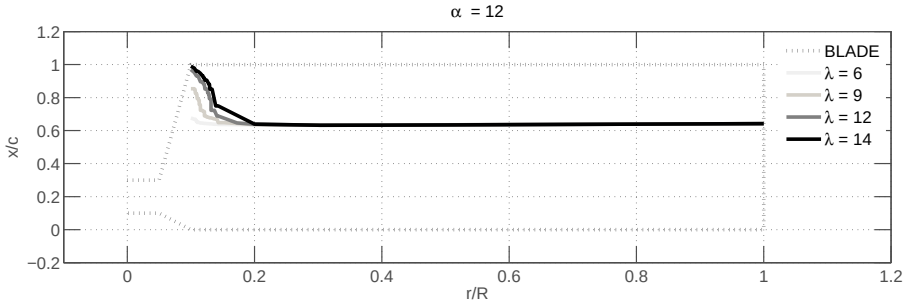

(b)

Figure 5.71: (a) Lift (b) Separation location. Tip speeds $\lambda = 6$, $\lambda = 9$, $\lambda = 12$ and $\lambda = 14$. Angle of incidence 12°.

5.7.4 Influence of rotation on the boundary layer parameters

In this section is presented an analysis of the influence of rotation on the boundary layer properties of a rotating wind turbine blade section. The study is centered on the suction surface of the airfoil, where the flow frequently undergoes separation at high angles of attack due to the existence of large pressure gradients. δ_1^*, θ_1, H, C_f, δ_2^*, θ_2 and β_W are the boundary layer parameters chosen for the present analysis. The airfoil section studied is a s809 section profile at Reynolds $1 \cdot 10^6$. The boundary layer is tripped to become turbulent at $0.05c$ from the leading edge. Two cases at different angle of attack are compared. For $\alpha = 4°$, the flow is fully attached to the airfoil surface. For $\alpha = 12°$, the flow has undergone trailing edge separation. For both cases three local aspect ratios are simulated: $c/r = 0.4$, in which the rotational effects have a weak influence on lift, drag and separation position, $c/r = 0.7$ and $c/r = 0.85$, in which rotational effects, as seen in the previous subsection, have a strong effect in lift and drag performance and therefore the boundary layer properties will be also strongly affected. In all the cases analyzed herein the rotational number is kept constant at $RO = 0.9$.

The behavior of the streamwise displacement thickness quantity, δ_1^*, is shown

in Figures 5.72(a) and 5.72(b). At $\alpha = 4°$, remarkable differences appear from the chordwise position $0.5c$ towards the trailing edge, as the given local aspect ratio increases, the boundary layer displacement thickness decreases due to the influence of Coriolis terms in the $\theta-momentum$ equation. Coriolis terms induce a thinner boundary layer that reduces the outwards displacement of the external streamlines. Reductions in the δ_1^* quantity can be seen as a diminution of the airfoil obstruction against the freestream flow due to the thinner boundary layer generated. At incidence $\alpha = 12°$, the flow is separated and the influence of rotational effects is stronger in the boundary layer quantities. The maximum value of δ_1^* is reduced almost 10 times from the ratio $c/r = 0.4$ to $c/r = 0.85$.

In terms of the streamwise momentum thickness quantity, θ_1, shown in Figures 5.72(c) and 5.72(d), very similar trend as for the δ_1^* quantity is observed when the flow is fully attached, $\alpha = 4°$. In the case where the flow undergoes trailing edge separation, $\alpha = 12°$, the momentum thickness quantity increases abruptly just before separation takes place for the cases $c/r = 0.4$ and $c/r = 0.7$. For $c/r = 0.85$, θ_1 has a fairly constant value on the last 50% of the chord, reducing the growth of the shape factor and retarding separation. It is important to remark that the streamwise momentum thickness reduction due to the rotational effects is smaller than the reduction of the streamwise displacement thickness quantity, hence the growth of the shape factor H is contained and separation delayed.

With respect to the shape factor behavior, H, presented in Figures 5.72(e) and 5.72(f): At $\alpha = 4°$ the shape factor does not grow larger than 2.5 for any of the given c/r ratios. As soon as the angle of attack increases differences in the shape factor magnitude between the different local aspect ratios grow drastically. As c/r is increased, the secondary spanwise flow increases together with the increment in the effect of Coriolis forces, having a stabilizing effect on the boundary layer, in this way the shape factor is considerably reduced and thereby the onset of separation retarded. At the position $c/r = 0.85$ the shape factor has been reduced drastically, reaching values larger than 2.5 only in the last 3% of the airfoil chord.

Concerning the friction coefficient, C_f, shown in Figures 5.72(g) and 5.72(h), in opposition to the effect of rotation on the shape factor, the friction coefficient increases due to the secondary radial flow. The radial flow increases the minimum total drag, mostly friction drag, as shown in the section above. This effect is particularly important on the last half of the airfoil chord. At $\alpha = 12°$ the skin friction on the rear part of the airfoil increases from zero to a positive value as the ratio c/r is reduced.

The behavior of the spanwise displacement thickness, δ_2^*, is shown in Figures 5.73(a) and 5.73(b). As the simulations c/r ratio increases, δ_2^* grows in absolute value, with opposite sign to the δ_1^* quantity. The growth of the spanwise displacement thickness is related with the outwards moving spanwise flow, which affects the streamlines displacing them outwards from the airfoil surface. After separation the rate of growth of $\delta_2^*$is larger for bigger c/r values.

The suction side streamwise momentum thickness distribution, θ_2, is plotted at incidence angles $\alpha = 4°$ and $\alpha = 12°$ as function of the chordwise direction in Figures 5.73(c) and 5.73(d). At $\alpha = 4°$, where there is not a separated flow

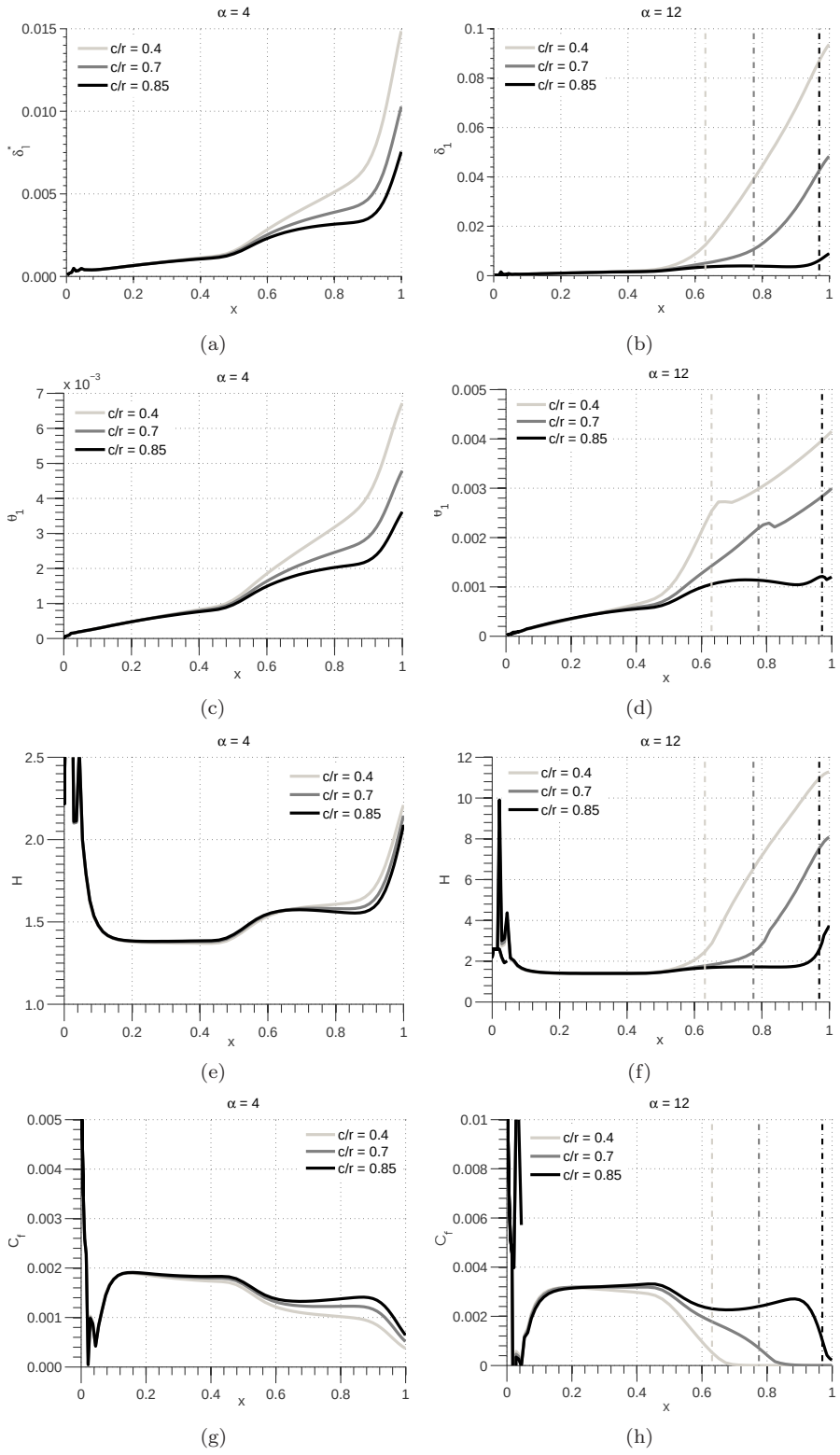

Figure 5.72: Boundary layer quantities δ_1^*, θ_1, H and C_f. $RO = 0.9$ with c/r 0.4, 0.7 and 0.85 Angles of incidence 4° and 12°. Separation location marked with vertical point-dash line.

region, θ_2 follows the same tendency as the δ_2^* quantity. At $\alpha = 12°$, under separated conditions, the rate of grown of θ_2 in absolute value is not as large as the one obtained for δ_2^*.

Rotation increases the angle between the limiting streamline and the boundary layer edge streamline, β_w, Figures 5.73(e) and 5.73(f). The angle is set to 0° at the position where the boundary layer becomes turbulent. During attached flow conditions, $\alpha = 4°$, as the ratio c/r increases, the angle β_w grows reaching a maximum of $\beta_w = 60°$ at the suction side of the trailing edge for $c/r = 0.85$. At $\alpha = 12°$, in the attached flow region, β_w follows the same tendency. Although after the flow separates, β_w grows with a steep increment towards 90°, staying almost constant at this value until the trailing edge is reached. After separation appears the limiting streamlines inside the boundary layer are perpendicular to the inviscid flow ones, a strong radial flow appears in the bottom of the separated boundary layer while further up and in the inviscid flow region the streamlines follow the θ direction.

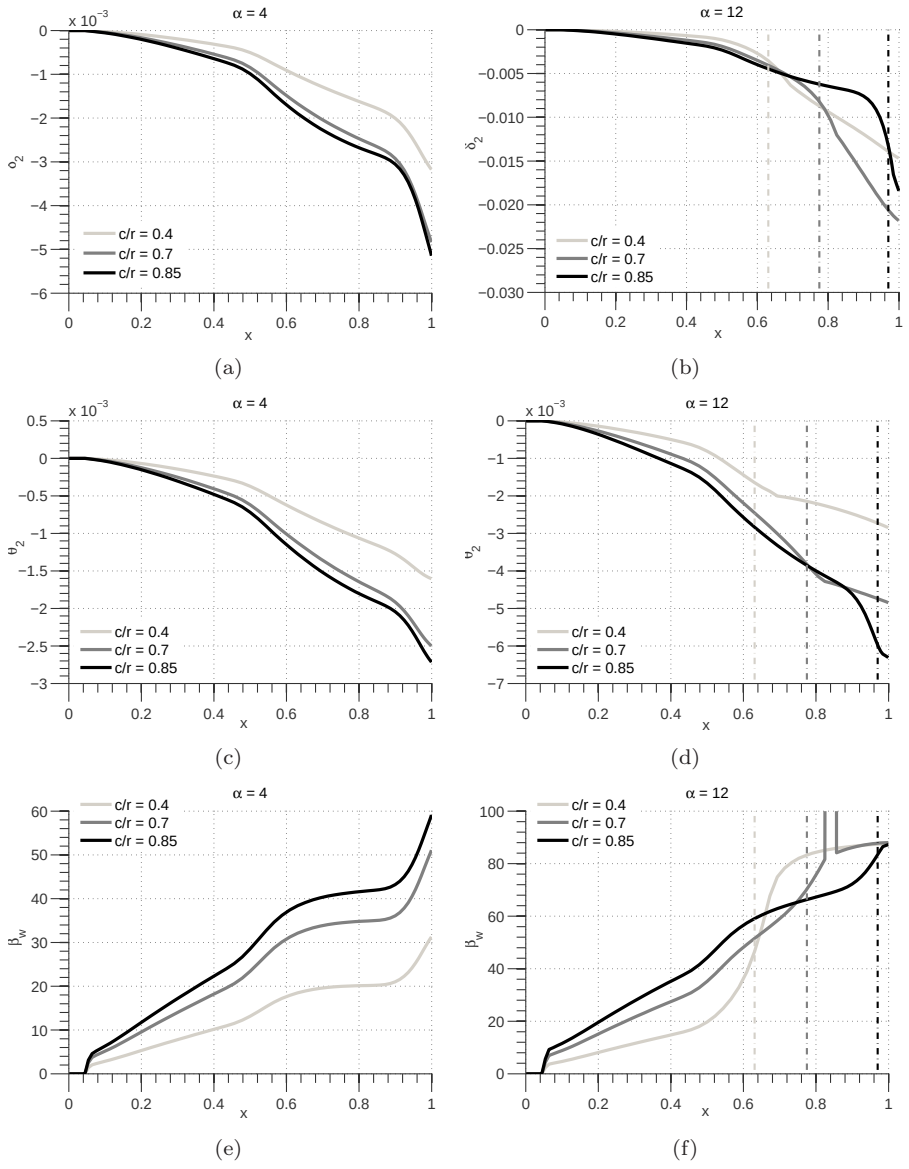

Figure 5.73: Boundary layer quantities δ_2^*, θ_2 and β_w. $RO = 0.9$ with c/r 0.4, 0.7 and 0.85. Angles of incidence 4° and 12°. Separation location marked with vertical point-dash line.

5.7.5 Analysis of rotation induced Coriolis and Centrifugal forces

The influence of centrifugal and Coriolis force terms in the integral boundary layer equations has been evaluated by comparison to the convective terms on the suction side of the airfoil. In Chapter 3, the integral form of the Quasi-3D boundary layer equations was derived. We here use these equations to evaluate the relative magnitude of the centrifugal and Coriolis terms:

- Relative magnitude of Coriolis force term, θ-momentum equation,

$$\frac{COR_\theta}{CONV} = \frac{\left| sw\ pr\ 2RO\ ls\ \delta_2^*\ \frac{1}{u_e\ c} \right|}{\left| \frac{\partial \theta_1}{\partial s} \right| + \left| \frac{\partial \theta_2}{\partial s} \right|} \tag{5.12}$$

- Relative magnitude of Coriolis force term, r-momentum equation,

$$\frac{COR_r}{CONV} = \frac{\left| sw\ pr\ ls\ \frac{2RO}{u_e}\ (\delta - \delta_1^*) \right|}{\left| \frac{\partial \theta_1}{\partial s} \right| + \left| \frac{\partial \theta_2}{\partial s} \right|} \tag{5.13}$$

- Relative magnitude of centrifugal force term, r-momentum equation,

$$\frac{CEN_r}{CONV} = \frac{\left| (ls/c)\ RO^2\ \delta \right|}{\left| \frac{\partial \theta_1}{\partial s} \right| + \left| \frac{\partial \theta_2}{\partial s} \right|} \tag{5.14}$$

These ratios can give an idea of the importance of Coriolis and centrifugal forces in the viscous boundary layer for both streamwise and spanwise directions in comparison with the convective terms. The present analysis is carried out for the wind turbine airfoil S809, with rotational number, $RO = 0.9$. Three local aspect ratios are included in the analysis: $c/r = 0.1$, $c/r = 0.7$ and $c/r = 0.9$. Two angles of attack are considered: $\alpha = 9^\circ$ and $\alpha = 12^\circ$.

Convergence problems arise when the flow undergoes separation. The θ momentum Coriolis term was determined as the source of the convergence problems. In order to reach a converged solution, the θ momentum Coriolis term is reduced artificially by a factor of 10 in the separated region. In the case that convergence was reached without any modification, the Coriolis ratio was predicted constant in the separated region with a value approximately equal to the one of the last attached location.

In the differential form of the boundary layer equations, the centrifugal force term $\Omega^2 r$ enters the system through the r-momentum equation. In the present formulation of the boundary layer equations the pressure terms do not appear explicitly, as the Bernoulli equation has been utilized to replace them by velocity relations on the edge of the boundary layer. In the $r - momentum$ equation the centrifugal force appears through the radial derivative of the streamwise velocity multiplied by the boundary layer thickness, $-\frac{1}{u_e}\frac{\partial u_e}{\partial r}\delta$. Centrifugal forces, due to its radial nature, does not enter the θ momentum equation.

The spanwise pressure gradient is given by Bernoulli equation which, formulated in a rotational frame of reference, reads

$$-\frac{1}{\rho}\frac{\partial p}{\partial r} = u_e\frac{\partial u_e}{\partial r} + v_e\frac{\partial v_e}{\partial r} + w_e\frac{\partial w_e}{\partial r} - \Omega^2 r \tag{5.15}$$

From Equation 5.15 it can be seen how the centrifugal force term is coupled to the radial velocity gradients via spanwise pressure gradients.

In the differential form of the equations, Coriolis forces enter the system through both the θ and $r - momentum$ equations, through the terms, $2\Omega v$ and $2\Omega u$. After manipulating the differential equations, transforming them into a Quasi 3D integral version, the Coriolis terms fake the following form: $sw\,pr\,2RO\,\frac{c}{r}\,\delta_2^*\,\frac{1}{u_e\,c}$ and $sw\,pr\,\frac{c}{r}\,\frac{2RO}{u_e}\,(\delta - \delta_1^*)$, respectively. Coriolis forces create a favorable pressure gradient in the chordwise pressure distribution, delaying separation and increasing $C_{L_{max}}$.

Due to the small-crossflow approximation, $\partial/\partial r << \partial/\partial s$, Coriolis forces are relatively small in the $\theta - momentum$ equation, whereas they are relatively large in the $r - momentum$ equation. The small-crossflow approximation only holds for low local aspect ratios. When c/r is large the spanwise component of the flow grows in importance and the small-crossflow approximation is not valid anymore.

In Figures 5.74, 5.75 and 5.76 we illustrate the relative importance of the fictitions forces by depicting Equations 5.12, 5.13 and 5.14 at different parameters.

As the local aspect ratio c/r increases, the Coriolis terms in the $\theta - momentum$ equation grow in magnitude. For $\alpha = 9°$ and $c/r = 0.1$, see Figure 5.74(a), before separationthe θ Coriolis term is more than 100 times smaller than the convective terms. Increasing the local aspect ratio to $c/r = 0.7$, the value of the $\theta - momentum$ Coriolis term just before separation is approximately 50% of the convective terms, see Figure 5.74(b). Finally, at $c/r = 0.9$, Figure 5.74(c), the Coriolis term has grown double as big as than the convective terms. Near the leading edge the rotational effects are less pronounced, due to the larger pressure gradients, which increases with the downstream location. In all the cases, the Coriolis term decreases around $0.5c$ coinciding with the rise in the shape parameter, to increase again before separation takes place.

The relative magnitude of the Coriolis term in the $r - momentum$ equation is presented in Figures 5.75(a), 5.75(b) and 5.75(c). This term also increases with the c/r ratio. However, his increment rate is very small in comparison with the θ−Coriolis term. In general Coriolis terms are larger for the lower angle of attack simulations. For $c/r = 0.1$, differences between $\alpha = 9°$ and $\alpha = 12°$ are larger after separation takes place. For $c/r = 0.7$, differences between $\alpha = 9°$ and $\alpha = 12°$ start growing before separation takes place. At $c/r = 0.9$, both angle of attack computations follow similar trends from the leading to the trailing edge, although the lower angle of attack maintains a higher value. In this case the boundary layer separation is pushed to the trailing edge due to the strong favorable pressure gradients created by rotation.

Computed changes on the r-centrifugal to convective terms ratio appeared to have, in all the cases, similar tendencies as those computed for the r-Coriolis terms ratio. However their order of magnitude was slightly lower, see Figures 5.76(a), 5.76(b) and 5.76(c). We may thus conclude that the spanwise direction Coriolis force influence is stronger than centrifugal force influence.

In Figure 5.77 centrifugal force terms are compared against Coriolis terms in the spanwise direction at $\alpha = 9°$ for three local aspect ratios c/r. In the nose region of the airfoil, the differences between the two force terms are small, after which the differences grow with the downstream position. The maximum difference between the two force ratios is generally located to the rear side of the airfoil.

Coriolis forces in the streamwise direction are an order of magnitude smaller than Coriolis and Centrifugal forces in the spanwise direction. Except at high local aspect ratios, $c/r = 0.9$, where the θ Coriolis forces are of the same order of magnitude as the Centrifugal forces.

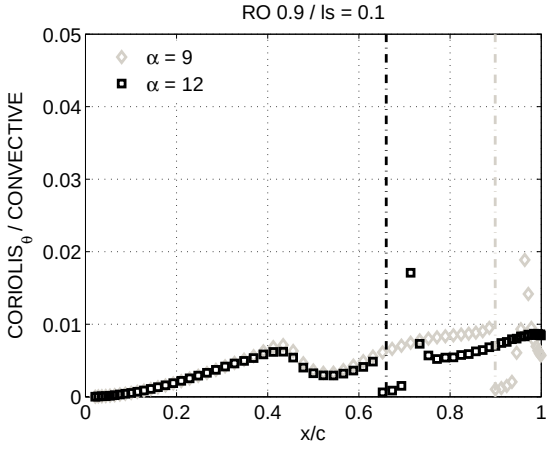

(a)

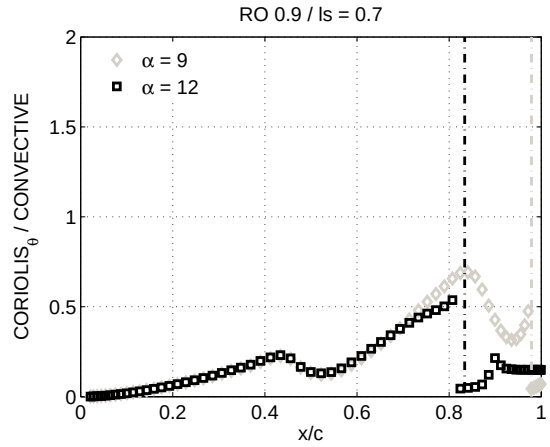

(b)

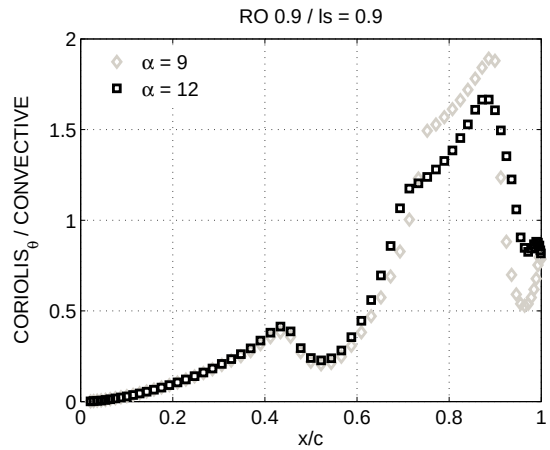

(c)

Figure 5.74: Relative magnitude of the Coriolis terms in the θ-momentum equations to the convective terms. Separation is marked with a vertical line.

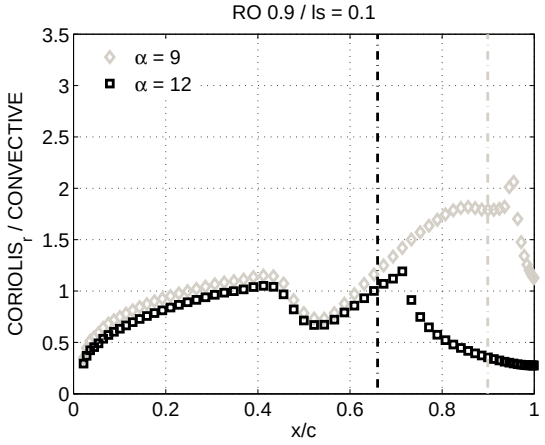

(a)

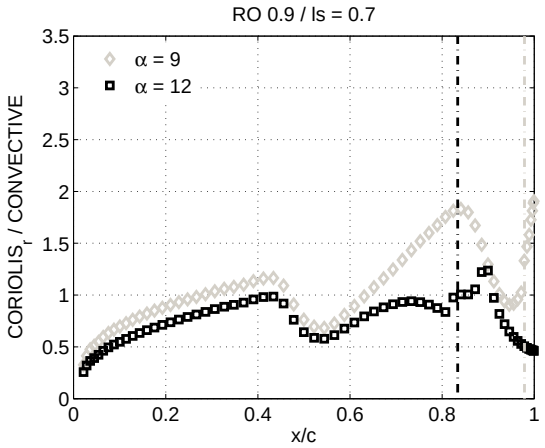

(b)

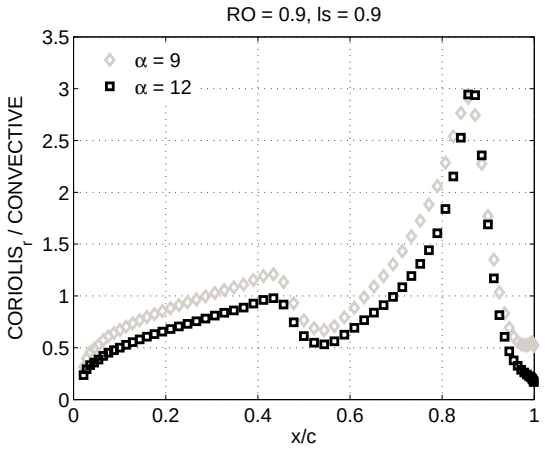

(c)

Figure 5.75: Relative magnitude of the Coriolis terms in the r-momentum equations to the convective terms. Separation is marked with a vertical line.

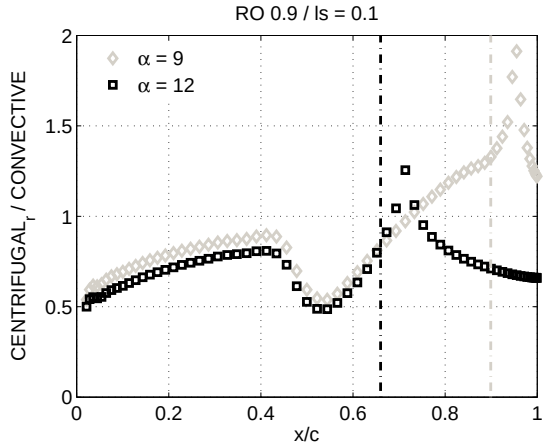

(a)

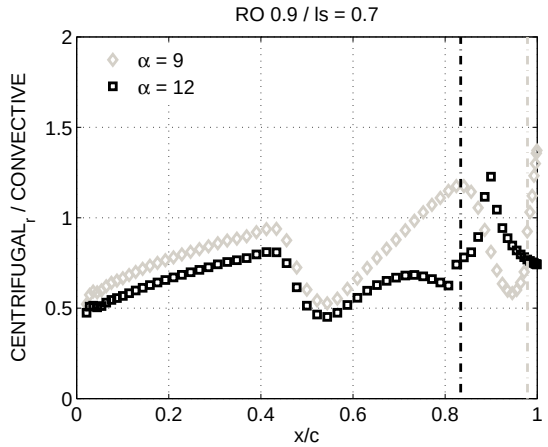

(b)

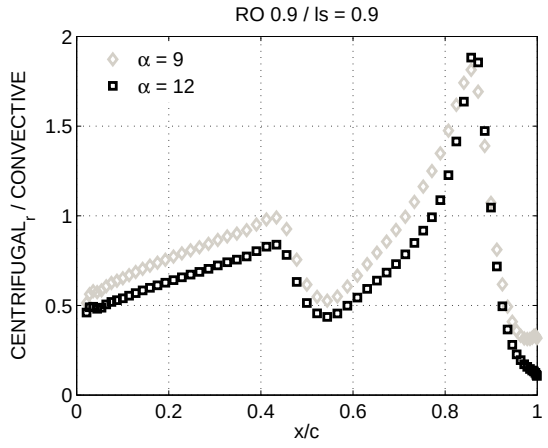

(c)

Figure 5.76: Relative magnitude of the centrifugal force terms in the r-momentum equations to the convective terms. Separation is marked with a vertical line.

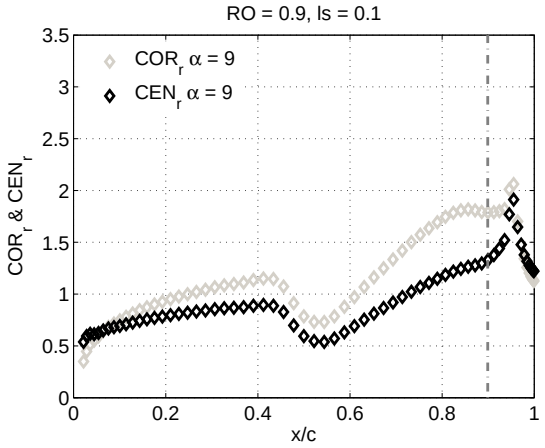

(a)

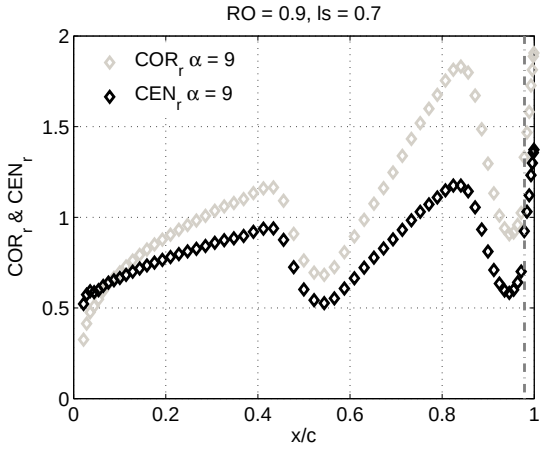

(b)

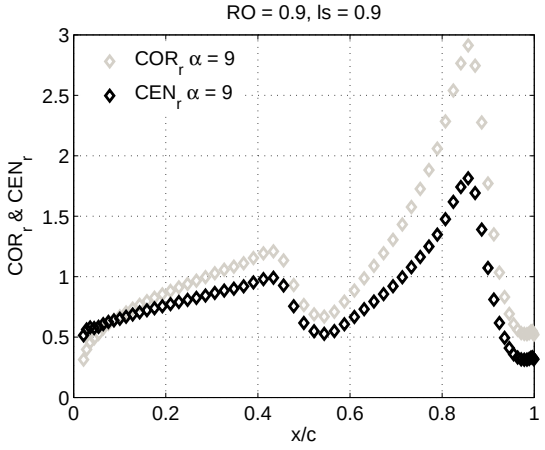

(c)

Figure 5.77: r-centrifugal vs r-Coriolis force terms ratio.

Summary of parametric study of the Quasi3D viscous-inviscid method

A parametric study of the influence of rotation on the aerodynamic behavior of an airfoil section has been presented in this chapter. It is concluded that the rotational effects increase with both ls and RO. Coriolis and centrifugal forces rising from rotation generate a favorable pressure gradient on the suction side of the airfoil which increases lift and retards the onset of separation. On the pressure side, the influence of rotation is not as large, but it is still present. Rotation increases slightly the total drag at low angles of attack, $\alpha < \alpha_{C_{L_{MAX}}}$, although at high incidence angles rotation tends to reduce the drag.

A study of an artificial wind turbine blade was performed concluding that the rotational effects are have an influence on the first 40% of the blade span. However thery are only significant on the first 20% where separation is clearly retarded and the lift increased considerably. On the other 60% of the blade span rotational effects are inapreciable.

Analyzing the influence of rotation on the integral boundary layer variables, it was concluded that rotation reduces drastically the streamwise displacement thickness. The shape factor, H, is also reduced, delaying the appearance of separation.

The influence of Coriolis and centrifugal forces has been studied and their order of magnitude has been analyzed. Coriolis terms appearing in the θ momentum equation became significant as the computations approached the blade root. Far away from the root, i.e at small c/r values, the θ-Coriolis terms are about 100 times smaller than the convective terms, while for a local aspect ratio $c/r = 0.9$ have the same order of magnitude as the convective terms. Coriolis and centrifugal terms in the r momentum equation also became larger as the simulations approached the blade root, but their growth is much more moderate. The r-Coriolis force terms are larger in magnitude than the centrifugal terms.

Chapter 6

Conclusion

Steady, unsteady, 2D and Quasi3D versions of a viscous-inviscid interactive boundary layer solver have been developed and presented in the dissertation. The solver has been developed during the last three years to become a design tool for wind turbine airfoil design. The code is capable of computing airfoil aerodynamic performance under rotational and unsteady effects with high accuracy and low computational costs.

The viscous part of the flow solver is made up using the integral Quasi3D form of the r and θ momentum equations together with the kinetic energy shape parameter equation and a set of closure relations. The inviscid part consists of a panel method. A strong viscous inviscid interaction is used in order to couple both parts. The strong interaction makes it possible to overcome the Goldstein singularity and compute the boundary layer flow at and after separation takes place. Under relaxation is needed at high angles of attack where the airfoil presents large regions of separation.

An study of airfoil aerodynamic performance for different geometries and Reynolds numbers has been presented and used for validation of the steady two dimensional version of the code. A good agreement is obtained against experiments for the predicted aerodynamic lift, while drag and pitching moment are slightly under predicted. The viscous-inviscid predicted pressure distributions around the airfoil surface were also in overall good agreement with experiments and with EllipSys2D computations.

The unsteady terms of the r momentum and kinetic energy shape parameter equations together with the implemented unsteady version of the Kutta condition using a single wake vortex model, allows the viscous-inviscid solver to simulate dynamic airfoil performance. Dynamic lift predictions are in good agreement with experimental data while drag and pitch moment computations in some cases lack accuracy.

The capability of the code to simulate a trailing edge flap has been proven in both steady and unsteady cases, as well as the capability of controlling the flap using a PI controller to maintain a constant lift.

The viscous-inviscid interactive code has been used for studying the effect of rotation for rotating wind turbine blades. It is concluded that the rotational effects have an influence on the 40% of the blade span from the root, having a

significant influence in the first 20% of the blade, where separation is retarded, lift increased and drag reduced. Rotational effects are negligible on the rest of the blade span.

A study on the influence of rotation showed that Coriolis and centrifugal forces act as a favorable streamwise pressure gradient that thinners the boundary layer, reducing the airfoil obstruction against the freestream and therefore increasing the lift. The drag coefficient is slightly increased by rotation at low angles of attack and reduced after stall takes place. Coriolis and centrifugal forces tend to move the separation point downstream, in some cases keeping it in the trailing edge vicinity.

In the future, a validation of the code against a wider span of airfoil geometries and flow conditions will be done. Furthermore, the important issue of transition will be addressed. In particular the convergence difficulties that arise from fast changes in the transition location.

Bibliography

[1] VR.C. Lock and B.R. Williams. Viscous-inviscid interactions in external aerodynamics. *Prog. Aerospace Sci*, 24:51–171, 1987.

[2] Mark Drela and Michael B. Giles. Viscous-inviscid analysis of transonic and low reynolds number airfoils. *AIAA journal*, 25:1347–1355, 1987.

[3] Zhaohui Du and M.S. Selig. The effect of rotation on the boundary layer of a wind turbine blade. *Renewable Energy*, 2000.

[4] Franklin D. Harris. Preliminary study of radial flow effects on rotor blades. *Journal of the American Helicopter Society*, 30, 1966.

[5] J.H. Preston. The calculation of lift taking account of the boundary layer. *ARC R M*, 2725, 1949.

[6] D.A. Spence. Prediction of the characteristics of two-dimensional aerofoils. *J. Aero. Sci.*, 21:577, 1954.

[7] M.J. Lighthill. On displacement thickness. *Journal of Fluid Mechanics*, 1958.

[8] B. J. Powell. The calculation of the pressure distribution of a thick cambered aerofoil at subsonic speeds including the effect of the boundary layer. Technical Report 1238, 1967.

[9] M.C.P. Firmin. The calculation of the pressure distribution, lift and drag, on single aerofoils at subcritical speeds. part i interim method. Technical Report 72235, 1973.

[10] J.E. Green. Application of head's entrainment method to the prediction of turbulent boundary layers and wajes in compressible flow. Technical Report R. M. No. 3788, 1976.

[11] J.C. Le Balleur. Strong matching method for computing transonic viscous flows including wakes and separations. *La Recherche Aérospatiale*, 3:21–45, 1981.

[12] Mark Drela. Xfoil, an analysis and design system for low reynolds number airfoils. *Conference on Low Reynolds Number Aerodynamics, Univeristy of Notre Dame*, 1989.

[13] Tuncer Cebeci and Hong Ming Jang. Interactive boundary-layer method for unsteady airfoil flows: Quasisteady model. *Journal of Aircraft*, 27:673–678, 1990.

[14] T. Cebeci, M. F. Platzer, H. M. Jang, and H. H. Chen. An inviscid-viscous interaction approach to the calculation of dynamic stall initiation on airfoils. *Journal of Turbomachinery*, 115:714–723, 1993.

[15] B. M. Maskew and F. A. Dvorak. The prediction of $c_{L_{MAX}}$ using a separated flow model. *Journal of the American Helicopter Society*, 23.

[16] Vasilis A. Riziotis and Spyros G. Voutsinas. Dynamic stall modelling on airfoils based on strong viscous-inviscid interaction coupling. *International journal for numerical methods in fluids*, 56:185–208, 2008.

[17] Simon Philippe Breton, Frank N. Coton, and Geir Moe. A study on rotational effects and different stall delay models using a prescribed wake vortex scheme and nrel phase vi experiment data. *Wind Energy*, 11:459–482, 2008.

[18] Pasquale M. Sforza. Effects of rotation on wind turbine blade boundary layers.

[19] Pasquale M. Sforza. First meeting of specialists on the aerodynamics of horizontal-axis wind turbines- a summary of findings, issues, recommendations. *NASA Wind Energy Project Office and Rocky Flats Wind Energy research Center, Wichita, Kansas*, 1983.

[20] Simms D.A Butterfield C.P, Jenks M.D and Musial W.P. Aerodynamic pressure measurements on a rotating wind turbine blade. *Solar Energy Research Institute*, 1990.

[21] L.E. Fogarty and W.R. Sears. Potential flow around a rotating, advcancing cylindrical blade. *Journal of Aero. Sci.*, 17, 1950.

[22] N. Rott and W.E Smith. Some examples of laminar boundary layer flow in rotating blades. *Journal of the Aeronautical Sciences*, 23, 1956.

[23] M.E Graham. Calculation of the laminar boundary layer on rotating blades. *PhD thesis, Cornel University*, 1954.

[24] W.R. Sears. Boundary layers in three-dimensional flow. *Applied Mechanics Reviews*, 7, 1954.

[25] F.K Moore. Three dimensional boundary layer theory. *Advances in Applied Mechanics*, 1956.

[26] A. Mager. Three dimensional laminar boundary layers. *Theory of Laminar Flows, Princeton Series*, 1964.

[27] J.H Horlock and J. Wordsworth. The three dimensional laminar boundary layer on a rotating helical blade. *Journal of Fluid Mechanics*, 23:305–314, 1965.

[28] B. Lakshminarayana, A. Jabbari, and H. Yamaoka. Turbulent boundary layer on a rotating helical blade. *Journal of Fluid Mechanics*, 51:545–569, 1972.

[29] W. J. McCroskey and P. F. Yaggy. Laminar boundary layers on helicopters rotors in forward flight. *AIAA journal*, 6:1919–1926, 1968.

[30] W. J. McCroskey, J. F. Nash, and J. G. Hicks. Turbulent boundary layer flow over a rotating flat plate blade. *AIAA journal*, 9:188–189, 1971.

[31] M. Takematsu. Laminar boundary layer over a rotating round-nosed blade. *AIAA journal*, 10:333–334, 1972.

[32] J.M Savino and T.W Nyland. Wind turbine flow visualization studies. *AWEA Wind Energy Conferences, San Francisco, CA*, 1985.

[33] Jens Nørkær Sørensen. *Three-level, viscous-inviscid interaction technique for the prediction of separated flow past rotation wings.* PhD thesis, Danmark Tekniske Universitet, 1986.

[34] R. Houwink H. Snel and J. Bosschers. Sectional prediction of lift coefficients on rotating wind turbines blades in stall. Technical Report ECN-C–93-052, 1994.

[35] Joseph Katz and Allen Plotkin. *Low speed aerodynamics: from wing theory to panel methods.* McGraw-Hill, 1977.

[36] B.C. Basu and G.J. Hancock. The unsteady motion of a two-dimensional aerofoil in incompressible inviscid flow. *Journal of Fluid Mechanics*, 87:159–178, 1978.

[37] L. Prandtl. Über flüssigkeitsbewegung bei sehr kleiner reibung. *Proc. III Intern. Math. Congress, Heidelberg*, 1904.

[38] Frank M. White. *Viscous Fluid Flow.* McGraw-Hill, 1974.

[39] A.D. Young. *Boundary Layers.* BSP Professional Books, 1989.

[40] Hermann Schlichting. *Boundary Layer Theory.* Mc Graw Hill Book Co. Inc, 1955.

[41] M.O.L. Hansen. Basic rotor aerodynamics applied to wind turbines. Technical report, 1998.

[42] J.C. Cook and M.G. Hall. Boundary layers in three dimensions. *Progress in Aero. Sci.*, 2, 1962.

[43] Casper Skøby. Master project, solution of boundary layer flows about rotating wings. *Danmark Tekniske Universitet*, 2008.

[44] and A. Dumitrache H.Dumitrescu, V. Cardos. Modelling of inboard stall delay due to rotation. *Journal of Physics, The Science of Making Torque from Wind, Conference Series*, 2007.

[45] G.G. Martinez J.N. Sørensen and W.Z Shen. 3d boundary layer study of a rotating wind turbine blade. *Journal Of Physics: Conference Series 75 012032*, 25, 2007.

[46] B. Lakshminarayana and T.R. Govindan. Analysis of turbulent boundary layer on cascade and rotor blades of turbomachinery. *AIAA journal*, 19:1333–1341, 1981.

[47] A. Mager. Generalization of boundary layer momentum integral equations to three-dimensional flow including those of rotating systems. Technical Report 1067, 1952.

[48] T. W. Swafford. Analytical approximation of two-dimensional seperated turbulent boundary-layer velocity profiles. *AIAA journal*, 21:923–926, 1983.

[49] F. H. Clauser. Turbulent boundary layers in adverse pressure gradients. *Journal of Aeronautical Sciences*, 21:91–108, 1954.

[50] Cousteix Jr. Gleyzes C. and Bonnet J.L. Theoretical an experimental study of low reynolds number transitional separation bubbles. *Conference of Low Reynolds number Airfoil Aerodynamics, University of Notre Dame*, 17, 1950.

[51] L. M Mack. Transition and laminar instability. Technical Report 77-15.

[52] A. E. P. Veldman and J. P. F. Carter. New quasi-simultaneous method to calculate interacting boundary layers. *AIAA Journal*, 19:79–85, 1981.

[53] Andrzej Krzysiak and Nikolaj Narkiewicz. Aerodynamic loads on airfoil with trailing-edge flap pitching with different frequencies. *Journal of aircraft*, 43:407–418, 2006.

[54] A. E von Doenhoff and F. T Abbott. The langley two-dimensional low-turbulence pressure tunnel. (1283), 1947.

[55] I. H Abbott and A. E Doenhoff. Theory of wing sections. *Dover Publications, Inc., New York*, 1959.

[56] D. Althaus. Niedriggechwinddigkeisprofile. *Technical Report, Vieweg, Braunshweig*, 1981.

[57] Robert W. Fox, Alan T. McDonald, and Philip J. Pritchard. *Introduction to Fluid Mechanics*.

[58] Franck Bertagnolio, Niels Sørensen, Jeppe Johansen, and Peter Fuglsang. Wind turbine airfoil catalogue. *Risø-R-1280(EN)*, 2001.

[59] Robert M. Pinkerton. The variation with reynolds number of pressure distribution over an airfoil section. *NACA Report No.613*.

[60] A. Björck. Coordinates and calculations for the ffa-w1-xxx, ffa-w2-xxx and ffa-w3-xxx series of airfoils for horizontal axis wind turbines. (FFA TN 1990-15), 1990.

[61] Niels Troldborg. Computational study of the risø-b1-18 airfil with a hinged flap providing variable trailing edge geometry. *Wind Energy*, 29:89–113, 2005.

[62] M.M Zdrakovich. Flow around circular cylinders. vol 1: Fundamentals. chap.6. 1977.

[63] Robert E. Sheldahl and Pau C. Klimas. Aerodynamic characteristics of seven symmetrical airfoil sections through 180 degree angle of attack for use in aerodynamic analysis of vertical axis wind turbines. 1981.

[64] R. A. McD Galbraith, M. W. Gracey, and E. Leich. Summary of pressure data for thirteen aerofoils on the university of glasgow's aerofoil database. *G.U Aero report 9221, University of Glasgow*, 1992.

[65] Jens N. Sørensen and Per J. Nygreen. Unsteady vorticity-streamfunction algorithm for external flows. *Computers and Fluids*, 30, 2001.

[66] X. Amandolese and E. Szechenyi. Experimental study of the effect of turbulence on a section model blade oscillating in stall. *Wind Energy*, 7:267–282, 2004.

Recent Ph.D.-dissertations in Fluid Mechanics

Sørensen, J.N. Three-Level, Viscous-Inviscid Interaction Technique for the Prediction of Separated Flow Past Rotating Wing, AFM 86-03, 1986

Michelsen, J.A. Modelling of Laminar Incompressible Rotating Fluid Flow, AFM 86-05, and Modelling of Turbulent Incompressible Rotating Fluid Flow, AFM 86-07, 1986

Sørensen, L.S. Three-Dimensional Electro-Fluid-Dynamics in Tuft Corona Wire-Plate Precipitators, AFM 89-03, 1989

Gervang, B. Numerical Simulations of 3-Dimensional Flow in Straight and Curved Ducts of Rectangular Cross Section, AFM 89-09, 1989

Andresen, E. Statistical Approach to Continuum Models for Turbulent Gas Particles Flows, AFM 90-04, 1990

Nielsen, N.F. Low Reynolds Number Fluid Dynamics with Applications to Suspending Feeding Animals, AFM 91-10, 1991

Zamany, J. Modelling of Particle Transport in Commercial Electrostatic Precipitators, Ph.D under ATV, EF316, 1992

Christensen, E.A. Laminar-Turbulent Transition in the Rotating Driven Cavity Problem, AFM 93-12, 1993

Trinh, C.M. Turbulence Modelling of Confined Swirling Flows, Risø-R-647,1993

Mayer, K.E. Experimental and Numerical Modelling of Turbulent Flows and Heat Transfer in Staggered Tube Bundles, AFM 94-03, 1994

Mayer, S. Particle Motion in Unsteady Three-Dimensional Flow at Low Reynolds Numbers , AFM 94-04, 1994

Hansen, M.O.L. Vorticity-Velocity Formulation of Navier-Stokes Equations for Aerodynamic Flows, AFM 94-07, 1994

Hvid, S.L. Curvature Based Smoothing of Plane Cubic B-spline Curves, AFM 93-08, Surface Description using Bicubic B-splines, AFM 93-10, QM3D, 3D Netgenerering, Brugermanual, AFM 94-02 and Three-Dimensional Algebraic Grid Generation, AFM 94-08 1993-94

Walther, J.H. Discrete Vortex Method for Two-Dimensional Flow past Bodies of Arbitrary Shape Undergoing Prescribed Rotary and Translational Motion, AFM 94-11, 1994

Nim, E. Energidissipation og Masseoverførsel af Gas i og Omkring Statiske Miksere med Boblestrømning, Ph.D. under ATV, EF410, 1994

Sørensen, N.N. General Purpose Flow Solver Applied to Flow over Hills, Risø-R-827(EN), 1995

Filippone, A. Interaction of Potential Flow Model with the Navier-Stokes Equations for Rotor Aerodynamics, AFM 95-07, 1995

Jensen, E. Optimization of the Electromagnetic Flowmeter, AFM 95-09, 1995

Schmidt, J.J. Experimental and Numerical Investigation of Separated Flows, ET-PHD 97-01 1997

Nygreen, P. A Vorticity-Streamfunction Formulation of the Navier-Stokes Equations for Predicting Unsteady Flow past Bodies in Arbitrary Movement, ET-PHD 97-02, 1997

Sørensen, D.N. Aerodynamic Modelling and Optimization of Axial Fans, ET-PHD 98-01, 1998

Lennart, A.S. Experimental and Theoretical/Numerical Study of Evaporation from Shallow Pools of Organic Liquids, at Simulated Work Conditions, ET-PHD 98-02, 1998

Johansen, J. Unsteady Airfoil Flows with Application to Aeroelastic Stability, Risø-R-1116(EN), 1999

Ullum, U. Imaging Techniques for Planar Velocity and Concentration Measurements, ET-PHD 99-03,1999

Jørgensen, B.H. Low-Dimensional Modelling and Dynamics of the Flow in a Lid Driven Cavity with a Rotating Rod, ET-PHD 2000-02, 2000

Myllerup, L. Turbulence Models for Complex Flows, ET-PHD 2000-03, 2000

Pedersen, N. Experimental Investigation of Flow Structures in a Centrifugal Pump Impeller using Particle Image Velocimetry, ET-PHD 2000-05, 2000

Voigt, L.P.K. Navier-Stokes Simulations of Airflows in Rooms and Around a Human Body, ET-PHD 2001-00, 2001

Gaunaa, M. Unsteady Aerodynamic Forces on NACA 0015 Airfoil in Harmonic Translatory Motion, MEK-FM-PHD 2002-02, 2002

Pedersen, J.M. Analysis of Planar Measurements of Turbulent Flows, MEK-FM-PHD 2003-01, 2003

Mikkelsen, R. Actuator Disc Methods Applied to Wind Turbines, MEK-FM-PHD 2003-02, 2003

Ullum, T.U. Investigation of Turbulence and Flow Structures in Electrostatic Precipitator, MEK-FM-PHD 2003-03, 2003

Hjort, S. Incompressible Boundary Layer Instability and Transition, MEK-FM-PHD 2004-01, 2004

Reck, M. Computational fluid dynamics, with detached eddy simulation and the immersed boundary technique, applied to oscillating airfoils and vortex generators, MEK-FM-PHD 2005-01, 2005

Cavar, D. Large Eddy Simulation of Industrially Relevant Flows, MEK-FM-PHD 2006-02, 2006

Dam B.S. Experimental and numerical investigations of sprays in two stroke diesel engines, MEK-FM-PHD 2006-02, 2006

Zhu W.J. Aero-Acoustic Computations of Wind Turbines, MEK-FM-PHD 2007-02, 2007

Troldborg N. Actuator Line Modeling of Wind Turbine Wakes, MEK-FM-PHD 2008-06, 2008

Velte C.M. Characterization of Vortex Generator Induced Flow, MEK-FM-PHD 2009-07, 2009

Rasmussen J.K. Inside-out electrical capacitance tomography for downhole multiphase flow evaluation, MEK-FM-PHD 2010-04, 2010

DTU Mechanical Engineering
Section of Fluid Mechanics
Technical University of Denmark

Nils Koppels Allé, Bld. 403
DK- 2800 Kgs. Lyngby
Denmark
Phone (+45) 45 25 43 00
Fax (+45) 45 88 43 25
www.mek.dtu.dk
ISBN: 978-87-90416-53-9

DCAMM
Danish Center for Applied Mathematics and Mechanics

Nils Koppels Allé, Bld. 404
DK-2800 Kgs. Lyngby
Denmark
Phone (+45) 4525 4250
Fax (+45) 4593 1475
www.dcamm.dk
ISSN: 0903-1685